

Synthesis of Transition Metal Based Magnetic Nanostructures and Their Characterization for Suitable Applications

A thesis submitted for the award of the degree of

Doctor of Philosophy

in

Physics

By

Debasish Sarkar

Department of Physics

University of Calcutta

Kolkata, India

May 2013

To my beloved parents.....

Acknowledgements

I joined in the Department of Condensed Matter Physics and Material Science at S N Bose National Centre for Basic Sciences, Kolkata, to pursue my research work as a Junior Research Fellow (JRF) under the supervision of Prof. Kalyan Mandal and Dr. Madhuri Mandal. First of all, I would like to convey my sincere thanks to them for their ever inspiring guidance to carry out my research in this specific field of nanotechnology. I would also like to thank them for their valuable comments and suggestions which have made me more precise about my research. Their deep understanding on the subject along with their vast experience helped me tremendously during last few years. I am really grateful and indebted to them for their constant inspiration, encouragement and mental support without which my thesis wouldn't have seen the light of this day.

I would like to thank Dr. Gobinda Gopal Khan, DST Inspire Faculty, Center for Research in Nanoscience and Nanotechnology, University of Calcutta, for his guidance and collaborative work which has added an extra dimension to my research.

I must thank Prof. Arup Kumar Raychaudhuri, Director of S N Bose National Centre for Basic Sciences, Kolkata, for his way to inspire students to strive for knowledge and success. Thanks are also due to all the faculty members of this institute for their helping hands.

I am grateful to Dr. Prabir Kumar Halder for his consistent encouragement during my college life and also in doing research.

I am extremely thankful to Council of Scientific and Industrial Research (CSIR), Government of India, for providing the financial support through Junior Research Fellowship (JRF) for first two years and then through Senior Research Fellowship (SRF) for following years (CSIR Award No.: 09/575(0077)/2010-EMR-I).

I would like to express my sincere thanks to Dr. Dipankar Das, Scientist-F, UGC-DAE CSR Kolkata, for the SQUID facility to avail during entire course of my research work.

I am also thankful to Central Research Facility (CRF), Indian Institute of Technology, Kharagpur, and Indian Association for the Cultivation of Science (IACS), Kolkata, for offering their materials characterization facilities for this investigation.

Thanks are due to Prof. Dr. Manfred Albrecht, Technical University of Chemnitz, Germany, for the help in AFM/MFM measurements.

I am really grateful to my lab mates Bipul Da, Debabrata Da, Arka Da, Shyamsundar, Rajasree, Arup, Ashutosh, Rupali and Monalisha, for their valuable suggestions, active help and support during the full course of my research work. I don't want to specify anyone as senior or junior because we were really good friends as we are now and will always. I am also thankful to my batch mates specially Surojit, Saikat, Semanti, Santu (SRFs, SNBNCBS, Kolkata), Moumita (SRF, IACS, Kolkata) and many more for their unconditional help whenever I needed. I would like to especially thank Ashutosh and Arup for their extreme co-operation in nanowire project and instrument development, respectively. I am grateful to my childhood friends Santanu and Avijit for their immense support during this whole tenure.

I am obliged to all the technical staffs including Surojit Da, Shakti Da, Piyali, Samik, Dipankar, Indra and Urmi of S N Bose National Centre for Basic Sciences, Kolkata, for helping me in the material characterization during the entire course of work.

Above all, I am really very grateful to my beloved parents, for their devotions, their encouragement, support and their inspirations that have made me more courageous, dedicated and patient. This is why I owe them a lot and they are the reasons for what I am today. I feel myself very fortunate to have them as parents, Dipankar, Dibakar as elder brothers, Paramita and Tuku as sister-in-laws and Dibyanka as sweet niece. I would love to extend my warm gratitude to Varsha, for her continuous support and encouragement in different phase of my research. It is their unconditional love, well wishes and confidence on me that have made this thesis a success.

Debasish Sarkar

List of Publications

1. "Enhanced electrical, optical and magnetic properties in multifunctional ZnO/ α -Fe₂O₃ semiconductor nanoheterostructures by heterojunction engineering", **Debasish Sarkar**, G. G. Khan, A. K. Singh, and K. Mandal, *Journal of Physical Chemistry C*, 116 (44), 23540–23546 (2012).
2. "Enhanced band gap emission and ferromagnetism in Au decorated α -Fe₂O₃ nanowires due to surface plasmon and interfacial effects", G. G. Khan, **Debasish Sarkar**, A. K. Singh and K. Mandal, *RSC Advances*, 3, 1722-1727 (2013).
3. "Domain Controlled Magnetic and Electric properties of variable sized Magnetite Nano-Hollow spheres", **Debasish Sarkar**, M. Mandal and K. Mandal, *Journal of Applied Physics*, 112, 064318 (2012).
4. "Detail study on ac-dc magnetic and dye absorption properties of Fe₃O₄ hollow spheres for biological and industrial application", **Debasish Sarkar**, K. Mandal, M. Mandal, *Journal of Nanoscience and Nanotechnology* (Accepted, 2012).
5. "Static and dynamic magnetic characterization of DNA templated chain-like magnetite nanoparticles, **Debasish Sarkar** and M. Mandal, *Journal of Physical Chemistry C*, 116, 3227–3234 (2012).
6. "Fabrication of Biologically Functionalized, Electrically Conducting and Aligned Magnetic Nanoparticles", **Debasish Sarkar**, K. Mandal, and M. Mandal, *IEEE Transactions on Magnetism*, 47, 3163-3166 (2011).
7. "Synthesis of Chainlike α -Fe₂O₃ Nanoparticles in DNA Template and Their Characterization", **Debasish Sarkar**, K. Mandal, and M. Mandal, *Nanoscience and Nanotechnology Letters*, Vol. 3, 1–5 (2011).
8. "Self-assembly of Fe₃O₄ Nanoparticles in Chainlike Array on DNA Template, their Characterization and Cancer Cell Identification", M. Mandal, **Debasish Sarkar**, A. Bandyopadhyay, *Journal of International Academy of Physical Sciences*, 15, 503-506 (2011).
9. "A detail study of the structural and physical properties of tri-functional Ni_{core}-Au_{shell} nano-chain engineered by DNA", B. Das, **Debasish Sarkar**, P. Das, K.

Mandal and M. Mandal, *Journal of Nanoscience and Nanotechnology* (Accepted, 2013).

10. "High Performance Pseudocapacitor Electrodes Based on α -Fe₂O₃ / MnO₂ Core - Shell Nanowire Heterostructure Arrays", **Debasish Sarkar**, G. G. Khan, A. K. Singh, and K. Mandal (Communicated).
11. "Synthesis of Magnetite (Fe₃O₄) Hollow Spheres and a Study on Magnetic Properties for Hyperthermia Application", **Debasish Sarkar**, M. Mandal and K. Mandal (Communicated).
12. "Mesoporous α -Fe₂O₃ nanoribbons and its multifunctional properties", **Debasish Sarkar**, M. Mandal and K. Mandal (Communicated).

Contents

Chapter 1 Introduction

1. Introduction	1
1.1 Nanoparticles and Nanostructures	1
1.2 Magnetic Nanostructures	2
1.3 Magnetic Properties	3
1.3.1 Magnetic Anisotropy Energy	3
1.3.1.1 Magnetocrystalline Anisotropy	4
1.3.1.2 Shape Anisotropy	5
1.3.1.3 Surface Anisotropy	5
1.3.2 Magnetic Domain Theory	5
1.3.3 Saturation Magnetization	7
1.3.4 Magnetic Hysteresis	7
1.4 Electronic Conductive Property	8
1.5 Optical Properties	9
1.6 Electrochemical Properties	11
1.7 Iron and its Oxides	13
1.8 Motivation and Objectives of Thesis	19
1.9 Organization of the Thesis	21

Chapter 2 Experimental Details

2. Material Synthesis and Characterization Techniques	27
2.1 Preamble	27
2.2 Nano Designing approach	27
2.2.1 Top-Down approach	28
2.2.2 Bottom-up approach	28
2.3 Formation of Nanoparticles	28
2.4 Fabrication Techniques of Different Nanostructures	31
2.4.1 Wet chemical Method	31
2.4.2 Chemical Co-precipitation	31
2.4.3 Solvothermal Method	33
2.4.4 Electrodeposition Technique	35
2.4.5 Direct Current (DC) sputtering deposition	37
2.5 Phase and Morphology Characterization Techniques	38
2.5.1 X-ray diffractometer	38
2.5.2 Electron Microscopes	39

2.5.3 X-ray Photoelectron Spectroscopy (XPS)	42
2.6 Magnetic Characterization Techniques	43
2.6.1 Vibrating Sample magnetometer (VSM)	43
2.6.2 Superconducting Quantum Interference Device (SQUID)	44
2.6.3 Atomic and Magnetic Force Microscopy (AFM and MFM)	45
2.6.4 AC Magnetic Measurement Technique	47
2.7 Optical Characterization Techniques	50
2.7.1 UV Visible Absorption Spectrometer	50
2.7.2 Circular Dichroism (CD) Spectrometer	51
2.7.3 Fourier Transformed Infrared Spectroscopy (FTIR)	52
2.7.4 Photoluminescence (PL) Spectroscopy	53

Chapter 3 Magnetite Nano - Hollow Spheres

3. Nano-Hollow Spheres of Magnetite: Facile Synthesis, Characterization and Applications **55**

3.1 Preamble	55
3.2 Synthesis of Fe ₃ O ₄ hollow spheres of different diameters	56
3.3 Results and Discussions	57
3.3.1 Phase and morphology	57
3.3.2 Magnetic Measurements	62
3.3.3 Frequency Dependent Measurements	72
3.3.4 Dynamic magnetic properties of hollow spheres	78
3.3.5 Dye adsorption properties of Fe ₃ O ₄ hollow spheres	86
3.4 Conclusion	95

Chapter 4 Nanochains of Metal and Metal Oxides

4. Fabrication of Biologically Functionalized, Chainlike Magnetic Nanoparticles

4.1 Preamble	99
4.2 Sample Preparation	100
4.2.1 Synthesis of Fe _{core} - Au _{shell} nanochain	100
4.2.2 Synthesis of α-Fe ₂ O ₃ Nanochain using DNA	101
4.2.3 Synthesis of DNA templated Fe ₃ O ₄ nanoparticles of different sizes	102
4.3 Results and Discussions	103
4.3.1 DNA templated Fe _{core} - Au _{shell} nanochain	103
4.3.2 DNA templated α-Fe ₂ O ₃ nanochain	112
4.3.3 DNA templated Fe ₃ O ₄ nanochain	119
4.4 Conclusion	134

Chapter 5 α -Fe₂O₃ Nanowires and Their Multidimensional Properties

5.1 Au and ZnO Modified α -Fe₂O₃ Nanowires: Enhanced Electronic, Optoelectronic and Magnetic properties 139

5.1.1 Preamble	139
5.1.2 Experimental	140
5.1.3 Results and Discussion: Au NP decorated α -Fe ₂ O ₃ nanowires	141
5.1.4 Results and Discussions: ZnO/ α -Fe ₂ O ₃ semiconductor nano-heterostructures (SNHs)	150
5.1.5 Conclusion	157

5.2 High Performance Pseudocapacitor Electrodes Based on α -Fe₂O₃/MnO₂ Core - Shell Nanowire Heterostructure Arrays 158

5.2.1 Preamble	158
5.2.2 Experimental Methods	159
5.2.3 Results and Discussion	160
5.2.4 Conclusions	172

Chapter 6 Conclusion and Scope for Future Work

6.1 Epilogue	178
6.2 Scope for Future Work	180

Chapter 1 | Introduction

This introductory chapter consists of the detailed literature review of various works that motivated me to work in this specific field and also a brief outline of my entire work.

1. Introduction

1.1 Nanoparticles and Nanostructures

The term nanotechnology refers to a science that deals with the synthesis, characterization and applications of various materials having extremely low dimension, in the range of 1 to 100 nm (1 nm = 10^{-9} m). Reduction of the size introduces physical and chemical constraints along one or more dimensions of the nanostructured materials leading to some novel even completely new properties in these materials in comparison to their bulk counterpart. These novel properties arise in these functional nanomaterials when their size becomes comparable to or less than certain characteristics length scales such as carrier mean free path, superconducting coherence length, magnetic domain wall width, spin diffusion length etc [1]. Due to the complex design of the nanostructures and also interplay between the constituent materials, they exhibit various properties depending on their size, shape and morphology. It has been found that materials having building blocks with same composition but different morphology can have different properties [2, 3]. Magnetic behavior, chemical reactivity, color, electronic excitation, charge transport etc. of metal or semiconductors nanoparticles have been found to be influenced significantly by their size. With reduction of size it has been observed that metals show non-metallic band gaps and thus showing electronic absorption spectra, clusters of non-magnetic materials show magnetic ordering, hence leading to giant magnetoresistance, enhanced coercivity and remanance and other properties of magnetic materials. As shown in Fig. 1.1, density of states (DOS) of electrons in the material changes from a continuous function ($D \propto E^{1/2}$) to delta function as we move from bulk to nanoscale, i.e. movement of electrons is constrained within an infinite potential well for extremely small particles. This change in DOS of electrons affects the macroscopic properties of the materials giving rise to a wide variety of new phenomena. These novel properties of the functional materials can also be tailored by manipulating self-assembly and self-organizing techniques of their nanoscale building blocks to produce a self-sustaining well-defined nanostructure [1]. Not only the fabrication of nanostructures of different functional materials is important, their

characterization is much more challenging. It is very important to fabricate the arrays of ultrafine nanostructures over macroscopic areas; i.e. ordered arrays of nanostructures is much more needed because one can then probe the individual and collective behavior of the nanomaterials in a well-defined and reproducible fashion.

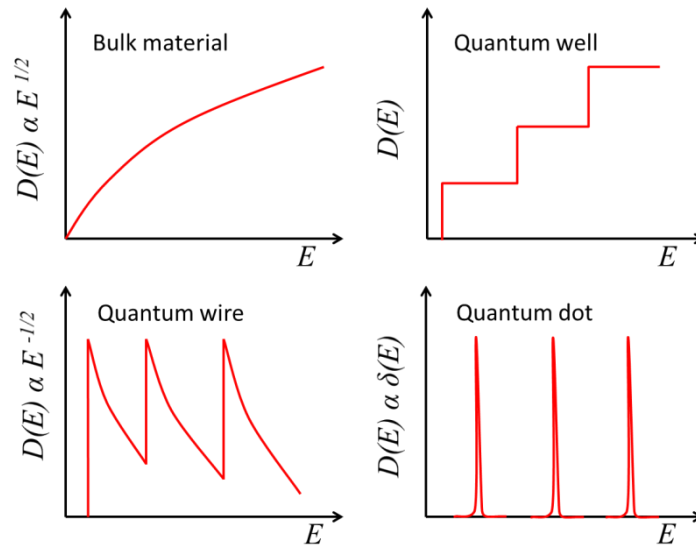


Figure 1.1 Change in density of states (DOS) with reducing size: starting from bulk to quantum well to quantum wire to quantum dot.

1.2 Magnetic Nanostructures

Recent advancement in magnetism and magnetic materials has made magnetic nanostructures a matter of immense research interest because of their wide scientific and technological applications such as in magnetic recording, magnetic random access memory (MRAM), magnetic switches [1, 4], magnetic fluids [5], catalysis [6, 7], biotechnology/biomedicine [8], contrast agents in magnetic resonance imaging (MRI) [9], water treatment [10], gas sensor, protein separation [11], cancer cell destruction [12], hyperthermia therapy [13] etc. This advancement takes place due to significant development in the theory, processing and characterization techniques that enables the scientists to design various interesting nanostructures of different magnetic materials. Not only the pristine nanostructures, fabrication of hybrid nanostructures is also preferable where one can enhance the basic properties of the base material and also can induce some new properties by

suitably choosing the other composite material(s) for hybrid system. Transition metal (TM) based magnetic nanostructures are of special interest because of their high saturation magnetization, coercivity, remanance and other fascinating electronic and opto-electronic properties. These unique properties make the TM based magnetic nanostructures a very special candidate for spintronics and optical devices in modern electronics technology. In bulk materials, magnetic properties are attributed to the collective behavior of individual particles or grains and how these grains interact with each other. However, with decreasing size surface effect dominates over the volume and hence reason behind different characteristic properties changes.

During last few decades, researchers have thoroughly investigated size and morphology dependent physical and chemical properties of different magnetic nanostructures including nanoparticles, nanorods, nanowires, nanotubes, tiles, blocks, flowers etc [14, 15]. With advancement in science several new techniques have been developed to fabricate intricate nanostructures having different compositions. However, before any practical application it is necessary to know about different parameters governing or influencing the characteristic properties (such as magnetic, optical, electronic etc.) of these nanostructured functional materials.

1.3 Magnetic Properties

1.3.1 Magnetic Anisotropy Energy

Magnetic anisotropy is the dependence of magnetic energy on the relative orientation of magnetization direction with the crystal axis. The associated energy is called the anisotropy energy. In a material, the magnetic anisotropy may arise due to the symmetry of the crystalline lattice or due to specific shape of that particular piece of material. In absence of any external magnetic field there is an energetically favorable direction for spontaneous magnetization, called the easy axis of that particular material that can be determined by sources of various magnetic anisotropy energies as given below.

1.3.1.1 Magnetocrystalline Anisotropy

Magnetocrystalline anisotropy is the most prominent contribution to the magnetic anisotropy which arises due to the symmetry axis of the local atomic structure. It arises because of spin-orbit coupling which is the exchange interaction via spin-spin coupling between neighboring spins. This strong spin-orbit coupling keeps the neighboring spins to be parallel or anti-parallel to each other. However, the associated energy is isotropic and therefore the coupling cannot contribute to the crystal anisotropy. Magnitude of this magnetocrystalline anisotropy depends on the ratio of the crystal field energy and spin orbit coupling [16]. There are two models to describe the magnetic anisotropy; (a) Néel model which says that the magnetic anisotropy arises due to pair interactions between two essentially magnetic ions [17] and (b) Single-ion or crystal field model which describes crystal field interactions with atoms that are not essentially magnetic [18]. As the magnetocrystalline energy is associated with the relative orientation of the total magnetization with respect to the magnetic easy axis of the crystal, i.e. θ , the magnetocrystalline anisotropy energy can be expressed as,

$$E_k = V(K_0 + K_1 \sin^2 \theta + K_2 \sin^4 \theta) \quad (1.1)$$

Where, K_n ($n= 0, 1, 2 \dots$) are the magnetocrystalline anisotropy constants. K_0 is θ independent, arbitrary and thus an irrelevant parameter.

In cubic crystals, like magnetite (Fe_3O_4), the magnetocrystalline anisotropy is given by a series expansion in terms of the angles between the magnetization direction and cube axes. However, it is sufficient to retain only the first two terms in the series expansion where each of the two terms contains an empirical constants associated with them known as first and second order anisotropy constants (K_1 and K_2 , respectively). In case of hexagonal crystals like hematite ($\alpha\text{-Fe}_2\text{O}_3$), magnetization generally lies along the c-axis, which is the direction of the anisotropy axis, leading to its antiferromagnetic behavior at lower temperature. Upon significant thermal excitation, these spins can tilt slightly along the basal plane rendering ferromagnetic behavior of the material.

1.3.1.2 Shape Anisotropy

In case of polycrystalline material with no preferred direction of its grains, has no overall crystalline anisotropy. If the material is perfectly spherical in shape, then the external applied field will magnetize it in every possible direction in same extent. However, if the material is not spherical but having a preferred growth direction, then it is easy to magnetize it along the long axis than along the short one. This type of crystalline anisotropy is known as shape anisotropy. In this case, demagnetization field comes into play which actually determines the actual field inside a specimen. For shape anisotropy, $K_1 = \mu_0(1-3D_m)M_s^2 / 4$, where D_m is the demagnetization factor which is 0 for long cylinders, 1/3 for spheres and 1 for plates [19].

1.3.1.3 Surface Anisotropy

This anisotropy was first introduced by Néel [17] in case of materials having complicated structures and morphologies such as monolayer transition metal films, multilayers, rough surfaces and especially in smaller particles. Generally surface anisotropy in nanoparticles is found to be one order of magnitude higher than the bulk value which is due to larger fraction of superficial ions in smaller particles [20, 21]. This surface spins are disordered because they resides within an uncompensated coordination sphere due to broken bonds, vacancies and also due to bond formation with some organic molecule [20]. Thus the surface anisotropy makes the surface layer magnetically harder than the core region of a fine nanoparticle. For a spherical particle the effective anisotropy energy (K_{eff}) can be written as, $K_{eff} = K_b + (6/D)K_s$, where K_b and K_s are the bulk and surface anisotropy energy density, respectively, and D is the diameter of the particle.

1.3.2 Magnetic Domain Theory

Domains constitute the fundamental concepts of magnetism in ferromagnetic or ferrimagnetic materials. Each magnetic material consists of small regions, called magnetic domains (having size 1-100's μm) that have uniform magnetization; i.e. the moments in individual domains are aligned in the same direction. These domains

are separated by the domain walls where the magnetization must change direction from that in one domain to that in the other one. These domain walls have finite width that is determined by exchange and magnetocrystalline energy. The magnetic behavior can be subdivided into three ranges depending on the grain size, as described below [22].

Large sized particles contain multidomain (MD) configuration. With increasing size they behave as bulk material. Domain wall nucleation and motion is the main mechanism behind the magnetization reversal of these MD particles.

With decrease of grain size, a critical size is reached where the grain can't accommodate a wall. Below this critical size, the grain contains a single domain (SD). An SD grain is uniformly magnetized to its saturation magnetization and magnetically hard as characterized by high coercivities and remanance.

With further decrease of grain size within SD regime, another critical threshold is reached, below which coercivity and remanance becomes zero. In this condition, the grain becomes superparamagnetic (SPM) even when the temperature is below the Curie or the Néel temperature. In SPM particles, the magnetic relaxation process can be represented by Néel - Arrhenus equation [20, 23], given as

$$f = f_0 \exp\left(-\frac{KV}{k_B T}\right), \quad (1.2)$$

Where, f_0 is the Larmour frequency lying in the range of 10^9 - 10^{12} sec⁻¹, K is the anisotropy constant, V is the particle volume, k_B is Boltzmann constant and T is the absolute temperature. As the size of the SPM particles are too small, therefore the small anisotropy energy ($E_A = KV$) allows the magnetization to fluctuate randomly between two energetically favorable ground states (up and down states) upon small thermal agitation; i.e. they behave paramagnetically, however their magnetization is much higher than the typical paramagnets. Hence the term superparamagnetism, which denotes a much higher susceptibility value as compared to that a simple paramagnet. For this type of particles, total magnetic moment at $T > 0K$ and in absence of any magnetic field will average to zero.

The exponential nature of the relaxation time on V and T makes it possible to define a blocking temperature, T_B (at constant volume), or blocking volume V_B , (at constant temperature) at which the magnetization goes from an unstable condition ($1/f_0 \ll t$) to a stable one ($1/f_0 \gg t$). Superparamagnetism is identified by three characteristics of magnetization curves. A superparamagnetic magnetization curve has zero coercivity and remanence, existence of T_B below which ferromagnetic order reappears and magnetization curves superimpose when plotting as H/T above T_B .

1.3.3 Saturation Magnetization

Saturation magnetization (M_s) is the maximum possible magnetization of a magnetic material under a large external field. Assuming each atom has the same magnetic moment; M_s is dependent on the magnitude of the atomic moment (μ) and also the density of atoms (n). M_s of nanomaterials is found to be affected significantly by their size and their synthesis procedure as there is a large fraction of superficial ions in nanomaterials. As we move from bulk to nanoscale, M_s decreases which may be due to different reasons. According to Gangopadhyay et al. [24] this reduction in M_s is due to formation of a disordered nonmagnetic shell layer over the magnetically aligned core in nanomaterials. According to other models this reduction in magnetization was due to surface spin canting. Similar argument was given by Parker et al. [25] where it has been suggested that the spin canting occurs in the whole sample due to quantum size effects. Moreover, for a bulk material where the temperature dependence of M_s is found to Bloch's $T^{3/2}$ law, the nanoparticles show a deviation from this $T^{3/2}$ behavior.

1.3.4 Magnetic Hysteresis

Magnetic hysteresis loop which is a plot of the variation of magnetization under applied magnetic field is the most common way to represent the bulk properties of a magnetic material. This hysteresis behavior, i.e. the inability to trace back the same magnetization curve is related to the presence of domains within the material. When these domains are magnetized in one direction, it needs some energy to turn them back again. This property of magnetic materials is very useful for

magnetic storage application. Magnetic anisotropy yields easy magnetization directions corresponding to local energy minima and energy barriers that separate the easy directions in a single domain particle. On an atomic scale, the barriers are easily overcome by thermal fluctuations, but on nanoscale or macroscopic length scales excitations are usually too weak to overcome the barriers. This is observed as magnetic hysteresis. The most useful information that one can get from the hysteresis loop is the maximum energy product which is the product of the maximum field (H_{max}) and the maximum magnetization (M_{max}). This is a measure of the maximum amount of work that can be performed by the magnetic material. Coercive field (H_C) is the field that is required to reduce the remanance magnetization (M_R) to zero. It is a measure of how strongly a magnetic material can oppose an external magnetic field. M_R is the magnetization of a magnetic material when the field is reduced to zero after its complete magnetization. For single domain non-interacting particles, Stoner and Wohlfarth theoretically determined that H_C is related to M_S and K according to the relation, $H_C = 2K / M_S$, where K is the anisotropy constant. It has been found that the order of magnitude of K for nanoparticles is higher than their corresponding bulk values which can be attributed to the exchange interaction at the core-shell interface, and/or the magnetoelastic energies caused by stress/pinning induced by the lattice mismatch at the coated surface [20, 21].

1.4 Electronic Conductive Property

The effect of size on the electrical conductivity of nanomaterials and also nanostructures is very intricate as it depends on various independent mechanisms. These mechanisms can be summarized into following categories; surface scattering including grain boundary effect, quantized electronic conduction, coulomb charging and tunneling, increase of band gap and change of microstructure [26]. In addition, improvement in crystal perfection, such as fewer defects, dislocations and impurities, would affect the electrical conductivity of the nanostructures also. Electron collisions with phonons are the source of thermal or phonon contribution, which increases with temperature. However, impurity atoms, defects such as

vacancies, and grain boundaries locally destroy the periodic electric potential of lattice and effectively causes electron scattering. Smaller nanocomposites have lots of grain boundaries, which behave as potential barrier for free flow of charge carriers, electrons and holes which cause reduction of electrical conductivity in smaller particles [27, 28]. Surface scattering of electrons also reduces the electrical conductivity as seen in nanowires and thin films. When the dimension of thin films or nanowires becomes comparable or smaller than the electron mean free path, the motion of electrons will be interrupted through elastic or inelastic collisions with the surface. In elastic collisions the electrons reflect in the same way and do not lose its energy or momentum. As a result the conductivity remains same as in the bulk, i.e. there is no size effect. However, in case of inelastic collisions, the electron trajectory or scattering angle after collision is random. The scattered electrons lose velocity parallel to the conduction direction and the electrical resistivity decreases. So, there will be a size effect on electrical conductivity [26]. However, in case of semiconductor nanowires it has been found that the crystallinity plays an important role on their conducting property. For example, in case of defect free Si nanowires having four atoms per unit cell, generally three conductance channels are observed [29]. Whereas, in the case of defect induced Si nanowires the number of such conductance channels varies causing significant variation in their conductance behavior. Doping also changes the conductivity. For example, annealing of ZnO nanorods in H₂ atmosphere introduces n-type carriers into it that changes its I-V characteristics [30].

1.5 Optical Properties

Nanoparticles and ordered nanostructures are also significantly important from the view point of optical characterization and device applications. Optical properties arises in materials (both bulk and nano regime) due to electronic transition between different energy states of those materials by absorbing photons. Semiconductors are well known for exhibiting optical properties because of their intrinsic band structure which allows electronic transition between valence band (VB) and conduction band (CB). However, with change in size from bulk to

nanoscale the band structure (specially the band gap) and density of states (DOS) of charge carrier changes significantly that determines their inherent optical properties. So, understanding the interplay between the nanoscale structure and optical properties of semiconductor materials is very important for their huge applications in solar cells [31] and optoelectronic devices [32]. Finite size effects in nanomaterials are normally investigated in isolated nanoparticles where the size can be tuned to vary the band gap. Now with the reduction of size, band gap will increase due to the additional energy from the degree of confinement and coulomb correlations. So, the effective band gap in nanomaterials becomes,

$$E_g = E_g^0 + \frac{\pi^2 n^2 \hbar^2}{2\mu r^2} - \frac{1.8e^2}{\epsilon r} \quad (1.3)$$

Where, E_g^0 is the band gap of the bulk material, r is the size of the nanocrystals, e is the electronic charge, ϵ is the effective dielectric constant and μ is the reduced effective mass of electrons and holes for a particular material [33]. For example, α -Fe₂O₃ is an n-type semiconductor having band gap (E_g) of 2.14 eV is a promising material as a photoelectrode. However, it has been observed that with decreasing size of α -Fe₂O₃, the quantum confinement effect begins to influence its optical properties when its size becomes smaller than 6 nm. The largest blue shift of about 1.0 eV has been observed for 2nm size α -Fe₂O₃ crystallites [33]. Not only the semiconductors, metals that don't have any band gap in bulk state can still show optical response in nano-regime. One of the interesting examples is that of the size dependent optical response of colloidal gold particles. The colloid changes color from purple/blue (for larger particles) to intense red color as the size of the particles reduces to less than 100 nm. This type of color change is associated with the introduction of band gap and it's widening with reduction of the size of metallic gold [34]. On the other hand, unusual green color has been observed for magnetite hollow spheres with a diameter of 650 nm and shell thickness of 40 nm, in contrast with usual bulk magnetite appearing black [35]. This color of magnetite is attributed to the Mie scattering as the size of the spheres (here 650 nm) is comparable to the wavelength of green light.

1D semiconductor nanostructures exhibit interesting luminescence characteristics that are quite different from their bulk counterparts. The photoluminescence (PL) study of the semiconductor nanowires is enriched with the information of the optical properties such as band-edge emission, radiative efficiency, trap states, carrier and photon confinement [36]. Light emission from the 1D semiconductor nanostructures are addressed on the basis of the emission intensity, width and peak of the emission spectra and the presence of impurity states in the spectra. Intense and sharp PL emission peak near the band edge is observed for the high quality crystalline nanowires. However, the information about the quality of the NWs can be derived from the width of the PL spectra. The low diameter (20–30 nm) nanowires possessing high optical quality, is believed to be due to better surface properties and lower level of impurities. The presence of the defect states in the semiconductor nanowire leads to the PL emission peaks at wavelengths much longer than the band-edge emission. However, the optical absorption and emission from NWs has been reported to be polarized along the long axis of the nanowires [37].

1.6 Electrochemical Properties

Study of the electrochemical properties of various nanoparticles and nanostructures of different redox active materials has achieved immense research interest for high potentiality of applications of these materials in synthesis of green energy and also its storage. Electrochemistry is a branch of chemistry that deals with the chemical reactions which take place in an ionic conductor, i.e. an electrolyte in presence of an electron conductor such as electrode of a metal or semiconductor. During an electrochemical process, oxidation-reduction (redox) reactions take place between electrode and electrolyte which release energy in the form of electric current. From this aspect of charge storage and release, scientists have developed a new type of energy storage device known as electrochemical capacitors, also known as supercapacitors, by employing the electrochemical activity of redox active materials. Depending on the charge storage mechanism supercapacitors have been classified into two categories, electrical double layer capacitors (EDLCs) and pseudocapacitors (or redox supercapacitors) [38]. EDLCs, using carbon-based active

materials with high surface area, build up electrical charge at the electrode/electrolyte interface. Charge separation occurs on polarization at the electrode-electrolyte interface, producing what Helmholtz described in 1853 as the double layer capacitance C :

$$C = \frac{\epsilon_0 \epsilon_r A}{d} \quad (1.4)$$

Where, ϵ_r is the electrolyte dielectric constant, ϵ_0 is the dielectric constant of the vacuum, d is the effective thickness of the double layer (charge separation distance) and A is the electrode surface area. On the other hand, pseudo-capacitors utilize fast and reversible surface or near surface reactions for charge storage. Metal oxides such as RuO_2 , Fe_3O_4 , MnO_2 or Co_3O_4 [39-41], as well as electronically conducting polymers, have been studied extensively during past few decades because of their high theoretical specific capacitance [38]. The specific pseudo-capacitance exceeds that of the carbon based EDLCs. They can complement or replace batteries in electrical energy storage and harvesting applications, when high power delivery or uptake is required. A notable improvement in performance has been achieved through recent advances in understanding charge storage mechanisms and the development of advanced nanostructured materials. As the pseudocapacitors store charges in the first few nanometers from surface, decrease of the particle size will increase the usage of active material. Recent reports suggest that supercapacitors based on thin films (thickness about several tens of nanometers) exhibit high specific capacitance due to their high specific surface area. For example, a thin film of MnO_2 provides capacitance as high as 698 F g^{-1} [42]. Similarly, Sugimoto's group has prepared hydrated RuO_2 nano-sheets with capacitance exceeding $1,300 \text{ F g}^{-1}$ [43] Nanostructures of redox active materials with significantly high surface area (such as nanowires, nanoflowers, nanoparticles, nanotubes etc.) have been reported as the efficient pseudocapacitive materials for energy storage. Cobalt oxide is another redox active material with very high theoretical specific capacitance of about 3560 Fg^{-1} . There are several reports on the synthesis and pseudocapacitor properties of various Co_3O_4 nanostructures such as nanowires, nanotubes and nanorods, nanosheets and nanoflakes, nanobowls, nano flowers and nanonets on different

substrates [41]. Not only that, combination of pseudo-capacitive nanomaterials, including oxides, nitrides and polymers, with the latest generation of nanostructured lithium electrodes has brought the energy density of electrochemical capacitors closer to that of batteries.

1.7 Iron and its Oxides

Iron is the most common element (by mass) forming the earth as a whole, forming much of earth's outer and inner core. It has the atomic number of 26 and is the first metal in transition metal series and also fourth most common element in earth's crust. Iron atoms arrange themselves in one of two stable crystal structures called the body-centered cubic (bcc) structure and the face-centered cubic (fcc) structure, as shown in the Fig. 1.2. The body-centered cubic structure of iron, which is called ferrite, is stable below 911°C and is known as α -iron. Above this temperature, face-centered cubic structure, which is called austenite (γ -iron), is stable. Above 1394°C , up to the melting point of about 1539°C , the body-centered cubic crystal structure is again the more stable form of δ -iron. The phenomenon through which a crystal structure changes from one to another form due to a change in temperature is referred to as a phase transformation and the phase diagram of pure iron is shown in Fig. 1.3. The temperature at which this phenomenon occurs is called the transformation temperature.

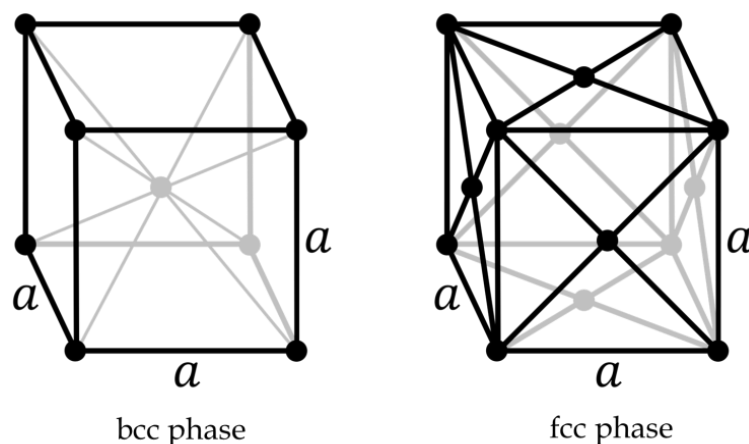


Figure 1.2 Crystal structure of iron; ' a ' represents the lattice parameter which is 0.28 nm.

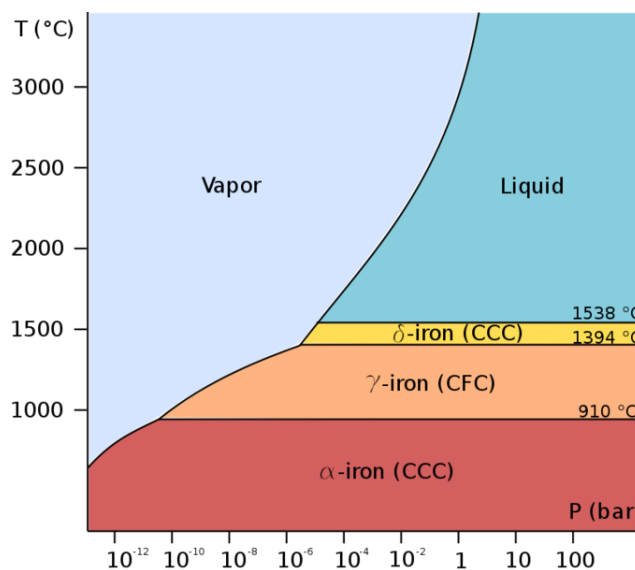


Figure 1.3 Low pressure phase diagram of pure iron.

Iron has intrinsic magnetic moment due to its unfilled d -orbital ($[\text{Ar}] 3d^6 4s^2$). However, when it passes through the Curie temperature, its crystalline structure remains the same but the magnetic domain structure changes, where each domain contains iron atoms with a particular spin direction. The intrinsic ferromagnetic behavior of iron has made it a perfect candidate for fabrication of magnetic memory devices. Moreover, nanoparticles of iron have been used for a wide range of sophisticated bio-medical applications [44]. However, decrease in particle size increases its reactivity and its magnetic properties are then dominated by superparamagnetism and surface effects [45]. Several techniques have already been adopted to passivate the surface of these nanoparticles by some inert shell including SiO_2 , Au, Ag, polymer etc [44]. Kauzlirch et al. demonstrated that the Au coated iron nanoparticles have high longitudinal relaxivity (r_1) ($6.87 \text{ mM}^{-1}\text{s}^{-1}$) and these nanoparticles are very effective as T_1 contrast agent in MRI [46]. This shell also stabilizes the iron core as iron is very prone to be oxidized in ambient atmosphere.

Like other group eight elements, iron exists in a wide range of oxidation states from +2 to +6, although +2 and +3 are most common. Altogether there are sixteen iron oxides. These compounds include Iron (II) Oxide (Wüstite, FeO), Iron (III) Oxide (Hematite ($\alpha\text{-Fe}_2\text{O}_3$)), Iron (II, III) Oxide (Magnetite (Fe_3O_4)) and their derivatives. Iron oxides, especially Fe_2O_3 yield pigments that have been widely used in cosmetic

industries because of their non-toxic, moisture resistant and non-bleeding nature. On the other hand, magnetite is well known for its high magnetic properties and very efficient for magnetic recording.

Hematite ($\alpha\text{-Fe}_2\text{O}_3$)

Hematite is an n-type semiconductor having a band gap of 2.14 eV and is the most stable iron oxide under ambient conditions, has versatile scientific and technological applications such as in catalysis, pigments, magnetic materials, gas sensors, for efficient conversion of solar energy, electrodes for supercapacitors and also li-ion batteries [47-52]. Its size and shape dependent physical properties have attracted much attention. Bulk hematite is antiferromagnetic in nature. However, in 1950, Morin reported a phase transition of hematite from antiferromagnetic (AFM) to a weakly ferromagnetic (WFM) state on heating above $T_M = 260\text{K}$ [53]. Not only magnetic properties, its semiconducting nature makes it also very efficient for electronic and opto-electronic applications.

Hematite ($\alpha\text{-Fe}_2\text{O}_3$) lattice is Trigonal. It has hexagonal unit cell with space group R-3c (No. 167). In bulk state, hematite has the lattice parameters as $a = 5.038 \text{ \AA}$, $c = 13.772 \text{ \AA}$ and $\alpha = \beta = 90^\circ$, $\gamma = 120^\circ$ [47, 54]. Iron and oxygen atoms are arranged in alternate planes (basal planes) along the [001] direction, as shown in Fig. 1.4.

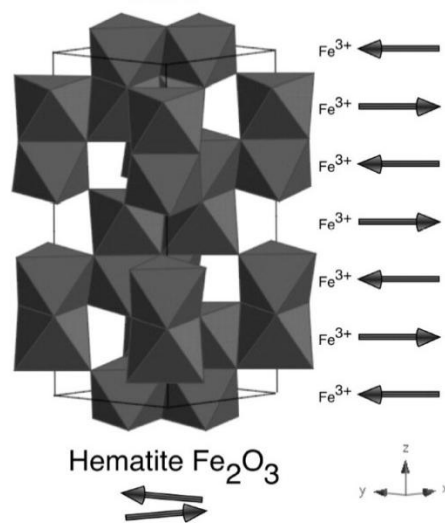


Figure 1.4 Representation of the crystal structure of $\alpha\text{-Fe}_2\text{O}_3$; the arrows show the directions of Fe^{3+} ions in the alternate planes of the lattice.

α -Fe₂O₃ has an anti-ferromagnetic spin structure, in which all the spins in same c-plane are aligned parallel whereas the spins in the adjacent planes, the A and B planes, are aligned anti-parallel to each other. The spin axis is along the easy axis, which is the c-axis below a certain temperature $T = 260$ K known as Morin transition temperature (T_M). Below this T_M , spin arrangement of α -Fe₂O₃ is antiferromagnetic. However, above this temperature, the spin axis changes from c-axis to c-plane giving rise to a canted spin structure which results a weak or parasitic ferromagnetism in the system. At Néel temperature, which is about 956 K, the common transition from antiferromagnetic to paramagnetic state takes place. However, in case of nanomaterials, the magnetic behavior changes significantly. For example, for polycrystalline hematite nanowires T_M and T_N were reported to be 80 and 350 K, respectively, much lower than those corresponding to the bulk material [55, 56]. Similarly, for ellipsoid-, spindle-, flattened- and rhombohedra-shaped α -Fe₂O₃ samples, prepared in solvothermal technique, the T_M is found to shift from highest 251.4K for ellipsoid to lowest 220.8K for rhombohedra structure, with intermediate values of T_M for the other two structures [57]. Cao et al. also showed lowering of Morin temperature for single crystalline dendritic micro-pine like nanostructures of α -Fe₂O₃ as compared to the bulk material [58]. Sorescu et al. have prepared different hematite nanostructures (such as plate like, needle like etc.) by hydrothermal method and they have reported the existence of weak ferromagnetic phase above T_M and coexistence of weakly ferromagnetic and anti-ferromagnetic phase below T_M [59].

There are several reports on the formation and growth mechanism of various nano- and microstructures of α -Fe₂O₃, such as nanospheres, nanowires, nanorods, spindles, cage like structures, cubes etc [47, 58, 60, 61]. According to Pu et al., concentration variation of precursor could result controlled variation of size and morphology of α -Fe₂O₃ [60]. Wen et al. synthesized vertically aligned α -Fe₂O₃ nanobelt and nanowire by direct oxidation of iron substrate under O₂ atmosphere [61]. Ivanisevic et al. described a unique way to fabricate heterostructured nanowires of α -Fe₂O₃ using DNA as a template [62].

Magnetite (Fe_3O_4)

Transition metal ferrites $\text{M}^{\text{II}}\text{Fe}_2^{\text{III}}\text{O}_4$ are magnetic materials which have a cubic spinel-type structure and have been extensively used in various technological applications during last few decades [63, 64]. Among various nanocrystalline ferrites, magnetite (Fe_3O_4) has attracted special interest because of its high potentiality for diverse applications in electronics, spintronics and also in biomedical fields (as discussed earlier). Moreover, Fe_3O_4 has high Curie temperature of about $T_C \sim 850$ K and nearly full spin polarization at room temperature; both properties make it suitable for fabrication of magneto-electronic and spin-valve devices based of thin films [65].

Magnetite is a prototype of inverse spinel. It has a cubic spinel structure with lattice parameter of 8.397 \AA (space group $Fd\bar{3}m$), at room temperature. The unit cell contains 32 O^{2-} ions arranged in a face centered cubic (*fcc*) lattice. Each unit cell has eight Fe^{3+} ions at the tetrahedral *A* sites with four nearest neighbor O^{2-} ions, and eight Fe^{3+} and eight Fe^{2+} ions at the octahedral *B* sites with six nearest neighbor O^{2-} ions [65, 66], as shown in the Fig. 1.5 (a).

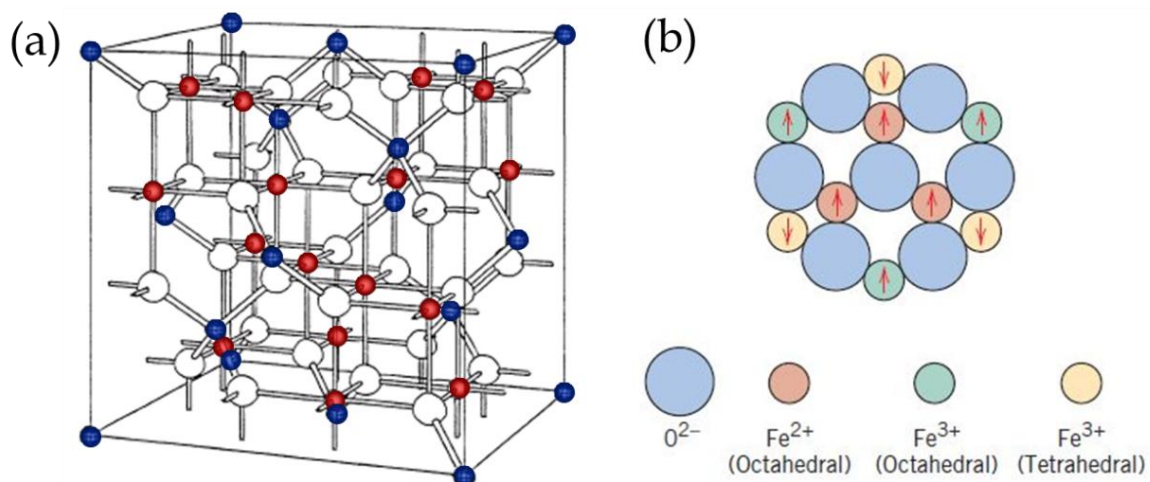


Figure 1.5 (a) Crystal structure of magnetite. White atoms are oxygen arranged in *fcc* lattice; blue atoms are Fe^{3+} ions in tetrahedral sites; red atoms are octahedrally coordinated, $\text{Fe}^{3+}/\text{Fe}^{2+}$ (50/50). © <http://www.ruf.rice.edu/~natelson/research.html>; (b) Schematic diagram showing the spin magnetic moment configuration for Fe^{3+} and Fe^{2+} ions in Fe_3O_4 [69].

Magnetite is a relatively good conductor at room temperature. However, on cooling below 120 K, its conductivity decreases sharply almost two orders of magnitude. Verwey observed this sharply anomaly in 1939 [67] and termed this phenomena as Verwey transition and the corresponding temperature as Verwey temperature (T_V). He explained this transition by a change from a dynamic disorder of electrons hopping on B site cations in alternate planes of Fe^{3+} and Fe^{2+} ions [68]. Additionally, on cooling below T_V , the crystal structure changes from cubic (space group $Fd\bar{3}m$) to monoclinic (space group $P2/c$) that yields a change in local symmetry around the cations [66].

Bulk magnetite has cubic magnetic anisotropy and $\langle 1\ 1\ 1 \rangle$ and $\langle 1\ 0\ 0 \rangle$ directions are the easy and hard axes of magnetization, respectively. The first order magnetocrystalline anisotropy is negative ($K_1 = -1.35 \times 10^5 \text{ erg/cm}^3$) at room temperature, that changes sign at low temperature. It passes through an isotropic point at a temperature few degrees above the T_V . Below T_V , change of crystal structure from cubic to monoclinic state results a change to uniaxial anisotropy with $\langle 0\ 0\ 1 \rangle$ easy axis [65]. In case of nanomagnetite, the dependence of the Verwey transition on the particle size is interesting, though contradicting. Both increase and decrease of the value of T_V has been observed depending on the size of the particles and there is no transition observed below 50 nm size [65, 66]. However, the studies were not performed in a broad temperature range and also the samples studied were made by different synthesis methods.

Magnetite is generally ferrimagnetic in nature below T_C due to the antiparallel arrangement of Fe^{3+} ions in tetrahedral sites (A) and Fe^{3+} and Fe^{2+} ions in octahedral sites (B), as shown in Fig. 1.5(b) [69]. A net spin magnetic moment exists for each Fe^{2+} and Fe^{3+} ion, which corresponds to 4 and 5 Bohr magnetons (μ_B), respectively, for the two ion types. Furthermore, the oxygen ions (O^{2-}) are magnetically neutral. The spin moments of all the Fe^{3+} ions in the octahedral positions are aligned parallel to one another; however, they are directed oppositely to the Fe^{3+} ions situated in the tetrahedral sites. This results from the antiparallel spin coupling of adjacent iron ions. Thus, the spin moments of all Fe^{3+} ions cancel each other and make no net

contribution to the total magnetization of the bulk solid. On the other hand, all the moments of Fe^{2+} ions are aligned in the same direction at octahedral sites; this total moment of Fe^{2+} ions is responsible for the net magnetization of bulk Fe_3O_4 . In nano-regime the magnetic properties changes significantly. Extremely small magnetite particles behave superparamagnetically at room temperature as observed by different authors. The particles undergo superparamagnetic to ferromagnetic change in magnetization upon cooling below a certain temperature, known as blocking temperature (T_B). However, the T_B is found to decrease with decreasing particle size as observed for magnetite nanoparticles prepared using different synthesis procedures [24, 70].

1.8 Motivation and Objectives of Thesis

Fabrication of functional magnetic nanomaterials of various morphologies and study of their morphology dependent properties has become a topic of great interest to the researchers during last few decades. During last few years, people have developed various procedures to synthesize different nano structures such as sphere, rod, wire, chain, disc, tiles, etc., either by controlled aggregation of nanoparticles or by self-assembling process and they have found different properties for different morphologies. However, fabrication of magnetic nano-hollow spheres is much more interesting because of its unique morphology and peculiar characteristics. These materials have low density due to hollow interior and large effective surface area because of their accessible inner and outer surface which makes them very efficient for toxic dye adsorption from water. It has been found that the special morphology of these nano hollow spheres affects their domain structure, thus controlling their magnetic and electronic properties. So, fabrication of magnetic nano hollow spheres of variable sizes and study of their size dependent magnetic and transport properties will be very interesting for the basic understanding of nanoscience as well as for their real world applications.

Magnetic nanoparticles with some biological functionalization are of immense interest. Therefore, biological molecules, such as proteins and nucleic acids, are used

extensively for the controlled organization of nanomaterials to fabricate some predefined nanostructures. Particularly, the combination of different metallic and its oxide nanoparticles with DNA and proteins is now being studied extensively for the fabrication of self-assembled hybrid structures, such as DNA-templated nanowires. Due to the high aspect ratio (=length/width), unique molecular recognition and mechanical self-assembling characteristics, DNA offers a great potentiality as a building block to create nanowires. Hence, manufacturing of various small substances with biological molecules is a very important job. But before use, proper engineering with such system and their extensive studies are necessary. Hence, the synthesis and study of nanobiomaterials having the magnetic, electrical conductive and optical properties is very important for their multifunctional applications.

One dimensional (1D) oxide semiconductor nanostructures have attracted considerable attention because of their unique tunable physical and chemical properties suitable for multifunctional applications. Specially, nanowires of the transition metal oxide Hematite ($\alpha\text{-Fe}_2\text{O}_3$) have drawn immense research interest because of their unique morphology and high aspect ratio which is very useful for wide variety of technological applications. However, despite its abundance, low cost, high stability, suitable band gap and valance band edge position, $\alpha\text{-Fe}_2\text{O}_3$ has not yet gained importance as an optoelectronic material though it has an energy band gap which corresponds to the visible wavelength region. In fact, the luminescence behavior of hematite nanostructures is very weak; the optical properties of the $\alpha\text{-Fe}_2\text{O}_3$ NWs including their luminescence characteristics are still not well studied. Therefore, the investigation and improvement of the luminescence characteristics of $\alpha\text{-Fe}_2\text{O}_3$ with a view of extending the versatility of the material in the area of optoelectronics seems to be very exciting. Moreover, the room temperature ferromagnetic (RTFM) behavior of different hematite nanostructures is also very weak. However, it has been reported that the surface modification of the oxide semiconductor nanostructures leads to a substantial change in their electronic, opto-electronic, magnetic and electrochemical properties. In this regard, the semiconductor magnetic nanostructures as a core material, covered by some nonmagnetic/magnetic metallic/non-metallic material, i.e. hybrid nanostructures

might possess very exciting electronic, optical, magnetic and electrochemical properties at the same time to achieve multifunctionality in a single material.

In this backdrop the main objectives of this work are summarized as follows:

- Template free solvothermal synthesis of Magnetite hollow spheres of different diameters, study of their size dependent electronic and magnetic (both AC and DC) properties.
- Application of these hollow spheres for adsorption of toxic dye material from water, i.e. for water treatment.
- Fabrication of nano-chains of Fe_{core}-Au_{shell}, α -Fe₂O₃ and Fe₃O₄ nanoparticles using DNA as template material and also to probe their magnetic and electrically conductive properties.
- Template assisted synthesis of α -Fe₂O₃ nanowires (NWs) and study of their magnetic, electronic and photoluminescence properties.
- Surface modification of these NWs with gold (Au) and zinc oxide (ZnO) for improvement of the above mentioned properties.
- Modification of NW surface with manganese di-oxide (MnO₂) for better electrochemical performance and fabrication of supercapacitors.

1.9 Organization of the Thesis

The entire thesis has been divided into five different chapters. A brief sketch of the chapters is given below.

Chapter 1 gives an introduction about different type of nanostructures of magnetic materials, their functional behavior and also applications. A literature review on the basic properties of iron and its oxides (hematite and magnetite) has been discussed. The motivation of the thesis has been justified with the outline of the work described in this thesis.

Chapter 2 describes the synthesis techniques for fabrication of different nanostructures and also various characterization techniques of these nanostructures. Development of home-made AC magnetic measurement setup is also described.

Chapter 3 is about the fabrication and characterization of variable sized magnetite nano hollow spheres. We have found some interesting size dependent magnetic and electric properties. We have done the AC magnetic measurements of these hollow spheres and used these spheres to remove dyes from water solution.

Chapter 4 presents a facile route for fabrication of nanochains of Fe_{core}-Au_{shell}, α -Fe₂O₃ and Fe₃O₄, using DNA as a template material and also their optical, electrical and magnetic characterizations. The magnetic properties of these materials are found to be significantly influenced by the DNA molecule.

Chapter 5 describes the template assisted synthesis of hematite nanowires and their surface modification by Au, ZnO and MnO₂ for improved electronic, optical, magnetic and electrochemical behavior.

Chapter 6 concludes the thesis with an idea about the scope for future work in this direction.

Bibliography

- [1] J.I. Martín, J. Nogués, K. Liu, J.L. Vicent, I. K. Schuller, J. Magn. Magn. Mater. 256, 449(2003)
- [2] E. Rabani, D. R. Reichman, P. L. Geissler, and L. E. Brus, Nature (London) 426, 271 (2003).
- [3] S. Sun, Adv. Mater. 18, 393 (2006)
- [4] R. P. Cowburn, Science 287, 1466 (2000)
- [5] S. Chikazumi, S. Taketomi, M. Ukita, M. Mizukami, H.Miyajima, M. Setogawa, Y. Kurihara, J. Magn. Magn. Mater. 65, 245 (1987)
- [6] A.-H. Lu, W. Schmidt, N. Matoussevitch, H. Bönnermann, B.Spliethoff, B. Tesche, E. Bill, W. Kiefer, F. Schüth, Angew. Chem. 116, 4403 (2004)
- [7] S. C. Tsang, V. Caps, I. Paraskevas, D. Chadwick, D. Thompsett, Angew. Chem. 116, 5763 (2004)
- [8] A. K. Gupta, and M. Gupta, Biomaterials 26, 3995 (2005)
- [9] Z. Li, L. Wei, M. Y. Gao, and H. Lei, Adv. Mater. 17, 1001 (2005)
- [10] B. Wang, H. Wu, L. Yu, R. Xu, T. T. Lim, and X. W. Lou, Adv. Mater., 24, 1111 (2012)
- [11] H. Gu, K. Xu , C. Xu and B. Xu Chem. Commun., 9, 941 (2006)
- [12] M. Sincai, D. Ganga, D. Bica, L. Vékás, J. Magn. Magn. Mater. 225, 235 (2001)
- [13] P. Pradhan, J. Giri, G. Samanta, H.D. Sarma, K.P. Mishra, J.Bellare, R. Banerjee, D. Bahadur, J. Biomed. Mater. Res. Part B Appl. Biomater. 12, 81B (2007)
- [14] J. Liu and D. F. Xue, Adv. Mater. 20, 2622 (2008)
- [15] Q. X. Guo, Y. S. Zhao, W. L. Mao, Z. W. Wang, Y. J. Xiong, and Y. N. Xia, Nano Lett. 8, 972 (2008)
- [16] H. Bethe, Ann. Physik 3, 133 (1929)
- [17] L. Neel, J. Phys. Radium 15, 225 (1954)
- [18] R. Skomski and J. M. D. Coey, *Permanent Magnetism*, 2nd ed. (Institute of Physics, Bristol, 1999)
- [19] J. A. Osborn, Phys. Rev. 67, 351 (1945)
- [20] D. Sarkar, and M. Mandal, J. Phys. Chem. C, 116, 3227 (2012)

- [21] X. Battle, and A. Labarta, *J. Phys. D: Appl. Phys.* 35, R15 (2002)
- [22] B. D. Cullity, *Introduction to Magnetic Materials* (Addison-Wesley, Reading, Massachusetts, 1972), p. 385.
- [23] L. Neel, *Ann. Geophys.* 5, 99 (1949)
- [24] S. Gangopadhyay, G. C. Hadjipanayis, B. Dale, C. M. Sorensen, K. J. Klabunde, V. Papaefthymiou, A. Kostikas, *Phys. Rev. B* 45, 9778 (1992)
- [25] F. T. Parker, and A. E. Berkowitz, *Phys. Rev. B* 44, 7437 (1991)
- [26] G. Cao, *Nanostructures and nanomaterials*, Imperial College Press (2004)
- [27] I. P. Muthuselvam, and R. N. Bhowmik, *J. Phys. D: Appl. Phys.* 43, 465002 (2010).
- [28] N. Ponpandian, and A. Narayanasamy, *J. Appl. Phys.* 92, 2770 (2002).
- [29] J. Zhao, C. Buia, J. Han and J. P. Lu, *Nanotechnology* 14, 501 (2003).
- [30] Y. W. Heoa, D. P. Nortona, L. C. Tiena, Y. Kwona, B. S. Kangb, F. Renb, S. J. Peartona and J. R. LaRoche, *Materials Science and Engineering R* 47, 1 (2004).
- [31] S. Ferrere, A. Zaban, and B. A. Gregg, *J. Phys. Chem. B* 101, 4490 (1997).
- [32] T. Hayakawa and M. Nogami, *Sci. Technol. Adv. Mater.* 6, 66 (2005).
- [33] M. B. Sahana, C. Sudakar, G. Setzler, A. Dixit, J. S. Thakur, G. Lawes, R. Naik, V. M. Naik, and P. P. Vaishnava, *Appl. Phys. Lett.* 93, 231909 (2008).
- [34] S. Zeng, K. T. Yong, I. Roy, X. Q. Dinh, X. Yu, F. Luan, *Plasmonics*, 6, 491 (2011)
- [35] Q. L. Ye, H. Yoshikawa, S. Bandow, and K. Awaga, *Appl. Phys. Lett.* 94, 063114 (2009).
- [36] X. Duan, Y. Huang, R. Argarawal, C.M. Lieber, *Nature*, 421, 241 (2003)
- [37] J. Wang, M. S. Gudiksen, X. Duan, Y. Cui and C. M. Lieber, *Science* 293, 1455 (2001)
- [38] P. Simon and Y. Gogotsi, *Nat. Mater.* 7, 845 (2008)
- [39] N. L. Wu, *Mater. Chem. Phys.* 75, 6 (2002).
- [40] T. Brousse, et al. *J. Electrochem. Soc.* 153, A2171 (2006).
- [41] R. B. Rakhi, Wei Chen, Dongkyu Cha, and H. N. Alshareef, *Nano Lett.* 12, 2559 (2012)
- [42] S. C. Pang, M. A. Anderson, T. W. Chapmanb, *J. Electrochem. Soc.* 147, 444 (2000)

- [43] W. Sugimoto, H. Iwata, Y. Yasunaga, Y. Murakami, Y. Takasu, *Angew. Chem. Int. Ed.* 42, 4092 (2003)
- [44] Z. Ban, Y. A. Barnakov, F. Li, V. O. Golub, and C. J. O'Connor, *J. Mater. Chem.* 15, 4660 (2005)
- [45] F. Bodker, S. Morup and S. Linderorth, *Phys. Rev. Lett.*, 72, 282 (1994)
- [46] S. J. Cho, B. R. Jarrett, A. Y. Louie and S. M. Kauzlarich, *Nanotechnology* 17, 640 (2006)
- [47] G. G. Khan, D. Sarkar, A. K. Singh, and K. Mandal, *RSC Advances*, 3, 1722 (2013)
- [48] H. H. Kung, *Transition Metal Oxides: Surface Chemistry and Catalysis*, Elsevier, New York, (1989)
- [49] L. Huo, W. Li, L. Lu, H. Cai, S. Xi, J. Wang, B. Zhao, Y. Shen, and Z. Lu, *Chem. Mater.* 12, 790 (2000)
- [50] M. A. Gondal, A. Hameed, Z. H. Yamani, and A. Suwaiyan, *Chem. Phys. Lett.* 385, 111 (2004)
- [51] Y. Wang, T. Yu, X. Chen, H. Zhang, S. Ouyang, Z. Li, J. Ye, and Z. Zou, *J. Phys. D* 40, 3925 (2007)
- [52] J. Chen, L. Xu, W. Li, and X. Gou, *Adv. Mater.* 17, 582 (2005)
- [53] F. Morin, *J. Phys. Rev.* 78, 819 (1950)
- [54] R. L. Blake, R. E. Hessevick, T. Zoltai, and L. W. Finger, *The Am. Mineral.* 51, 123 (1966)
- [55] D. S. Xue, C. X. Gao, Q. F. Liu, and L. Y. Zhang, *J. Phys.: Condens. Matter* 15, 1455 (2003)
- [56] L. Y. Zhang, D. S. Xue, F. Xu, A. B. Gui, and C. X. Gao, *J. Phys.: Condens. Matter* 16, 4541 (2004)
- [57] S. Mitra, S. Das, S. Basu, P. Sahu, and K. Mandal, *J. Magn. Magn. Mater.* 321, 2925 (2009)
- [58] M. Cao, T. Liu, S. Gao, G. Sun, X. Wu, C. Hu, and Z. L. Wang, *Angew Chem. Int. Ed. (Communications)* 44, 2 (2005)
- [59] M. Sorescu, R. A. Brand, D. Mihaila-Tarabasanu, and L. Diamandescu, *J. Appl. Phys.* 85, 5546 (1999)
- [60] Z. Pu, M. Cao, J. Yang, K. Huang, and C. Hu, *Nanotechnology* 17, 799 (2006)

- [61] X. Wen, S. Wang, Y. Ding, Z. L. Wang, and S. Yang, *J. Phys. Chem. B* 109, 215 (2005)
- [62] H. Jaganathan, and A. Ivanisevic, *Appl. Phys. Lett.* 93, 263104 (2008)
- [63] A. R. West, *Basic Solid State Chemistry* (New York: Wiley) p 57 (1984)
- [64] L. Smart, and E. Moore, *Solid State Chemistry: An Introduction* (Singapore: Fong and Sons Printers Pte Ltd) p 24 (1992)
- [65] G. F. Goya, T. S. Berquo', F. C. Fonseca, and M. P. Morales, *J. Appl. Phys.* 94, 3520 (2003)
- [66] I. Dézsi, Cs. Fetzler, Á. Gombkötő, I. Szűcs, J. Gubicza, and T. Ungár, *J. Appl. Phys.* 103, 104312 (2008)
- [67] E. J. W. Verwey, *Nature (London)* 144, 327 (1939)
- [68] E. J. W. Verwey, P. W. Haaymann, and F. C. Romejn, *J. Chem. Phys.* 15, 181 (1947)
- [69] R. A. Flinn, and P. K. Trojan, *Engineering Materials and Their Applications*, 4th edition. Copyright 1990 by John Wiley & Sons, Inc.
- [70] D. Caruntu, G. Caruntu, and C. J O'Connor, *J. Phys. D: Appl. Phys.* 40, 5801 (2007)

Chapter 2 | Experimental Details

In this chapter we have described different synthesis methods of nanomaterials and also various techniques to characterize them.

2. Material Synthesis and Characterization Techniques

2.1 Preamble

In this chapter we will give an overview about different experimental techniques that have been used to synthesize unique nanostructures of various materials along with their characterization processes employed to investigate different properties of these nanostructured materials. Synthesis techniques of different nanostructures include chemical co-precipitation, solvothermal, electrochemical deposition, chemical deep-in etc. methods.

The phase and morphology the synthesized nanostructures are studied using X-Ray Diffraction (XRD), Scanning Electron Microscope (SEM), Field Emission Scanning Electron Microscope (FESEM), Transmission Electron Microscope (TEM), High Resolution Transmission Electron Microscope (HRTEM), Energy Dispersive X-Ray Analysis (EDAX), Selected Area Electron Diffraction (SAED). The chemical analysis on the electronic structure of the nanostructures is conducted by employing electron energy loss spectrometry (EELS) in conjunction with TEM. Spectroscopic analyses are carried out using UV visible spectrometer, Fourier Transformed Infrared Spectrometer (FTIR), Circular Dichroism (CD) and spectrofluorometer (for photoluminescence study). The magnetic characterizations are carried out employing Vibrating Sample Magnetometer (VSM) and Superconducting Quantum Interference Device (SQUID). AC conductivity has been measured in an impedance analyzer. We have developed a homemade setup for measuring the high frequency behavior of different nanostructures under an AC magnetic field.

2.2 Nano Designing Approach

There are varieties of techniques that have been devised to create nanomaterials with specific structures and unique properties. These methods can be summarized as to-down (i.e. bulk to nanoparticle) and bottom-up (i.e. atom to nanoparticles) approaches.

2.2.1 Top-Down approach

In this method, natural and man-made chunks or blocks are cast, sawed or machined into precisely formed products, small or large, ranging from micro to nano scale. This method includes high energy ball milling or attrition, repeated quenching, mechano-chemical processing, etching, electro explosion, sonication etc. Nanoparticles produced through high energy attrition of bulk materials have broad size distribution, non-uniformity of shape and geometry and most of all different impurities and defects can be introduced from the milling medium. Repeated thermal cycling can also break larger particles if their thermal conductivity is very small but can undergo large volume change with temperature. This method can produce very fine particles, however it is very difficult to design and control the process to fabricate particles with desired shape and size. The biggest drawback of the top-down process is the imperfection in surface structures that can have significant effect on the physical properties and surface chemistry of the nanostructures.

2.2.2 Bottom-up approach

This method refers to build-up of a material from bottom level, i.e. from atom by atom, molecule by molecule or cluster by cluster. This approach ensures better possibility to produce nanostructures with fewer defects, more homogeneity in chemical composition and better long and short range ordering. The key to the application of nanotechnology will be the development of processes that can control the placement of individual atoms to form products of great complexity at extremely small dimension [1].

2.3 Formation of Nanoparticles

Nanoparticles are formed usually via two steps, nucleation and growth. Supersaturation of growth species is the main criteria to form nanoparticles through homogeneous nucleation that can be done either by reduction of solution temperature or by in situ chemical reactions. Then we have to calculate the overall free energy changes (ΔG) associated with the homogeneous nucleation process,

which is the total change in free energy between a small solid particle of a solute and the solute in solution. This ΔG is equal to the sum of the excess surface free energy, ΔG_s , between the surface of the nanoparticle and the corresponding bulk material, and another term, excess volume free energy, ΔG_v , which is the excess free energy of a very large particle and the solute in the solution. ΔG_s is a positive and ΔG_v is negative in a supersaturated solution and their dependence on particle size (r) can be observed from Eq. (2.1) and also depicted in the Fig. 2.1 [2].

$$\Delta G = \Delta G_s + \Delta G_v = 4\pi r^2 \gamma + (4/3)\pi r^3 \Delta G_v \quad (2.1)$$

where, ΔG_v is the free energy change per unit volume and γ is the interfacial tension between the growing nanoparticle surface and the supersaturated solution.

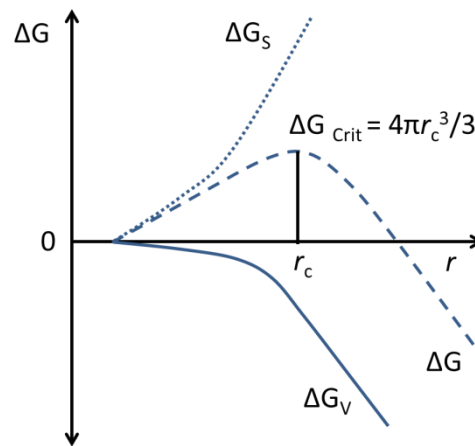


Figure 2.1 Free-energy diagram for nucleation process. (© S. Kumar, and T. Nann, *Small*, 2, 316 (2006))

From Fig. 2.1, it is clear that the total excess free energy, ΔG , passes through a maximum, ΔG_{crit} , that corresponds to the critical nucleus, r_c , and can be calculated by making

$$\left. \frac{dG}{dr} \right|_{r=r_c} = 8\pi r_c \gamma + 4\pi r_c^2 \Delta G_v = 0 \quad (2.2)$$

$$\Rightarrow r_c = -\frac{2\gamma}{\Delta G_v} \quad (2.3)$$

From equations (2.1) and (2.3), we can obtain the critical value of ΔG as

$$\Delta G|_{r=r_c} = \Delta G_{Crit} = \frac{16\pi\gamma^3}{3(\Delta G_v)^2} = \frac{4\pi\gamma r_c^2}{3} \quad (2.4)$$

i.e. the minimum energy barrier that a nucleation process must overcome is ΔG_{crit} , which corresponds to the minimum size of a stable spherical nucleus (r_c). Any nucleus having size smaller than r_c will dissolve in the solution to minimize its net free energy, whereas larger nucleus having $r > r_c$ is stable and continues its growth. Crystal structure, size and morphology of the growing particles mainly depend on the system and reaction parameter. Shape of the crystallites occurs either in order to minimize the surface energy of the particles or because of the kinetics of the growth. If kinetics dominates, the shape is then determined by the rate at which different crystal faces grow. In thermal equilibrium, crystal shape is determined by minimization of surface energy.

As the nuclei grow through molecular addition, at times nucleation stops because of drop in concentration below a certain level. However, the growth of the particles continues via molecular addition until the equilibrium concentration of the precipitated species is attained. At this time, smaller particles continue to grow at a faster rate than the larger particles because of their higher free energy driving force than the larger one. Nearly monodisperse particles can be obtained at this stage either by stopping the reaction (nucleation and growth) quickly or by adding reactants to maintain a saturated state during the full course of reaction. On the other hand, when there is depletion of reactants due to particle formation, Ostwald ripening occurs, due to which larger crystals grow from those of smaller size which have a higher solubility than the bigger ones. For colloidal particles in solution media, various chemical equilibria can exist between solid-liquid interfaces depending on each experimental setting. Now, the concentration of solutes across the bulk solution varies due to non-uniformity of the crystallites. Therefore, to homogenize this concentration gradient, smaller crystallites completely dissolve into the solution as a result of the growth of large crystallites [3].

According to Gibbs-Thompson equation [4], the equilibrium solute concentration near small particles is higher than near large particles because the

chemical potential of a particle increases with decreasing particle diameter. This concentration gradient leads to transport of solute from small particles to large particles resulting growth of faceted particles if it occurs near equilibrium. However, there is significant difference in surface energies of different crystallographic phases. Crystal growth through aggregation happens through series of mechanisms, producing assemblies built from randomly oriented to highly oriented particles. However, this mechanism can incorporate different defects such as edge and screw dislocations in initially defect free nanoparticles. These defects, porosity and particle morphology give important clues to mechanisms by which primary building blocks assemble to produce bigger particles.

2.4 Fabrication Techniques of Different Nanostructures

2.4.1 Wet Chemical Method

Wet chemical method refers to a particular group of methods where generally nano- or ultra- dispersed inorganic materials have been produced in aqueous or non-aqueous solutions. It is different from conventional solid state procedure in respect to that it can only be done in liquid phase and more importantly it can produce much smaller, monodisperse grains or crystallites usually at lower temperature and have shorter duration of phase formation. It is mainly a “bottom-up” method to synthesize nanoparticles basically by chemical reduction of metal salts, electrochemical trails or through controlled decomposition of different metastable organometallic compounds.

2.4.2 Chemical Co-precipitation

Co-precipitation is the carrying down by a precipitate of two or more substances simultaneously that are generally soluble in the solvent under employed conditions. This method is employed extensively in material science and industry to synthesize complex oxides with high crystallinity, compositional homogeneity and better stoichiometry. The co-precipitation setup used in our laboratory for fabrication of various oxide nanoparticles is shown in Fig. 2.1.

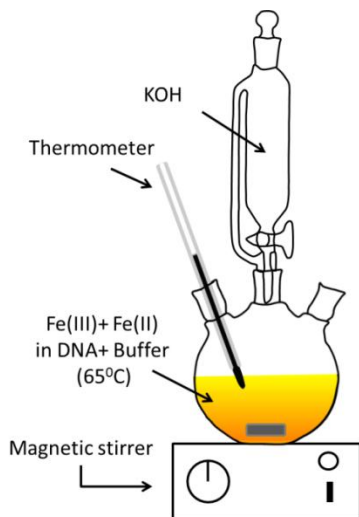


Figure 2.1

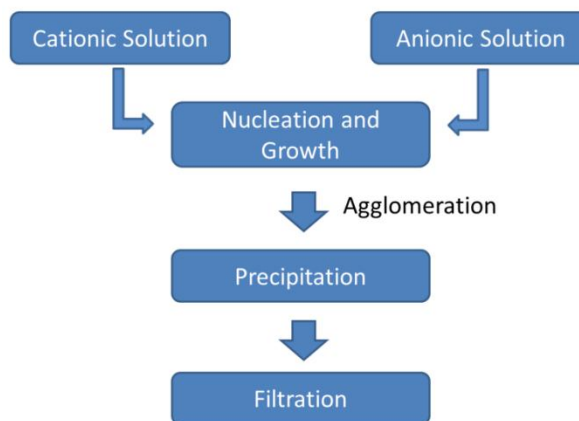


Figure 2.2

Figure 2.1 Setup for co-precipitation technique. **Figure 2.2** Block diagram of co-precipitation method for synthesis of micro or nano particles.

In the co-precipitation technique, first of all, salts of the constituent materials of the complex oxide are dissolved in aqueous medium and magnetically stirred to make it a completely homogeneous mixture. The solution temperature can be in the range between 0°C to 80°C depending on the materials dissolved in the solution. When the desired temperature of the primary solution is achieved, another solution of dissolved precipitating agent such as ammonium oxide (NH_4OH) or potassium hydroxide (KOH) is added into it. The precipitation of the desired oxides is then filtrated and dried to make powder of the product. Colloidal chemistry plays an important role to produce these powder oxides from the solution phase as depicted in Fig. 2.2. After the nucleation of the particles they come close together due to their inter-particle interaction to form larger agglomerates and also to reduce their surface energy. During this time the agglomeration rate largely depends on the rate of collisions between nucleates due to Brownian motion, convection and also sheer forces caused by magnetic stirring. Net balance of these forces determines whether the freshly prepared nucleates adhere to form bigger grains or not. If the net force is attractive Vander Wall type that includes dipole-dipole, dipole-non dipole and also non dipole-non dipole interactions, smaller nucleates will adhere together to form bigger grains. However, Vander Wall's force decreases sharply with distance between the particles. There is another important force for stabilization of freshly

prepared nanocrystalline grains named surface charge or Zeta potential that originates due to non-stoichiometric adsorption or desorption of an ionic species at the surface of the particles or through chemical reactions in aqueous media. For stabilization, this surface charge should be zero at a point, known as "Isoelectric point" [5]. By controlling the pH of the solution, surface charges can be made zero or minimum. The mean size of the particles can be controlled by adjusting the solution temperature and also the rate of addition of precipitating agent in the precursor solution. Actually it is found that mean particle size increases with decreasing rate of addition of precipitating agent. The processing parameters, nature of precursor reagents, pH of the solution etc. affects the size, morphology and also crystallinity of the product.

2.4.3 Solvothermal Method

Solvothermal technique is a method for fabrication of crystallizing nano materials and also nanostructures of various metals, semiconductors, ceramics and also polymers from mainly non-aqueous medium by controlling different thermodynamic (temperature, pressure and chemical composition) and non-thermodynamic (magnetic stirring etc.) variables. This process involves different polar or non-polar supercritical fluids as solvents (like Benzene, Ethylene Glycol, Ethylene di-amine etc.) at moderate to high pressure (typically between 1 atm to 10,000 atm) and temperature (typically between 100°C and 1000°C) to facilitate the interaction of different precursor molecules during the synthesis procedure. This method is very much similar to hydrothermal route; however, the only difference being that the precursor solution is usually non aqueous.

The particles are obtained in solvothermal synthesis by the dissolution and crystallization mechanism. As the solubility and activity of the reactants changes at higher temperatures, some additional parameters are obtained whose controlled variation leads to high quality nanoparticles and nanostructures that are not possible in other methods. This technique starts with the dissolution of the precursors solutes in the solvent by magnetic stirring at room temperature. After some time the

homogeneous mixture is transferred into Teflon lined stainless steel autoclave chamber, as shown in Fig. 2.3.

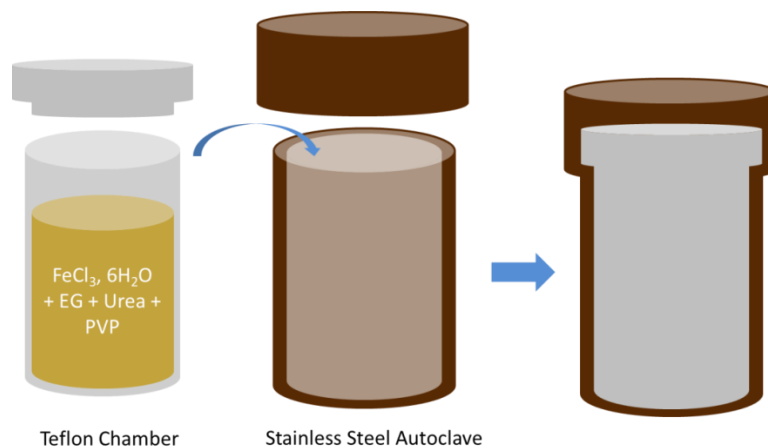


Figure 2.3 Schematic diagrams of an autoclave and a Teflon chamber used in solvothermal synthesis.

The precursor solution is poured in the chamber in such a way that 80% of it should be filled. The autoclave is then heated to a certain temperature in an oven in order to create two temperature regions. As a result, a convection process starts where the solvent below gets heated and ascends and the cold solvent from the top descends. The nutrients dissolve in the hotter region and the saturated solution in the lower part is transferred to the upper part by convective motion of the solution. This convective process continues for a very long time until the entire solution attains at its equilibrium i.e. temperature becomes same everywhere. The solution becomes supersaturated in the upper region as the result of the reduction in temperature and then crystallization starts. This method can be used to prepare various types of nanostructures such as powders, wires, rods, single crystals and many more. Not only that, the nanostructures formed in this procedure can be easily controlled by changing the solvent supersaturation, concentration and also through kinetic control. This technique can also be employed to prepare different thermodynamically stable or metastable states of novel materials that cannot be formed easily through other methods. There are different thermodynamic and crystallographic reasoning behind the formation of such fascinating nanostructures such as oriented attachment of phases [2, 6, 7], selective adsorption of surfactants [8],

minimization of surface free energy (thermodynamic theory) [9, 10], molecular template mechanism [2, 11] etc.

2.4.4 Electrodeposition Technique

Electrodeposition technique for fabrication of specially nanowires (NWs), nanotubes (NTs) etc. is a very cost effective and relatively simpler process as compared to the lithography processes, e.g. optical, electron beam, ion beam lithography etc. We have employed a commercial electrodeposition set-up (Autolab PGSTAT 302n) in order to prepare magnetic NWs within the nano pores of alumina (AAO) having average pore diameter of ~ 200 nm with a thickness of ~ 50 nm and an average pore density of $\sim 10^9$ cm $^{-2}$.

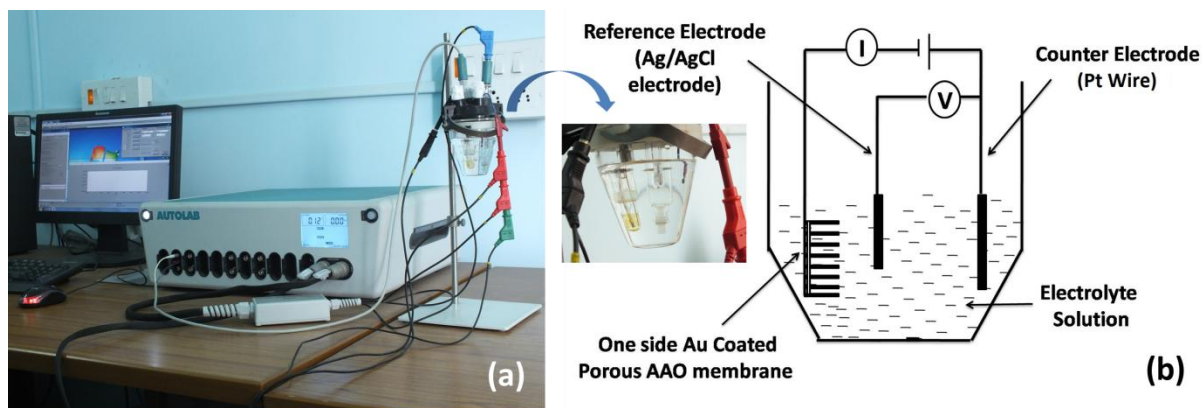


Figure 2.4 (a) Electrodeposition setup for fabrication of metallic NWs; (b) Schematic diagram of the electrochemical cell with various operating electrodes.

The set-up consists of a software controlled conventional electrochemical cell and a power supply (Potentiostat AutoLab-30), as shown in Fig. 2.4 (a). The electrochemical cell, as shown in Fig. 2.4 (b), consists of three electrodes: working electrode (WE), counter electrode (CE) and reference electrodes (RE). The working electrode is generally the template on which the desired electrochemical depositions are carried out. To deposit the metal ions in the pores of AAO template in order to synthesize NWs, we use AAO membrane as working electrode. However first of all, one side of the AAO membranes is coated with a conductive gold (Au) layer of ~ 100 nm thicknesses either by thermal evaporation or by RF sputtering technique. For polycarbonate membranes, sputtering is necessary as the evaporation technique

melts and burns the membranes at elevated temperature. For alumina membranes, both the techniques are applicable. In case of metal deposition from the aqueous solutions of their salts, the working electrode is connected to the negative terminal of the power supply, i.e. it is used as cathode. We have used a platinum wire as the counter electrode having the purity of $\sim 99.99\%$ commercially purchased from Sigma-Aldrich. The reference electrode is Ag/AgCl in saturated KCl solution electrode that is used to measure the other electrode potentials with respect to it. The cell has the volume capacity of ~ 100 cc for the electrolyte solutions.

Nanowires are deposited in the pores of alumina template by choosing a particular potential of corresponding depositions from linear sweep voltammetry (LSV) scan. The LSV scan gives a current vs. voltage profile for a particular electrolyte solution and for a particular choice of electrodes. LSV scanned between 0 V to -1.3 V is presented in Fig. 2.5. It shows, up to a certain value of the applied voltage, the current remain near zero value and with the increase in voltage, no deposition of cations at cathode is observed. After that, the current suddenly increases with further increase in voltage and attain a maximum value. The sudden increase in current indicates deposition of metal ion at cathode. Simultaneously, the pH value of the solution during the LSV scan is also recorded. The pH graph shows a spike near the potential where the sudden jump in current has started. We choose the potential of deposition just before the pH spike and very near to the start of the jump in current value. The working electrode i.e., the one sided Au coated porous alumina membranes, is placed vertically within the electrolyte solution with the open end of the nano-pores facing towards counter electrode (Pt wire). Under a negative potential of the working electrode with respect to the counter, the positively charged metal ions move towards the working electrode membrane and enter to the nano channels through the open end. Inside the nano channels, formation of NWs is the consequence of reduction of metal ions by capturing electron from gold thin film at the other end of the pores. Usually higher rate of ion deposition leads to formation of NWs whereas the lower rate leads to NTs formation within the nano channels. We have prepared iron NWs under a constant potential of

~ 1.03 V following LSV results. Details of the synthesis of metallic NWs is described elaborately in *Chapter 5* of this thesis.

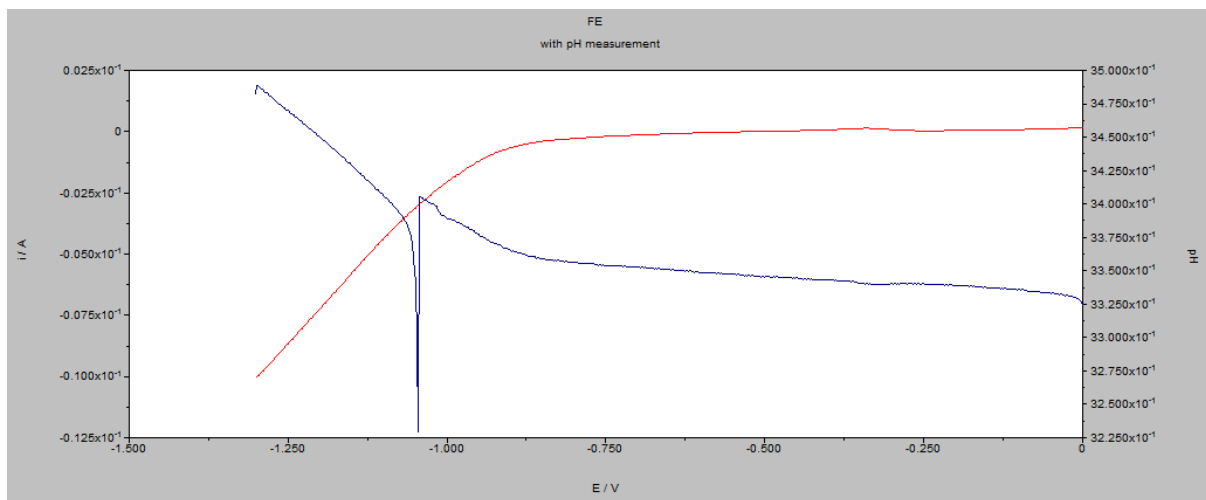


Figure 2.5 LSV scans (curves in red solid lines) for deposition of Fe NWs in porous alumina template. Blue solid lines in the terminals represent corresponding pH changes of the electrolytes during the potential sweeps.

2.4.5 Direct Current (DC) sputtering deposition

We have used this technique to deposit thin gold films on one side of the AAO template and also over the as grown nanowires (discussed in *Chapter 5*). The setup diagram of the dc sputtering system is shown in Fig. 2.6.

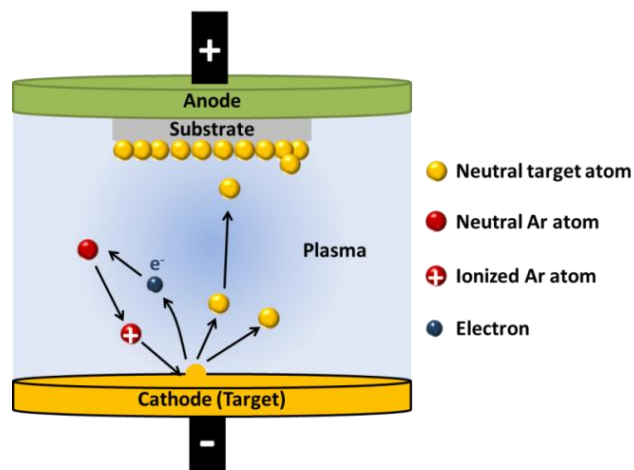


Figure 2.6 Schematic diagram of DC sputtering deposition setup.

In our case target, i.e. Au, and the substrate are placed inside a vacuum chamber where the pressure is maintained at $\sim 10^{-5}$ mbar during the sputtering

process. Once the vacuum is reached, argon gas is introduced in the chamber. This Ar gas is ionized and form plasma by a strong potential difference between anode (substrate) and cathode (Au) and these positive ions are accelerated to the target (cathode). After impact with the target, a momentum transfer is happened and then the target atoms are released from the target, travel to the positive substrate where they form layers of atoms. For efficient momentum transfer to happen, atomic weight of the sputtering gas should be close to that of the target material. Actually, dc sputtering is used for conducting materials. However, for non-conducting materials there is positive charge buildup on the material which stops the sputtering. In such cases, RF sputtering is efficient where a magnet is used to increase the electron path length, therefore, enhancing the probability of electron collision with the Ar atoms and hence increases the ionization efficiency.

2.5 Phase and Morphology Characterization Techniques

2.5.1 X-ray diffractometer

X-ray crystallography is a method of determining atomic and molecular structure of a crystalline material in which the atomic planes of the material diffract x-rays in different specific directions depending on their orientations. By measuring the angle and intensity of the diffracted beams, a three dimensional idea of the density of electrons within the specified crystal can be obtained. From this density of electrons, mean position of the atoms in the crystal can be determined.

In a practical setup as shown in Fig. 2.7 (a), a monochromatic beam of x-rays (Cu K_{α} , $\lambda \sim 1.54 \text{ \AA}$) is made to fall on a crystalline sample. These x-rays are scattered elastically by the electrons within the crystal planes and form outgoing spherical waves. Now, these scattered waves will interfere constructively in few specific directions that can be determined by Bragg's law given as:

$$2d \sin\theta = n\lambda \quad (2.5)$$

where, d is the crystal plane spacing, θ is the diffraction angle and n is an integer. The angles and intensities of the diffracted beams are processed and recorded electronically using a detector, electronics and specialized software resulting in

Intensity vs. 2θ plot for the specific sample, as shown in Fig. 2.7 (b) for Fe_3O_4 samples.

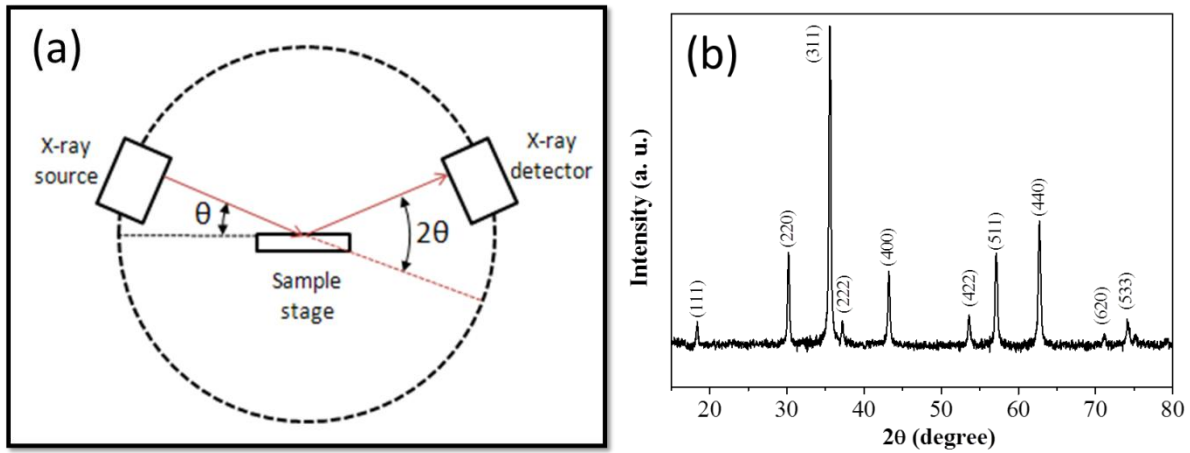


Figure 2.7 (a) Schematic diagram of X-ray diffractometer in θ - 2θ mode, © chemwiki.ucdavis.edu. (b) X-ray diffraction pattern of Fe_3O_4 hollow sphere of 250 nm diameter.

The grain size (d) of the sample can be calculated by observing the width of the diffraction peaks and using the relation as given by Debye-Scherrer:

$$d = 0.9\lambda / (\beta \cos \theta) \quad (2.6)$$

where, β is the full width at the half maximum of the diffraction peak at a diffraction angle of 2θ [12].

2.5.2 Electron Microscopes

An electron microscope is a type of microscope that uses a beam of highly energetic electrons to illuminate a specimen and produce its magnified image. We have used two types of electron microscopes to analyze our samples as described below.

Scanning Electron Microscope (SEM)

SEM (schematically shown in Fig. 2.8 (a)) produces image by probing the specimen with a focused electron beam, either emitted thermo-ionically or field emitted [13], that is scanned across a rectangular area of the specimen (raster scanning). It works on a voltage window between 2 to 50 kV. When an energetic

electron interacts with the specimen, it loses energy via variety of mechanisms and produces a variety of signals. These signals include low energy secondary electrons (produced by inelastic scattering of incident electrons with the atoms of the sample), high energy backscattered electrons, diffracted backscattered electrons, characteristic X-rays (produced by inelastic collisions of the incident electrons with electrons in discrete orbitals of the atoms of sample), visible light (cathodo-luminescence) and heat. These signals give information about the properties of the specimen surface. Generally, the image displayed by an SEM is a mapping of the varying intensity of the signal produced by the secondary electrons into the image in a position corresponding to the exact position of the beam on the specimen (as shown in Fig. 2.8 (b)). Whereas the characteristic x-rays are used for elemental analysis, also known as Energy Dispersive Analysis of X-rays (EDAX).

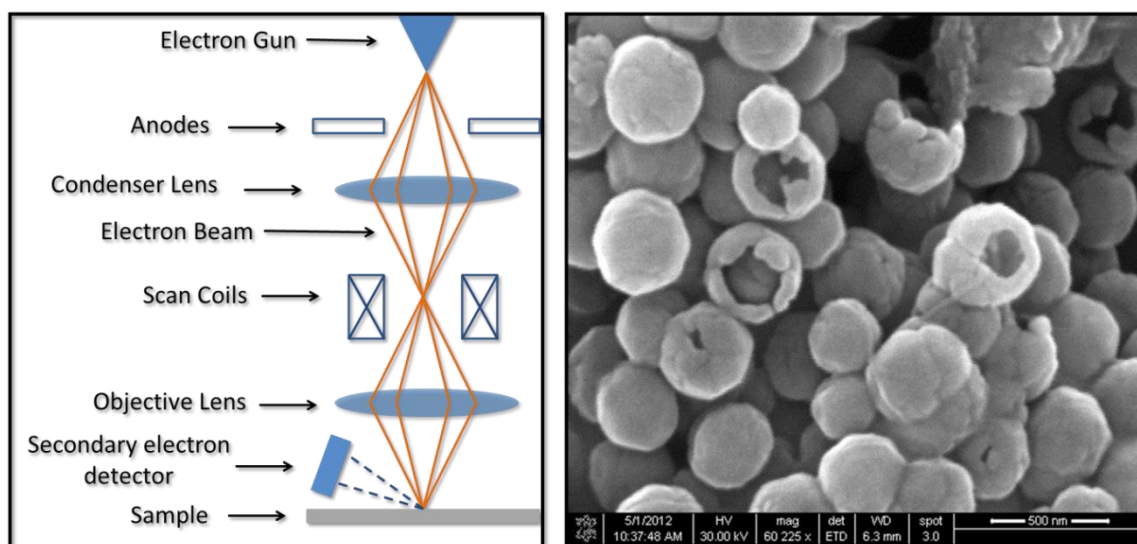


Figure 2.8 (a) Schematic diagram of SEM; (b) SEM image of Fe₃O₄ hollow spheres.

Transmission Electron Microscope (TEM)

In TEM, mainly two different types of interactions between the electron beam and specimen have been used to construct an image; these are unscattered electrons (transmitted beam) and elastically scattered electrons (diffracted beam). Schematic diagram of a TEM is shown in Fig. 2.9. In this process, incident electrons are transmitted through the thin specimen without any interaction occurring inside the specimen. The transmission of unscattered electrons is inversely proportional to the

specimen thickness. Areas of the specimen that are thicker will have fewer transmitted unscattered electrons and so will appear darker, conversely the thinner areas will have more transmitted and thus will appear lighter. This mode of operation to create contrast in image is known as bright field imaging mode.

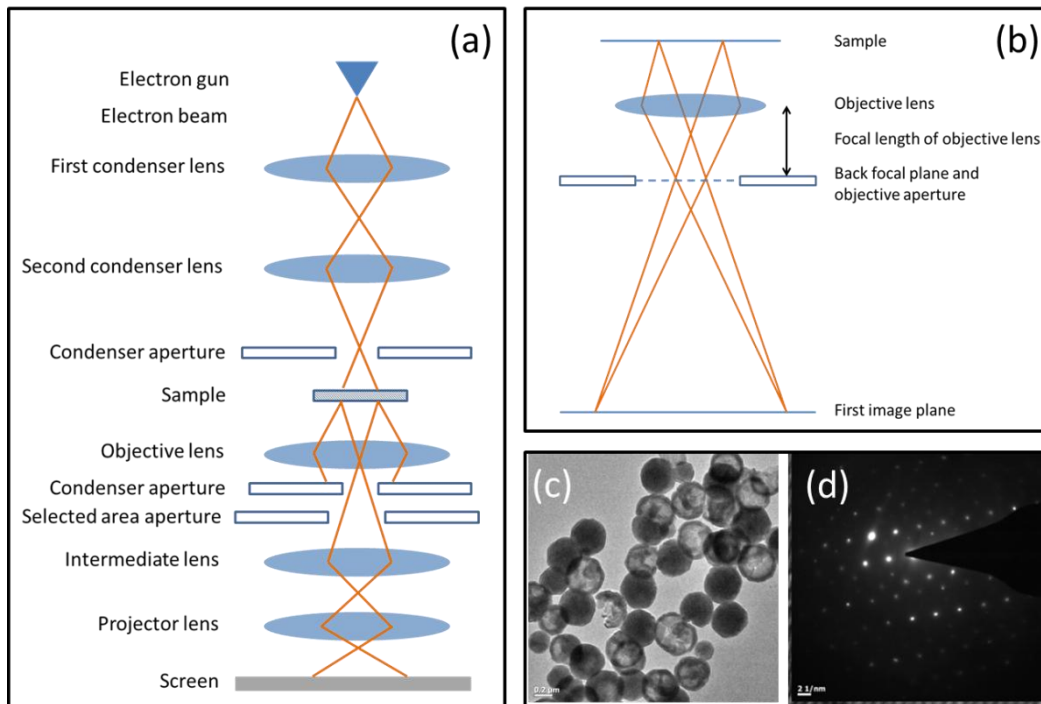


Figure 2.9 (a) Schematic diagram of TEM and image forming by electron beam (b), (c) and (d) are the TEM image and electron diffraction pattern, respectively of magnetite hollow spheres.

Another important mode of TEM imaging is electron diffraction. In case of crystalline sample the electron beam undergoes Bragg scattering in accordance with the Bragg's law as given by Eq. (2.5). All incident electrons have the same energy (thus wavelength) and enter the specimen normal to its surface. Now, the electrons that are scattered by the same set of parallel planes can be collated using magnetic lenses to form a pattern of spots; each spot corresponding to a specific atomic spacing (or crystalline plane). This pattern can then yield information about the orientation, atomic arrangements and phases present in the area being examined.

In case of high resolution TEM (HRTEM) mode we can achieve a resolution as much as 0.2 nm which is very efficient in observing the lattice fringes of the specimen under observation.

Energy filtered transmission electron microscopy (EFTEM) is a technique used in TEM where electrons of particular energies are used to form an image or diffraction pattern. This technique provides information about the elemental composition of the material under observation.

Another technique that is performed in TEM is electron energy loss spectroscopy (EELS) where a material is illuminated with electrons having known narrow range of kinetic energy. These electrons undergo inelastic scattering with some energy loss. The amount of energy loss is measured in an electron spectrometer and represented in terms of what caused the energy loss.

2.5.3 X-ray Photoelectron Spectroscopy (XPS)

XPS is a quantitative spectroscopic technique to measure the elemental composition, chemical formula, chemical state and electronic state of elements that exist within the material under observation. XPS spectra is obtained by illuminating the sample by x-rays and simultaneously measuring the kinetic energies and the number of electrons that escape from the top 1-10 nm of the substance being analyzed. As the energy of the irradiating x-ray photon (E_{photon}) is known, the binding energy (E_{Binding}) of each electron emitted from the surface of the material can be calculated using the Ernest Rutherford equation as given below.

$$E_{\text{Binding}} = E_{\text{photon}} - (E_{\text{Kinetic}} + \Phi) \quad (2.7)$$

where, E_{Kinetic} is the kinetic energy of the emitted electron and Φ is the work function of the spectrometer. XPS spectrum is a plot of the number of electrons detected (Y-axis) with the binding energy of that electrons (X-axis). Each material produces its characteristics XPS peaks that corresponds to the electronic configuration of the electrons in different orbitals such as 1s, 2s, 2p etc. and the number of electrons detected is directly proportional to the amount of that element present in the irradiated portion of the sample. As the electron counting detector in XPS instruments is typically 1 m away from the x-ray irradiated sample, so, XPS must be performed in ultra-high vacuum (UHV) condition. The schematic diagram of the XPS system is shown in Fig. 2.10.

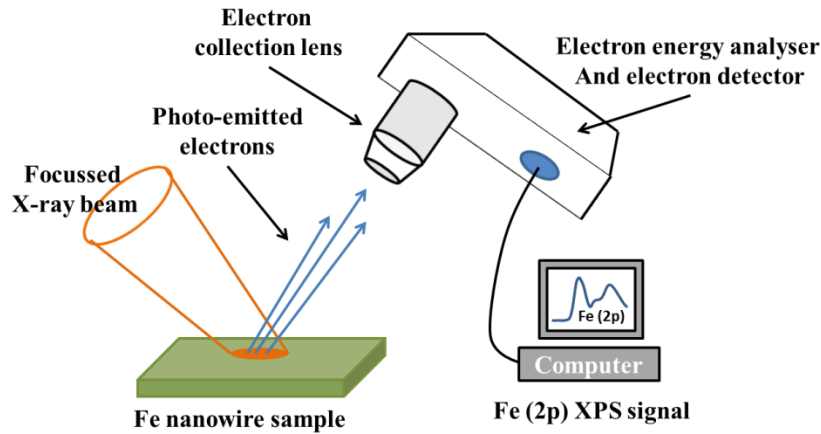


Figure 2.10 Schematic diagram of an XPS spectrometer.

2.6 Magnetic Characterization Techniques

2.6.1 Vibrating Sample Magnetometer (VSM)

In a VSM, the sample is placed in a DC magnetic field (H) and made it to oscillate sinusoidally so that the resulting flux (B) changes will induce a voltage in pickup coils. According to Faraday's law of electromagnetic induction, the voltage induced (emf) in a pickup coil of N turns with a cross-sectional area A is given by

$$V = -NA \frac{dB}{dt}, \quad (2.8)$$

where, $B = \mu_0 H$.

Now, if a sample having magnetization M is placed in the pickup coil, the total magnetic induction B can be written as

$$B = \mu_0 (H + M) \quad (2.9)$$

So, change in flux due to sample insertion, $\Delta B = \mu_0 M$

Hence, the Eq. (2.8), can be rewritten as $V dt = -\mu_0 NAM$ (2.10)

The intensity of the signal is proportional to the magnetic moment of the sample and the frequency is the same as that of the sinusoidal motion. The schematic diagram of the sample holder and detection mechanism of a VSM (Lakeshore model) that we use in our laboratory is shown in Fig. 2.11. Maximum magnetic field that can be generated without cryogenic system is 2.1 T and 1.76 T with Liq. N₂/Liq. He dewar between the coils. Temperature dependent hysteresis loops can be measured

using a cryogenic system (Liq. N₂) that can operate within a temperature range of 80 to 400 K with temperature stability of ± 0.2 K controlled by a temperature controller (331, Lakeshore) having temperature resolution of 0.001 K.

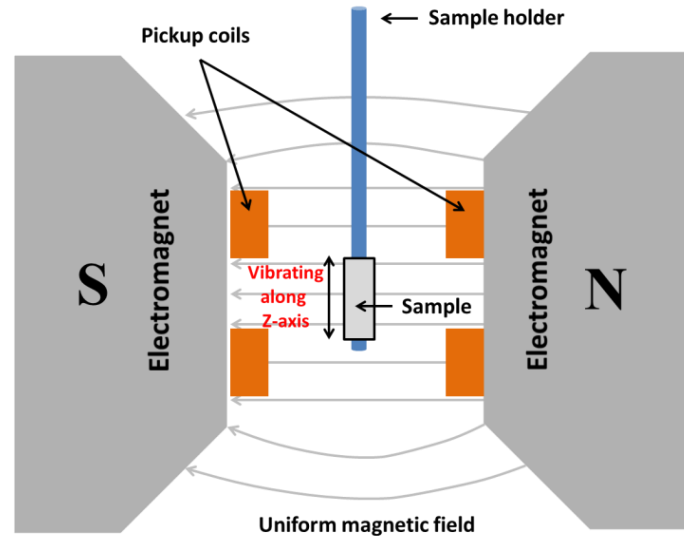


Figure 2.11 VSM sample holder and detection mechanism

2.6.2 Superconducting Quantum Interference Device (SQUID)

SQUID is the most sensitive and effective device that have been designed till now to detect incredibly small magnetic field and moment. It consists of two superconductors separated by a thin insulating layer to form two parallel Josephson junctions, as shown in the Fig. 2.12.

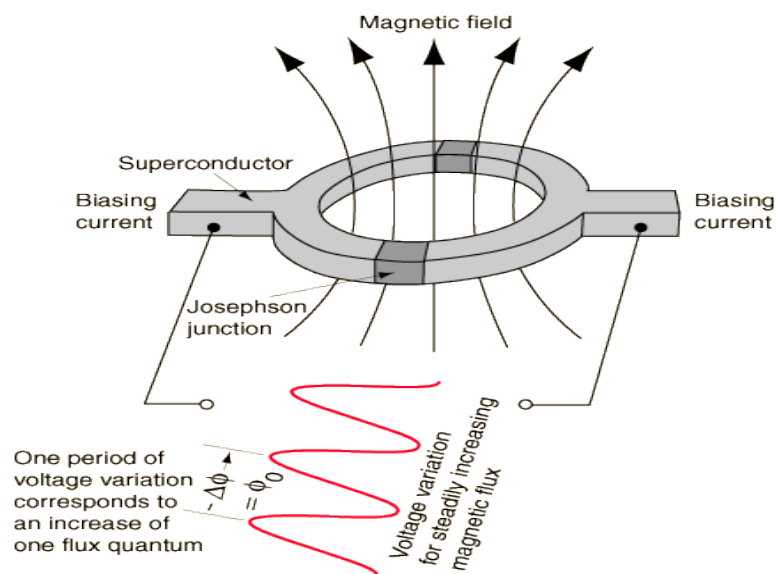


Figure 2.12 Schematic diagram of Josephson junction used in SQUID.

The insulating layer is thin enough such that the Cooper pairs can easily tunnel through the insulating junction. In the absence of any external magnetic field, the biasing current ' I ' splits into the two branches equally. As a superconductor excludes magnetic flux through it, so, if a small external magnetic field is applied to the superconducting loop, a screening current, ' I_s ', will generate to cancel the externally applied field. The induced current is in the same direction as ' I ' in one of the branches of the superconducting loop, and is opposite to ' I ' in the other branch. As soon as the current in either branch exceeds the critical current (I_c) of the Josephson junction, a voltage appears across the junction. Now consider the external flux is further increased until it exceeds $\Phi_0/2$, half the magnetic flux quantum. Since the flux enclosed by the superconducting loop must be an integral number of flux quanta, instead of screening the flux the SQUID now energetically prefers to increase it to Φ_0 . The screening current now flows in the opposite direction. Thus the screening current changes direction every time the flux increases by half integer multiples of Φ_0 . The SQUID detects the change in this current to deduce the magnetic moment of the sample [14].

We have used SQUID (Quantum Design) system to investigate the low temperature magnetic properties at *UGC-DAE CSIR, Kolkata*. The system is capable of providing magnetic fields in the range ± 70 kOe with field ramp possible as high as 700 Oe/s and sample temperature ranging from 2 K to 330 K. Sensitivity is 1×10^{-8} emu at zero magnetic field and 5×10^{-8} emu at 70 kOe.

2.6.3 Atomic and Magnetic Force Microscopy (AFM and MFM)

AFM and MFM are special type of scanning probe microscopy where the sample is scanned by a small probe to gather information about the surface and the magnetic properties of the sample [15]. In case of AFM, the force between the probe, which is very tiny sharp tip located at the end of a cantilever, and the specimen surface is measured in two different modes. In contact mode, the tip is directly in contact with the surface and the interaction force is dominated by Van der Waals interaction. The other mode is the tapping mode, a non-contact mode. Here the probe is oscillated by a mechanical oscillator. The interaction between the tip and the

surface changes the cantilever oscillation amplitude or phase relative to the drive signal.

In case of MFM, the AFM tip is coated with a thin layer of magnetic film, such as Ni or Co with high coercivity so that the tip's magnetic state does not change during imaging. The tip-sample magnetic interactions are measured and used to reconstruct the magnetic profile of sample surface. The magnetic force between the sample and tip can be expressed as [15]

$$F = \mu_0(m \cdot \nabla)H, \quad (2.11)$$

where, m is the magnetic moment of the tip approximated as a point dipole, H is the magnetic stray field from the sample surface and μ_0 is the free space permeability. The stray magnetic field from the sample can affect the magnetic state of the tip, and vice versa. Thus, interpretation of the MFM measurement is not straightforward. Fig. 2.13(a) shows schematic diagram of the magnetic tip movement over a magnetic sample. The stray field of the MFM tip magnetizes the sample surface locally along its own direction of magnetization. Typical resolution of 30 nm can be achieved [16], although resolutions as low as 10 to 20 nm are attainable. Fig. 2.13 (b) and 2.13 (c) below show typical AFM and MFM micrographs, respectively, of magnetite hollow spheres having average diameter of 725 nm. In MFM micrographs, the bright and dark spots may correspond to the local magnetic stray field of the sample either in the upward or in the downward direction with respect to sample's horizontal surface.

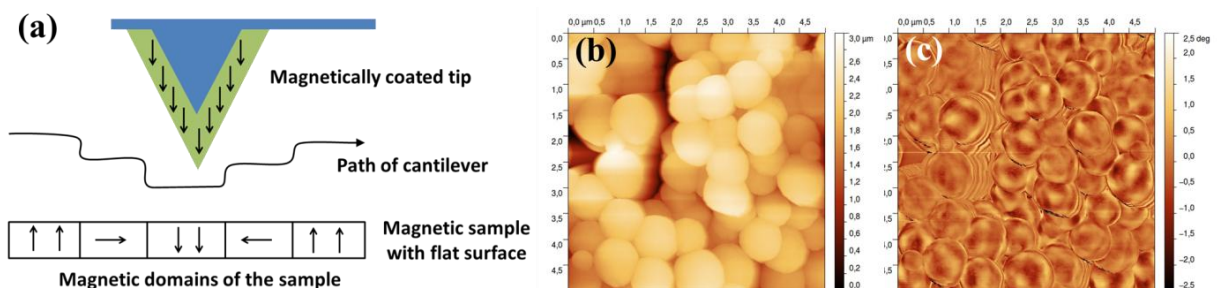


Figure 2.13 (a) Schematic diagram of a MFM tip scan over a flat magnetic surface, (b) AFM and (c) MFM micrographs of magnetite hollow spheres of 725 nm diameter.

2.6.4 AC Magnetic Measurement Technique

When a cylindrical sample is placed under a varying magnetic field (AC field), the magnetization in the sample also undergoes a periodic variation. This variation can be picked up by a pickup coil which is placed coaxially with the sample. We have developed an AC hysteresis loop measurement set up as described below. The schematic diagram of the whole circuit is shown in Fig. 2.14. The whole setup is a combination of mainly two circuits; one is the primary circuit consisting of the magnetizing coil (here solenoid) and the secondary circuit consisting of detection system. The solenoid is wound by insulated copper wires of diameter 0.75 mm over a plastic tube of inner and outer diameters of 60 mm and 35 mm. The solenoid is 25 cm long that consists of 1600 turns of copper wire.

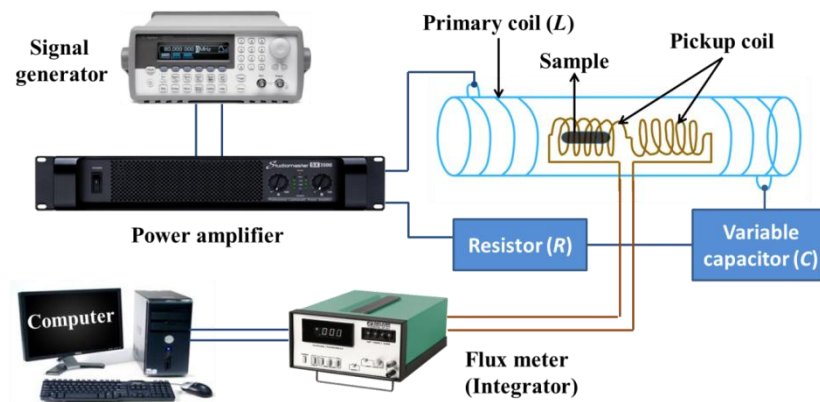


Figure 2.14 Schematic diagram of the ac magnetic hysteresis loop measurement setup.

The solenoid is designed to provide maximum possible magnetic within the specified volume. A sinusoidal voltage from a signal generator (Agilent 33120A; frequency ranging from 1 Hz - 15 MHz with maximum amplitude of 10 V_{p-p}) after amplification by a power amplifier (*Stuudio-master, DPA 5000*), is fed to the primary solenoid. The voltage proportional to magnetic field is taken from a low impedance high power resistor R and is supplied to the H -channel of a picoscope. The secondary circuit consists of the compensated pick-up coil pair (connected in series opposition so that there is zero net signal in absence of any sample), the electronic integrator (*Walker Scientific Fluxmeter MF- 3D*). The integrated pick-up voltage is finally supplied to the M -channel of the picoscope. This picoscope is directly

interfaced with a computer to make the data analysis more comfortable. In our system, the secondary coil is a set of two identical coils wound by 0.04 mm insulated copper wires having 1200 turns in each coil. Unlike VSM, in AC measurements, the moment of the sample is actually changing in response to an applied ac field, allowing the dynamics of the magnetic system to be studied.

The pickup coils were located coaxially within the long primary solenoid that produces a homogenous field along the length of the sample [17, 18]. The change in flux in presence of the sample is measured with the integrating flux meter. The MF-3D is a precision electronic integrating flux meter which measures the magnetic flux coupling within a coil or loop of wire. It integrates the volt-second signals induced across a coil, by the flux coupling to the coil. The output is representative of the change in flux coupling during the integrating period. Each magnetic line (Maxwell), in linking a conductor induces a 10^{-8} volt-second impulse in it. For a coil of N turns, the signal input received is $N\Phi$ Maxwell-turns or $N\Phi 10^{-8}$ volt-seconds. Therefore the induced voltage in presence of the sample is

$$V = N(d\Phi / dt)10^{-8} \quad (2.12)$$

Alternately, the flux can be expressed as AB where A is the area of the coil in which a flux density B is experienced and then the input impulse becomes $NAB 10^{-8}$ volt-seconds. By virtue of the heavy feedback employed in the integrator, its input impedance appears as the resistance value set in on the decade dial. A current, $(NAB/R) \times 10^{-8}$ ampere-seconds flows in this resistor and is constrained by the feedback to flow solely into the integrating capacitor which is free to move in voltage only at the output terminal. From the relationship, voltage equals charge (ampere-seconds) divided by capacitance, we obtain the output voltage (in volts)

$$V = \frac{N\Phi}{RC}10^{-8} = \frac{NAB}{RC}10^{-8} \quad (2.13)$$

The value of R (ohm) is 100 times the setting of the decade dial and the value of C (F) is 10^{-7} , 10^{-6} or 10^{-5} depending on the range selected. This integrated voltage which is proportional to the magnetization (as $B = 4\pi M$) of the sample was recorded as a

function of the voltage proportional to the magnetic field produced by the uniform solenoid. These voltages corresponding to M and H are displayed in the computer through the Picoscope Analog to Digital convertor (ADC-212). The M - H curve of the sample under observation is finally obtained after calibration of these voltages.

From the circuit displayed above we can measure the M - H loops of various samples up to frequency of 750 Hz. Due to increasing frequency of the applied ac signal the total impedance of the circuit ($R + j\omega L$) increases, where L is the inductance of the primary solenoid. However, to deal with this difficulty at higher frequencies we have formed a series L - C - R circuit by adding variable capacitors (C) with the circuit. We know that in a series L - C - R circuit, the total impedance can be written as follows.

$$Z = \sqrt{R^2 + \left(\omega L - \frac{1}{\omega C} \right)^2}, \quad (2.14)$$

By changing the series capacitance we can have a resonance at a particular frequency value. At series resonance the inductive reactance (ωL) and capacitive reactance ($1/\omega C$) becomes equal. Hence the effect of the increasing inductive reactance with increasing frequency is nullified and high current can be obtained at higher frequencies. With this L - C - R configuration we can achieve a magnetic field of nearly 56 kA/m at a frequency of 750 Hz whereas the field can be as high as 100 kA/m at 150 Hz field frequency.

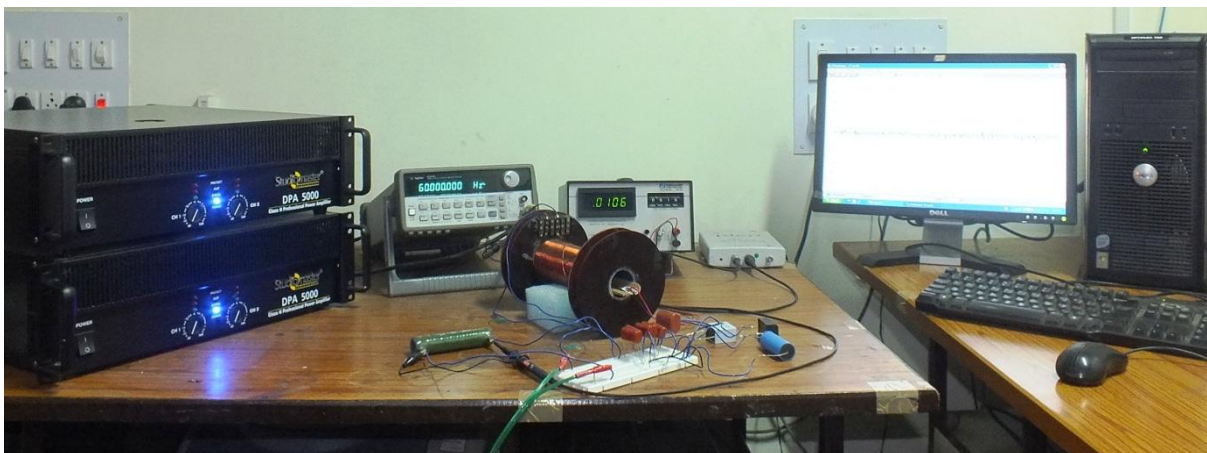


Figure 2.15 Photograph of the homemade setup for ac hysteresis loop measurement.

The hysteresis loops of magnetite hollow spheres of diameter 350 nm at different frequencies are shown in Fig.2.16 (see *Chapter 3* for details). We have also measured the hysteresis loops for NiFeO₄ nanoparticles, Ni nanowires, microwires of alloys etc.

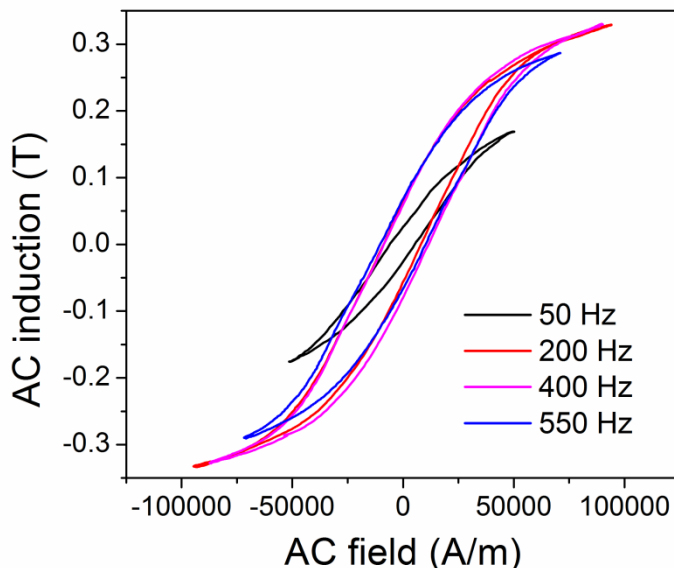


Figure 2.16 Frequency variations of hysteresis loops of magnetite hollow spheres.

2.7 Optical Characterization Techniques

2.7.1 UV Visible Absorption Spectrometer

In visible and adjacent (near-UV and near-infrared (NIR)) region of electromagnetic spectrum the molecules undergo electronic transition from ground state to another excited state. This technique is often used to measure the concentration of an absorbing species in solution media using Beer-Lambert law as given below.

$$A = \log_{10}(I_0 / I) = \varepsilon \cdot c \cdot L \quad (2.15)$$

where, A is the measured absorbance, I_0 is the intensity of the incident light at a given wavelength, I is that for the transmitted light, L is the path length through the sample, c is the concentration of the absorbing species and ε is the molar absorptivity or molar extinction coefficient that is constant for a particular absorber. The schematic diagram of the UV-visible spectrometer is shown in Fig. 2.17. We have used Shimadzu UV-2450 spectrophotometer to measure the steady state UV-visible absorption of the molecules.

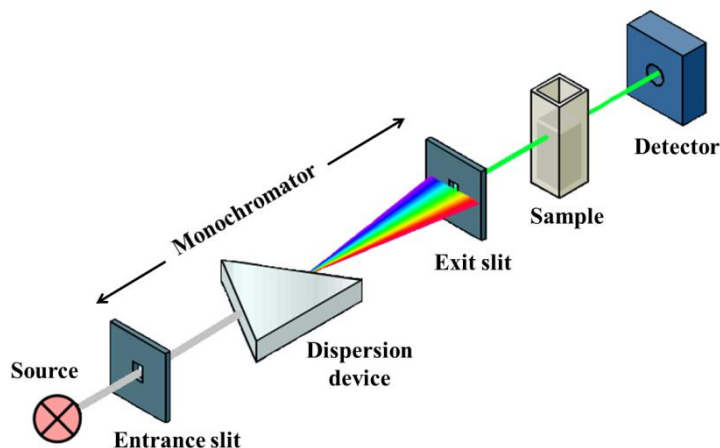


Figure 2.17 Schematic diagram of a UV-visible spectrometer.

2.7.2 Circular Dichroism (CD) Spectrometer

Circular dichroism (CD) is a form of spectroscopy based on the differential absorption of left and right-handed circularly polarized light. It can be used to determine different structures of macromolecules (including the secondary and tertiary structure of proteins). The CD measurements were done in a JASCO spectropolarimeter with a temperature controller attachment (Peltier) and the schematic diagram is shown in Fig. 2.18.

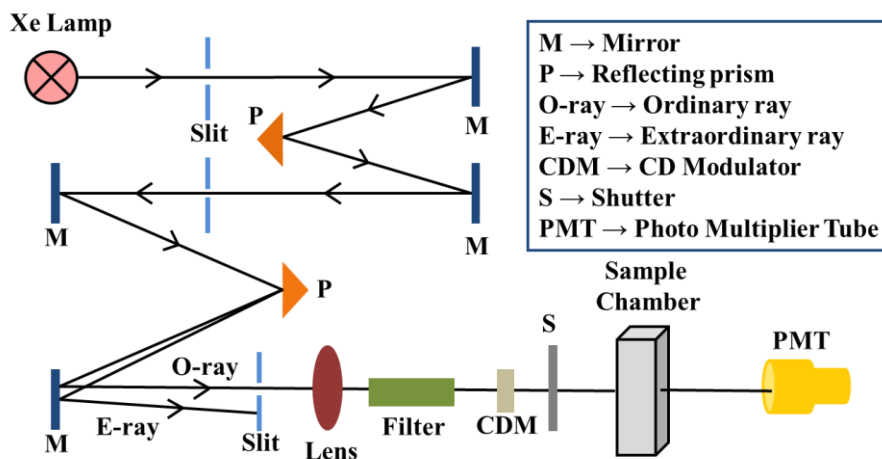


Figure 2.18 Schematic ray diagram of a Circular Dichroism spectropolarimeter.

A linearly polarized light can be considered as a combination of a right circularly polarized (RCP) and left circularly polarized (LCP) lights. So, when a plane polarized light passes through an optically active sample the speeds between

right and left polarizations differ ($c_L \neq c_R$) as well as their wavelength ($\lambda_L \neq \lambda_R$) and the extent to which they are absorbed ($\varepsilon_L \neq \varepsilon_R$). This difference in the absorbance of the left and right circularly polarized light, i.e., $\Delta A = A_L - A_R$, is defined as Circular Dichroism (CD) [19]. Most of the spectropolarimeters measure the CD spectrum in terms of ellipticity (θ) expressed in milli degrees and calculated using following equation.

$$\theta = \frac{2.303 \times 180 \times (A_L - A_R)}{4\pi} \text{ degrees.} \quad (2.16)$$

Molar ellipticity is defined as $[\theta] = \theta / cl$, where c is in moles per liter and l is in cm.

2.7.3 Fourier Transformed Infrared Spectroscopy (FTIR)

Fourier Transform Infrared spectroscopy (FTIR) is a powerful tool for identifying types of chemical bonds in a molecule by producing an infrared absorption spectrum that is like a molecular fingerprint. As different materials have different combination of atoms, no two compounds can produce exactly same kind of spectrum. Additionally, the intensity and sharpness of the peaks represent the amount of material present and its nature of crystallinity. The two beam Michelson interferometer, the heart of the FTIR, is schematically shown in Fig. 2.19.

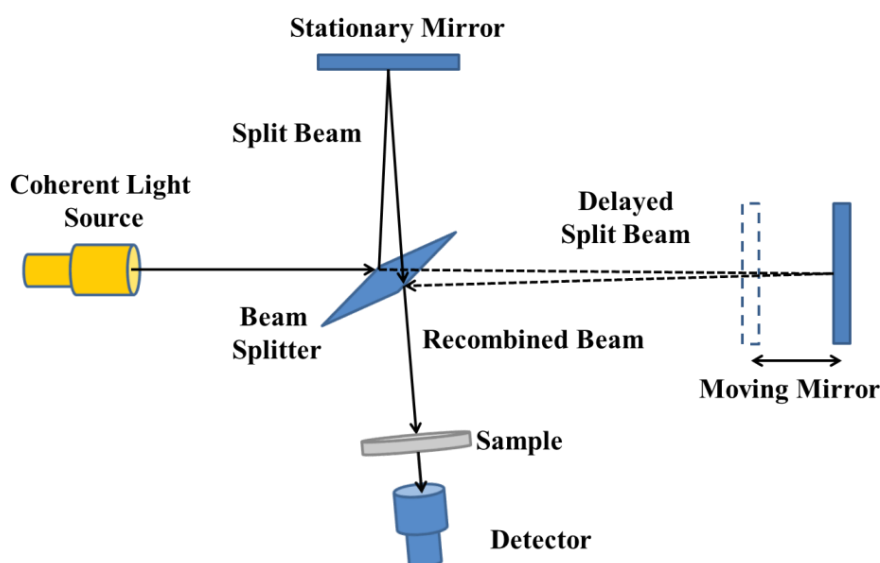


Figure 2.19 Schematic diagram of Michelson Interferometer, configured for FTIR.

As shown in the diagram, the collimated IR beam is partially reflected by and transmitted through the beam splitter (a half silvered mirror) and moves to the stationary and moving mirrors, respectively. Now the transmitted beam from the fixed mirror and reflected beam from the moving mirror may interfere constructively or destructively at the back side of the beam splitter depending on the wavelengths of the lights and the optical path difference introduced by the moving mirror. This resulting signal is called interferogram. At last, Fourier transformation of this interferogram is performed to have a frequency spectrum (plot of intensity at each frequency). For the FTIR measurements, powdered samples were mixed with KBr powder and pelletized. The background correction was made using a reference pure KBr pellet before every measurement.

2.7.4 Photoluminescence (PL) Spectroscopy

PL is a process in which a specimen absorbs photons (electromagnetic radiation) of particular energy and then re-radiates photons with different energies. Quantum mechanically, this can be described as excitation of an electron to a higher energy state by absorbing photons and then a return to a lower energy state with the emission of photons. The period between absorption and emission is very short, in the order of 10 nanoseconds. Steady state PL measurements of our samples were done in Horiba Jobin Yvon Fluorolog 3 spectrofluorimeter. Schematic diagram of the PL spectrometer is shown in Fig. 2.20.

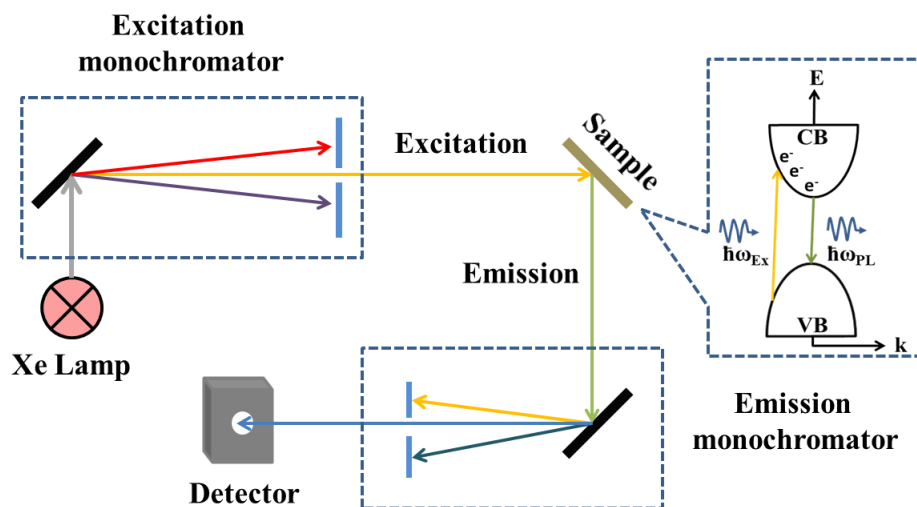


Figure 2.20 Schematic diagram of photoluminescence spectrometer.

Bibliography

- [1] K. M. Abu-Salah, A. A. Ansari, and S. A. Alrokayan, *J. Biomed. Biotech.* Article ID 715295, 1-15, doi:10.1155/2010/715295 (2010).
- [2] S. Kumar, and T. Nann, *Small*, **2**, 316 (2006).
- [3] H. C. Zeng, *Current Nanoscience*, **3**, 177 (2007).
- [4] C. L. Jackson, and G. B. McKenna, *J. Chem. Phys.* **93** (12), 9002 (1990).
- [5] Z. L. Wang, Y. Liu, and Z. Zhang *Handbook of Nanophase and Nanostructured Materials* (Kluwer Academic, Beijing 100085, China, 2000), Vol. 3.
- [6] R. L. Penn and J.F. Bannfield, *Am. Mineral.* **83**, 10771082 (1998).
- [7] Z. Tang, N.A. Kotov and M. Giersig, *Science* **297**, 237240 (2002).
- [8] L. Manna, E.C. Scher and A.P. Alivisatos, *J. Am. Chem. Soc.* **122**, 1270012706 (2000).
- [9] C. Burda, X. Chen, R. Narayanan and M.A. El-Sayed, *Chem. Rev.* **105**, 1025 (2005).
- [10] J. Mullin, *Crystallization*, 4th ed. (Butterworth Heinemann, Boston, 2001).
- [11] Y. D. Li , H. W. Liao , Y. Ding , Y. T. Qian , L. Yang , and G. E. Zhou, *Chem. Mater.* **10** (9), 2301 (1998).
- [12] B. D. Cullity, S. R. Stock, *Elements of X-ray Diffraction*, 3rd Edition, Prentice Hall (2001).
- [13] T.R. Groves, H.C. Pfeiffer, T.H. Newman, and F.J. Hohn, *J. Vac. Sci. Technol. B*, **6**(6), 2028 (1988).
- [14] E. du Trémolet de Lacheisserie, D. Gignoux, and M. Schlenker (editors) *Magnetism: Materials and Applications*. **2**. Springer (2005).
- [15] D. C. Jiles, *Introduction to Magnetism and Magnetic Materials*, 2nd edition, Springer (1998).
- [16] L. Abelmann, S. Porthun, et al. *J. Magn. Magn. Mater.*, **190**, 135 (1998).
- [17] Q. Design, "Introduction to AC Susceptibility", <http://www.qdusa.com> (Accessed in 2012).
- [18] A. Bajpai and A. Banerjee *Rev. Sci. Instrum.* **68**, 11 (1997).
- [19] A. Rodger, and B. Nordén, *Circular Dichroism and Linear Dichroism*, Oxford University Press, (1997).

Chapter 3

Magnetite (Fe_3O_4) Nano-Hollow Spheres

In this chapter we have discussed about the synthesis, characterization and possible applications of variable sized Magnetite nano-hollow spheres.

3. Nano - Hollow Spheres of Magnetite: Facile Synthesis, Characterization and Applications

3.1 Preamble

Magnetite hollow spheres fall in a distinguished class of materials having various unique properties which mainly come out due to their hollow nature. It has been found that the magnetic domain structure of these hollow spheres can be tuned by changing the diameter of the spheres and as well as the thickness of the shell. This change in domain structure from single domain to multi domain configuration also changes their magnetic and electric properties making it unique among all other nanostructures of magnetite [1, 2].

Traditional and effective routes for fabricating magnetite hollow spheres includes different template assisted methods where silica spheres, polystyrene latex spheres, polymer micelles, surfactant vesicles, liquid droplets etc. have been used as templates [3-6]. In this method Fe_3O_4 nanoparticles are first accumulated on surfaces of the templates followed by controlled removal of the templates that renders the inner part of the Fe_3O_4 system hollow. But this method is very cost effective for large scale production of hollow spheres and also removal of template is a very difficult and annoying for such large scale synthesis. So, template free synthesis is more feasible and very effective for industrial production.

In this chapter we will discuss about the facile synthesis of Fe_3O_4 hollow spheres of five different diameters (ranging from 100 nm to 725 nm) in a template free solvothermal method and explore their size dependent magnetic and electric properties [6]. Domain structure of these hollow spheres is found to change from pseudo single domain (PSD) to multidomain (MD) state as we move from smaller spheres to bigger spheres. Magnetic hysteresis, electrical conductivity and dielectric permittivity of these hollow spheres have found to be influenced significantly due to this size variation. Actually, with decrease of particle size not only the domain structure changes but the grain boundary effect becomes more prominent due to increase in number of grains. This grain boundaries act as potential barrier for free

movement of charge carriers. So, the simultaneous effect of domain configuration and the grain boundaries is expected to be occurred in the smaller particles.

Spinel ferrites are very suitable for applications in microwave domain, i.e. in MHz to GHz frequency range. Here, we have also studied the high frequency response of these nano-hollow spheres for their possible application in hyperthermia treatment, inductive devices, sensors, as microwave absorbers etc. Coercivity of these spheres changes much with increase in applied AC field frequency from which we can calculate the power loss of these materials. This hysteresis loss of materials results in heating of surrounding atmosphere which can be utilized to destroy certain diseased cells.

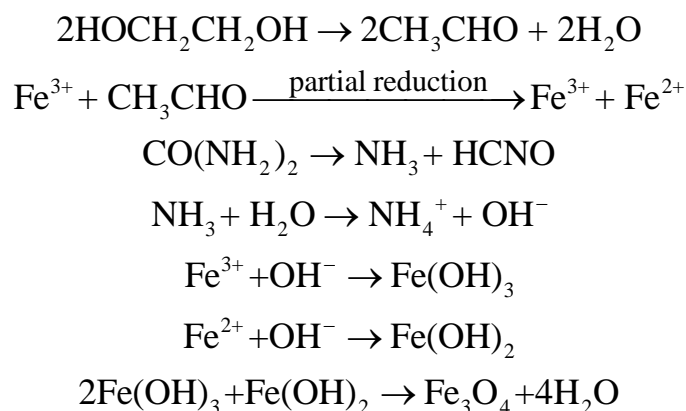
As these materials have hollow interior and also can interact with other cationic and anionic molecules electrostatically in solution phase, this materials can be effectively used for water treatment, i.e. can separate dyes or other chemicals from water by adsorption. We have applied these hollow spheres for purification of water and have discussed their dye adsorption capacity that has been found to be greatly affected by several factors like initial dye concentration, amount of adsorbent, pH of the solution etc.

3.2 Synthesis of Fe_3O_4 hollow spheres of different diameters

We have prepared magnetite (Fe_3O_4) hollow spheres in a template free solvothermal method as described by Wangchang Li et al. [6, 7]. Here, we have modified the synthesis technique to vary the inner and outer diameter of the hollow spheres. In a typical synthesis procedure, 2.03 g of $FeCl_3 \cdot 6H_2O$ was mixed with 60 ml Ethylene Glycol (EG) solution. This solution was stirred with a magnetic stirrer until the Ferric chloride was completely dissolved in the EG solution. Then 0.93 g of Urea and x ($0.07 \leq x \leq 0.4$) g of PVP was added in this solution. This solution was again stirred until it became completely transparent. This final solution was then transferred in an 80 ml Teflon lined stainless steel autoclave for the solvothermal process. The solvothermal process was carried out at $120^\circ C$ for 20 hrs. After 20 hrs, resultant black solution was washed in alcohol for several times and then dried at $60^\circ C$ overnight. Diameter of the magnetite hollow spheres was varied by changing

the concentration of PVP. We synthesized five sets of hollow spheres by varying PVP amount and they are termed as follows: Set 1 for 0.40 g PVP; Set 2 for 0.30 g PVP; Set 3 for 0.15 g PVP; Set 4 for 0.10 g PVP and Set 5 for 0.07 g PVP [6].

Here, role of Ethylene Glycol (EG) was to partially reduce the Fe³⁺ ions to Fe²⁺ ions. Urea helped to precipitate Fe³⁺ and Fe²⁺ to their corresponding hydroxides where the hydroxyl group came from ammonium-hydroxide produced from urea and after the heat treatment both the iron hydroxides removed water with production of Fe₃O₄. The possible chemical reaction is given below [6]:



Here Fe³⁺ in presence of OH⁻ might form Fe(OH)₃ or FeOOH (iron oxide hydroxide) and ultimately Fe₃O₄ was formed in presence of Fe(OH)₂. It has to keep in mind that no water has been used in any part of the whole synthesis procedure.

3.3 Results and Discussions

3.3.1 Phase and morphology

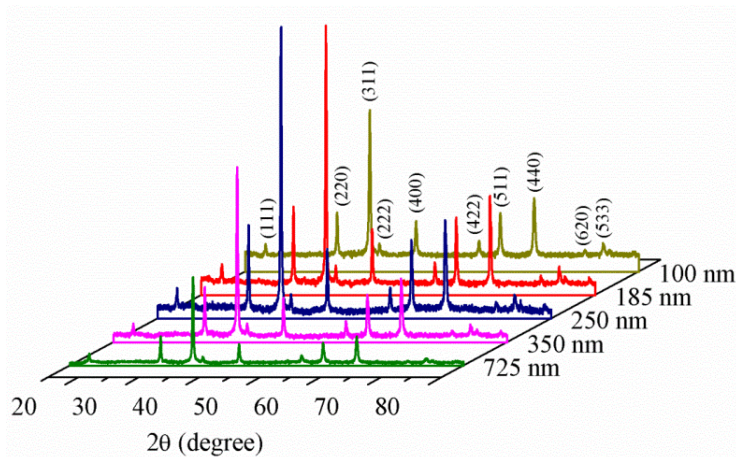


Figure 3.1 x - ray diffraction patterns of all sets of magnetite hollow spheres.

Figure 3.1 shows the XRD pattern of all sets of samples and the peaks are indexed as well (ICDD, Ref. No. 00-003-0862). From this pattern it is clear that all the samples are of pure phase Fe_3O_4 and under minute observation it is found that the peaks become sharper with increase of crystallite size. The crystallite size (d) of all the samples is calculated from the Debye-Scherrer equation given below:

$$d = \frac{0.9\lambda}{\beta \cos \theta} \quad (3.1)$$

where, λ is the wavelength of the Cu $K\alpha$ radiation (1.54 Å) and β is the full width at half maximum (FWHM) at the diffraction angle 2θ . SEM and TEM images of all sets of samples are depicted in Figure 3.2.

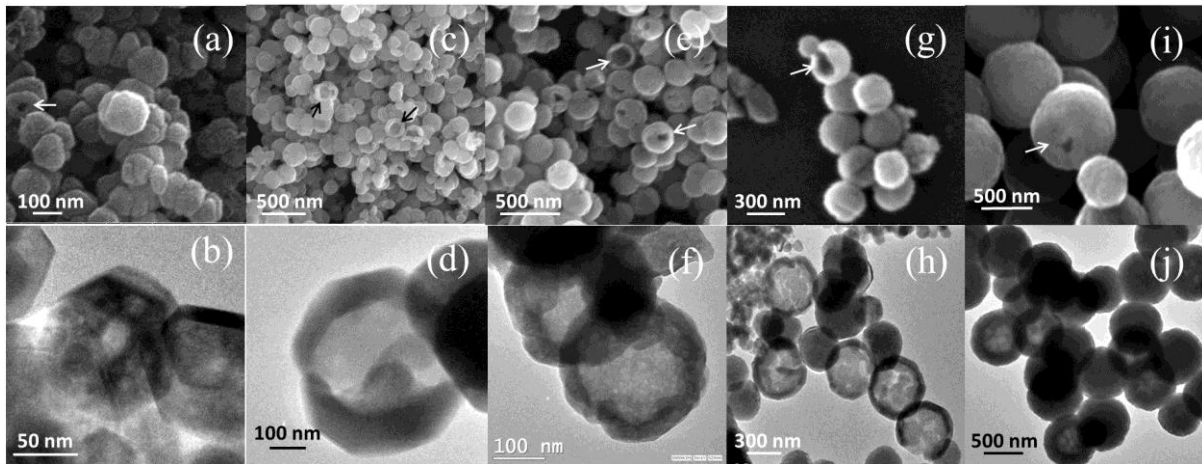


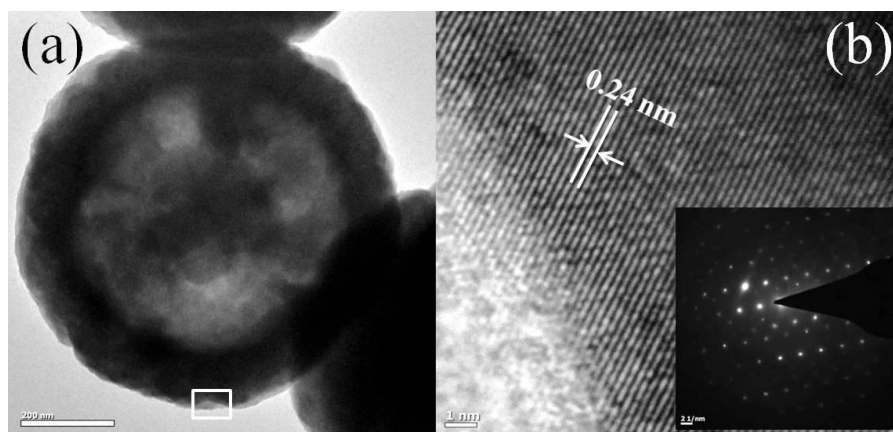
Figure 3.2 SEM and TEM images of the hollow spheres; (a), (c), (e), (g) and (i) are the SEM images of Set 1, Set 2, Set 3, Set 4 and Set 5 sets of hollow spheres, respectively; (b), (d), (f), (h) and (j) are the corresponding TEM images of Set 1, Set 2, Set 3, Set 4 and Set 5 sets of hollow spheres, respectively. Arrows in the SEM images are to show the hollow nature of the spheres.

These images confirm the synthesis of regular and uniform hollow spheres of Fe_3O_4 . The rough surface of the hollow spheres (in SEM images) implies that these are composed of smaller Fe_3O_4 nano crystals [6]. Some broken parts of the spheres can also be seen in the SEM images which represents the hollow interior of the spheres. The average diameter of the hollow spheres (D) and their shell thickness (t), as calculated from SEM and TEM micrographs along with the crystallite size (d) are summarized in Table 3.1.

Table 3.1 Values of 'D', 't' and 'd' of all sets of Fe_3O_4 hollow spheres.

Sample name	PVP amount (mg)	Average diameter (D) (nm)	Crystallite size (d) (nm)	Shell thickness (t) (nm)
Set 1	400	100 (± 5)	29.89	30
Set 2	300	185 (± 10)	35.09	35
Set 3	150	250 (± 9)	36.65	50
Set 4	100	350 (± 15)	38.56	65
Set 5	75	725 (± 17)	39.57	150

From the Table 3.1 it is clear that the crystallite size as well as shell thickness of the hollow spheres increases with increasing average diameter of the spheres. TEM images of all set of samples also confirm the hollow nature of the nano spheres. The difference in contrast between the margin and the interior of the spheres confirms its hollow nature supporting the SEM results. For more detailed investigation of the crystalline structure and the growth direction of synthesized products, high resolution TEM (HRTEM) analysis was done for all sets of samples. A representative TEM image of a single hollow sphere of "Set 5" sample and the corresponding HRTEM micrograph of the white square marked area are shown in Fig. 3.3(a) and 3.3(b), respectively.

**Figure 3.3** TEM image of hollow sphere (a) and HRTEM image of the area selected by the white rectangle (b); (inset) SAED pattern of that selected area.

The clearly resolved atomic lattice fringes can be seen in the HRTEM micrograph and the measured average spacing between the crystallographic planes is nearly 0.24 nm that corresponds to the (311) lattice planes of a typical cubic Fe_3O_4 crystals [6]. Selected area electron diffraction (SAED) pattern for the hollow sphere (as shown in the inset of Fig. 3.3(b)) shows bright diffractive dots that represent the single crystalline nature of the Fe_3O_4 nano crystals. From these analyses it is clear that the hollow spheres are made of single crystalline Fe_3O_4 nano crystals with same crystal orientation.

FTIR analysis of all sets of hollow spheres is performed to confirm the exact phase of the hollow spheres and the corresponding spectra are shown in Fig. 3.4. All sets of spheres show absorption peaks in the region of $3250\text{--}3750\text{ cm}^{-1}$ which can be assigned to the stretching vibration of the hydroxyl ($-OH$) group present in nano hollow spheres coming from atmospheric water. Two distinct absorption peaks around 567 cm^{-1} and 430 cm^{-1} correspond to the vibration of $Fe^{2+}-O^{2-}$ and $Fe^{3+}-O^{2-}$ respectively of Fe_3O_4 [6, 8, 9]. There are no other peaks of PVP in the spectrum which confirms its complete removal after the hollow sphere synthesis. So, this analysis again confirms that the phase of the as-prepared hollow spheres is magnetite.

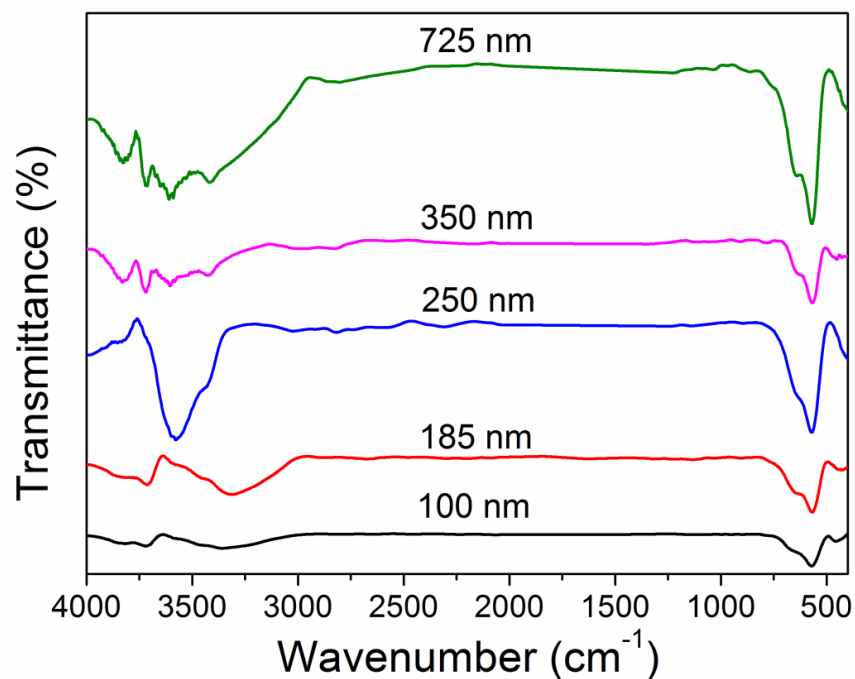


Figure 3.4 FTIR spectra of all sets of hollow spheres.

Formation of Hollow Spheres

As the solvothermal process takes 20 hrs to complete, to investigate the formation procedure and growth mechanism of the hollow nano spheres we have repeated the same solvothermal synthesis procedure at 4 hrs interval and the TEM images of the corresponding products are shown in Fig. 3.5.

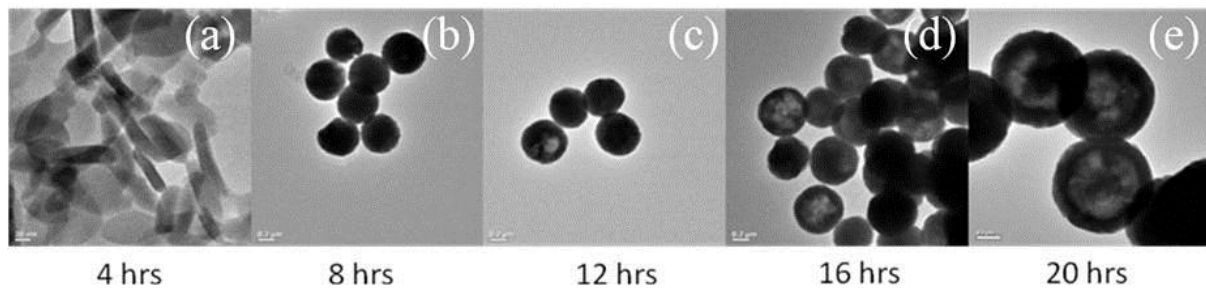


Figure 3.5 Formation procedure of Fe_3O_4 hollow spheres and representative TEM images of five intermediate steps: (a) 4 hrs, (b) 8 hrs, (c) 12 hrs, (d) 16 hrs and (e) 20 hrs.

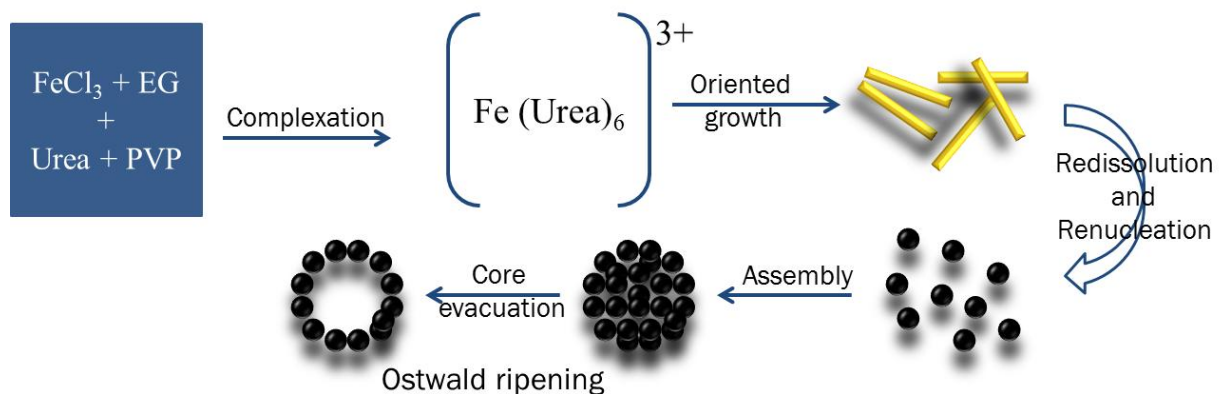


Figure 3.6 Proposed mechanism for the formation of Fe_3O_4 nano-hollow spheres.

From these experiments, the formation procedure of the hollow spheres can be depicted in Fig. 3.6 and is summarized below: Ferric chloride in presence of urea and EG forms octahedral shaped $Fe [(Urea)_6]Cl_3$ which after their oriented growth forms rod like structures (Fig. 3.5(a)). During this solvothermal synthesis phase, this rod shaped structures dissolve in the EG solution and renucleates to form nanoparticles of Fe_3O_4 (an intermediate stage between 4hrs and 8 hrs). As the particles are coated with PVP, they come close together due to their dipole-dipole interaction and also due to attraction between long chains of PVP to form solid

spheres of Fe_3O_4 (after 8 hrs) (Fig. 3.5(b)). As the freshly prepared Fe_3O_4 molecules are aggregating over these solid spheres, difference between the inner and the outer parts of the spherical aggregates increases. As a result the nanoparticles inside the solid spheres come out of the bigger spheres to form smaller spheres making the former sphere hollow (Fig. 3.5(c) – 3.5(e)). This inside out procedure is spontaneous for minimization of total surface energy of the spheres and this process is known as Ostwald ripening.

3.3.2 Magnetic Measurements

Temperature dependent zero field cooled (ZFC) and field cooled (FC) magnetization measurements of all sets of Fe_3O_4 hollow spheres were performed from 80 K to 300 K at 100 Oe reference field and are shown in Fig. 3.7.

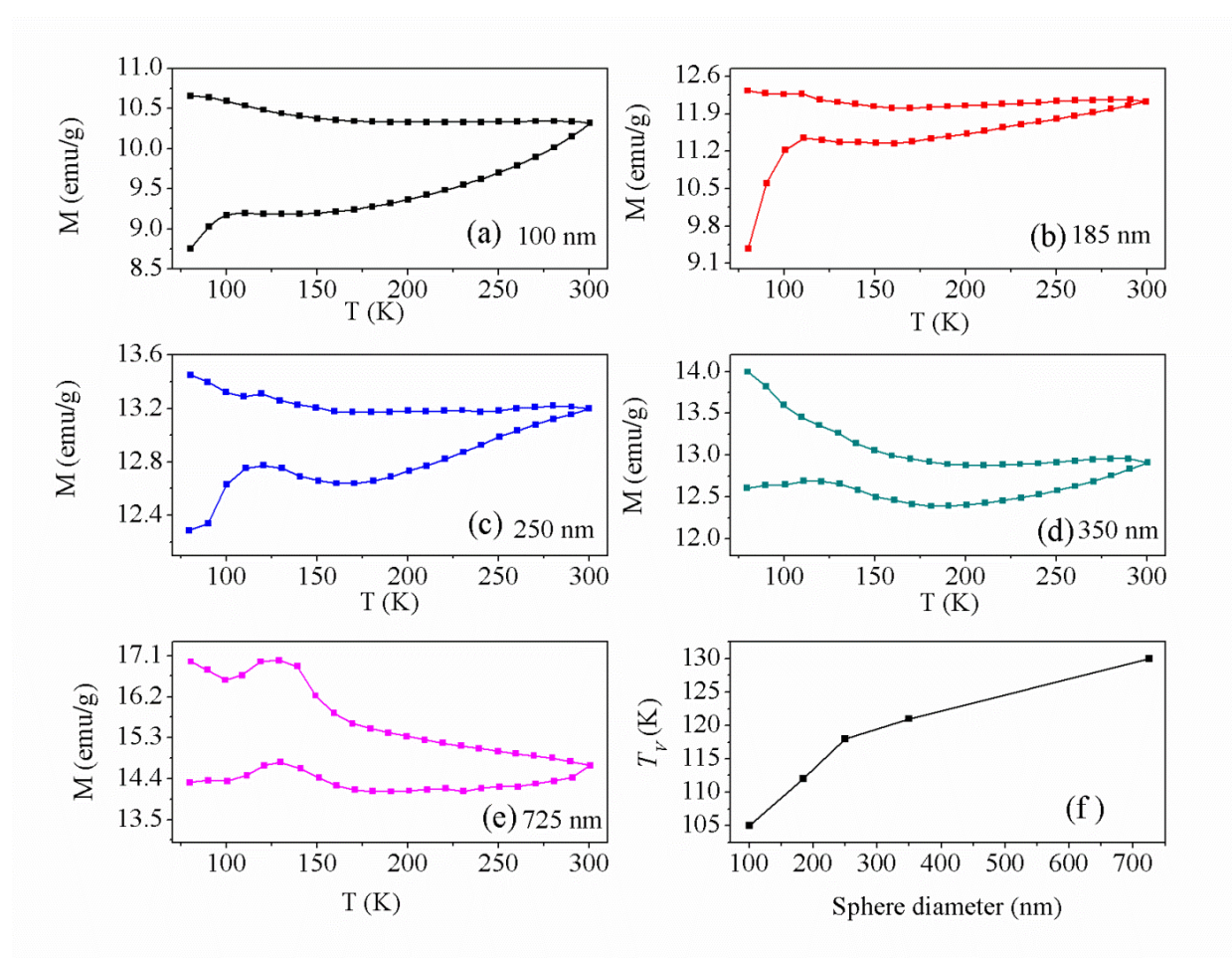


Figure 3.7 Temperature (T) dependence of Magnetization (M) of all sets of spheres; (a) Set 1 (100 nm), (b) Set 2 (185 nm), (c) Set 3 (250 nm), (d) Set 4 (350 nm) and (e) Set 5 (725 nm); (f) Variation of Verway transition temperature (T_V) with hollow sphere diameter (D).

FC and ZFC curves of all the samples split at $T = 300$ K indicating that these particles are ferromagnetic within 80 K to 300 K having blocking temperature at or above 300 K. During ZFC measurement, with increase in temperature from 80 K, magnetization of all the hollow spheres increases showing a cusp around a certain temperature (T_V) which is related to the Verwey transition of Fe_3O_4 hollow spheres [10, 11]. After T_V , magnetization either increases slightly (Figure 3.7(a)-3.7(d)) or remains almost constant (Fig. 3.7(e)) with increasing temperature up to room temperature. During this Verwey transition, Fe_3O_4 undergoes a phase transition from cubic state to monoclinic state upon cooling below Verwey transition temperature (T_V) which results in a sharp drop of conductivity almost two orders of magnitude as well as magnetization below T_V [11]. Upon minutely observing the cusps of the ZFC curves, it is found that the T_V of the hollow spheres changes slightly from 105 K to 126 K as the average diameter of the hollow spheres increases from 100 nm to 725 nm and this variation is shown in Fig. 3.7(f). This type of change in T_V both above and below the bulk value (T_V (bulk) = 120 K) was also found depending on the Fe_3O_4 grain size by other authors [10, 11]. T_V is also found to be depending not only upon grain size but also the geometrical size of the particles. So, in our case, as the diameter of the hollow spheres changes, the T_V values also changes accordingly. The field cooled (FC) magnetization curves also show such sign of Verwey transition as in ZFC case for all sets of magnetite hollow spheres.

To investigate the difference between magnetic properties of magnetite hollow spheres of different diameters, hysteresis loops of five sets of samples were measured carefully at basal temperature (80 K) and at room temperature (300 K) and are depicted in Fig. 3.8. Fig. 3.8(a) represents the M (H) loops at $T = 80$ K and Fig. 3.8(b) represents the same at $T = 300$ K. From the hysteresis loops it is clear that smaller spheres have higher remanence (M_R) but have low saturation magnetization (M_S) than the bigger spheres that possess larger M_S and smaller M_R values. But both the M_R and M_S values decreases with increasing temperature (from $T = 80$ K to 300 K) due to increase in thermal fluctuation at higher temperature. Maximum value of M_S is found to be 86.74 emu/g for Set 5 magnetite hollow spheres which is slightly less than the bulk M_S value of Fe_3O_4 (M_S (bulk) = 92 emu/g).

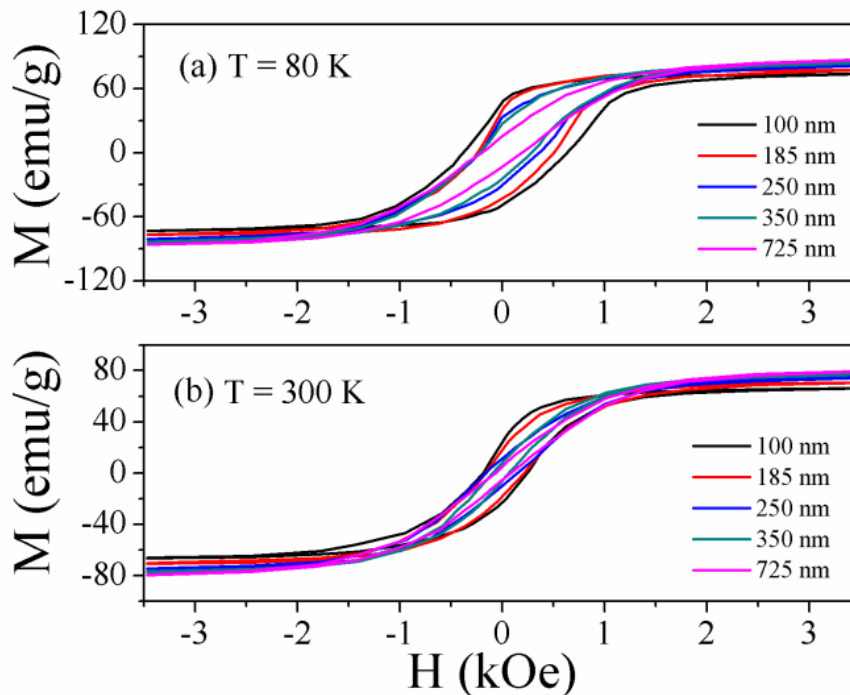


Figure 3.8 Magnetic hysteresis loops of magnetite hollow spheres at different temperatures (a) at $T = 80$ K and (b) $T = 300$ K.

For other sets of hollow spheres the M_s values are considerably smaller than the bulk values. This decrease in M_s values with decreasing sphere diameter is due to higher surface to volume ratio in smaller particles [9, 12]. Fraction of superficial spins increases with decreasing particle diameter. These spins can have broken bonds and also canted spin structure due to many reasons. Actually in ferrites, the antiferromagnetic interaction between the Fe^{3+} ions in A site and Fe^{2+} ions in B site is mediated by the intervening oxygen atom. Now, if this oxygen atom is missing from the intermediate site, then the bond will be broken. Additionally, if the metal ions are attached with some other organic molecules then the electrons involved there can no longer take part in the exchange interaction which also leads to broken bonds and canted spin structure [13]. This type of spin canting and broken bonds make the particle surface a disordered shell due to which the M_s values decrease by considerable amount from bulk values [6, 9]. Among all sets of hollow spheres, maximum remanence M_r is found to be the ~ 49 emu/g for Set 1 spheres that have average diameter of 100 nm and for others the remanence decreases with increasing sphere diameter and also with increasing temperature of measurement.

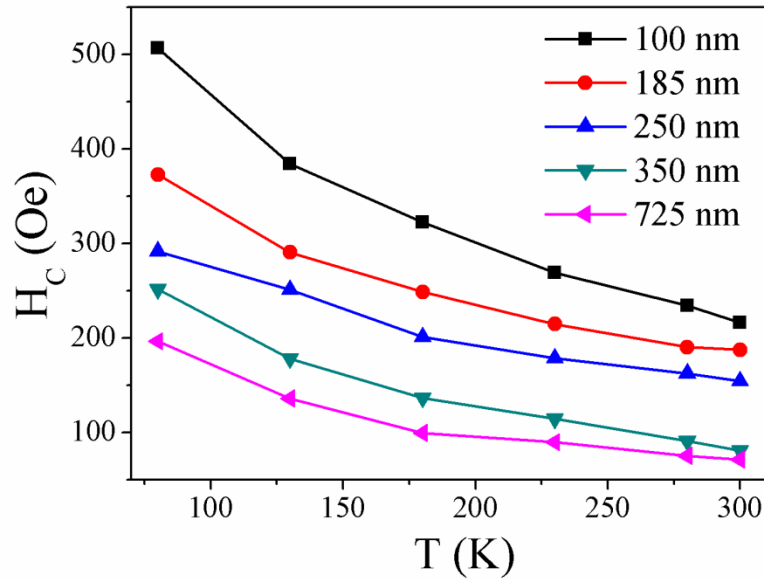


Figure 3.9 Coercive field (H_C) vs. temperature (T) plot of hollow spheres of different diameters.

Variation of coercive fields (H_C) with temperature (T) for all sets of magnetite hollow spheres is shown in Fig. 3.9. The trend of variation of H_C is nearly the same for all sets of samples, i.e. decreasing with increasing temperature. From this plot it is clear that the smallest hollow spheres (Set 1) have the largest value of H_C which is ~ 507 Oe at $T = 80$ K. The H_C values decrease from 507 – 197 Oe at $T = 80$ K and 216 – 71 Oe at $T = 300$ K as the size of the hollow spheres increases from 100 nm to 725 nm. This decrease in coercive values with increasing particle diameter can be attributed to the increase in saturation magnetization (M_s) and also to the decrease in magneto crystalline anisotropy constant (K).

Domain Structure

To analyse the magnetic hysteresis behaviour of hollow spheres of different diameters, domain structure analysis is very much important because all the magnetic behaviours are mainly controlled by magnetic domains. Here the possible domain structures of variable sized magnetite hollow spheres are investigated in terms of Day plot which is a graphical mapping of M_{rs}/M_s vs. H_{cr}/H_c , where H_{cr} is the value of the field under which the $M-H$ loop shows a remanence $M_r = 0.5 M_{rs}$ [1, 6]. The Day plots for all the hollow spheres of various diameters in the temperature range of 80 K to 300 K are shown in Fig. 3.10.

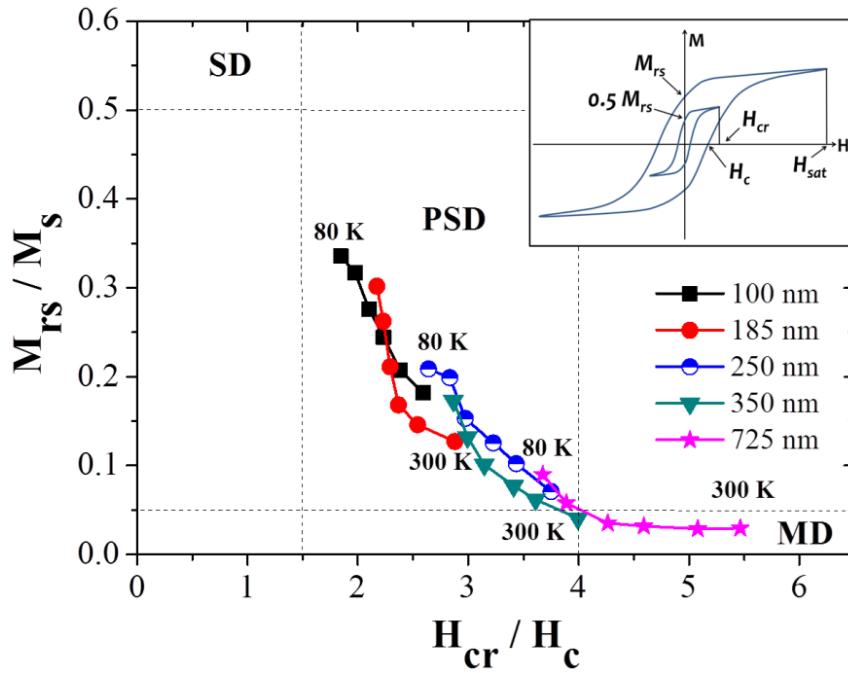


Figure 3.10 Day plots to represent the possible domain state of the hollow spheres of different diameters. It is a graphical representation of M_{rs} / M_s vs. H_{cr} / H_c , where H_{cr} is the value of the field under which the $M - H$ loop shows a remanence $M_r = 0.5 M_{rs}$ (as shown in inset figure). Domain states are separated in single domain (SD), pseudo single domain (PSD) and multi domain (MD) states.

In this graph the Single Domain (SD), Pseudo Single Domain (PSD) and Multi Domain (MD) regions are separated by the dashed lines. From the plot it is clear that within the selected temperature range Set 1 to Set 4 hollow spheres fall in the PSD range whereas the Set 5 spheres are in the MD region. PSD structure means that the corresponding hollow spheres have domains that are intermediate between SD and MD configuration. It is found that, Set 1 and Set 2 hollow spheres have domain structure that are close to the SD region in lower temperature range and with increase in diameter of the magnetite hollow spheres (in other words with increasing magnetite grain size) the domain structure shifts from PSD region to MD region (Set 3 and Set 4 hollow spheres).

According to Ye et al. the change in magnetization in response to the external magnetic field in single domain hollow spherical structures is due to change of the domain structure from curling vortex state to saturated state via an intermediate stage termed as onion state, as shown in the Fig. 3.11 [1, 14].

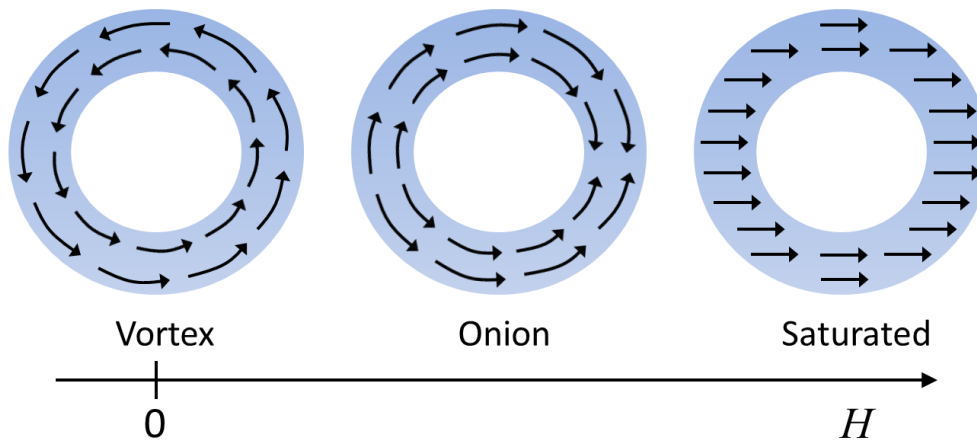


Figure 3.11 Field dependent domain states in hollow spheres; from Vortex to Saturated state through Onion state.

At zero fields, vortex state of the magnetic moments is the most stable one for a spherical hollow magnet with low magnetocrystalline anisotropy. In this state, the magnetization directly follows the surface of the spheres to minimize the magnetic stray fields and the vortex has its singularities at the poles of the hollow sphere. With increase of external field these moments try to align with the external field direction and at sufficiently higher field all the moments must align along the field direction. This is the saturated state. Within this two domain states there is another domain structure proposed by various authors which is characterized by two head to head domain walls with opposite magnetization direction [14]. This intermediate state is known as onion state (Fig. 3.11). By considering the total energies of zero field magnetization states it has been theoretically predicted that the single domain state, two domain or four domain state and multidomain states are the most energetically stable states for smaller, slightly larger and bigger particles, respectively [2]. So, from the magnetization results of the magnetite hollow sphere system we can conclude that the smaller hollow spheres (Set 1 - 4) having small shell thickness may have two domain states (for uniaxial anisotropy) or four domain states (for cubic anisotropy) whereas two coaxial cylindrically symmetric domains or multidomain configuration may be formed within the biggest hollow spheres (having diameter of 725 nm with \sim 165 nm thick shell) [2, 6]. That's why the Set 1 - 4 hollow spheres appear in the PSD region and Set 5 spheres are in MD region in the Day plots.

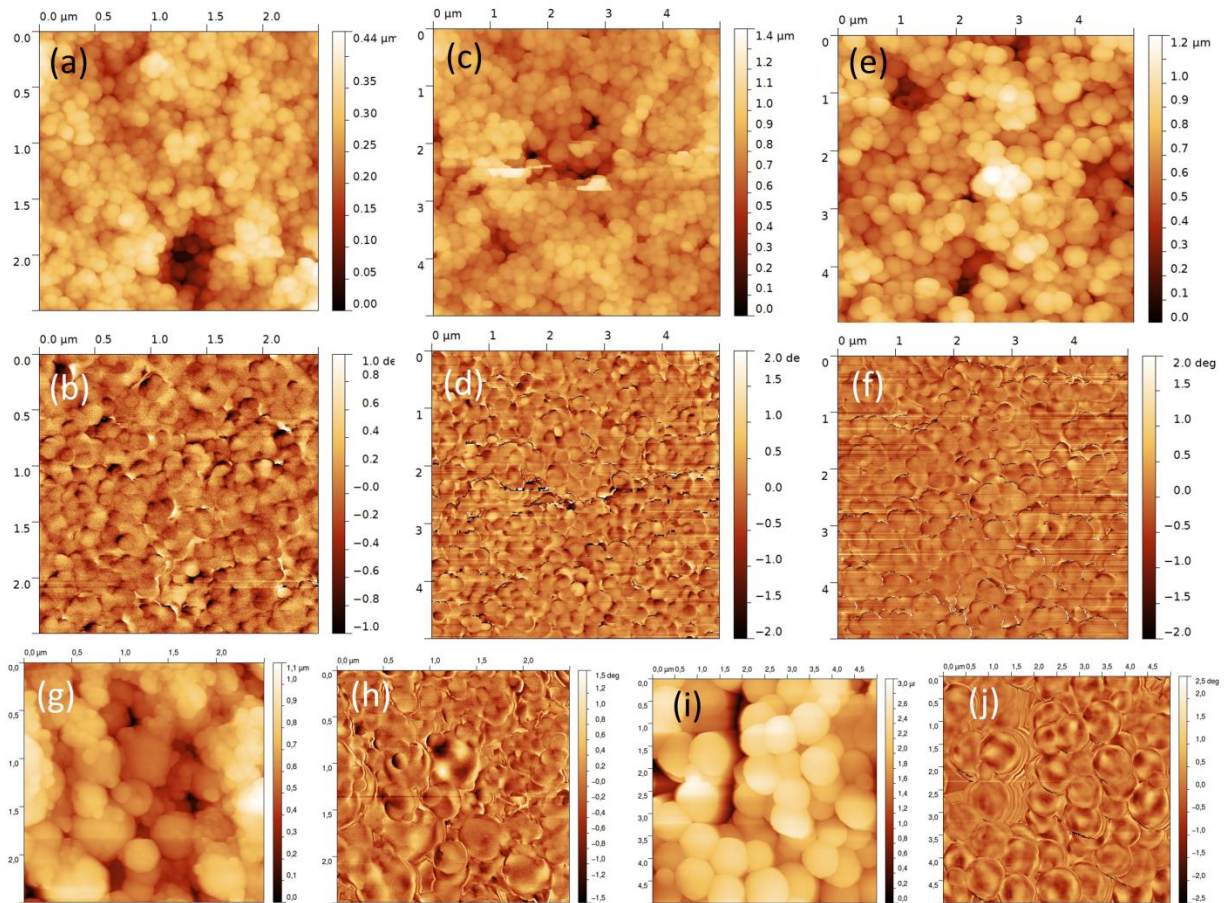


Figure 3.12 AFM and MFM images of the hollow spheres; (a), (c), (e), (g) and (i) are the AFM images of Set 1, Set 2, Set 3, Set 4 and Set 5 hollow spheres, respectively; (b), (d), (f), (h) and (j) are the corresponding MFM images of Set 1, Set 2, Set 3, Set 4 and Set 5 hollow spheres, respectively.

Figure 3.12 depicts the AFM and MFM images of all sets of hollow spheres and from the MFM micrographs we can conclude that the estimation of domain structure by Day's plot is correct. The uniform size distribution of all sets of hollow spheres can be seen from their corresponding AFM images. Bright and dark spots in the MFM micrographs signify that the magnetization direction of the hollow spheres is either in upward or in downward directions, respectively, with respect to the samples horizontal surface. Lower contrast between bright and dark spots in the MFM micrographs for Set 1, Set 2 and Set 3 hollow sphere samples represent their single domain or pseudo single domain structure whereas higher contrast in case of biggest hollow spheres (Set 5) confirms their multi domain structure. In case of Set 4 sample, there is a mixture of higher and lower contrast of dark and bright spots which is indicative of the fact that some spheres have multi domain structure and

others have single domain structure. So, from this study it is clear that the magnetic domain structure of the hollow spheres can be tuned simply by tuning their size and their shell thickness.

Bloch's theorem in nano-spheres

Temperature variation of saturation magnetization (M_s) of all sets of hollow spheres, as measured at an applied field of 16 kOe, is depicted in Fig. 3.13. To analyse these results we recall the spin wave theory. According to this theory, demagnetization of ferromagnetic or ferrimagnetic substance from $M_s(0)$ (value of magnetization at $T = 0$ K) with temperature is due to the excitation of spin waves of long wavelengths ($K \rightarrow 0$) and the excitation energy E_k of the spin waves can be written as follows [6, 15]

$$E_k = Dk^2 + Ek^4 + g\mu_B(H_0 + H_A + H_D) \quad (3.2)$$

Here D is the spin-wave stiffness co-efficient; E is a constant for k^4 term. H_0 , H_A and H_D is the externally applied field, anisotropy field and demagnetization field, respectively. In general, at temperatures well below T_C , the temperature dependence of saturation magnetization follows the Bloch law given by [16]

$$M_s(T) = M_s(0)(1 - BT^b) \quad (3.3)$$

where, B is the Bloch constant proportional to the inverse of exchange constant (J) and b is the Bloch exponent which is $3/2$ for a three dimensional system [17]. In nano sized particles a clear deviation from Bloch's law is found at low temperature, which is due to presence of magnons having wavelength larger than the particle dimension that cannot be excited [17]. The Bloch power law exponent (b) is found to be strongly dependent on size of the particles, its chemical composition, and synthesis route but independent of the structure of nanoparticles [18]. For ferrite system ' b ' is found to vary from 1.5 to 1.9 for particle sizes of 5 to 15 nm [19]. However, this value is sufficiently larger than $b = 0.9$ for $CoCrFeO_4$ nanoparticles of average size 8.1 nm as obtained by Xiong and his co-workers [20].

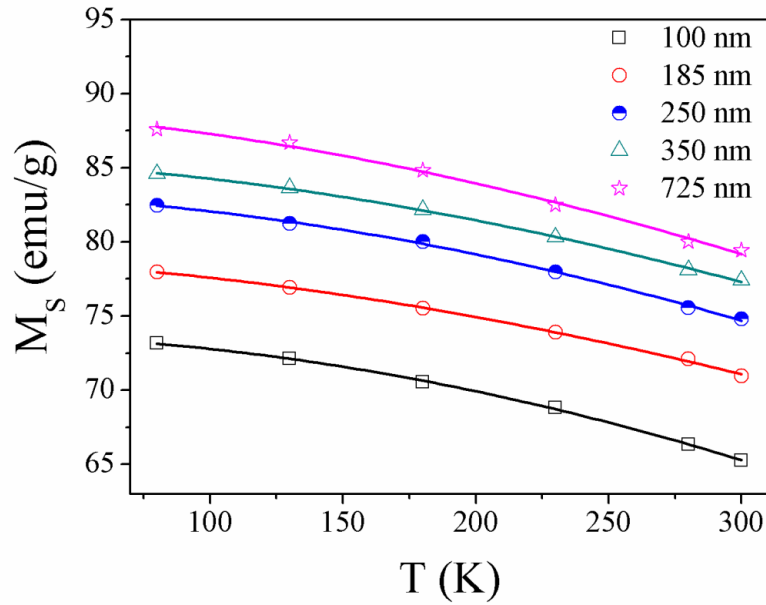


Figure 3.13 High field magnetization (M_S) vs. temperature (T) plot for the hollow spheres; Solid lines are the Bloch power law (Eq. 3.3) fitting to the experimental data.

From Fig. 3.13 it is clear that temperature dependency of M_S increases with decreasing hollow sphere diameter. The solid lines in Fig. 3.13 represent the fitting of the experimental data for all sets of hollow spheres with Bloch's law as given by Eq. (3.3) and the corresponding values of $M_S(0)$, B and b are summarized in Table 3.2.

Table 3.2 Values of $M_S(0)$, b , B as obtained by fitting Eq. (3.3) with experimental data and values of J_{AB} , D as obtained using Eq. (3.4) and Eq. (3.5), respectively.

	Average diameter (nm)	$M_S(0)$ (emu/g)	b	$B (\times 10^{-5})$ ($K^{-3/2}$)	J_{AB} (K)	D (meV-Å ²)
Set 1	100	73.78	1.94	1.73	14.59	171.68
Set 2	185	78.73	1.73	1.66	14.99	176.38
Set 3	250	83.18	1.84	1.33	17.42	204.98
Set 4	350	85.44	1.76	1.12	19.45	228.87
Set 5	725	88.77	1.69	0.9	21.70	255.35

The Bloch exponents (b) for all sets of hollow spheres lie in the range of 1.6 to 1.9 i.e. greater than the ' b ' value (1.5) for bulk material and there is a trend of

increase of 'b' value with decreasing hollow spheres diameter. Hendriksen et al. also showed that the value of the Bloch exponent is inversely proportional to the dimension of the particles and it should lie above 3/2 as the size of the particle decreases, consistent with our results [18]. All the calculated 'B' values are quite larger than the bulk value of 'B' ($3.3 \times 10^{-6} \text{ K}^{-3/2}$) which can be attributed to the increase of surface fraction of spins in smaller particles. The first theoretical studies of spin waves in nonbulk materials was carried out by Wildpaner and co-workers [21, 22] using simulations and Mills and Maradudin using calculation. By considering the surface spins, Mills and Maradudin theoretically predicted the Bloch constant for the surface which is twice of the bulk value, i.e. $B_{\text{surface}} = 2B_{\text{bulk}}$ [23]. Xiao and Chen also found that the surface fluctuation of spins can lead to an increase in 'B' value by almost 2 – 3.5 times than that for the interior spins [24]. The 'B' values for all sets of Fe₃O₄ hollow spheres are in same order of magnitude with the 'B' value for Fe₃O₄ nanocrystals reported by Goya et al [10]. The 'B' value is found to depend also on the effective co-ordination number in the system that varies spin to spin in the cluster and approaches to the bulk value with increasing cluster size [18]. Here for the hollow spheres the 'B' values decreases from $1.73 \times 10^{-5} \text{ K}^{-2/3}$ to $0.9 \times 10^{-5} \text{ K}^{-2/3}$ as the size of the spheres increases from 100 nm to 725 nm, i.e. with increase of magnetite cluster size the 'B' value shifts towards bulk value of magnetite. So from Table 3.2 it can be concluded that the smallest hollow spheres (Set 1) have extremely low co-ordination numbers among all other sets.

From the B values we can calculate the exchange constant (J_{AB}) between tetrahedral (A sublattice) and octahedral (B sublattice) sites of magnetite using the equation as given below [6, 25]:

$$J_{AB} = \frac{16(S_{B1} + S_{B2} - S_A)k_B}{11S_A(S_{B1} + S_{B2})} \left[\frac{0.05864}{4B(S_{B1} + S_{B2} - S_A)} \right]^{2/3} \quad (3.4)$$

where, S_A and S_{B1} are the spin of Fe³⁺ and equal to 5/2. $S_{B2} = 2$ is the spin of Fe²⁺ ions in octahedral site of magnetite lattice. Using the calculated value of J_{AB} , the value of spin wave stiffness constant can be determined using the relationship given as follows [26]

$$D = \frac{11J_{AB}S_A S_B a^2}{16|S_A - 2S_B|} \quad (3.5)$$

with $S_B = (S_{B1} + S_{B2})/2$ and $a = 8.4 \text{ \AA}$, a lattice parameter of the unit cell. All the calculated values of J_{AB} and D for all sets of hollow spheres are also given in Table 3.2. Both the J_{AB} and D values for all sets of hollow spheres are less than their single crystalline values ($J_{AB} = 23 \text{ K}$ and $D = 320 \text{ meV-\AA}^2$) which is attributed to the smaller co-ordination number of the surface spins in hollow spheres than in the single magnetite crystals. The increase in J_{AB} values with increasing hollow spheres size is also indicative of the fact that effective co-ordination of the surface spins increases with increasing particle diameter.

3.3.3 Frequency Dependent Measurements

Impedance Spectroscopy

The real (Z') and imaginary (Z'') part of the complex impedance $Z(f)$ ($= Z' + jZ''$) of all sets of magnetite hollow spheres are measured in Agilent 4294 precision impedance analyser in the frequency range of 40– 10^6 Hz at room temperature and is shown in Fig. 3.14. At low frequencies the Z' value remains constant for all sets but after a certain frequency it starts decreasing (Fig. 3.14(a)). But the frequency dependence of Z'' which is related to the dielectric relaxation, show Debye-like peaks [27] with characteristics frequency maxima (f_{\max}) that shifts towards higher frequency side with increasing hollow sphere diameter implying a decrease of relaxation time ($\tau = 1/2\pi f_{\max}$) [6] with increasing cluster diameter (Fig. 3.14(b)). We also analysed the real and imaginary parts of the complex impedance of all sets of samples in terms of Nyquist or Cole – Cole plot. Figure 3.14(c) represents the Cole – Cole plots of all the hollow spheres at room temperature ($T = 303 \text{ K}$) with large characteristic semi circles for each sample which intersects the real (Z') axis at higher value, i.e. at smaller frequency region. The grain boundary resistance (R_{gb}) of the hollow spheres were estimated from the Z'' vs. Z' experimental curves where the curves intersect the Z' axis at higher Z' value (or lower frequency side) as shown in Fig. 3.14(c).

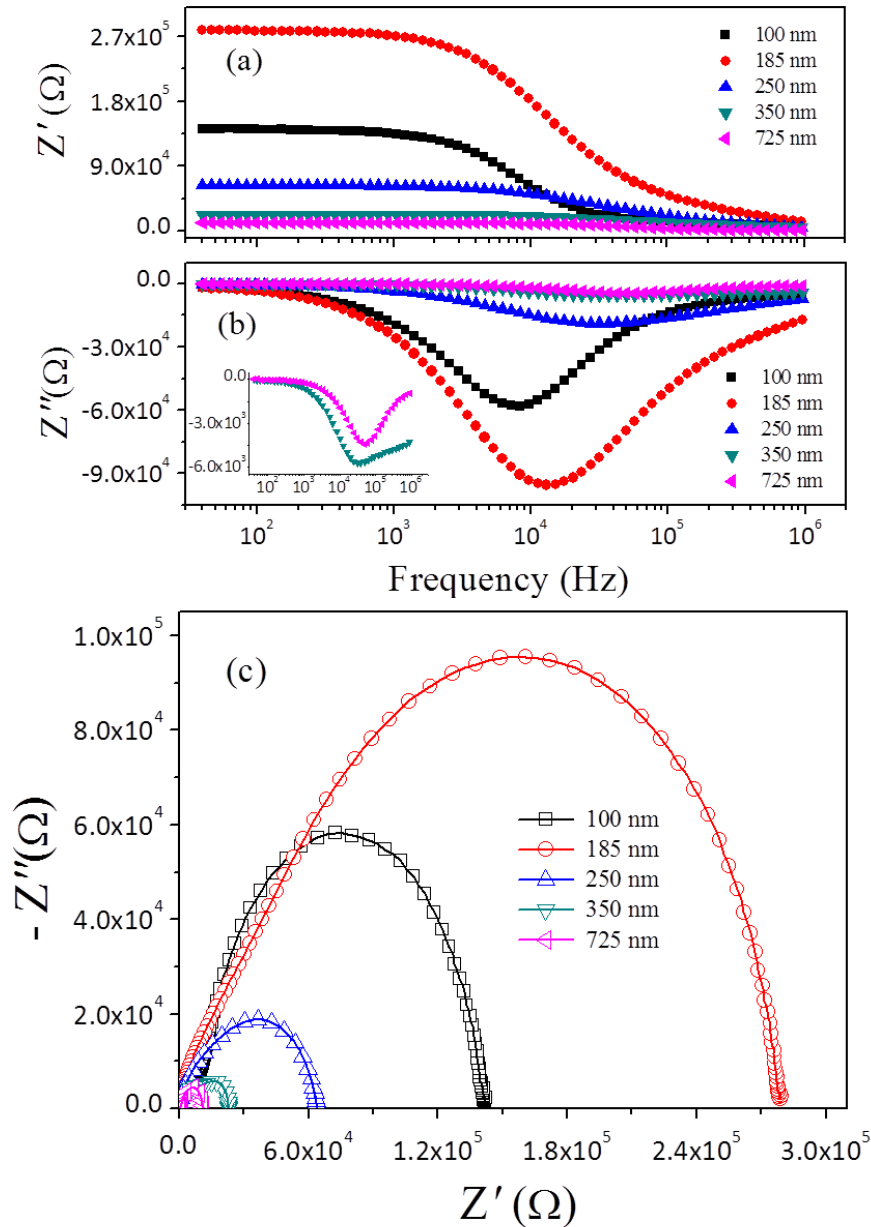


Figure 3.14 Frequency (f) dependence of real (Z') part (a) and imaginary (Z'') part (b) of impedance; (c) Cole - Cole plot for the hollow spheres of different diameters.

Incorporating sample dimension the grain boundary resistivity (ρ_{gb}) is found to be 6.080 $K\Omega$ -m, 12.802 $K\Omega$ -m, 2.899 $K\Omega$ -m, 1.068 $K\Omega$ -m and 0.165 $K\Omega$ -m for hollow spheres having average diameter 100 nm, 185 nm, 250 nm, 350 nm and 725 nm, respectively. It can be seen that the grain boundary resistivity (ρ_{gb}) is highest for the 185 nm hollow spheres then it decreases with increasing diameter of the hollow spheres.

Electrical Conductivity

Figure 3.15 represents the frequency dependence of ac conductivity of all sets of magnetite hollow spheres at room temperature. These AC conductivity (σ) values for all sets of samples were calculated from the complex impedance (Z' and Z'') data using the equation given below [6, 28]

$$\sigma' = Y' \times \frac{t}{A} = \frac{Z'}{(Z'^2 + Z''^2)} \times \frac{t}{A} \quad (3.6)$$

where, σ' , Y' , Z' and Z'' are real part of ac conductivity, conductance, real and imaginary parts of impedance $Z(f)$, respectively. ' t ' is the width and ' A ' is the area of the sample.

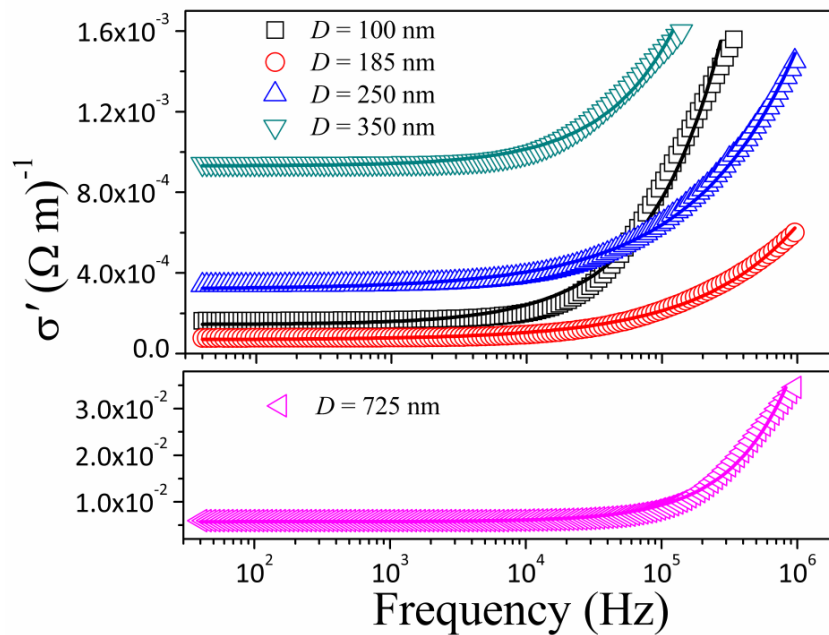


Figure 3.15 Variation of real part of conductivity (σ') with frequency (f) of ac excitation. The solid lines are the fittings of the experimental data with Jonscher's power law.

All the conductivity curves show a flat region (i.e. the frequency independent region) up to a certain frequency (f_p), followed by an abrupt increase in conductivity with increasing frequency. Normally, the frequency dependence of the real component of ac conductivity (σ') of disordered solids follows the Jonscher's power law given as follows [28]

$$\sigma'(f) = \sigma_{dc} \left[1 + \left(\frac{f}{f_P} \right)^n \right] \quad (3.7)$$

where, σ_{dc} is the dc conductivity, f and f_P are the excitation frequency and relaxation frequency, respectively and n is an exponent which is less than 1. At lower frequencies, (below f_P), due to the presence of poorly conductive regions, charge transport cannot extend over long distances and as a result the conductivity remains frequency independent (dc conductivity) and known as diffusive conductivity. But at higher frequencies (above f_P), conductivity increases with increasing frequency (dispersion in conductivity) following a power law (as given by Eq. (3.7)) due to subdiffusive motion of the localized charge carriers present in the local conductive regions [28]. Such type of power law dependence of conductivity at higher frequencies, characteristics of hopping conduction, has also been seen in many other ferrite systems.

The solid lines in Fig. 3.15 are the power law fitting (Eq. (3.7)) to the experimental data for the hollow spheres of different diameters and the corresponding fitting parameters as obtained from the best fitted graphs are summarized in Table 3.3.

Table 3.3 Jonscher's power law (Eq. (3.7)) fitting parameters: σ_{dc} , f_P and n

Hollow sphere diameter (d) (nm)	σ_{dc} ($\Omega \text{ m}$) ⁻¹	f_P (Hz)	n
100	1.46×10^{-4}	1.629×10^4	0.808
185	4.27×10^{-5}	1.049×10^4	0.566
250	3.20×10^{-4}	1.008×10^5	0.574
350	9.31×10^{-4}	1.780×10^5	0.832
725	5.73×10^{-3}	1.609×10^5	0.988

From the fitted results it is clear that the conduction behavior of the magnetite hollow spheres follows the Jonscher's power law very well over the measured

frequency regime while the value of the exponent (n) varies from 0.8 to 0.98, lying below 1 as expected. The dc conductivity limit in Jonscher's power law is mainly due to presence of free charge carriers (electrons and holes) within the system [29]. With increase of the size of hollow spheres it is found that the dc conductivity increases which may be attributed to the increase in conductive regions that introduces more free charge carriers in the system. Besides this, smaller grains have lots more grain boundaries than bigger grains and also more disorder that act as potential barrier to the free flow of charge carriers (electrons and holes) which results smaller conductivity in smaller hollow spheres than bigger ones [29, 30]. Here, it is interesting to note that the relaxation frequency (f_p) decreases with decreasing sphere diameter which is also evident from the Z'' data. Actually the number of grain boundary as well as the dipoles increases with decreasing grain size. So, this decrease in relaxation rate can be attributed to the increasing interaction between the dipoles at grain boundary with the reduction of grain size [30, 31].

Electrical Permittivity

Figure 3.16 illustrates the frequency variation of complex permittivity ($\epsilon_r = \epsilon_r' - j\epsilon_r''$) of all sets of hollow sphere samples.

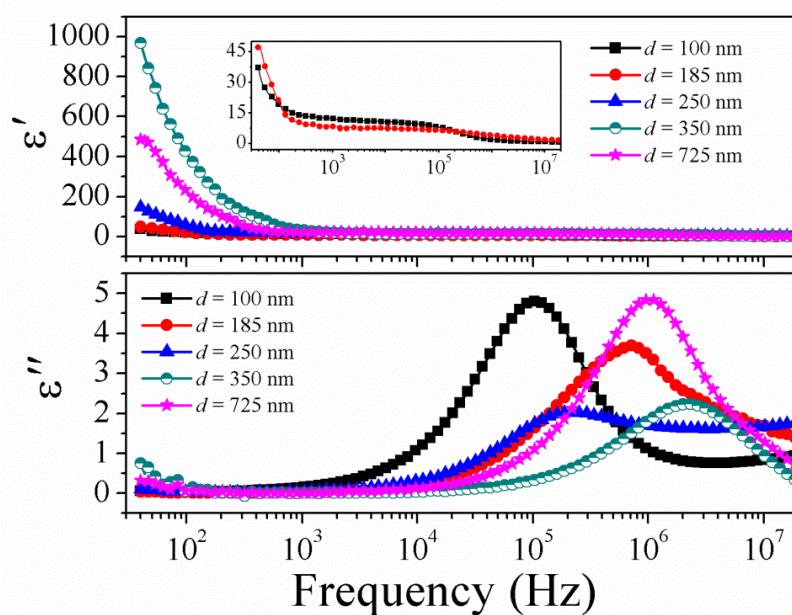


Figure 3.16 Frequency (f) variations of real (ϵ') and imaginary (ϵ'') parts of dielectric permittivity of hollow spheres of magnetite.

The real and imaginary parts of dielectric permittivity were measured by using the equations given below:

$$\varepsilon_r' = \frac{C_p \times t}{\varepsilon_0 \pi \left(\frac{d}{2}\right)^2} \text{ and } \varepsilon_r'' = \frac{\varepsilon_r'}{D} \quad (3.8)$$

where, ' C_p ' and ' D ' are the equivalent parallel capacitance of the sample under measurement and dissipation factor ($D = \tan \delta$); ' t ' is the thickness and ' d ' is the diameter of the sample, ε_0 is the free space permittivity (8.854×10^{-12} F/m). All the hollow spheres show same trend of frequency variation for both ε_r' and ε_r'' .

From Fig. 3.16 it can be seen that the real part of permittivity (ε_r') increases remarkably at lower frequencies with increase in hollow sphere diameter up to 350 nm then it decreases for 725 nm hollow spheres and the rate of increase is also higher for the 350 nm spheres than the others. With increase in frequency real part ε_r' decreases but the imaginary part ε_r'' increases and resonance peaks occurs at higher frequencies. The resonance peak positions vary from 0.103 MHz to 2.22 MHz with varying hollow spheres diameter which are very much less than that reported by other authors [30, 31]. Normally permittivity originates from electronic, atomic and orientation polarization when a sample is placed under an electromagnetic field [30]. It is found that the low frequency resonance occurs due to presence of pores and vacancies in the system and resonance at high frequency side is due to electronic and atomic polarization [31, 32]. Now as we are dealing with the hollow spheres of different diameters, so it is very obvious that the resonance peaks should occur at the low frequency regime due to presence of large amount of pores in the magnetite system. Decrease of ε_r' with hollow sphere diameter can be attributed to the reduction in the number of Fe³⁺- Fe²⁺ ion pairs in the octahedral ' B ' site of ferrite lattice in smaller grains [30]. Nearly sharp resonance peaks for the present hollow sphere system is indicative of the fact that Debye type single relaxation process is happening in the system [33] which is also evident from the Z'' vs. f data, as discussed earlier.

3.3.4 Dynamic magnetic properties of hollow spheres

AC magnetic behavior of all sets of hollow sphere samples was measured at different frequencies in our lab made instrument (described in *Chapter 2*). The maximum magnetic field that can be applied in doing the ac measurements in our instrument is ~ 57 kA/m, at frequencies as high as 750 Hz though at lower frequencies (200 Hz) we can have magnetic field as high as 100 kA/m. However, at higher frequencies (more than 750 Hz) the maximum achievable field is reduced due to increase in impedance with increasing frequency. AC magnetization of all the samples increases nonlinearly with ac field as shown in Fig. 3.17. This nonlinear behavior indicates the interacting nature of the Fe_3O_4 particles [34] though the rate of increase of magnetization with field is slow. From the figure it is obvious that with increasing size of the hollow spheres, magnetization increases as bigger spheres has larger number of atomic moments.

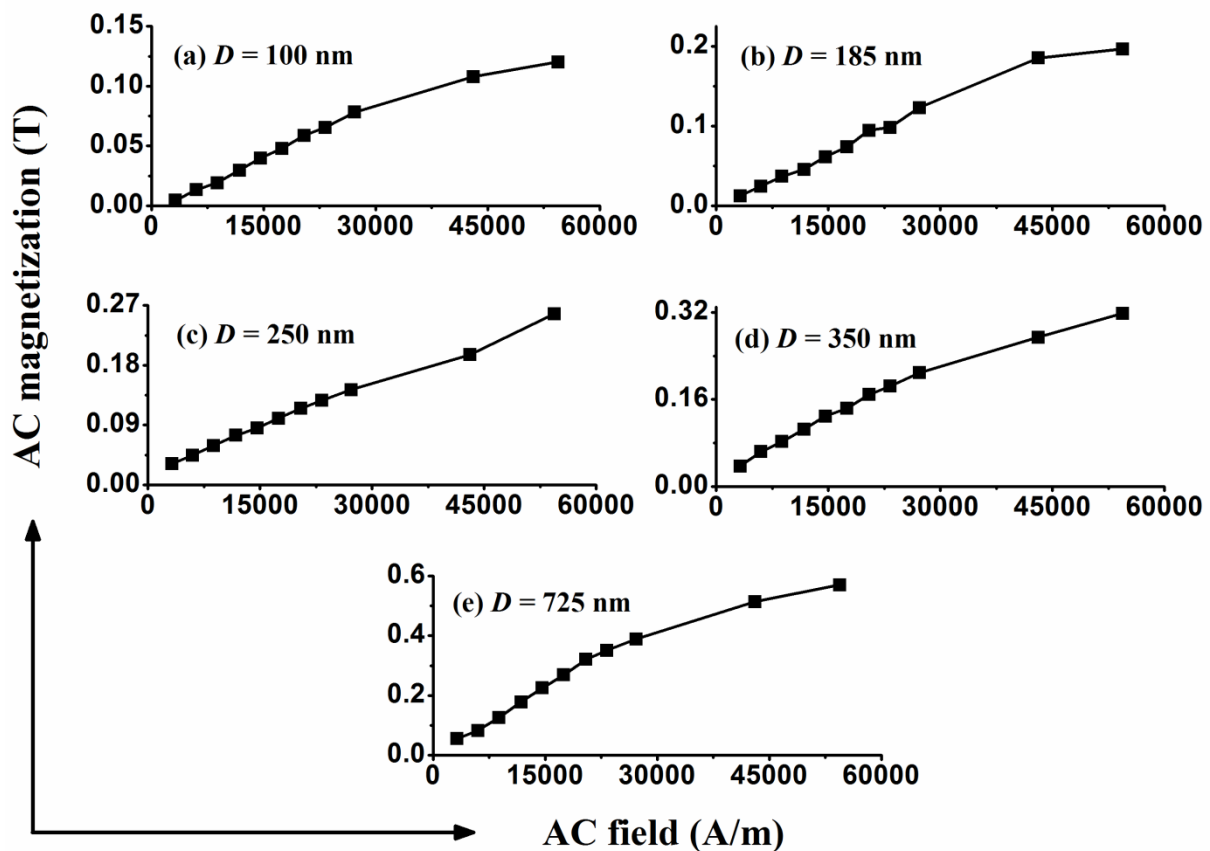


Figure 3.17 Variation of magnetization with AC field for magnetite hollow spheres of different diameters; (a) $D = 100$ nm, (b) $D = 185$ nm, (c) $D = 250$ nm, (d) $D = 350$ nm and (e) $D = 725$ nm.

AC hysteresis loops of all sets of samples have been measured in the frequency range of 20 Hz to 750 Hz. All samples show nearly same type of loops though has different saturation magnetization, coercive fields, remanance and also magnetic losses as extracted from these loops. The corresponding hysteresis loops at different frequencies for a set of hollow sphere of average diameter 250 nm are shown in Fig. 3.18.

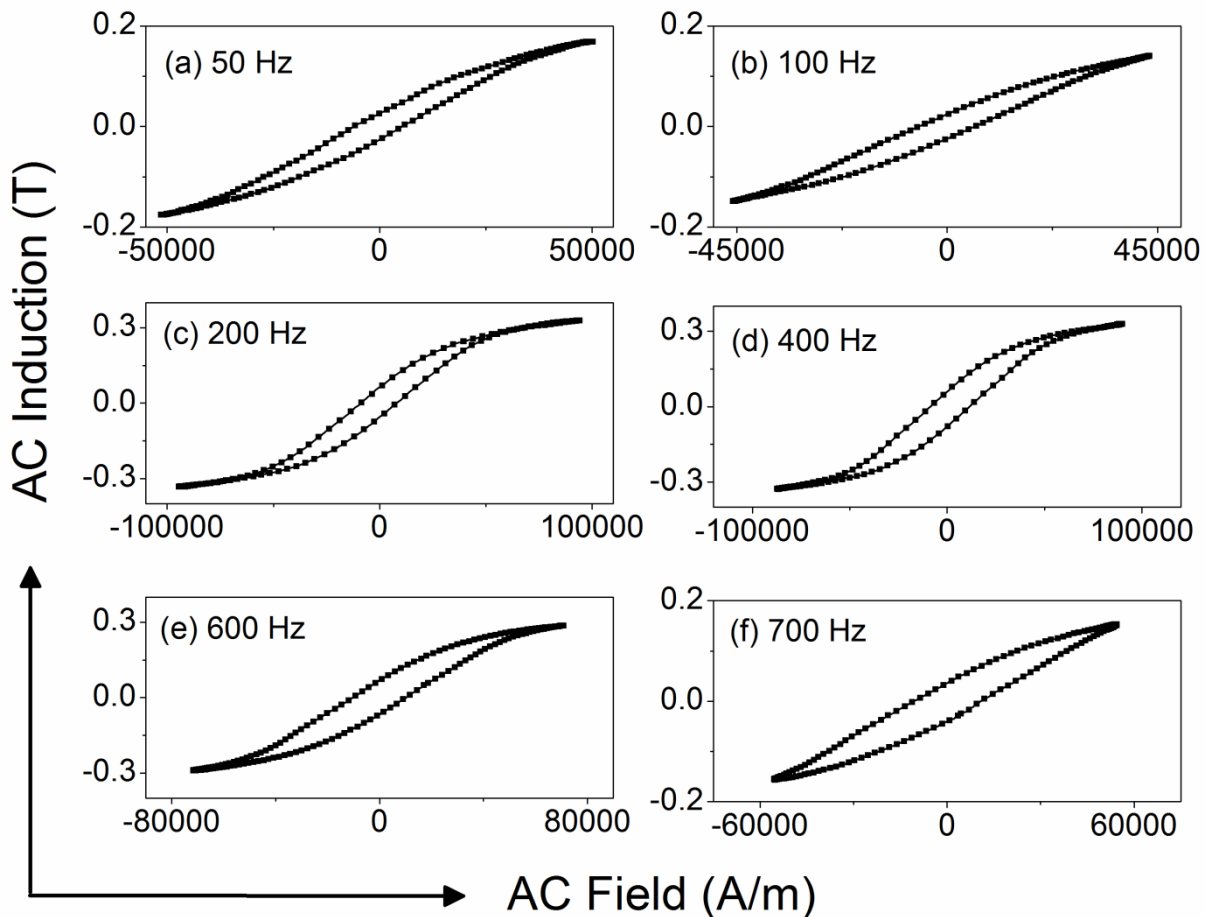


Figure 3.18 AC hysteresis loops of 250 nm hollow spheres measured at frequencies $f = 50, 100, 200, 400, 600$ and 700 Hz.

From this experiment it is clear that, magnetization is out of phase with the applied ac magnetic field from the lowest frequency, that's why all sets of hollow spheres show considerable coercivity and hysteresis in response to the ac excitation at low frequency range. This type of opening in the $M-H$ loops is also present in the high frequency regime. However, all the ac hysteresis loops as shown here are minor loops because, the applied ac field is not enough to saturate the moments for this

type of hollow spheres having large diameter though some hysteresis loops show some sort of saturated behavior.

The coercivity or the coercive field (H_C) is defined as the field at which the remanance magnetization becomes zero. Estimation of this coercive field for every hysteresis loop is very important because it defines the energy dissipated as heat in each magnetization cycle. To compare the variation of coercivity of the variable sized hollow spheres we have measured the hysteresis loops of all sets of spheres at different frequencies ranging from 20 Hz to 750 Hz within a certain ac field range, which is ± 57 kA/m in this case. The ac hysteresis loops measured for all the samples at a frequency of 50 Hz is shown in the Fig. 3.19. Now, from these hysteresis loops as shown in Fig. 3.18 and Fig. 3.19, it can be observed that the coercivity of the spheres significantly depends on the applied field frequency and also the size of the particles which we will discuss one by one.

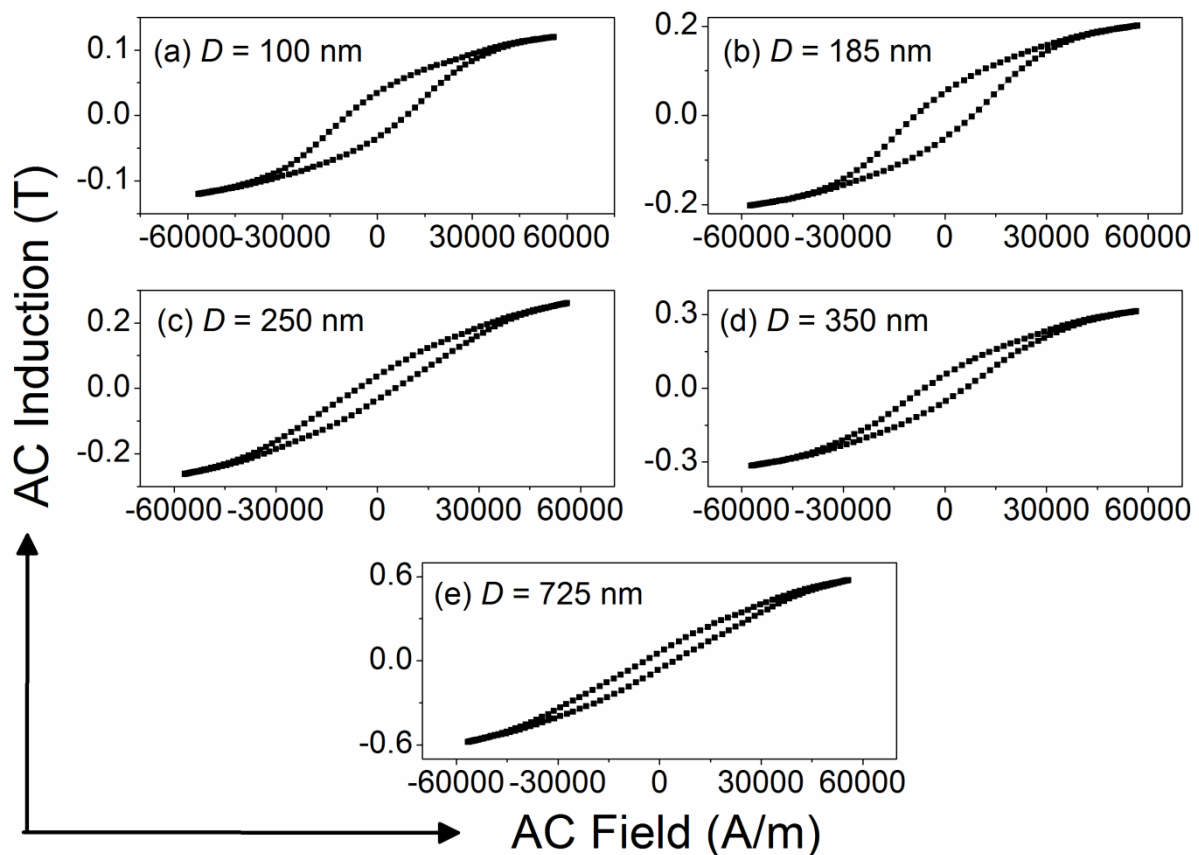


Figure 3.19 Hysteresis loops observed at 50Hz of all sets of hollow spheres; (a) 100 nm, (b) 185 nm, (c) 250 nm, (d) 350 nm and (e) 725 nm.

To know about the frequency dependence of coercivity we have plotted the coercivity of all sets of samples, calculated from the ac hysteresis loops, as a function of applied ac field frequency and is shown in Fig. 3.20. The general form of all the curves is near about similar consisting of rapid increase of coercivity at lower frequencies followed by a knee, and then a gradual rise as the frequency is increased further. However, for bigger spheres having diameter greater than 185 nm, this knee in H_C vs. f curve is much more prominent than the smaller ones.

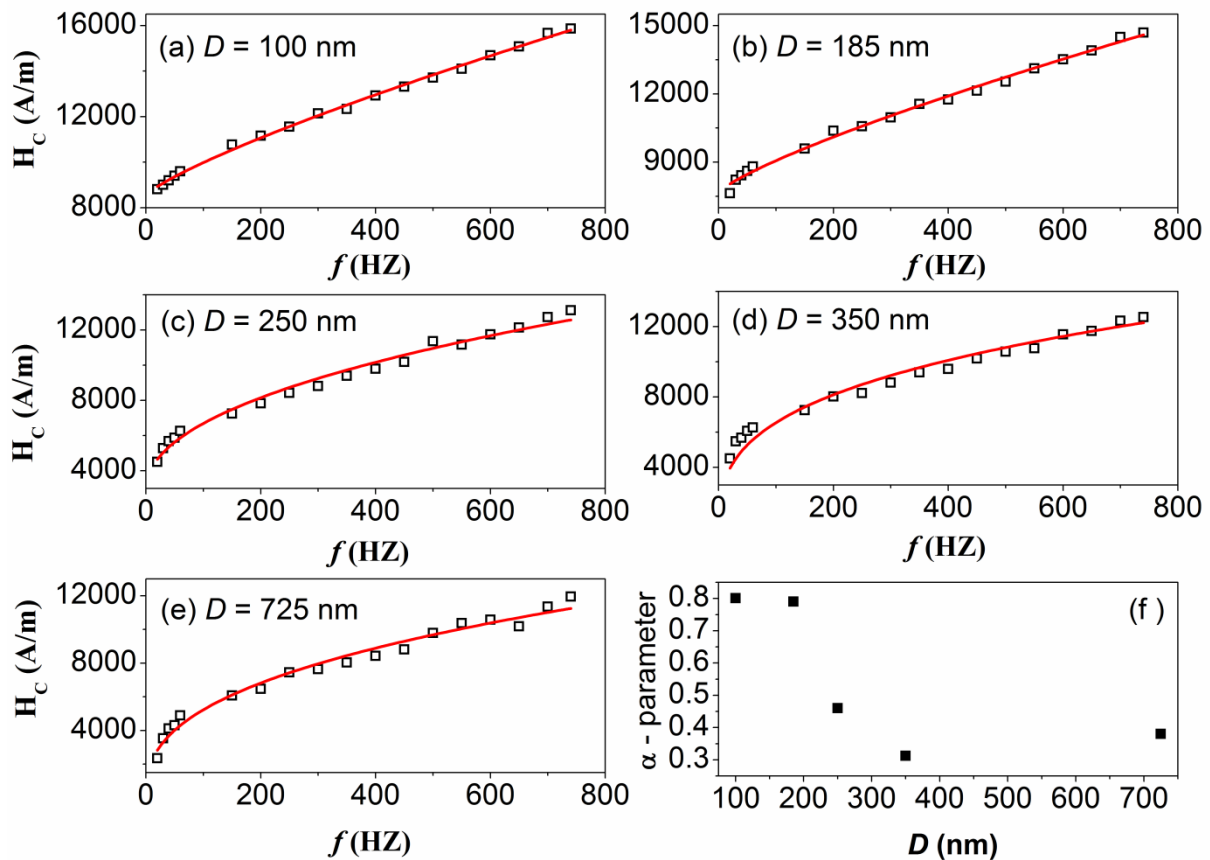


Figure 3.20 Coercivity vs. frequency plot of all sets of hollow spheres; (a) 100 nm, (b) 185 nm, (c) 250 nm, (d) 350 nm and (e) 725 nm. (Solid red lines are the fit of the experimental data with the formula $H_C \sim A \times f^\alpha$) (f) The plot of the fit exponent (α) of coercivity vs. frequency data as a function of sphere diameter.

Here it can be seen that for all sets of samples coercivity decreases with decrease in measuring frequency; i.e. with increase in experimental time window. Actually the hollow spheres are composed of smaller nano crystals as is evident from the SEM and TEM images, which may behave like superparamagnetic (SPM) particles or ferromagnetic (FM) particles depending on their size. Generally,

nanoparticles having size ≤ 20 nm are considered to be SPM particles and others behave as ferromagnetic particles. In case of single domain particles having uniaxial anisotropy direction, magnetic moments fluctuate between two energetically favorable ground states, i.e. up and down states, in a time scale, known as the relaxation time, given by [34, 35]

$$\tau = \tau_0 \exp \left[\frac{Kv_p}{k_B T} \right], \quad (3.9)$$

where, τ_0 is a constant ($\sim 10^{-9} - 10^{-13}$ sec), K is the anisotropy energy constant, v_p is the particle volume, k_B is the Boltzmann constant and T is the temperature. So, at lower frequencies, i.e. in the regime of higher measuring time window (τ_m), most of the particles having relaxation time (τ) less than the τ_m can flip their spin state randomly from up to down configuration, i.e. they behave like SPM particles. However, with increase in filed frequency, in other words decreasing the measuring time window ($\tau_m < \tau$), the particles which behaved as superparamagnetic particles at low frequency may now behave as ferromagnetic particles at higher frequencies. Again with increasing frequency, bigger particles cannot change their spin state within this short time period (less than their relaxation time) and behave ferromagnetically. As a result proportion of ferromagnetic particles increases with increasing frequency and consequently width of the hysteresis loops increases; i.e. coercivity increases with increasing frequency of the applied ac field.

The frequency variation of coercivity in each case has been fitted with an empirical formula having functional form $H_c \sim A \times f^\alpha$, where the parameters ' A ' and ' α ' were selected by the computer for the best fit for each set of hollow spheres [36, 37]. This particular functional form corresponds to the Gyorgy's proposed one to account for the frequency variation of coercivity, as given below [37]:

$$H_c = \left[\frac{\pi f \beta x H_a}{M} \right]^{1/2}, \quad (3.10)$$

where, f is the frequency of the applied ac field H_a , x is the average domain wall spacing, β is the eddy current damping constant and M is the saturation

magnetization. This type of frequency dependence is mainly due to the eddy current damping within the material under observation.

According to this Gyorgy's proposed model, the exponent should be exactly equal to 0.5. However, in our case, the value of the exponent (α) varies from 0.79 to 0.3 as the size of the hollow spheres changes from 100 nm to 725 nm with a value 0.46 for 250 nm hollow spheres. Such deviation has also been observed in other ribbon like (crystalline or amorphous) structures where the value 0.33 is found to be common [37]. This type of discrepancy in the value of ' α ' is mainly due to the dependence of the average domain wall spacing (x) on frequency in addition to the sphere diameter [37, 38]. These results also imply that the domain wall separation for a particular hollow sphere depends on the frequency. For a given size, domain wall spacing decreases with increase in measurement frequency. Conversely, the average number of domains increases with increase in applied field frequency.

By comparing the hysteresis loops shown in Fig. 3.19, we can say that great differences in the loops can be possible depending on the size, shape and microstructure of the nanocrystals that constitutes the hollow spheres of variable diameters. To have an exact idea about the size dependence of coercivity of all sets of hollow spheres we have plotted the H_C vs. D graph at a frequency of 50 Hz, shown in Fig. 3.21(a). These results suggest that the coercivity (H_C) strongly depends on the

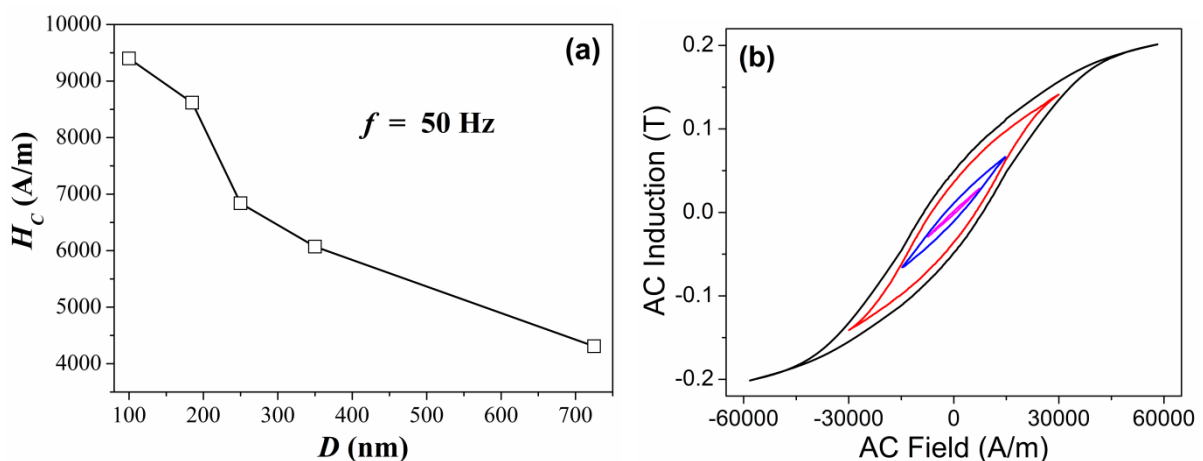


Figure 3.21 (a) Variation of coercivity (H_C) with the size (D) of hollow spheres at a frequency of 50 Hz. (b) Hysteresis loops of 185 nm hollow spheres with four different loop amplitudes measured at $f = 50$ Hz.

size of the spheres, tending to decrease with increase in their size. For bigger particles ($D > 100$ nm) whose sizes exceed the domain wall width, remagnetization process occurs due to domain wall displacement. When domain wall moves through these particles they can be pinned at the domain boundaries and then additional energy is required to continue this movement. This pinning of domain walls is one of the main causes of coercivity. In case of larger particles with multidomain configuration, theory predicts that H_C varies as inverse of the diameter of the particles as given by following equation [39]

$$H_C = p_1 \frac{\sqrt{AK}}{J_e D} \propto D^{-1}, \quad (3.11)$$

where, p_1 is a constant, K is the anisotropy energy constant, J_e is the exchange energy density, A represents the exchange stiffness and D is the diameter of the particle. Therefore, reducing the size of the particles will increase the pinning sites and thus the coercivity. However, for ultrafine particles another type of size variation of H_C has been predicted and is given as follows [39]

$$H_C = p_2 \frac{D^6 K^4}{J_e A} \propto D^6, \quad (3.12)$$

where, p_2 is another parameter. The boundary line of these two cases is given by the ferromagnetic exchange length (D_{ex}) given as $D_{ex} = \sqrt{A/K}$, which is found to be nearly 27 nm using material parameters of magnetite ($K = 1.35 \times 10^4$ J/m³ and $A = 10^{-11}$ J/m) [39]. So, below D_{ex} , H_C will decrease rapidly with decreasing particle size. In our case, as the diameter of the hollow spheres (D) is much larger than D_{ex} , the increase of H_C with decreasing D is consistent with theoretical prediction.

Dominated by pseudo single domain behavior, smallest hollow spheres exhibit the maximum coercivity of about 9.4 kA/m and very high hysteresis losses. So, at first sight this material seems to be very suitable for magnetic heating for hyperthermia treatment. However, in hyperthermia, full hysteresis loop of the magnetic sample can rarely be used because of restrictions on ac field amplitude for mainly technical reasons. So, under such condition one can expect rapid decrease of hysteresis loop area with decreasing field amplitude that can also be seen from Fig. 3.21 (b).

For hysteresis loops of nearly rectangular shape, the hysteresis loss can be approximately estimated using the relation given below [39]:

$$P_{hys} = pM_s H_c f, \quad (3.13)$$

where, p is a constant factor, M_s is saturation magnetization and f is the field frequency. However, the hysteresis loss of the hollow spheres is mainly due to domain wall motion and the AC hysteresis loops, so called Rayleigh loops, are significantly different from the loops as measured in static magnetic field. So, in this case the loss can be estimated by calculating the area of the hysteresis loop in an AC magnetic field [40]. In order to evaluate the maximum power that can be obtained for hyperthermia, we have determined the power loss of all sets of hollow spheres following the relation $P_{hys} = \text{AC hysteresis loop area} \times \text{AC field frequency}$ and is plotted against frequency as shown in Fig. 3.22 (a).

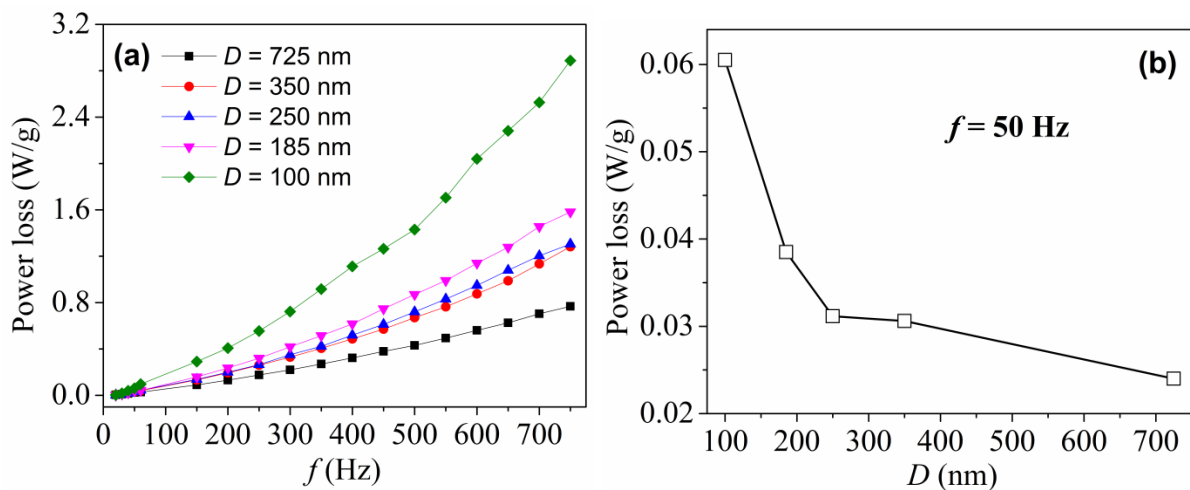


Figure 3.22(a) Power loss vs. frequency plot of the hollow spheres. (b) Size dependence of power loss measured at $f = 50 \text{ Hz}$.

Considerable power loss can be observed for all sets of spheres and it increases consistently with increasing frequency of AC field as is evident from the Fig. 3.22 (a). Maximum power loss of about 2.8 W/g is obtained for hollow spheres having diameter of 100 nm at a frequency of 750 Hz. In this case also the tendency of variation of power loss with size of spheres is perfectly similar to that of the H_c , i.e. power loss $\sim D^{-1}$, as the size of all the spheres is much larger than D_{ex} for magnetite (Fig. 3.22(b)). For these types of spheres hysteresis loss is the main loss mechanism

under an AC magnetic field with low frequency. However, relaxation losses come into play when the size reduces below D_{ex} .

3.3.5 Dye adsorption properties of Fe_3O_4 hollow spheres

Now-a-days, dyes and pigments have been used widely mostly in textile industries, paper industries, food industries, cosmetic industries etc. for coloring their products [41]. However, the wastewater releasing from this industries is very hazardous for environment and may create significant disorder in human immune system. Most of the dyes are toxic and should be removed from wastewater before discharge into receiving stream because it may harm the environment by affecting the photosynthesis process [42].

There are several well investigated conventional methods for separation of dyes from wastewater such as nano filtering, chemical precipitation, activated sludge, adsorption, photo degradation etc [41, 43]. However, adsorption technique has been used widely for water treatment because it can separate certain class of toxic materials which remain unaffected after conventional wastewater treatment. This technique is found to be more superior to others because it can handle fairly large water flow, very cost effective, simple removal mechanism and easy to perform at anywhere [41, 44]. Currently carbon and silicon based materials have been used as adsorbent material and they show significant adsorption capability. However, modification of pore surface of silica based mesoporous materials is necessary for better performance and higher cost of carbon based materials limits its large scale applications [45, 46].

Recently, nanostructured iron oxides have attracted great deal of interest to the researchers as a potential adsorbent of toxic ions due to their magnetic properties, very low toxicity, environment friendly nature, chemical stability and excellent recycling capability [47, 48]. Specially, nanostructures with hollow interior have extra advantage because of their low density, high effective surface area etc. On the other hand, among all iron oxides magnetite is most preferable because of its higher magnetization which can be utilized for magnetic separation of adsorbent

from water after dye adsorption. So, hollow spheres of magnetite can be a very efficient adsorbing agent for purification of water.

Here in this section we have studied dye adsorbing property of magnetite hollow spheres with both anionic (Eosin) and cationic (Methylene Blue, MB) dyes and it is found that these hollow magnetite spheres can play a better and efficient role as dye absorber. However, as the adsorption process is mainly a surface effect, before doing any type of adsorption experiments we have investigated the Brunauer–Emmett–Teller (BET) surface area and pore size distribution of the all sets of hollow spheres from the N_2 adsorption–desorption data and one corresponding data for 185 nm hollow sphere is shown in Fig. 3.23. Among all sets of spheres maximum specific surface area and pore volume was found to be $23 \text{ m}^2\text{g}^{-1}$ and $0.0244 \text{ cm}^3\text{g}^{-1}$, respectively for 185 nm hollow sphere. Smaller surface area of 100 nm spheres than 185 nm may be due to its porous structure (not completely hollow), as evident from the SEM and TEM images (*Section 3.3.1, Fig. 3.2*). These values of specific surface area of hollow spheres are larger than the other reported values [8, 49]. The isotherm has an apparent hysteresis loop within $0.5–1 P/P_0$ (Type IV isotherm), indicating the presence of mesopores [49]. Additionally, the Barret–Joyner–Halenda (BJH) pore size distributions for both types of hollow spheres (inset of Fig. 3.23) reveal that the spheres contain pores having size less than 10 nm.

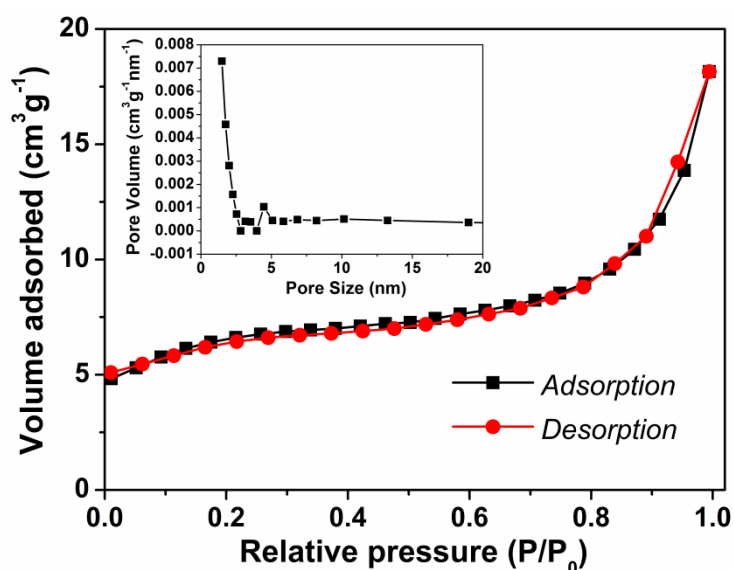


Figure 3.23 Nitrogen adsorption–desorption isotherms and pore size distribution curves (inset) for hollow spheres with average diameter of 185 nm.

Adsorption experiments

Batch experiments were carried out to investigate the adsorption characteristics of Eosin and MB dyes by the hollow spheres. At first, Eosin and MB stock solutions of known concentration were prepared and then known amount of Fe₃O₄ hollow spheres were mixed with them. The solutions were then held on the platform of a vortex shaker to provide a gentle shaking for 24 hrs. After shaking, the mixtures were placed under magnetic field to separate the dye adsorbed particles from solution. The supernatant solutions were then filtered and used for UV adsorption spectroscopy to measure the Eosin and MB concentration in the filtrate.

The Eosin/MB uptake at equilibrium (q_e) was calculated using the following equation:

$$q_e = \frac{V(C_i - C_e)}{m} \quad (3.14)$$

where, q_e is the Eosin/MB uptake at equilibrium (mg/g), V is the volume of the Eosin/MB solution (ml), C_i is initial concentration of Eosin/MB in solution, C_e is the final concentration of Eosin/MB at equilibrium and m is the mass of the adsorbent. All the experimental data measured at pH 5.6 are plotted and then fitted according to the Langmuir and Freundlich equations as given below [41, 43]

$$\frac{C_e}{q_e} = \frac{1}{K_L} + \frac{\alpha_L}{K_L} C_e \quad (3.15)$$

$$\ln(q_e) = \ln(K_F) + \left(\frac{1}{n_F} \ln C_e\right) \quad (3.16)$$

where, K_L , α_L are the Langmuir isotherm constants and K_F , n_F represents the Freundlich isotherm constants. The maximum adsorption capacity (q_m) of the adsorbent is numerically equal to K_L / α_L . The $1/n_F$ is a measure of non-linearity between the solution concentration and the adsorption capacity at equilibrium [30]. These equations are very much useful for measuring adsorption and also interpret the nature of adsorption of Eosin/MB on magnetite hollow spheres.

Effect of the size of adsorbent

Variation in surface area of the hollow spheres affects their adsorption capacity (q_e) which can be seen in the Fig. 3.24(a). For same amount of adsorbent, adsorption capacity is found to be maximum for 185 nm hollow spheres as compared to other spheres. As adsorption process is mainly a surface effect where dye molecules reside on the surface of the adsorbent by electrostatic attraction, higher specific surface area of smaller spheres allows more dye molecules to interact with it resulting higher adsorption capacity. For the same reason adsorption capacity increases with increasing amount of adsorbent, inset of Fig. 3.24(a).

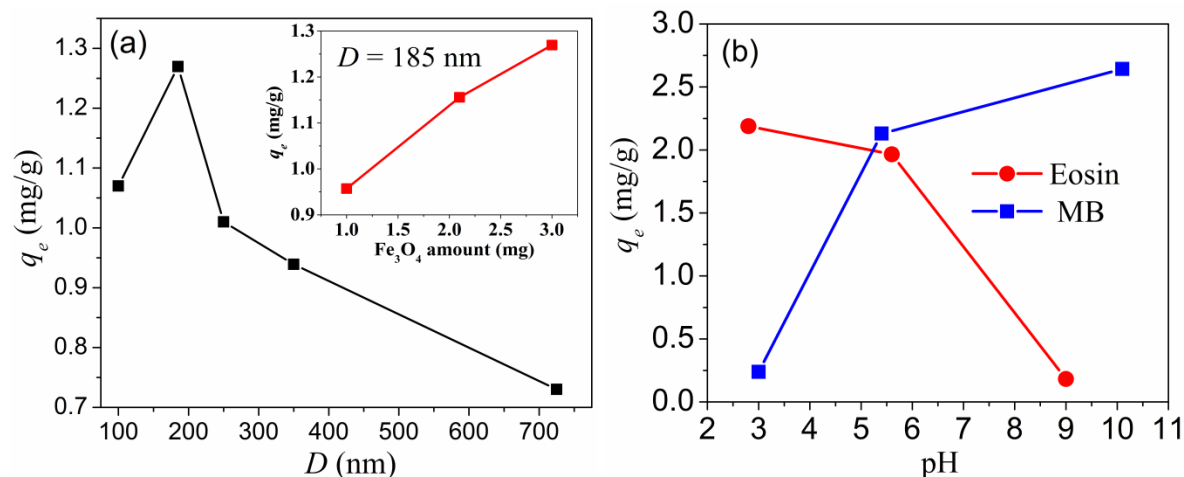


Figure 3.24 (a) Effect of size of adsorbent on the adsorption capacity of Eosin dye, inset shows the variation of q_e with the amount of adsorbent ($D = 185$ nm); (b) Effect of pH on the adsorption capacity of Eosin and MB by Fe_3O_4 hollow spheres of 185 nm diameter.

Effect of pH:

Effect of pH on Eosin adsorption by the magnetite hollow spheres of average diameter of 185 nm was investigated in the pH range of 2.8 to 10.1 for a contact time of 24 hrs with Eosin concentration 1.66 mg/L and MB concentration 1.12 mg/L. The pH dependence of adsorption capacity q_e (mg/g), which is a measure of degree of adsorption, is shown in Fig. 3.24(b). From the plot it is obvious that the Eosin adsorption decreases as pH increases and maximum adsorption occurs at pH 2.8 whereas the MB adsorption increases with increasing pH with a maximum at pH 10.1. These results clearly suggest that magnetite hollow spheres can adsorb Eosin more effectively in acidic pH regime and MB in basic pH region.

Surface -OH groups which arise from adsorption of water or from structural -OH are the main functional groups of magnetite. These -OH groups contain a double pair of electrons and a dissociable hydrogen atom which help magnetite to interact with both bases and acids. According to Cornell and Schwertmann [43], depending on the pH, magnetite can generate Fe^{2+} and its hydrolysis products, such as $FeOH^+$, $Fe(OH)_2^0$ and $Fe(OH)_3^-$. As the acidity constant of magnetite, pK_{a1} is 5.6, at $pH < 5.6$ dominant functional groups on magnetite surface would be Fe^{2+} and $FeOH^+$. So this can easily attract negatively charged Eosin ions at lower pH. But at $pH > 5.6$ dominant functional groups on magnetite surface are $Fe(OH)_2^0$ and $Fe(OH)_3^-$. So, at higher pH, magnetite would repel the negatively charged Eosin ions whereas it will attract cationic MB dye. That's why, with increasing pH of solution, the Eosin adsorption capacity decreases and MB adsorption increases.

Adsorptions results

All the adsorptions experiments were performed at pH 5.4 for Eosin and pH 9.3 for MB, at room temperature and are shown pictorially in Fig. 3.25.

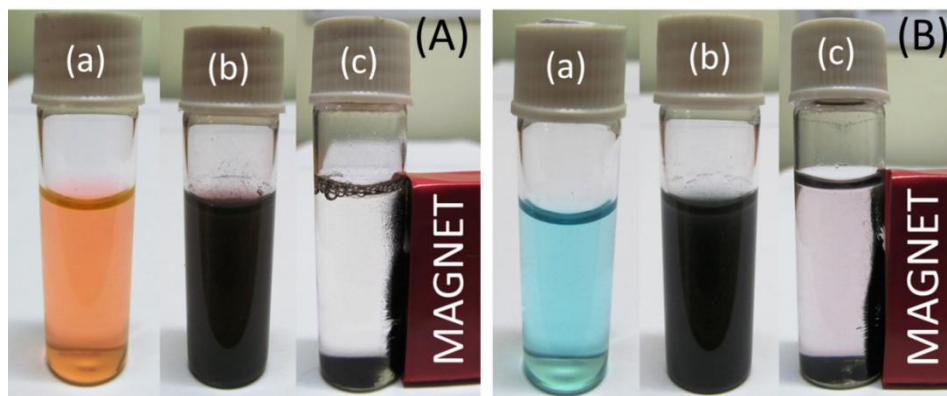


Figure 3.25 Adsorption of (A) Eosin and (B) MB dyes by 185 nm Fe_3O_4 hollow spheres and their magnetic separation from liquid phase. (a) Dye solution; (b) Fe_3O_4 hollow spheres in dye solution and (c) magnetic separation of adsorbent after dye removal.

From Fig. 3.25 it is qualitatively clear that the Fe_3O_4 hollow spheres are very efficient in adsorbing Eosin and MB dyes from water. Discoloration of dye solutions after few minutes of addition of adsorbent material confirms complete removal of dyes from solution and also higher adsorptive performance of these materials.

Actually it is observed that Eosin solution takes 6-7 minutes to discolor completely whereas MB solution takes slightly lower time (4 minutes) which represents superior interaction of magnetite with MB dye in higher pH regime than Eosin. Finally, after dye adsorption, the magnetic adsorbent has been separated completely from the solution by a magnet as shown in Figs. 3.25A(c) and 3.25B(c).

For the adsorption isotherm measurements Eosin and MB dyes were taken at different initial concentrations but the amount of Fe_3O_4 hollow spheres was kept constant at 1.5 g/L for Eosin adsorption and 1.45 g/L for MB adsorption.

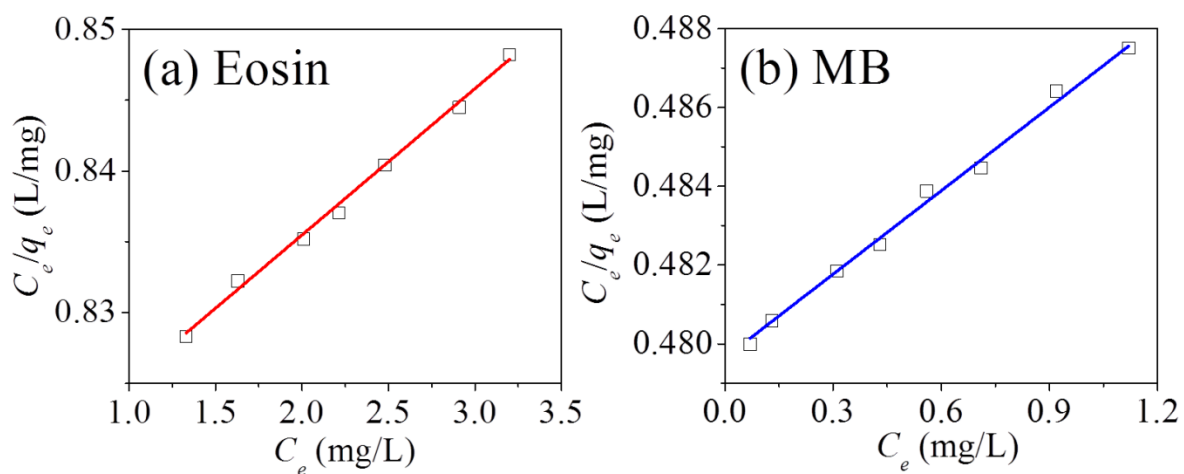


Figure 3.26 (a) Langmuir isotherm plot for Eosin adsorption onto Fe_3O_4 hollow spheres (initial concentration 2.7 – 6.92 mg/L; contact time 24 h; pH 5.4; Fe_3O_4 hollow spheres dose 1.5 g/L); (b) Langmuir isotherm plot for MB adsorption by Fe_3O_4 hollow spheres (initial concentration 0.64 – 2.65 mg/L; contact time 24 h; pH 9.3; Fe_3O_4 hollow spheres dose 1.45 g/L).

Adsorption data for the adsorption isotherms are given here for hollow spheres of average diameter 185 nm because it has already been seen that 185 nm hollow spheres have more adsorption capacity than the others. Then these data were fitted with the Langmuir and Freundlich isotherm equations (Eq. (3.15) and Eq. (3.16), respectively) to identify the most favorable adsorption parameters. The experimental data fitted with Langmuir isotherm model for Eosin and MB dyes are shown in Fig. 3.26(a) and 3.26(b), respectively. Maximum adsorption capacity q_m (mg/g) was measured from the Langmuir isotherm model. In this case, the maximum Eosin adsorption capacity for the 185 nm magnetite hollow spheres at room temperature as

calculated from the Langmuir isotherm was 96.71 mg/g, i.e. 139.78 $\mu\text{mol/g}$ whereas the q_m for MB was found to be 141.64 mg/g, i.e. 442.83 $\mu\text{mol/g}$. This q_m for MB is much higher than the adsorption of neutral red dye by 200 – 300 nm sized Fe₃O₄ hollow spheres as reported by Iram et al [41]. However, the values of q_m for these hollow spheres are smaller than the adsorption results as reported by other authors [50-52]. Actually adsorption depends on several factors like specific surface area of adsorbent, initial solute concentration (C_i), pH of the solution, reaction time etc. Any of these parameters can change the adsorption capacity of same adsorbent in same solution. In this case, smaller surface area of these hollow spheres compared to others, [50-52] reduces their adsorption capacity. Additionally, initial concentration of dye taken was in micro-molar range. Because of such low concentration of dye the adsorption takes place at a very slow rate, consequently a low adsorption capacity of these hollow spheres. The other values of Langmuir and Freundlich constants and also the correlation coefficients (R^2) as obtained from the fittings (solid lines in Fig. 3.26(a) and 3.26(b)) are given in Table 3.4.

Table 3.4 Langmuir and Freundlich isotherm parameters for the Eosin and MB dyes adsorption by Fe₃O₄ hollow spheres.

Eosin				Methylene Blue (MB)			
Langmuir Constants		Freundlich Constants		Langmuir Constants		Freundlich Constants	
R^2	0.99	R^2	0.99	R^2	0.98	R^2	1
K_L (L/g)	1.227	$\text{Ln}(K_F)$	0.197	K_L (L/g)	2.085	$\text{Ln}(K_F)$	0.722
a_L (L/mg)	0.0126	$1/n_F$	0.973	a_L (L/mg)	0.0147	$1/n_F$	0.994
q_m (mg/g)	96.71			q_m (mg/g)	141.64		

Figure 3.27(a) shows the effect of initial dye concentration on the adsorption capacity of 185 nm Fe₃O₄ hollow spheres. It reveals that for the same amount of Fe₃O₄ adsorbent, adsorption capacity increases with increasing solute concentration because the driving force which allows the mass transfer of Eosin/MB dye between aqueous and solid phases increases with increasing Eosin concentration [41]. Increase in dye uptake at equilibrium by hollow spheres (from 1.6 to 3.7 mg/g for

Eosin and 0.14 to 2.19 mg/g for MB) was a result of increase in the driving force with increasing initial concentration of dye in solution.

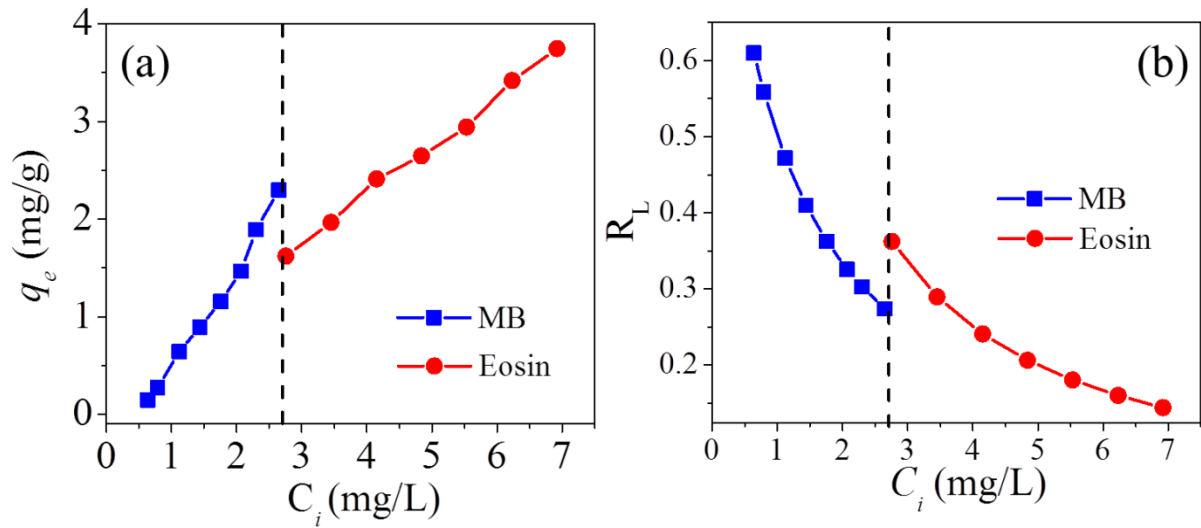


Figure 3.27 (a) Effect of initial dye concentration (C_i) on the adsorption capacity (q_e); (b) Effect of initial dye concentration (C_i) on the separation factor (R_L) for the adsorption of Eosin and MB dye on magnetite hollow spheres.

To calculate the adsorption efficiency of the process, a dimensionless equilibrium parameter, called separation factor (R_L) was determined using following equation:

$$R_L = \frac{1}{1 + \alpha_L C_i} \quad (3.17)$$

where, C_i (mg/L) is the initial dye concentration and α_L is the Langmuir isotherm constant related to the adsorption energy (L/mg) [41,43]. A value of R_L in between 0 and 1 represents favorable adsorption, a value greater than 1 represents unfavorable adsorption and $R_L = 0$ represents irreversible adsorption process [41, 43].

The calculated values of R_L are plotted as a function of C_i in Fig. 3.27(b). The values of R_L range from 0.36 to 0.14 for Eosin whereas it lays within 0.27 to 0.6 for MB, i.e. between 0-1 which confirms favorable adsorption process of both types of dyes on Fe₃O₄ hollow sphere surface [41].

The change in standard Gibbs free energy (ΔG^0 , kJ/mol), related to the adsorption process was calculated using the following equation [41]

$$\Delta G^0 = -RTL \ln K_L \quad (3.18)$$

where, K_L is the Langmuir constant (L/mol), R is the universal gas constant (8.314 J/mol/K) and T is the temperature (K). The values of ΔG^0 were found to be -0.526 kJ/mol and -1.832 kJ/mol for Eosin and MB, respectively. This negative value of Gibbs free energy suggests that the dye adsorption process by the magnetite hollow spheres is spontaneous and thermodynamically stable [41, 43]. More negative Gibbs free energy for MB than Eosin implies higher spontaneous adsorption of MB onto the magnetite hollow spheres surface.

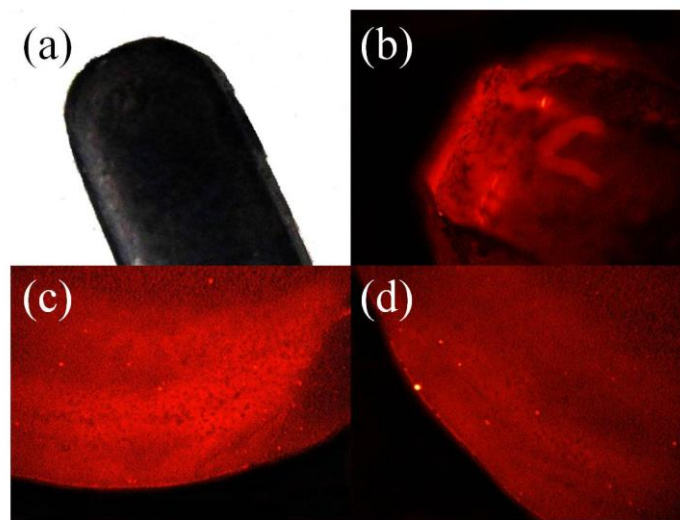


Figure 3.28 Images of (a) Eosin dye adsorbed magnetite nanoparticles collected on a magnetic needle; (b) that needle placed under microscope; (c) and (d) droplets of the Eosin dye adsorbed magnetite hollow spheres under microscope.

These hollow spheres after interacting with Eosin dye for 24 hours, were separated from the solution by magnetic separation process using a magnetic needle and then washed with water and alcohol for several times. The images of these spheres were taken in fluorescence microscope in reflection mode. Figure 3.28 depicts that images of dye adsorbed Fe_3O_4 hollow spheres collected in a magnetic needle Fig. 3.28(a), that needle placed under microscope Fig. 3.28(b) and droplets of the solution containing dye adsorbed Fe_3O_4 spheres after separated from that needle by ultra-sonication and placed under microscope (Fig. 3.28(c) and Fig. 3.28(d)). From these dark red images it is clear that the Eosin molecules are effectively adsorbed on the surface of Fe_3O_4 spheres as only Fe_3O_4 spheres without interaction with dye do

not give such red colored images. Dye adsorbed spheres give such red emission since dye aggregation takes place during adsorption and the aggregate gives strong emission.

3.4 Conclusion

In a nutshell, we have prepared magnetite hollow spheres of five different diameters by simply changing the PVP amount. PVP plays a crucial role in controlling the size of the magnetite nanoparticles primarily and then the diameter of the hollow spheres as a whole. All the spheres are ferromagnetic within temperature range of 80K to 300 K. The Verway transition temperature (T_V) of these hollow spheres is found to decrease with decreasing sphere diameter and T_V value of largest sphere is nearly same as the bulk value. Day plots give an insight of the domain structure of these spheres. Domain structure changes from PSD to MD structure as the size of the spheres increases. Smaller spheres have domain structure that is close to the SD type at lower temperatures. This change in domain structure controls the magnetic properties of these spheres such as coercivity, remanance as well as electrical properties like conductivity, permittivity etc. AC hysteresis measurements of the samples show that the coercivity significantly depends on the applied field amplitude, field frequency and also the diameter of the spheres. The coercivity and power loss of these spheres follows a power law decrease with increasing diameter. Considerable power loss of these spheres under AC magnetic field enhances its possibility of application in hyperthermia therapy at very high frequencies. These materials are very efficient in dye adsorption as observed from the Langmuir isotherms and the adsorption process is spontaneous and thermodynamically stable. So, this type of environment friendly, nontoxic, stable material can be effectively utilized for removal of heavy metals like As, Sb, Cd etc. from ground water i.e. for water treatment.

Bibliography

- [1] Q. L. Ye, Y. Kozuka, H. Yoshikawa, K. Awaga, S. Bandow, and S. Iijima, *Phys. Rev. B* 75, 224404 (2007).
- [2] D. Goll, A. E. Berkowitz, and H. N. Bertram, *Phys. Rev. B* 70, 184432 (2004).
- [3] N. Guan, Y. Wang, D. Sun, and J. Xu, *Nanotechnology* 20, 105603 (2009).
- [4] Y. G. Sun, and Y. N. Xia, *Science* 298, 2176 (2002).
- [5] X. W. Lou, L. A. Archer, and Z. C. Yang, *Adv. Mater.* 20, 3987 (2008).
- [6] D. Sarkar, M. Mandal and K. Mandal, *J. Appl. Phys.* 112, 064318 (2012).
- [7] W. Li, X. Qiao, Q. Zheng, and T. Zhang, *J. Alloys and Compounds* 509, 6206 (2011).
- [8] S. Ahmad, U. Riaz, A. Kaushik, and J. Alam, *J. Inorg. Organomet. Polym.* 19, 355 (2009).
- [9] D. Sarkar and M. Mandal, *J. Phys. Chem. C* 116, 3227 (2012).
- [10] G. F. Goya, T. S. Berquo, F. C. Fonseca, and M. P. Morales, *J. Appl. Phys.* 94, 3520 (2003).
- [11] I. Dézsi, Cs. Fetzter, Á. Gombkötő, I. Szűcs, J. Gubicza, and T. Ungár, *J. Appl. Phys.* 103, 104312 (2008).
- [12] S. Gangopadhyay, G. C. Hadjipanayis, B. Dale, C. M. Sorensen, K. J. Klabunde, V. Papaefthymiou and A. Kostikas, *Phys. Rev. B* 45, 9778 (1992).
- [13] R. H. Kodama, A. E. Berkowitz, E. J. McNiff and S. Foner, *J. Appl. Phys.* 81, 5552 (1997).
- [14] Q. L. Ye, H. Yoshikawa, and K. Awaga, *Materials*, 3, 1244 (2010).
- [15] A. K. Majumdar, V. Oestreich, D. Weschenfelder, and F. E. Luborsky, *Phys. Rev. B* 27, 5618 (1983).
- [16] R.H. Kodama, *J. Magn. Magn. Mater.* 200, 359 (1999).
- [17] D. Zhang, K. J. Klabunde, C. M. Sorensen, and G. C. Hadjipanayis, *Phys. Rev. B* 58, 14167 (1998).
- [18] P. V. Hendriksen, S. Linderorth, and P. A. Lindgard, *Phys. Rev. B*, 48, 7259 (1993).
- [19] J. P. Chen, C. M. Sorensen, K. J. Klabunde, G. C. Hadjipanayis, E. Devlin, and A. Kostikas, *Phys. Rev. B* 54, 9288 (1996).

- [20] G. Xiong, Z. Mai, M. Xu, and S. Cui, *Chem. Mater.* **13**, 1943 (2001).
- [21] K. Binder, H. Rauch, and V. Wildpaner, *J. Phys. Chem. Solids* **31**, 391 ~1970!.
- [22] V. Wildpaner, *Z. Phys.* **270**, 215 ~1974!.
- [23] D. L. Mills and A. A. Maradudin, *J. Phys. Chem. Solids* **28**, 1855 (1967).
- [24] G. Xiao and C. L. Chien, *J. Appl. Phys.* **61**, 3308 (1987).
- [25] V. B. Barbeta, R. F. Jardim, P. K. Kiyohara, F. B. Effenberger, and L. M. Rossi, *J. App. Phys.* **107**, 073913 (2010).
- [26] C. M. Srivastava and R. Aiyar, *J. Phys. C: Solid State Phys.* **20**, 1119 (1987).
- [27] J. Wu, and J. Wang, *J. App. Phys.* **105**, 124107 (2009).
- [28] J. Gass, P. Poddar, J. Almand, S. Srinath, and H. Srikanth, *Adv. Funct. Mater.* **16**, 71 (2006).
- [29] I. P. Muthuselvam, and R. N. Bhowmik, *J. Phys. D: Appl. Phys.* **43**, 465002 (2010).
- [30] N. Ponpandian, and A. Narayanasamy, *J. Appl. Phys.* **92**, 2770 (2002).
- [31] Z. Li, Y. Deng, B. Shen and W. Hu, *Materials Science and Engineering B* **164**, 112 (2009).
- [32] A. Verma, A.K. Saxena, and D.C. Dube, *J. Magn. Magn. Mater.* **263**, 228 (2003).
- [33] R. N. Bhowmik, and N. Naresh, *International Journal of Engineering, Science and Technology* **2**, 40 (2010).
- [34] S. Mukherjee, D. Das, S. Mukherjee, and P. K. Chakrabarti, *J. Phys. Chem. C* **114**, 14763 (2010).
- [35] D. Sarkar, M. Mandal, R. Das, and K. Mandal, *IEEE Transactions on Magnetism* **47**, 3163 (2011).
- [36] S. Chakraborty, K. Mandal, D. Sarkar, V. J. Cremaschi, and J. M. Silveyra, *Physica B*, **406**, 1915 (2011).
- [37] C. Piotrowski, M. Yagi, and T. Sawa, *J. App. Phys.* **69** (8), 5337 (1991).
- [38] W. J. Yuana, S. J. Panga, F. J. Liub, and T. Zhanga, *J. alloys compd.* **504**, 142 (2010).
- [39] M. Ma, Y. Wu, J. Zhou, Y. Sun, Y. Zhang, and N. Gu, *J. Magn. Magn. Mater.* **268**, 33 (2004).

- [40] R. Hergt, W. Andr a, C. G. d'Ambly, I. Hilger, W. A. Kaiser, U. Richter, and H. G. Schmidt, *IEEE Transactions on Magnetics* 34, 3745 (1998).
- [41] M. Iram, C. Guoa, Y. Guan, A. Ishfaq, H. Liu, *J. Hazardous Mater.* 181,1039 (2010).
- [42] R. Gong, M. Li, C. Yang, Y. Sun, and J. Chen, *J. Hazard. Mater.* 121, 247 (2005).
- [43] S. R. Chowdhury, E. K. Yanful, A. R. Pratt, *Environ. Earth Sci.* 64, 411 (2010).
- [44] G. Crini, *Bioresource Technol.* 97, 1061 (2006).
- [45] M. A. M. Khraisheh, and M. S. Alg-Houti, *Adsorption* 11, 547 (2005).
- [46] F.C. Wu, and R.L. Tseng, *J. Hazard. Mater.* 152, 1256 (2008).
- [47] J. S. Hu, L. S. Zhong, W. G. Song, and L. J. Wan, *Adv. Mater.* 20, 2977 (2008).
- [48] L. S. Zhong, J. S. Hu, H. P. Liang, A. M. Cao, W. G. Song, and L. J. Wan, *Adv. Mater.* 18, 2426 (2006).
- [49] L. P. Zhu, H. M. Xiao, W. D. Zhang, G. Yang, and S.Y. Fu, *Crystal Growth & Design* 8, 957 (2008).
- [50] N. Yang, S. Zhu, D. Zhang, S. Xu, *Mater. Lett.* 62, 645 (2008).
- [51] B. Wang, H. Wu, L. Yu, R. Xu, T. T. Lim, X. W. Lou, *Adv. Mater.*, 24, 1111 (2012).
- [52] G. Xie , P. Xi , H. Liu , F. Chen , L. Huang , Y. Shi , F. Hou , Z. Zeng , C. Shao, J. Wang, *J. Mater. Chem.* 22, 1033 (2012).

Chapter 4

Nanochain of Metal and Metal Oxides

In this chapter, we have studied the synthesis and characterization of some chainlike metallic and metal oxide nanoparticles. $\text{Fe}_{\text{core}}\text{-Au}_{\text{shell}}$, Hematite ($\alpha\text{-Fe}_2\text{O}_3$) and Magnetite (Fe_3O_4) nanoparticles have been arranged in chainlike fashion using unique structure of DNA as template.

4. Fabrication of Biologically Functionalized Chainlike Magnetic Nanoparticles

4.1 Preamble

Magnetic nanoparticles with some biological functionalization are of immense interest. Therefore biological molecules, such as proteins and nucleic acids etc. are used extensively for the organization of nano materials. Particularly, the combination of different metallic nanoparticles with DNA and proteins are now being studied extensively for the fabrication of self-assembled hybrid structures, such as DNA-templated nanowires [1-4]. Due to the high aspect ratio, self-assembling characteristics and its unique molecular recognition properties, DNA offers a great potentiality as a building block to create nanowires. With proper engineering, such materials may work as nanorobot, healer, nano machine, targeted drug delivery agent etc. In recent years, many studies have been devoted to develop DNA sensors due to the simplicity, specificity, exceptional sensitivity and selectivity for the detection of specific genes [5-7]. Due to their electrical conductivity it may be useful in biocomputer interconnect and for their magnetic properties they may do many marvelous things in biomedical treatment like, treatment of cancer by hyperthermia therapy, magnetic resonance imaging, brain research etc. But before use, proper engineering with such system and their extensive studies are necessary. Hence, the synthesis and study of different nano-bio-materials having magnetic, optical and electrically conducting properties is very important. For this we need to understand how different biomolecules play role with attachment of different tiny magnetic nanoparticles. In this section we have reported the synthesis of gold coated Fe nanochain ($\text{Fe}_{\text{core}} - \text{Au}_{\text{shell}}$) by DNA directing method and investigated its conducting, optical and detailed magnetic properties all together [8]. We have coated the DNA templated Fe nanochain with gold, because after the gold coating Fe becomes very stable as gold is inert to atmospheric oxygen. This kind of material can be monitored by its optical property in one hand and by magnetic property on the other. Moreover the electrical property of this material has added some more advantages.

Nanomaterials of iron oxides have attracted a great interest in nanotechnology because of their various physical and chemical properties such as magnetic properties, semiconducting properties [9] as well as optical properties. Especially, hematite ($\alpha\text{-Fe}_2\text{O}_3$) is a stable, biocompatible, nontoxic material and their nanoparticles are found to be suitable for application as pigment, catalysts, gas-sensing and photoelectrochemical cell [9] with some special biomedical applications such as in labeling cancerous tissues, magnetically controlled transport of pharmaceuticals, localized thermotherapy (where the tissue is labeled by iron oxide nanoparticles, then magnetically heated by application of high frequency AC magnetic field to particles), molecular diagnostics etc. [10] Here in this chapter, we have also discussed the organization $\alpha\text{-Fe}_2\text{O}_3$ nanoparticles in chainlike fashion using DNA template and their characterization for their further technological applications [11].

Properties of the magnetic materials are found to vary significantly when their sizes are reduced from bulk to nanoscale due to change in their band structure and also due to increase in surface to volume ratio, as discussed in *Chapter 1*. Here we have studied the finite size effect on the magnetic properties of DNA templated Fe_3O_4 nanoparticles of variable sizes [12]. Size of the Fe_3O_4 nanoparticles is varied from 7-17.6 nm by simply changing the duration of addition of co-precipitating agent. Finite size introduces surface spin disorder due to increase in surface to volume ratio and single domain magnetic structure of the nanosized particles. Bonding of the magnetic cations with the biological molecule also creates surface spin disorder, thus influences the magnetic properties of the particles.

4.2 Sample Preparation

4.2.1 Synthesis of $\text{Fe}_{\text{core}} - \text{Au}_{\text{shell}}$ nanochain using DNA

A Stock DNA solution (1 g/L) was prepared by mixing appropriate amounts of DNA with Tris-EDTA buffer (pH 7.4) and was stirred overnight. The buffer solution helps to prepare a homogeneous DNA solution without any pop off of A and G bases in DNA and was stored in a refrigerator. A stock solution of ferric chloride of 0.1 (M) and a stock solution of 0.05 (M) aqueous gold chloride (HAuCl_4)

were made. The stock solution of ferric chloride was mixed with stock DNA solution at ratio 2:1 and the mixture was stirred for 30 min using a magnetic stirrer at a temperature of 65 - 69°C. The resulting solution was then treated with sodium borohydride (NaBH_4). The solution color was turned to black, which indicates formation of iron nanoparticles by the reduction of iron ion to iron metal particles. Thereafter, 500 μL stock aqueous gold chloride (HAuCl_4) solution of 0.05 (M) was added to this dispersion. The formation of gold nanoparticles was evident by appearance of a blackish pink coloration of the solution. The whole synthesis process was carried out under a constant flow of N_2 gas so that there would be no atmospheric oxygen present to oxidize the freshly prepared iron nanoparticles, as shown in the Fig. 4.1 below.

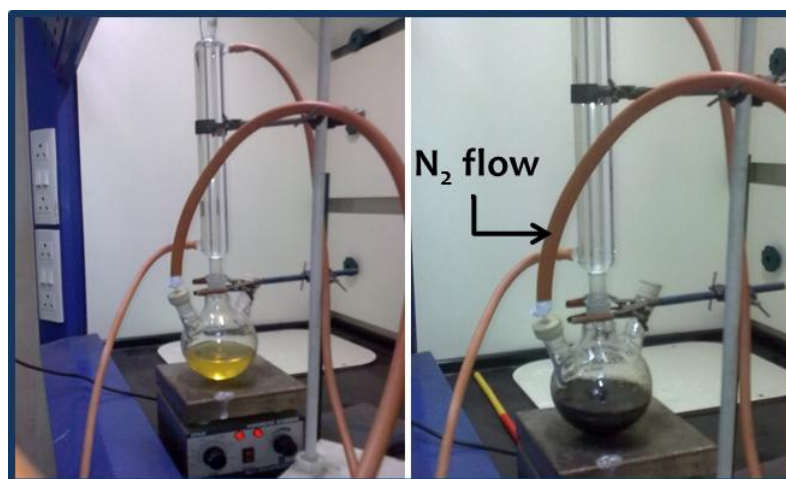


Figure 4.1 Experimental setup for the preparation of $\text{Fe}_{\text{core}} - \text{Au}_{\text{shell}}$ nanoparticles in DNA template; before the synthesis (left one) and after synthesis (right one), black color represents the synthesis of $\text{Fe}_{\text{core}} - \text{Au}_{\text{shell}}$ nanoparticles.

4.2.2 Synthesis of $\alpha\text{-Fe}_2\text{O}_3$ nanochain using DNA

A stock DNA (source Herring sperm) solution (100 $\mu\text{g}/\text{ml}$) was prepared by mixing appropriate amounts of DNA with water and was stirred and kept for overnight. A stock solution of Ferric Chloride (0.1M) was mixed with stock DNA solution at a ratio of 1:1 (by volume), and the mixture was stirred for 30 min using a magnetic stirrer at a temperature of 60° C. Then Potassium Hydroxide (KOH) solution was added drop by drop to precipitate $\alpha\text{-Fe}_2\text{O}_3$ from FeCl_3 salts. A brick-red colored solution confirmed the formation of $\alpha\text{-Fe}_2\text{O}_3$ particles. The solution was

then allowed to cool at room temperature. The particles are separated by centrifugation and then dried up in an oven at 50^o C.

4.2.3 Synthesis of DNA templated Fe₃O₄ nanoparticles of different sizes

DNA (source Herring sperm) solution (100 μg/ml) was prepared by mixing appropriate amounts of DNA with 100 ml tris-buffer and was stirred and kept for overnight. The whole synthesis procedure of the nanochains of Fe₃O₄ of variable size is pictorially depicted in Fig. 4.2.

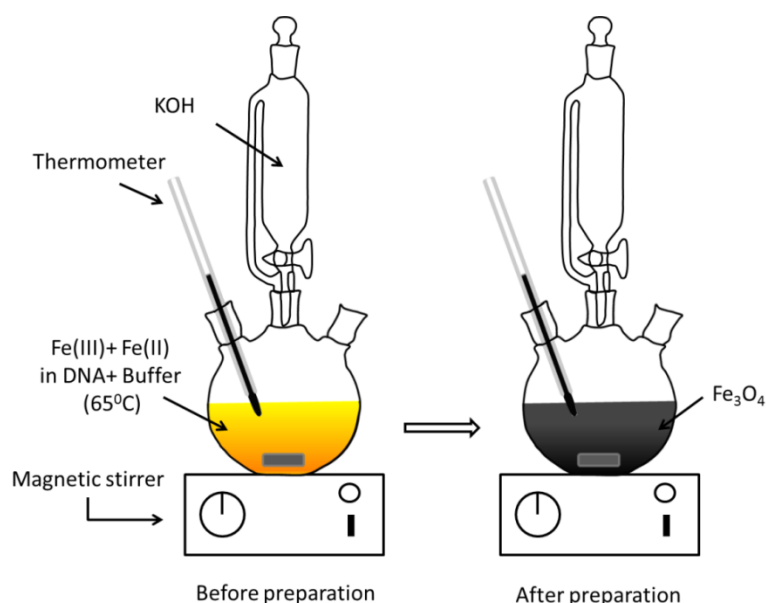


Figure 4.2 Schematic diagram representing the synthesis of Fe₃O₄ nanoparticles in DNA template.

A 100 ml stock solution of Ferric ammonium sulphate (10 mM) and Ferrous ammonium sulphate (5 mM) was prepared where Fe(III) and Fe(II) were taken in 2:1 molar ratio. Now the iron salt solution was mixed with the DNA-buffer solution and the mixture was stirred for 30 mins using a magnetic stirrer at a temperature of 65^oC. 10 ml Potassium Hydroxide (KOH) solution (56 mM) was added drop by drop to precipitate Fe₃O₄ from iron salts solution on DNA. A black colored solution confirmed the formation of Fe₃O₄ particles. Here three sets of samples 1, 2 and 3 were prepared by varying the duration time of addition of KOH by 3 min, 8 min and 12 min respectively. Duration time was changed to obtain the particles of different sizes. The solution was allowed to cool at room temperature. The particles were then

separated by centrifugation, washed by water three times and dried up in an oven at 50°C.

4.3 Results and Discussions

4.3.1 DNA templated Fe_{core} - Au_{shell} nanochain

The crystallographic nature of the as prepared Fe/Au core/shell nanoparticles was analyzed by the x-ray diffraction and the corresponding diffraction pattern is shown in Fig. 4.3 (a). The pattern contains only the peaks of metallic iron and metallic gold (Au) and no peak for any other iron oxides have been observed which confirms a perfect coating of Au metal over iron nanoparticles because iron is very prone to be oxidized in ambient atmosphere. TEM image after the synthesis of gold coated iron nanoparticles attached on DNA chain is shown in Fig. 4.3(b). The image indicates a clear attachment of these metallic nanoparticles on DNA chain. The size of the Au coated Fe nanoparticles as estimated from the width of the chain is of ~16 nm. DNA consisting of negatively charged phosphate, amino groups is good binding agents of metal ions of positive charge, which direct the formation of chain like composite structure.

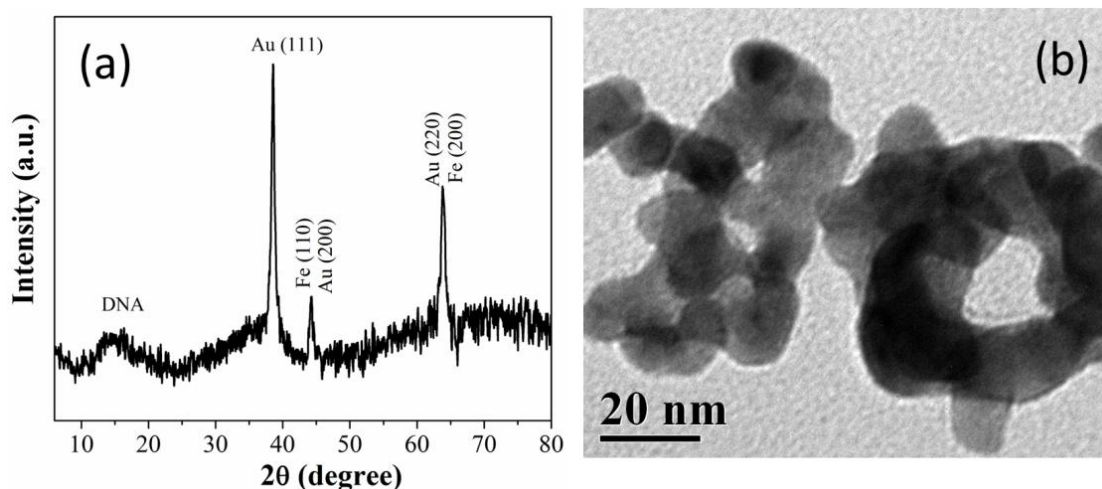


Figure 4.3 (a) X- ray diffraction pattern of the Fe_{core} - Au_{shell} nanochain, (b) TEM image of DNA templated chainlike core-shell Fe-Au nanoparticles.

Circular Dichroism (CD) spectra were taken at all the steps of solution preparation and addition of different reagents for particles formation. The secondary

structure of DNA can be determined by CD spectroscopy in the UV visible region. CD spectra taken for solutions at different stages of synthesis of material are shown in Fig. 4.4A (a, b, c, d, and e), where (a) is for tris-buffer solution, (b) is for DNA in buffer solution, (c) is after addition of ferric chloride in the solution, (d) is after Fe nanoparticles formation on DNA chain and (e) is after gold coating on Fe nanoparticles attached to DNA chain. From these spectra it is evident that no denaturation of DNA takes place after attachment of metal nanoparticles onto it as the position of both positive and negative bands of CD spectra remain almost unaltered but a small change in intensity takes place. This indicates a minor change in asymmetric structure with no denaturation of DNA. This structural change takes place due to electrostatic bond formation between DNA and ferric chloride. Hence DNA without melting or denaturation successfully acts as template to grow the particles in chain like fashion. To prevent the melting of DNA here the synthesis temperature was maintained at a range between 65 to 69°C.

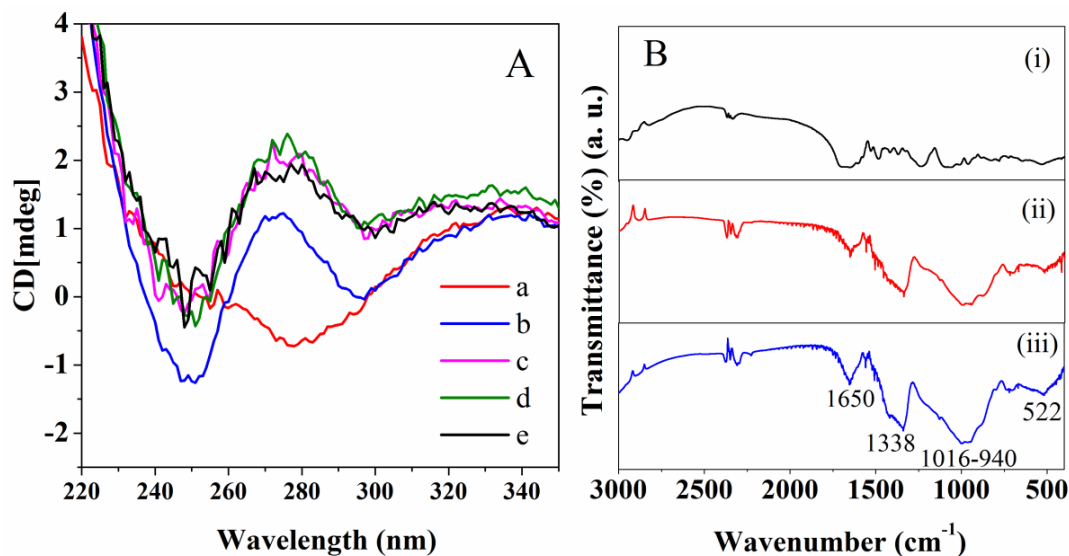


Figure 4.4 A: CD spectra; (a) is for buffer solution, (b) is for DNA in buffer solution, (c) is after addition of ferric chloride to the solution, (d) is after Fe nanoparticles formation on DNA chain and (e) is after gold coating on Fe nanoparticles attached to DNA chain. **Figure 3B**: FTIR spectra; only DNA (i), Fe attached DNA (ii) and Fe_{core} - Au_{shell} attached on DNA (iii).

The analysis of FTIR spectra (Figure 4.4B) taken from only DNA (i), Fe attached DNA (ii) and Fe_{core} - Au_{shell} attached on DNA (iii) authenticates the formation of Fe-Oxygen bond in both the cases of spectra (ii) and (iii). In the curves

(ii) and (iii), a peak at 522 cm^{-1} is observed which is due to stretching vibration of the bond between iron and the oxygen, present in phosphate backbone of DNA molecule. In curves (ii) and (iii) the major broad peak from 940 to 1016 cm^{-1} is due to overlapping of vibrational mode of PO_3^{2-} and P-O-Fe bonds of which vibrational mode of PO_3^{2-} appears at lower region (at $\sim 950\text{ cm}^{-1}$) and P-O-Fe vibration appears at higher region ($\sim 1016\text{ cm}^{-1}$). After formation of bonding with Fe and phosphate backbone the peak at $\sim 1016\text{ cm}^{-1}$ becomes intense [13]. The broad peak at ~ 1750 - 1600 cm^{-1} is due to the vibration plane of the G-C and A-T base pairs. But after the formation of bonding between iron and DNA molecule, the nature of peak changes and it becomes sharper and appears at $\sim 1650\text{ cm}^{-1}$ [14]. This information authenticates interaction of Fe with DNA which directs the growth of a chain like structure of gold coated iron attached to DNA. The peak at 1338 cm^{-1} is due to stretching mode of vibration of C-N bond present in DNA. From these above analyses the mechanism of formation of chainlike structure can be depicted pictorially as follows:

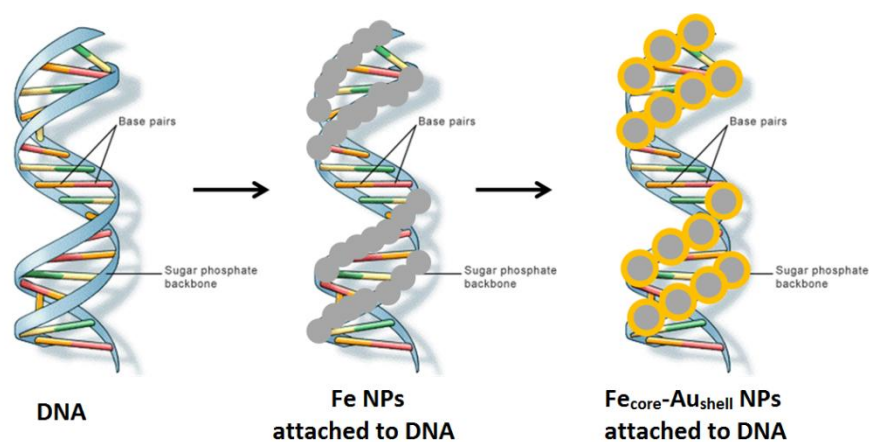


Figure 4.5 Schematic diagram of DNA templated chain like $\text{Fe}_{\text{core}} - \text{Au}_{\text{shell}} - \text{DNA}$ tri functional composite structure possessing optical, conducting and magnetic properties in one material.

The experimental data of zero field cooled (ZFC) and field cooled (FC) magnetization against temperature at a reference field of 100 Oe is plotted in Fig. 4.6(a) for DNA templated gold coated iron samples. In case of ZFC measurement, magnetization of the sample gradually increases within $80 \leq T \leq 400\text{ K}$. But in FC condition, magnetization remains almost constant ($\sim 4.6\text{ emu/g}$) up to 260 K and

then it slightly decreases (~ 4.4 emu/g) at 400 K. The ZFC magnetization curve does not show any peak within $80 \leq T \leq 400$ K which indicates that the DNA templated $\text{Fe}_{\text{core}} - \text{Au}_{\text{shell}}$ nanoparticles remain ferromagnetic within that temperature range.

For a single domain superparamagnetic (SPM) nanoparticle, the ZFC magnetization increases with temperature because the small thermal fluctuation helps the magnetization direction to align along the external field direction. However, after a certain temperature (T_B) called Blocking temperature, anisotropy energy is no longer sufficient to make up large thermal fluctuations and due to randomization of moment directions, magnetization usually decreases beyond T_B . For FC measurements, the moments were initially oriented along external field direction. With increase of temperature, high thermal fluctuation reduces the component of magnetization along field direction.

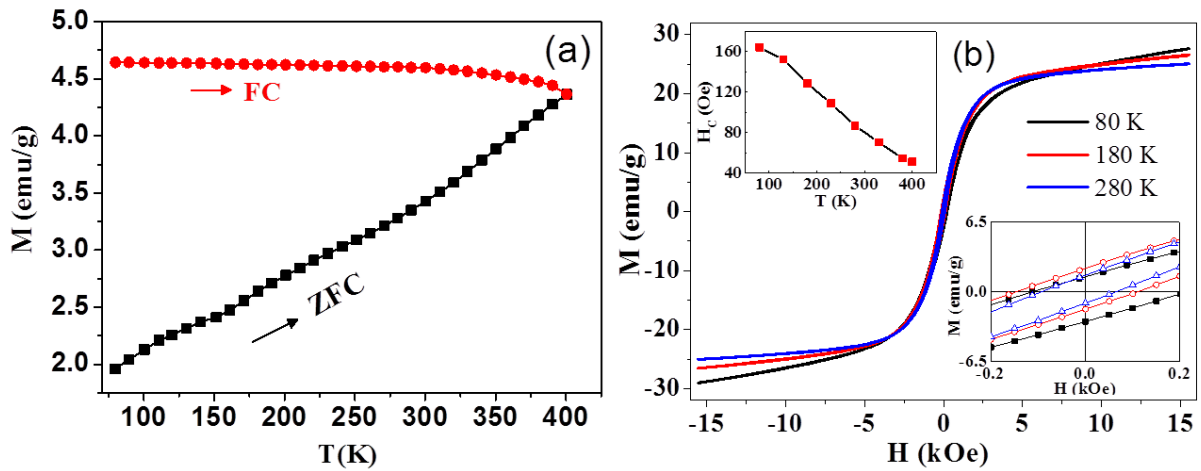


Figure 4.6 (a) Zero Field Cooled (ZFC) and Field Cooled (FC) plots. (b) M-H loops at $T = 80, 180$ and 280 K of the particles, (Inset: Coercivity vs. Temperature plot).

Magnetic nanoparticles with size below 50 nm usually consist of single domains. At a particular temperature and in absence of any magnetic field, the ferromagnetically aligned magnetic moments within these single domain particles having volume v_p fluctuate between their two energetically degenerate ground states on a time scale given as

$$\tau = \tau_0 \exp \left[\frac{k_{\text{eff}} v_p}{k_B T} \right] \quad (4.1)$$

where, τ is the relaxation time, τ_0 is constant ($\sim 10^{-9} - 10^{-13}$ s), $k_{\text{eff}} v_P$ is the total anisotropy energy (E_A) of the particle and k_{eff} is the effective anisotropy constant [15]. Now the temperature at which $\tau = \tau_m$, time constant of the instrument, is called the Blocking temperature (T_B) of the particle. This magnetic moment relaxation time τ decreases with increase in sample temperature and also with decrease in particle volume. The size of the DNA templated $\text{Fe}_{\text{core}} - \text{Au}_{\text{shell}}$ particles is found to be ~ 16 nm which we can consider as single domain particle. Having such a small volume (v_P), these particles should have low anisotropy energy (E_A) and a small thermal fluctuation would be sufficient for magnetic moments to cross the energy barrier (E_A) i.e. they should behave like superparamagnetic (SPM) particles within this measurement temperature regime. In other words, T_B should be small for this type of single domain particles. Actually it has been found that free $\text{Fe}_{\text{core}} - \text{Au}_{\text{shell}}$ nanoparticles (i.e. not attached to DNA or any other template) having sizes within 7-20 nm behave superparamagnetically with very low T_B [16-18]. However, in our case, high T_B (> 400 K) can be attributed to the templating action of DNA molecule. As the particles are formed uniformly on the DNA chain, they are strongly coupled ferromagnetically which results such an increase in anisotropy energy (E_A).

Figure 4.6(b) shows the field variation of magnetization at $T = 80, 180$ and 280 K which represents the ferromagnetic behavior of the particles. Thermal variation of coercivity (H_C (Oe)) of the particles (inset of Figure 4.6(b)) shows gradual decrease within $80 \leq T \leq 400$ K and it reaches ~ 80 emu /g at room temperature. Decrease of saturation magnetization with increase in temperature is due to increasing thermal fluctuation of the spins, also evident from the M-H loops.

Behavior of high field magnetization of the $\text{Fe}_{\text{core}} - \text{Au}_{\text{shell}}$ nanoparticles with temperature can be seen in Fig. 4.7. Magnetization values were measured at a field of 16 kOe. The magnetocrystalline anisotropy field that can be estimated from the field at which the spins start to saturate along the external field direction is found to be ~ 1.03 kOe for this type of chainlike particles and is much smaller than the maximum applied field (16 kOe). As the sample is polycrystalline and also anisotropic, we can consider those magnetization values to be nearly equal to their saturated values.

Therefore, spin wave theory can be recalled to analyze the temperature dependency of these high field magnetization results.

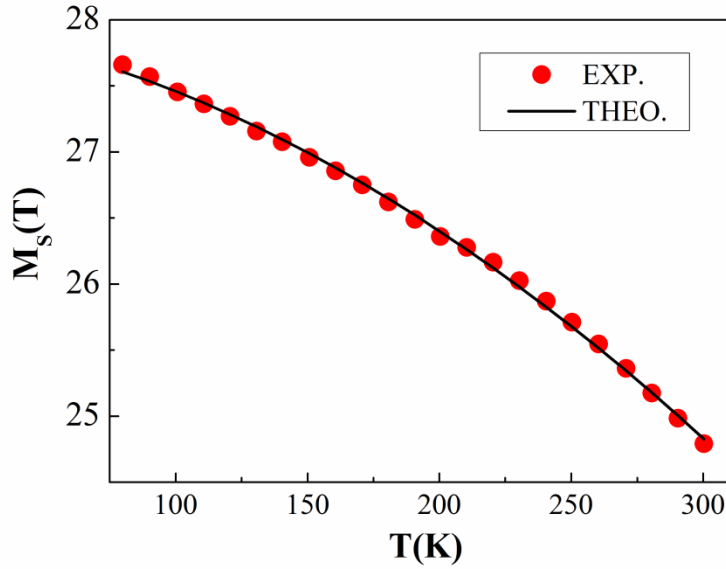


Figure 4.7 Saturation magnetization vs. temperature plot (Expt. data: solid dots; Theo. Fit: solid line).

The low energy collective excitations of an ordered magnetic system are termed as spin waves or magnons. According to spin wave theory, in thermodynamic equilibrium demagnetization of ferromagnetic state at $T \ll T_C$ is due to excitation of these spin waves [19, 20]. The spin wave dispersion relation, in the presence of an external magnetic field and in small wave vector limit ($k \rightarrow 0$), is given by the relation

$$\varepsilon_k = Dk^2 + Ek^4 + g\mu_B (H_0 + H_A + H_D) \quad (4.2)$$

where 'D' is the spin wave stiffness constant and 'E' is the proportionality constant for the k^4 term. H_0 , H_A and H_D are the applied field, anisotropy field and demagnetization field respectively. The decrease in magnetization $M(T)$, at low T from its saturated value $M(0)$ can be determined from the relation given as [19, 20]:

$$\frac{M(0) - M(T)}{M(0)} = \frac{g\mu_B}{2\pi^2} \int_0^\infty \frac{k^2 dk}{e^{\beta\varepsilon_k} - 1} = Bz \left[\frac{3}{2}, \frac{T_g}{T} \right] T^{3/2} + Cz \left[\frac{5}{2}, \frac{T_g}{T} \right] T^{5/2}$$

$$\text{or, } M(T) = M(0) \left[1 - Bz \left[\frac{3}{2}, \frac{T_g}{T} \right] T^{3/2} - Cz \left[\frac{5}{2}, \frac{T_g}{T} \right] T^{5/2} \right] \quad (4.3)$$

The functions $z\left[\frac{3}{2}, \frac{T_g}{T}\right]$ and $z\left[\frac{5}{2}, \frac{T_g}{T}\right]$ which multiply the B and C coefficient reduce to unity if the applied and effective internal magnetic fields vanish. Inclusion of these fields produces a gap of ' $k_B T_g$ ' in the spin wave spectrum with resultant field and temperature dependence. The half integer powers of T, shown explicitly in Eq. (4.3), are an adequate description of spin-wave phenomena in the temperature range as discussed here. The above functions are given by Argyle, Charap and Pugh [20] and can be expressed as:

$$z\left(m, \frac{T_g}{T}\right) = \frac{1}{\zeta(m)} \sum_{n=1}^{\infty} n^{-m} \exp\left(-n \frac{T_g}{T}\right), \quad (4.4)$$

where $\zeta(m) = \sum_{s=1}^{\infty} s^{-m}$ is the Riemann zeta function and $T_g = g\mu_B(H_0 + H_A + H_D) / k_B$.

The coefficients B and C are related with the spin wave stiffness constant (D) and average mean square range of the exchange interaction $\langle r^2 \rangle$ by [21]

$$D = \frac{k_B}{4\pi} \left(\frac{2.612V_0}{B} \right)^{2/3} \dots (4.5) \quad \text{and} \quad \langle r^2 \rangle = 1.948 \left(\frac{16}{3k_B} \right) \frac{CD}{B} \dots (4.6),$$

where V_0 is the atomic volume [20]. If \bar{a} is the most probable nearest neighbor distance in the Fe_{core} - Au_{shell} sample, we can also calculate the average exchange interaction range in terms of \bar{a} as

$$n = \langle r^2 \rangle^{1/2} / \bar{a}. \quad (4.7)$$

If we start from a simple dispersion relation given as $\varepsilon_k = Dk^2 + g\mu_B H$ with a temperature dependent stiffness constant $D(T) = D(0)(1 + AT^{5/2})$, we can obtain

$$\frac{\Delta M(T)}{M(0)} = z\left[\frac{3}{2}, \frac{T_g}{T}\right] (BT^{3/2} + FT^4 + \dots), \quad (4.8)$$

i.e., if we consider the temperature dependent stiffness constant, the first correction term to the Bloch law is of the order T^4 . Though the T^4 term in Eq. (4.8) is a

consequence of dynamical interactions, however the $T^{5/2}$ term in Eq. (4.3) is only due to the k^4 term in the spin-wave dispersion relation as given in Eq. (4.2) [20].

Now for spherically shaped particle demagnetizing field is given by $H_D = (1/3) M_S = 255.97$ Oe and anisotropy field $H_A \sim 1$ kOe. As H_D and $H_A \ll H_0$, so T_g can be determined by entirely H_0 and is found to be 2.15 K. The experimental data are then fitted to the Eq. (4.3). The solid line in Fig. 4.7 indicates the fit using Eq. (4.2). The values of $M(0)$, B and C are found to be 27.93 emu/g, $1.88 \times 10^{-5} \text{ K}^{-3/2}$ and $1.54 \times 10^{-8} \text{ K}^{-5/2}$ respectively. Putting these values of 'B' and 'C' in Eq.s (4.5) and (4.6), we have found the value of spin-wave stiffness constant (D) as $141.54 \text{ meV } \text{\AA}^2$ and average mean square range of the exchange interaction $\langle r^2 \rangle$ as 13.93 \AA^2 . However, the value of the spin wave constant (B) is found to be considerably larger than that for bulk Fe ($3.3 \times 10^{-6} \text{ K}^{-3/2}$) [20, 22]. There may be different reasons behind this increase. Study on magnetic thin films has revealed that the fluctuation of the surface spins is much larger than that of the interior spins. This causes the value of spin wave constant (B) for the surface spins 2-3.5 times larger than that for the interior moments [22]. For ultrafine Fe particles having diameter ~ 2 nm, the contribution from surface atoms exceeds 50%, assuming the surface layer being a combination of two atomic layers [22]. Again the finite size effect results energy gap between the ground state and the first excited state and reduces the mean number of nearest neighbor spins, which causes deviation from the bulk behavior that can be well explained from the phenomenon of higher value of 'B' than the bulk [23]. The value of the spin-wave stiffness constant (D) is found to be smaller than the bulk Fe ($\sim 289 \pm 15 \text{ meV } \text{\AA}^2$) which may be a consequence of small number of nearest neighbors in such small dimension. The small value of exchange interaction $\langle r^2 \rangle$ implies that the interaction is of very short range in nature. We can also calculate the exchange constant (J) of the DNA templated core/shell Fe/Au system from the equation given as $D = 2J/a^2$, ('S' is the total spin and 'a' is the cubic lattice parameter) [24]. The J value is found to be 3.85 meV with $S = 2.23$ and $a = 2.87 \text{ \AA}$, which is much smaller than $J = 11.6 \text{ meV}$ as reported by other groups [24, 25]. This large discrepancy is mainly due to the fact that there is relatively smaller number of

nearest neighbors for the surface spins of nanoparticles leading to smaller value of J as compared to others having larger dimension.

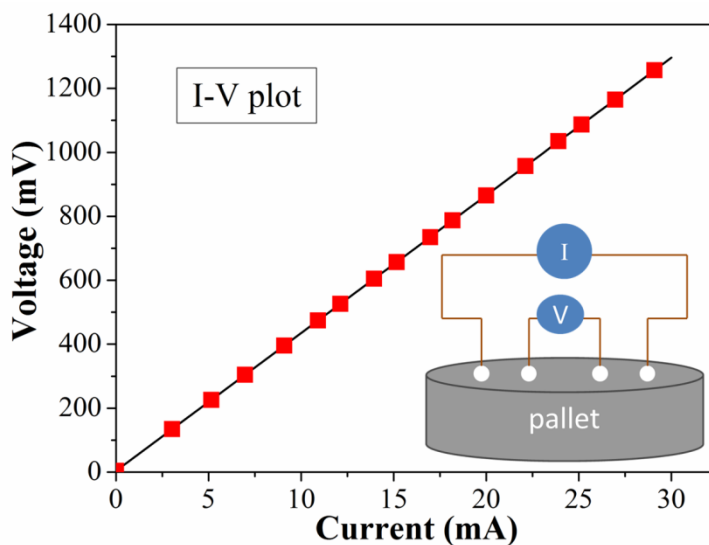


Figure 4.8 Current (I) - Voltage (V) characteristics of the nanoparticles. Inset shows the four probe connections for I-V measurement.

The current-voltage characteristic of these chainlike nanoparticles is shown in Fig.4.8. The conductive property of the DNA templated gold coated Fe nanoparticles was investigated using four probe methods (shown in the inset of Fig. 4.8) to eliminate the impedance contribution of the wiring and the contact resistance that arises at the point of contact of the connecting leads and the sample. A pallet of the DNA templated particles was made using a palletizer. The diameter and the thickness of the pallet were 12.1 mm and 0.62 mm, respectively. The behavior of I-V curve is Ohmic as evident from the corresponding figure and has low resistance (~ 42.81 ohm). The resistivity (ρ) of the sample is found to be $\sim 12.8 \times 10^{-2}$ ohm-m and the equivalent conductivity $\sigma = 7.78$ S/m which is in the semiconducting range (10^{-6} to 10^5 S/m). The observed conductivity is also much less than that for bulk gold (Au) and bulk irons (Fe) (4.52×10^7 S/m for Au and 1.04×10^7 S/m for Fe). No hysteresis in the I-V curve indicates good contacts and continuous arrangement of particles on DNA chain. This type of conducting nanoparticles chain may have great possibility of application for fabrication of connecting leads in bio-devices.

4.3.2 DNA templated α -Fe₂O₃ nanochain

X-Ray Diffraction pattern shown in Fig. 4.9(a) reveals intense and sharp peaks that can be unambiguously indexed to rhombohedral α -Fe₂O₃ with cell parameters around $a = 5.038 \text{ \AA}$, $c = 13.772 \text{ \AA}$ and space group R3c (167) (ICDD card no. 00-001-1053). There is a peak for DNA at angle $2\theta \sim 14.53^\circ$. XRD pattern of α -Fe₂O₃ shows sharp maximum peak at $2\theta = 33.26^\circ$, and several small peaks at angles $2\theta = 24.09^\circ$, 35.51° , 40.95° , 49.56° , 54.05° , 57.62° , 62.49° , 63.98° , 69.79° , 72.05° and 75.42° corresponding to (104), (012), (110), (113), (024), (116), (122), (214), (300), (208), (1010) and (217) planes, respectively. The iron oxide nanoparticles are phase pure, as the spectrum does not show any trace of other phases of Fe₂O₃, such as β , γ or δ phase or any other phase of iron oxide or hydroxides, such as FeOOH, or Fe (OH)₃.

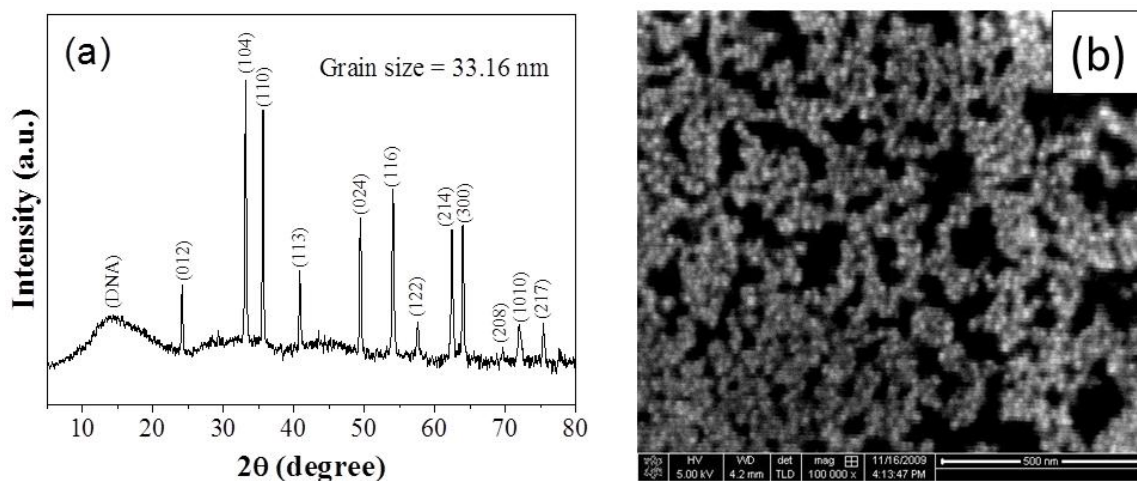


Figure 4.9 (a) X- ray diffraction pattern of DNA templated α -Fe₂O₃ nanoparticles; (b) Field Emission Scanning Electron Micrograph of DNA templated chainlike α - Fe₂O₃ nanoparticles.

We have found the α -Fe₂O₃ grain size (D) as nearly 33.16 nm using Debye-Scherrer formula given as:

$$D = \frac{0.9\lambda}{\beta \cos \theta} \quad (4.9)$$

where, ' λ ' is the wavelength of x-ray ($\lambda = 1.54 \text{ \AA}$); ' β ' is the width of the diffraction peak at half maximum (expressed in radians) for the diffraction angle 2θ .

Figure 4.9(b) shows the Field Emission Scanning Electron Microscopy (FESEM) image that shows the chainlike growth of the α - Fe_2O_3 nanoparticles on the DNA template. From the image, the particle size in DNA template was estimated to be nearly 35 nm which confirms that the particle size is very close to the grain size as obtained from Debye-Scherrer equation.

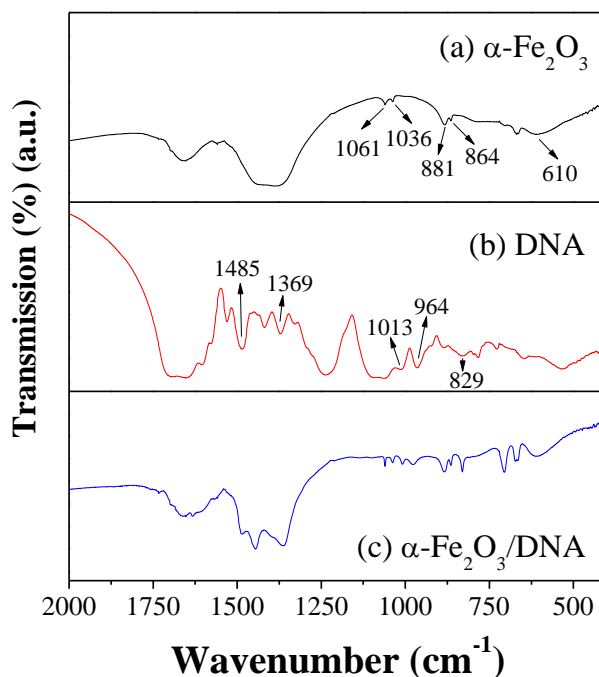


Figure 4.10 FTIR spectrums of (a) pristine α - Fe_2O_3 nanoparticles; (b) ds DNA and (c) α - Fe_2O_3 nanoparticles attached to DNA chain.

FTIR measurements were done to characterize the bonding between metallic ions and the DNA chain. Figure 4.10 shows typical FTIR spectrum of DNA templated α - Fe_2O_3 nanoparticles. Figures 4.10 (a), (b), (c) are the FTIR spectra of α - Fe_2O_3 , ds DNA and α - Fe_2O_3 /DNA nanocomposite, respectively. The IR spectrum of simple α - Fe_2O_3 (Fig. 4.10(a)) shows a typical absorption peak at 610 cm^{-1} , corresponding to the vibration of Fe-O bond of Fe_2O_3 molecule. But in Fe_2O_3 /DNA spectra (Figure 4.10(c)), this characteristic bond occurs at 613 cm^{-1} . This slight shift ($\sim 3\text{ cm}^{-1}$) towards a higher wave number side is due to the interaction of the α - Fe_2O_3 molecule with phosphate backbone of DNA. The 800 to 1000 cm^{-1} region in the IR spectrum is signature of deoxyribose region (Figure 4.10(b)). Comparing Fe_2O_3 and Fe_2O_3 /DNA spectra, it can be seen that some changes occur in that range in case of

Fe₂O₃/DNA spectra (extra peak at 974 cm⁻¹). This change indicates conformational change of DNA due to its interaction with Fe₂O₃ particles which is also evident from the Circular Dichroism (CD) study that will be discussed later. The 1000 to 1100 cm⁻¹ absorption region is due to oscillation of the phosphate group of DNA chain. Spectral change in this region in case of Fe₂O₃/DNA spectra is due to interaction of phosphate backbone with the surface of Fe₂O₃ particles. The IR absorption at 1241cm⁻¹ in DNA spectra (Fig. 4.10(b)) is due to asymmetric stretching of PO²⁻ group which disappears in Fe₂O₃/DNA spectra. This also indicates the attachment of Fe₂O₃ with DNA. The FTIR spectrum of the Fe₂O₃/DNA (Fig. 4.10(c)) nanoparticles is composed of peaks that belongs to both of DNA (829,964, 1010, 1369, 1485 cm⁻¹, etc) and of Fe₂O₃ nanoparticles (610, 864, 881, 1036 cm⁻¹, etc.), which concludes that DNA is present in combination with the Fe₂O₃ nanoparticles [26].

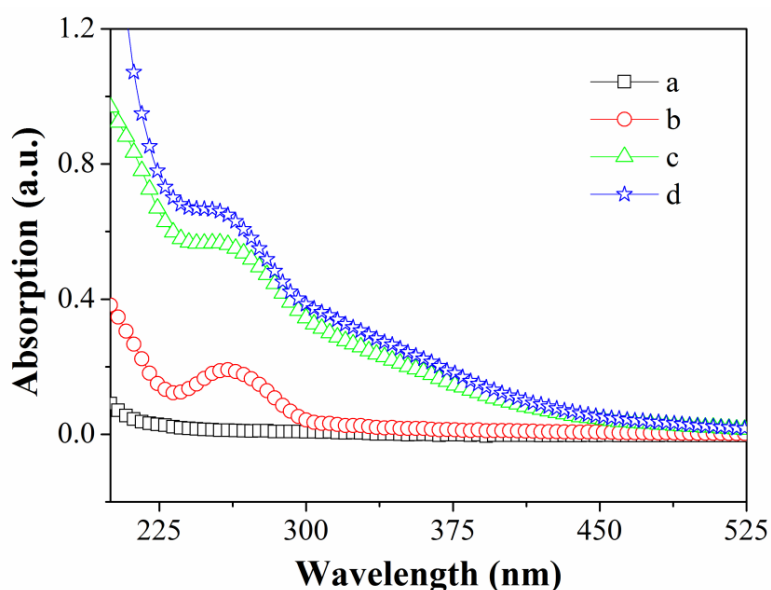


Figure 4.11 UV absorption spectrum of different stages of preparation of DNA templated α -Fe₂O₃ particles; (a) water, (b) DNA, (c) FeCl₃/DNA and (D) Fe₂O₃/DNA.

Figure 4.11 shows the ultra violet absorption spectroscopy taken at different steps of the α -Fe₂O₃ nanoparticle preparation using DNA template. It is clear that simple water (Fig. 4.11(a)) doesn't show any absorption peak within the whole UV visible spectrum. With the addition of DNA the resultant solution shows absorption peak at 260 nm which is due to the B-structure of DNA (Fig. 4.11(b)) [11]. With

further addition of ferric chloride (FeCl_3) solution, the resultant solution shows increase in intensity of the peak at 260 nm (Fig. 4.11(c)). This is actually due to the formation of the new type of molecule which is formed due to electrostatic attraction between the metal ions and the oxygen ion of the phosphate (PO_3^{4-}) background of the DNA chain. Due to such bond formation a change in position of the turn in double helix DNA structure takes place which may lead to increase in number of base pairs per turn. This phenomenon results in chromophoric peptide of DNA to be more exposed with the solvent hence increase in intensity. However, the position of the DNA absorption peak remains in the same position during the formation of $\alpha\text{-Fe}_2\text{O}_3$ particles (Fig. 4.11(d)) which confirms the stability of DNA double helix structure throughout the whole synthesis procedure.

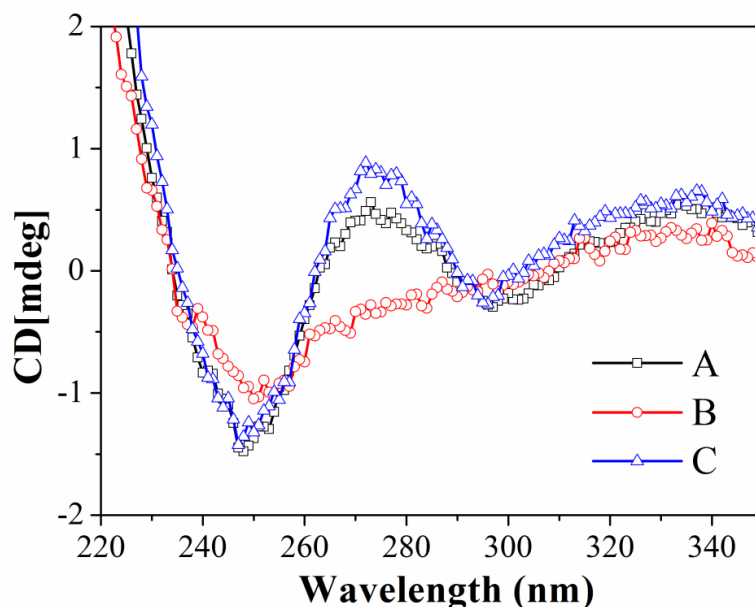


Figure 4.12 Circular Dichroism (CD) spectrum of different stages of preparation of DNA templated $\alpha\text{-Fe}_2\text{O}_3$ particles; (A) ds DNA; (B) FeCl_3/DNA ; (C) $\text{Fe}_2\text{O}_3/\text{DNA}$.

Circular Dichroism (CD) data reveals the differential absorption of Left Circularly Polarized (LCP) and Right Circularly Polarized (RCP) light when the plane polarized light passes through the sample. CD spectrum at different stages of sample preparation is showed in Fig. 4.12. Double stranded (ds) DNA shows optically activeness, characterized by the positive band at 275 nm and a negative band at 247 nm which corresponds to its B-form [27] (Fig. 4.12(A)). After the addition of FeCl_3 the intensity of positive band at 274 nm as well as the negative

band at 248 nm both decreases which was for slight denaturation of DNA (Fig. 4.12(B)). In this case Fe (III) ions form bonds with phosphate groups of DNA. As a result, change in secondary structure of DNA that is a conformational change, that is twist of DNA at some different position takes place. Additionally, presence of FeCl_3 lowered the pH of the solution as FeCl_3 is a Lewis acid. But after the addition of KOH (strong base), pH of the solution got raised to nearly 8 and DNA structure was reformed and we get nearly same CD spectra for $\text{Fe}_2\text{O}_3/\text{DNA}$ (Fig. 4.12(C)) as that of the bare DNA with no sign of DNA denaturation or helix alteration. Slight increase in intensity of the positive peak at 275 nm in case of $\text{Fe}_2\text{O}_3/\text{DNA}$ CD spectra, is due to some conformational changes of DNA as it interacts with $\alpha\text{-Fe}_2\text{O}_3$.

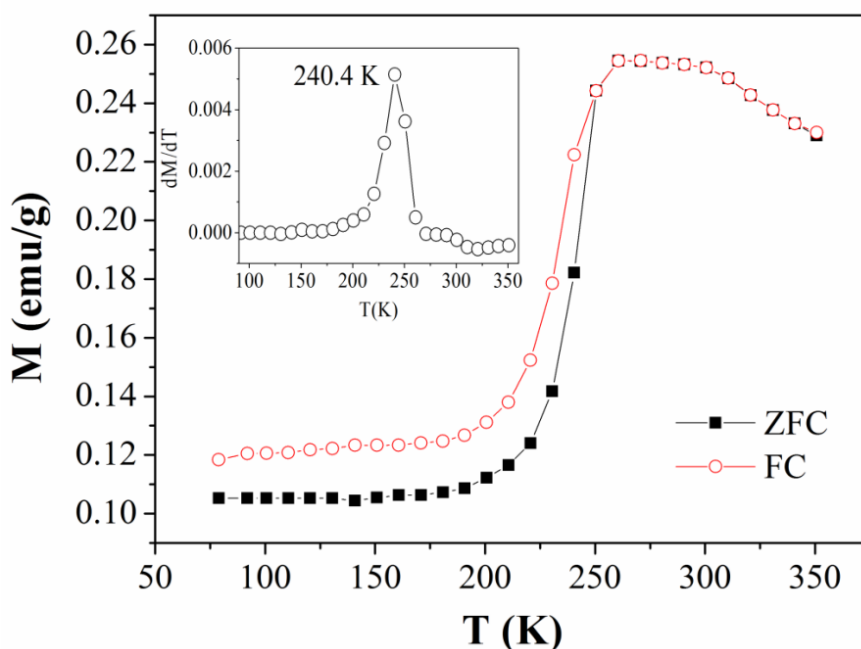


Figure 4.13 Zero-Field-Cooled (ZFC) and Field-Cooled (FC) magnetization measurements at a magnetic field of 5 kOe. The inset shows the dM/dT versus T plot giving the position of Morin transition at temperature 240.4 K.

Figure 4.13 shows the zero field cooled (ZFC) and field cooled (FC) magnetization vs. temperature curves of the DNA templated $\alpha\text{-Fe}_2\text{O}_3$ nanoparticles measured at the temperature range of 80K to 350K under a reference field of 5 kOe. In both cases, magnetization does not change much up to 190 K. At around 220 K, a sudden large change in slope is observed. After 260 K magnetization started decreasing with the increase in temperature. dM/dT versus T plot of the ZFC curve

(inset of Fig. 4.13) shows a peak at $T \sim 240.4$ K which is called the Morin transition temperature (T_M) of α -Fe₂O₃. According to Artman et al., Morin transition arises from the coexistence of two competitive anisotropy components with total energy of comparable magnitudes, opposite signs and having different temperature dependences [11, 28, 29]. The spin direction of iron atoms depends on the spin-spin and spin-orbital interactions; i.e. the magneto crystalline anisotropy (K). Again magnetocrystalline anisotropy consists of fine structure anisotropy (K_{FS}) and magnetic dipolar anisotropy (K_{MD}) components, i.e.

$$K = K_{FS} + K_{MD}, \quad (4.10)$$

where, $K_{FS} = K_{FS}(0)[2(S+1) - 3B_s(x)\coth(x)/2S] \times (2S-1)$,

$$K_{MD} = K_{MD}(0)B_s(x),$$

$x = [3S/(S+1)](T_N/T)B_s(x)$, $S = 5/2$ and $B_s(x)$ is the Brillouin function, S is the number of spins in each atom and T_N is the Neel temperature of α -Fe₂O₃.

In Eq. (4.10), K_{FS} is positive and arises from the higher order of spin-orbit coupling of the individual metal ions and tends to direct the magnetic easy axis along the crystal easy axis (c-axis), whereas K_{MD} is negative and directs the magnetic easy axis along the c-plane. At 0°K, fine structure anisotropy is larger than the magnetic dipolar anisotropy. With increase in temperature thermal fluctuations decrease the anisotropy energies but in different ways. K_{MD} falls off as the inverse cube of dipole separation distance and K_{FS} decreases exponentially with the spin separation distance. Therefore, fine structure anisotropy decreases rapidly with increasing temperature and at Morin transition temperature (T_M), total anisotropy is equal to zero. Above T_M , the magnetic dipolar anisotropy is larger than the fine structure anisotropy. This change in anisotropy energy causes the spin axis to change from [111] direction to (111) plane [28-30]. Because of this spin canting, magnetic moments are not completely compensated. As a result, weak or parasitic ferromagnetism is developed above Morin transition temperature.

Morin transition temperature (T_M) is found to be strongly dependent on particle size, decreases with it and tends to vanish for spherical particle having diameter ~ 8 nm and less [31–33]. Yamamoto demonstrated that the T_M shifts to the lower values as the crystal lattice expands along both a - and c -axes. According to him, this shift can be ascribed to the change of the dipolar magnetic field due to this type of expansion in lattice volume [34]. There are other reports which suggest that the intrinsic defects present at the surface of the fine nanoparticles can pin the spins leading to a change in the value of T_M . However, the main causes for the reduction of Morin temperature have been found as strain, crystal defects (e.g. low crystallinity of particles, vacancies), stoichiometric deviations and surface effects [33]. For this DNA templated α -Fe₂O₃ sample, T_M is found to be ~ 240 K which is slightly higher than that (~ 220 K) of the free α -Fe₂O₃ nanoparticles of equivalent size [35]. This can be attributed to the templating action of the DNA chain. In this case magnetic spins are strongly bound to the template (actually with PO₃²⁻) by electrostatic attraction which restricts the free movement of the spins. As a result higher temperature is necessary for canting the moments from c -axis to c -plane leading to the higher Morin temperature. This pinning of spins also affects the hysteresis behavior of the DNA templated nanoparticles leading to higher coercivity above T_M which will be discussed shortly.

It is interesting to note that at the field of 5 kOe, the low temperature region of FC - ZFC curve splits up below the T_M whereas above T_M it is superposed. This can be attributed to the presence of the competition between the shape and magnetocrystalline anisotropies. At high magnetic field (~ 5 kOe), ferromagnetic ordering in the α -Fe₂O₃ samples is dominating over antiferromagnetic ordering throughout the temperature ranges which causes the hysteric behavior of magnetization values in FC curve. The superposition of the FC and ZFC curves at higher temperature represents that the nanoparticles are in blocked state [29].

The magnetic hysteresis loops at different temperatures for DNA templated α -Fe₂O₃ particles are shown in Fig. 4.14. At 150 and 200 K, magnetization increases almost linearly with field which is an indication of antiferromagnetic behavior. The

presence of small coercive field below T_M ($H_C \sim 0.14$ kOe and ~ 0.21 kOe at $T = 150$ K and 200 K, respectively) is due to the noncompensation of magnetic moments at the surface of nanoparticles [32]. But at $T = 250$ K and 300 K the particles become ferromagnetic with very high coercive fields (~ 2.54 kOe at 250 K and ~ 2.75 kOe at 300 K) which may also be due to templating action of DNA. As the particles are uniformly distributed over the DNA chain through chemical bond formation, they are strongly coupled ferromagnetically above the Morin temperature that causes this type of high coercive fields.

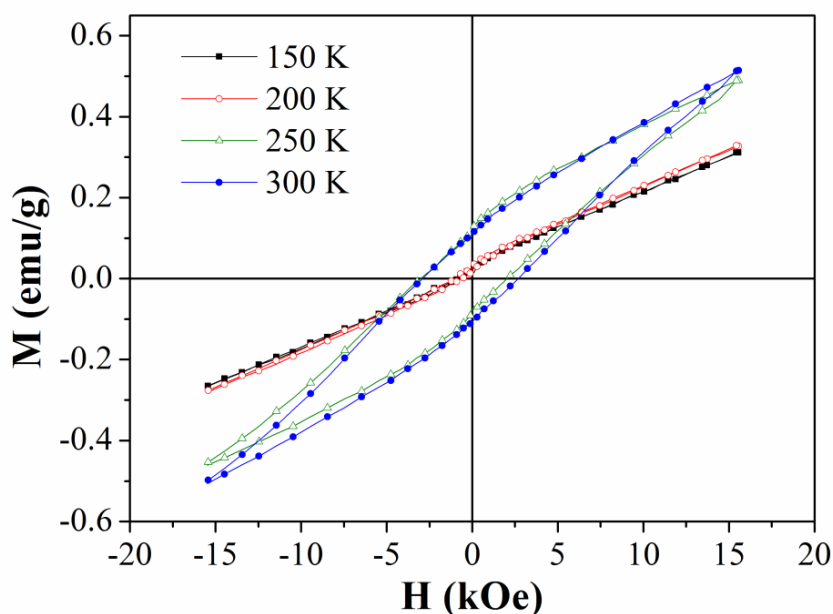


Figure 4.14 The M-H plots of DNA templated α - Fe_2O_3 sample at $T = 150, 200, 250$ and 300 K.

4.3.3 DNA templated Fe_3O_4 nanochain

Figure 4.15 shows the XRD patterns of the three samples of DNA templated Fe_3O_4 nanochains. From the XRD peak analysis we observed that all the samples are phase pure Fe_3O_4 and broadening of the peak decreases with increase of the duration of addition of KOH.

Crystalline sizes of three samples were calculated by Debye-Scherrer formula given in Eq. (4.9). Crystalline sizes were found to be 7.23 nm, 11 nm and 17.6 nm for samples 1, 2 and 3, respectively. In all three XRD patterns there is a hump at $2\theta \approx 13^\circ$ which represents the presence of DNA molecule. The TEM images of all three

samples and the Selected Area Electron Diffraction (SAED) pattern of Sample 1 are shown in Fig. 4.16.

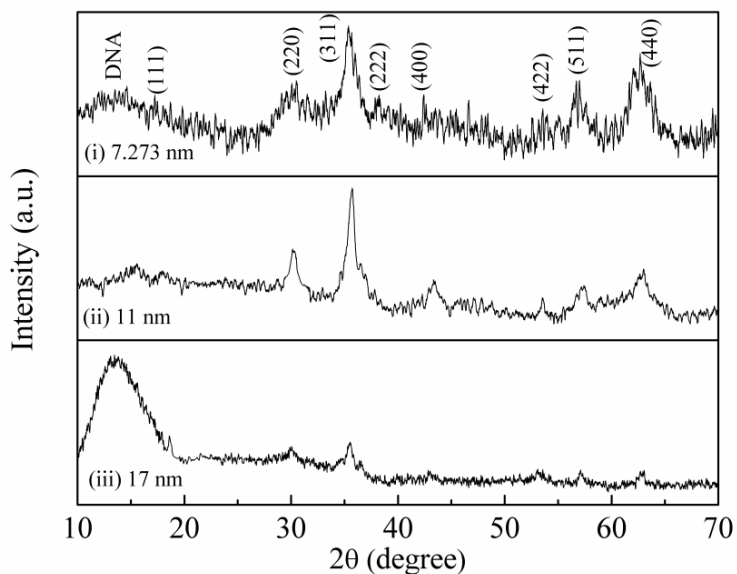


Figure 4.15 XRD pattern of Fe_3O_4 nanoparticles in DNA template; (i) Sample 1 (7.273 nm); (ii) Sample 2 (11 nm) and (iii) Sample 3 (17 nm).

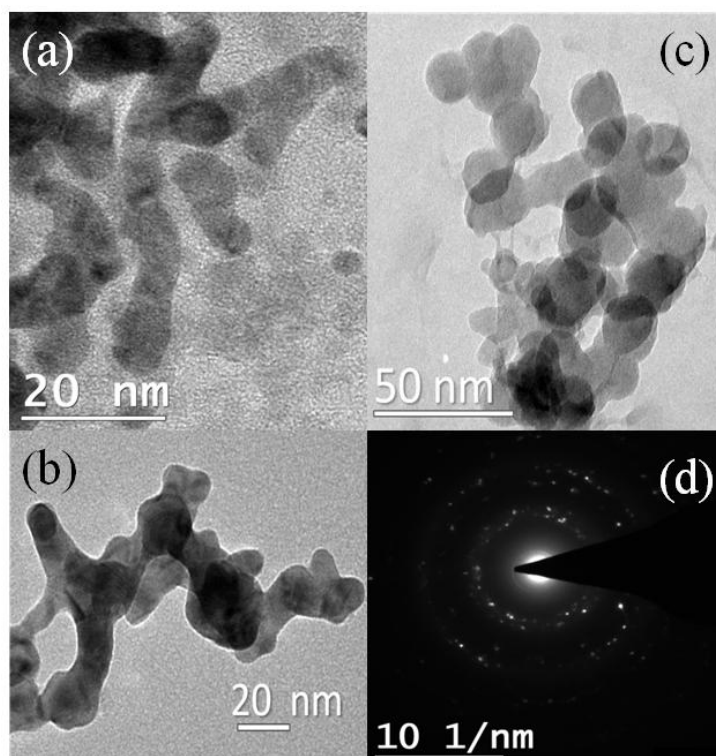


Figure 4.16 TEM micrograph of DNA templated chainlike Fe_3O_4 nanoparticle of different sizes; (a) Sample 1; (b) Sample 2; (c) Sample 3 and (d) Selected Area Electron Diffraction (SAED) pattern of Sample 1.

From the TEM images we observed the average particle sizes are 7 ± 0.3 nm, 11 ± 0.2 and 17 ± 0.5 nm for samples 1, 2 and 3, respectively. Average crystalline size calculated from XRD pattern and the average particle size estimated from TEM images are very close to each other. Usually it is found that the crystalline size and the particles size remain almost same when the particle size is less than 100 nm [36]. From the TEM micrograph it is clear that all the particles form chainlike structure which is due to the presence of DNA. DNA here acts as template and helps to grow the particles in a chain like fashion. The particle size increases with the increase of duration time of addition of KOH.

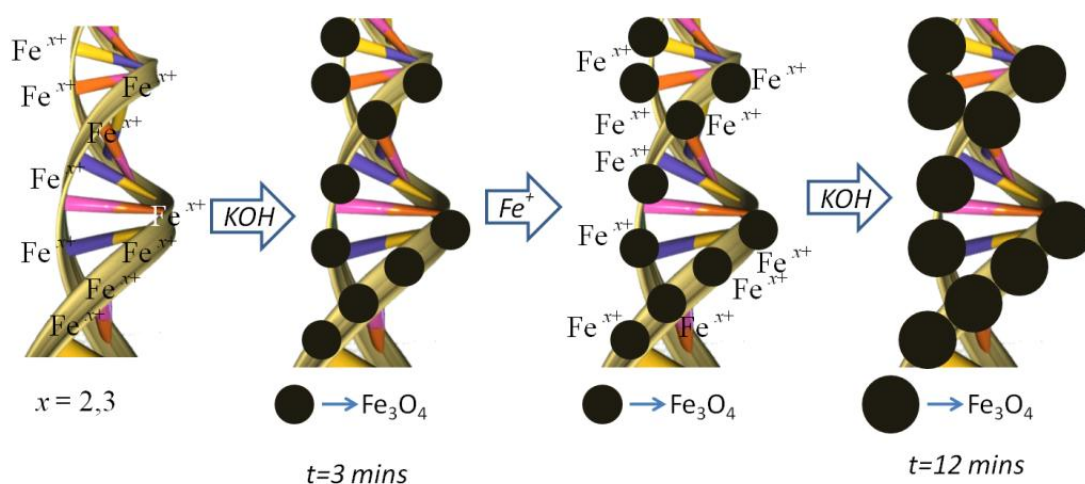


Figure 4.17 Schematic diagram showing stepwise formation and growth of Fe_3O_4 particles on DNA template with change in duration of addition of KOH.

A plausible mechanism of formation of particles and their growth with increase of duration time is shown in a schematic diagram (Fig. 4.17) from which it will be clear how bigger particles are formed with increase of duration time. Initially the iron ions (positively charged) are attached on phosphate backbone (negatively charged) of DNA by an electrostatic force of attraction. After addition of KOH, iron ions form a precipitate of Fe_3O_4 on DNA. This phenomenon occurs repeatedly, when rate of addition of KOH is sufficiently low. Just after the nucleation, these freshly prepared nanoparticles get enough time to agglomerate among themselves to reduce their surface energy. Hence, bigger particles are formed with decrease of rate of addition of KOH. The crystallinity of the chainlike nanoparticles has been further investigated by electron diffraction and the corresponding selected area electron

diffraction (SAED) pattern for Sample 1 is shown in Fig. 4.16(d). All three samples exhibit polycrystalline nature characterized by dots arranged in concentric circles around the electron beam path, as shown in the Fig. 4.16(d).

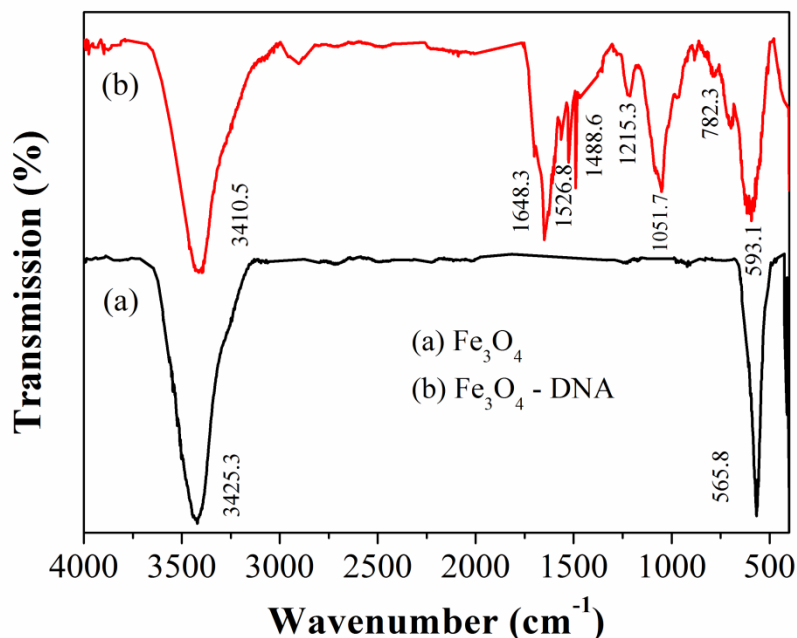


Figure 4.18 FTIR spectroscopy of as prepared Fe₃O₄ nanoparticles (a) and DNA templated Fe₃O₄ nanoparticles (b).

The FTIR spectra of both pristine Fe₃O₄ nanoparticles and DNA templated Fe₃O₄ nanoparticles, as shown in Fig. 4.18, exhibit a broad absorption peak from 3700 to 3100 cm⁻¹, which is due to the stretching vibration of -OH group arising from the hydroxyl groups on nanoparticles, DNA and water [37, 38]. The strong absorption band at 565 cm⁻¹ corresponds to the vibration of Fe₂⁺-O₂⁻ functional group which again confirms that the phase of the nanoparticles attached to the DNA chain is magnetite (Fe₃O₄) [37]. In Fe₃O₄-DNA spectrum this characteristic peak appears at 593 cm⁻¹. This shift in vibrational energy towards higher wave number is due to interaction of Fe₃O₄ nanoparticles with the phosphate backbone of DNA chain. The peaks around 2930 to 2850 cm⁻¹ in Fe₃O₄-DNA spectrum is due to symmetric and asymmetric vibrations of C-H bond of -CH₂- group present in DNA molecule [36]. The band centered at 1054 cm⁻¹ of C-O-C stretching also came from the DNA. All the characteristics absorption peaks for DNA in Fe₃O₄-DNA spectrum is summarized in Table 4.1.

Table 4.1 IR assignments for biomolecules (DNA)

IR frequency range (cm ⁻¹)	IR absorbing bonds
1648.3 (1733-1596)	amide I: C=O, C-N, N-H [13]
1526.8 (1529- 1503)	CO-N [8]
1488.6 (1492-1481)	bending (δ) of C-H bond in CH ₂ [13, 39]
1215 (1256-1186)	asymmetric stretching (ν_{as}) of PO ₂ ⁻
1051.7 (1141-990)	ν (C-O-C, C-C) [13]
782.3	Out of plane bending vibration of =C-H and -CH ₂

Generally in free DNA, IR absorption of amide bond takes place at 1550-1540 cm⁻¹. But in our case due to interaction of Fe₃O₄ with N, absorption frequency decreases to 1526 cm⁻¹. Similar case happens for phosphate backbone stretching vibration in Fe₃O₄-DNA composite. In most of the cases IR absorption frequencies shift toward lower values which is due to interaction of DNA molecule with Fe₃O₄ nanoparticles. The IR spectra for Fe₃O₄-DNA composite consists of peaks that belongs to both of Fe₃O₄ molecule and DNA molecule which ensures that DNA makes a composite like structure with Fe₃O₄ molecules through chemical bonding [26].

Figure 4.19 illustrates thermal variation of field cooled (FC) and zero field cooled (ZFC) magnetization (M) of variable sized Fe₃O₄ nanoparticles embedded in DNA template. Both FC and ZFC magnetization measurements were performed at 100 Oe reference field. The FC and ZFC magnetization curves which coincide initially, tend to follow separate route after a certain temperature (say, T_p) as temperature decreases from 300 K to 5 K (Fig. 4.19(a)) and from 400K to 80 K (Fig. 4.19(b)). This separation between FC and ZFC magnetization curves refers to a non-equilibrium magnetization state below T_p for the ZFC case [40, 41]. For FC mode, the magnetization either increases slightly (Fig. 4.19(a) and 4.19(b)) or remains almost constant when temperature is being lowered from room temperature (Fig. 4.19(c)) whereas in ZFC mode, magnetization increases up to a certain maximum and then decreases steadily in low temperature regime.

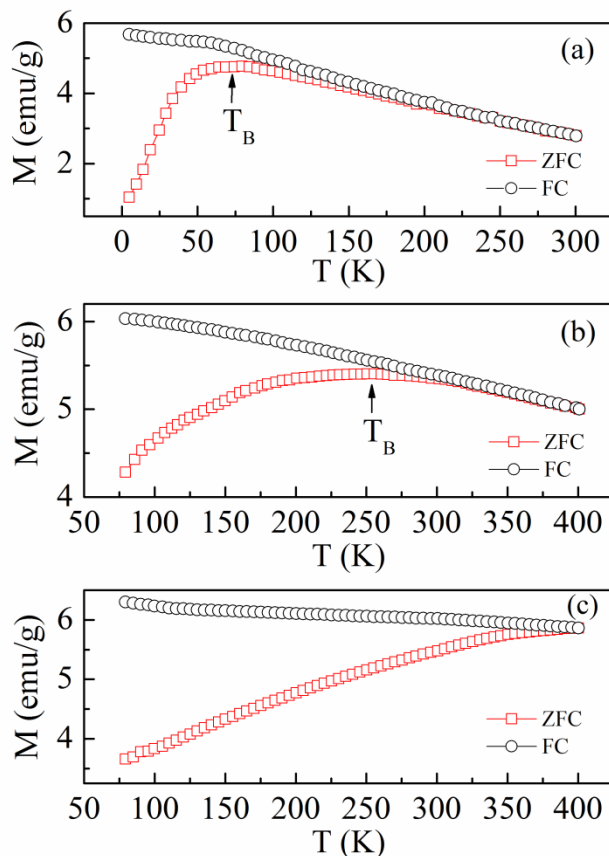


Figure 4.19 FC and ZFC magnetization curves of DNA templated Fe_3O_4 nanoparticles having different sizes: (a) 7.23 nm, (b) 11 nm and (c) 17.4 nm, respectively.

In ZFC mode, all the spins freeze randomly when temperature is reduced from room temperature. Now, in presence of external reference field, when temperature is increased, all the spins try to align along external field (H) direction leading to increase in magnetization with increasing temperature. In this low temperature region thermal energy ($k_B T$) remains smaller than the anisotropy energy (E_a) and helps the moments to orient along the reference field direction. Maximum in the ZFC magnetization curve occurs at a certain temperature when thermal energy becomes comparable to the anisotropy energy of the particles. This particular temperature is known as Blocking temperature (T_B), i.e. below this temperature the moments get freeze or blocked. After T_B , magnetization decreases with increasing temperature due to rapid fluctuation of spins between two directions of easy axis, i.e. between up and down states (Superparamagnetic relaxation) [42, 36]. But in FC mode, magnetization was initially oriented along field direction. So, any thermal fluctuation would lead to decrease of the component of magnetization along H .

In our case, the blocking temperature (T_B) varies from 79 K (for 7.23 nm sized particles) to 255 K (for 11 nm sized particles) (Fig.s 4.19(a) and 4.19(b)). Broadening of ZFC peak for Sample 2 happens due to presence of size distribution of particles. But the ZFC curve for 17 nm sized particles does not show any maximum within $80 \leq T \leq 400$ K (Fig. 4.19(c)). But as the ZFC curve shows a shoulder at high temperature region, we can assume that the blocking temperature of bigger nanocrystals is greater than 400 K. This increase of blocking temperature can be attributed due to increase in anisotropy energy (E_a) with increasing volume (V) of Fe_3O_4 particles which is consistent with Stoner-Wohlfarth theory given as:

$$T_B = \frac{KV}{25k_B}, \quad (4.11)$$

where, k_B is the Boltzmann constant and K is the anisotropy energy constant [42]. Considering the magnetic interaction between DNA templated Fe_3O_4 nanoparticles very small and have uniaxial anisotropy axis, we can use the T_B values to calculate the anisotropy constant using the above relation. The K values are found to be 1.47×10^5 J/m³ and 1.25×10^5 J/m³ for particles having average diameters 7.23 nm and 11 nm, respectively. These values are in good agreement with the K values estimated by Mossbauer spectroscopy for 6 nm ($K = 1.4 \times 10^5$ J/m³) and 12 nm ($K = 0.9 \times 10^5$ J/m³) sized particles [42]. But the estimated K values are one order of magnitude higher than the bulk value given as $K_{\text{bulk}} = 0.135 \times 10^5$ J/m³ and are found to decrease with increase in particle diameter [42, 43]. For these DNA templated Fe_3O_4 nanocrystalline particles the effective anisotropy constant (K) can depend on several intrinsic factors including magnetocrystalline anisotropy, shape anisotropy and surface anisotropy [42, 43, 36].

Now considering the invariance of magnetocrystalline anisotropy of the DNA templated Fe_3O_4 nanoparticles to the reaction environment (i.e. solvent type, reaction time) and the shape of the nanoparticles does not change significantly with particle diameter, the tendency of the increase of the effective anisotropy constant (K) with decreasing particle size can be attributed due to the concomitant effect of inter particle interactions and surface anisotropy effects [42]. More specifically, in our

DNA templated Fe_3O_4 nanoparticle system induction of surface anisotropy is due to the disorder of surface spins which is due to broken bonds and uncompensated coordination environment at the surface [42, 40, 36]. Change in coordination of surface cations results in a variation of exchange fields from positive to negative with respect to a cation's sublattice. The antiferromagnetic exchange bond between metal ions will vanish when the mediating oxygen ion is missing and also if metal ions make bond with some organic molecule [40]. Actually, when a metal ions makes a bond with some organic molecule, the electrons involve there cannot take part in the exchange interaction inducing disorder in the crystal structure. Thus the effective coordination of surface cations will be reduced by these types of broken exchange bonds. Now in our case, with decrease of particle size fraction of superficial iron ions increases which induce higher surface anisotropy. Additionally, as the metal ions of Fe_3O_4 nanoparticles are bonded with the phosphate anion of DNA chain, this also incorporates broken bonds in the nanoparticle surface which results higher anisotropy.

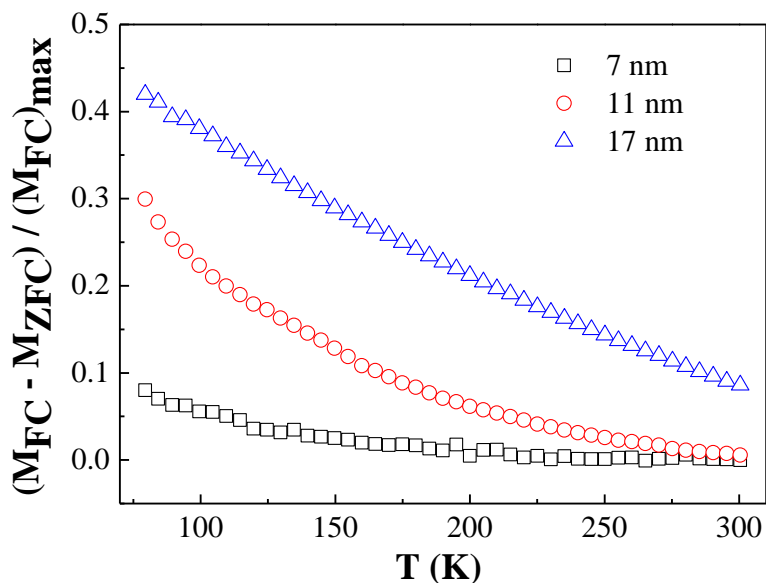


Figure 4.20 Magnetic irreversibility defined as $(M_{\text{FC}} - M_{\text{ZFC}}) / (M_{\text{FC}})_{\text{max}}$ vs. temperature (T) for samples of three different diameters.

A clear sign of irreversibility can be seen between FC and ZFC measurements which evolve due to competition between the thermal energy ($k_{\text{B}}T$) and the energy

barrier (E_a) that separates two energetically favorable ground states of spins (up and down states). The FC magnetization state is nearly an equilibrium state in which almost all the moments of the particles are oriented along the external field direction leading to a nearly constant value of magnetization in low temperature regime [41]. But ZFC magnetization is not a true equilibrium state. This irreversibility between FC and ZFC magnetization is associated with the energy required for a particle moment to relax, overcoming an energy barrier which is due to magnetocrystalline, shape or surface anisotropy [36]. This irreversibility, calculated by the difference between FC and ZFC magnetization values divided by the maximum FC magnetization value ($(M_{FC})_{max}$), is plotted as a function temperature in Fig. 4.20. At room temperature, magnetic irreversibility is very small for particles having average diameters ~ 7 nm and ~ 11 nm while it is still higher for 17 nm sized particles. This indicates the presence of either some degree of magnetic correlation or a non-negligible amount of particles that are still in blocked state [41]. In fact, the maximum of ZFC is the largest for particles having average diameter of ~ 17 nm among all the three systems. At a particular temperature, the magnetic irreversibility increases with increasing particle diameter (as obvious from the figure) which is also due to the higher degree of magnetic correlation in larger particles [36, 41].

Figure 4.21 shows the magnetic hysteresis loops ($M(H)$) for all the samples at temperatures 80 K and 300 K. In accordance with the FC-ZFC magnetization measurements, 7 nm and 11 nm Fe_3O_4 particles show superparamagnetic behavior at 300 K. But the particles having average diameter of 17 nm are ferromagnetic with very low coercivity (H_C) and remanance (M_R). At $T = 80$ K, Fe_3O_4 nanoparticles having average diameter of 11 nm and 17 nm show ferromagnetic characteristics whereas 7 nm particles are still superparamagnetic as it has a low blocking temperature ($T_B < 80$ K). However, the 7 nm particles show hysteric behavior in magnetization at much lower temperature as is evident from the corresponding M-H loop recorded at $T = 5$ K (Fig. 4.21 (d)). The reported value of the critical size is 20 nm for Fe_3O_4 nanoparticles to be superparamagnetic [42]. However in our case, the particles having average diameter of 17 nm show ferromagnetic behavior at room temperature ($T = 300$ K). This kind of behavior can be attributed to the pinning effect

of spins of Fe_3O_4 nanoparticles, which arise due to the electrostatic attraction between Fe_3O_4 nanoparticles and the DNA. Because of such type of interactions, spin motions are restricted and hence the nanoparticles show ferromagnetic behavior even when their size is below the critical size as mentioned previously.

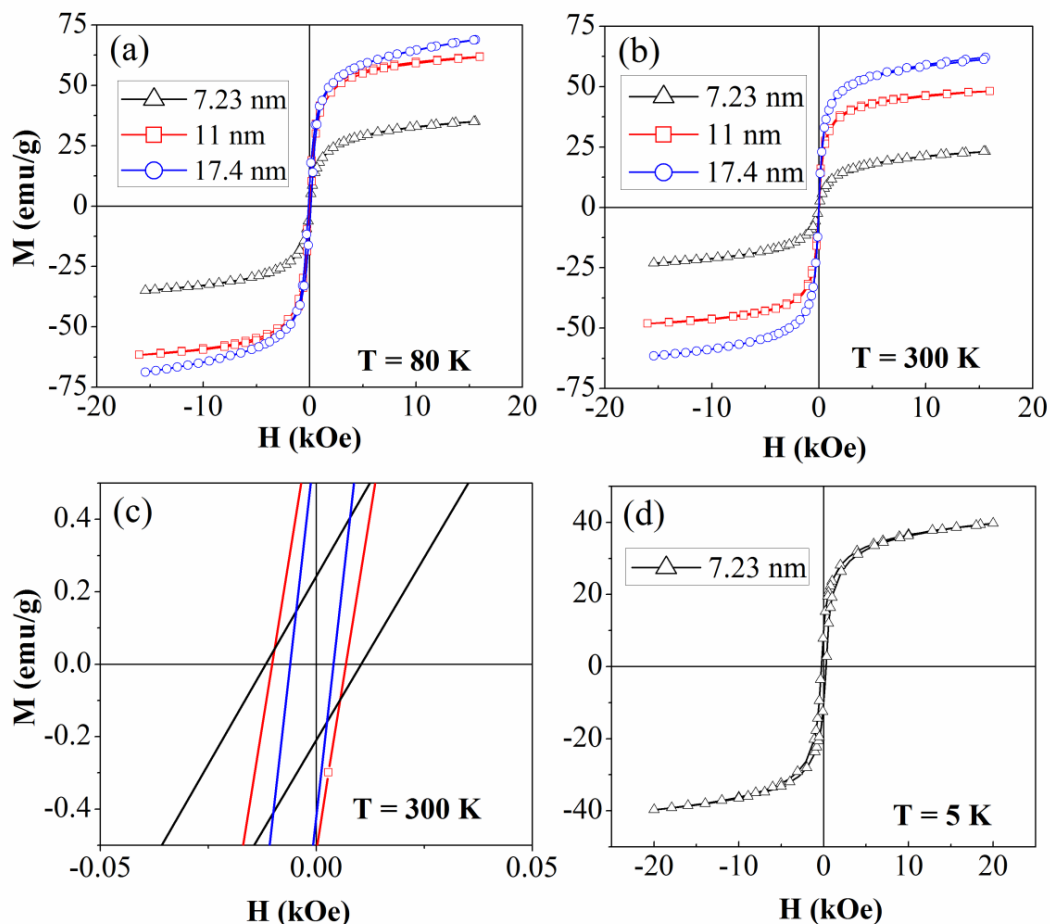


Figure 4.21 Magnetization (M) as a function of magnetic field (H) measured at 80 K (a) and 300 K (b) for DNA-templated Fe_3O_4 nanoparticles of sizes 7.23, 11, and 17.4 nm. Enlarged M - H loops at $T = 300 \text{ K}$ to show that largest particles have smallest H_C (c). M - H curve at $T = 5 \text{ K}$ for smallest Fe_3O_4 nanocrystals (7.23 nm diameter) (d).

As the magnetization curves of the samples (specially having larger particles) were not saturated, therefore the saturation magnetization (M_S) of the samples were evaluated from M vs. $1/H^2$ plot by extrapolating the value of magnetization (M) to infinite fields (following the “Law of approach of the magnetization to saturation”) [44]. The corresponding values of blocking temperature (T_B), saturation magnetization (M_S) and coercivity (H_C) are all given in the Table 4.2.

Table 4.2 Values of T_B , M_S and H_C of all the three Fe_3O_4 samples

Average size (nm)	T_B (K)	M_S (emu/g)			H_C (Oe)		
		5 K	80 K	300 K	5 K	80 K	300 K
7.28	79	41.8	37.3	25.52	270.5	18.5	10.8
11	254	—	63.7	48.97	—	77	8.5
17.4	> 400	—	77.3	68.09	—	120	4.95

The M_S value is found to increase with increasing particle volume but the coercivity follows opposite trend. At 300 K, the saturation magnetization has values which are considerably smaller than the corresponding values at 80 K which is due to high thermal fluctuation of magnetic moments of Fe_3O_4 nanoparticles at higher temperatures. Magnetization values vary from 25 to 69 emu/g as the average particle size varies from 7 to 17 nm respectively though these values are much smaller than the M_S value of bulk Fe_3O_4 (92 emu/g) [45]. This decrease of saturation magnetization with decreasing size is associated with the higher surface to volume ratio in smaller particles [44, 45]. Gangopadhyay et al. proposed a core-shell type model for nanoparticles to investigate such decrease of M_S [44]. The Fe_3O_4 nanoparticles can assumed to be spherical and to be composed of a single crystalline core (with saturation magnetization of $M_C = 92$ emu/g and density $\rho_C = 5.23$ g/cm³, corresponds to their bulk values) and a magnetically disordered shell [42, 45]. This poorly magnetic surface layer (shell) consists of iron ions with unsaturated coordination environment which may be due to absence of some oxygen ions in spinel lattice and/or due to the bond formation of metal ions with the long chain organic molecules (here DNA) [42, 40]. For a particle of total radius r , consisting of core surrounded by a shell of thickness $dr \ll r$, the core diameter (d_c) can be estimated using the equation given below [44, 45]:

$$d_c = \left[\frac{(\rho_s / \rho_c)}{\{(\rho_s / \rho_c) + (M_c - M_s) / (M_s - M_{shell})\}} \right]^{1/3} d_{total} \quad (4.12)$$

where, ρ_s = magnetically disordered shell density, roughly assigned to 5 gm/cm^3 , d_c = core diameter; d_{total} = total diameter of the particle and M_{shell} = shell magnetization which is zero considering nonmagnetic shell. Using Eq. (4.12), we have calculated the core diameter from total particle diameter and then plotted as a function of total diameter, d_{total} , at two different temperatures (as shown in Fig. 4.22). From the regression fit to the data, the equations of the straight lines are found to be as $d_c = (1.08d_{total} - 2.44) \text{ nm}$ and $d_c = (1.06d_{total} - 3) \text{ nm}$ at $T = 80 \text{ K}$ and $T = 300 \text{ K}$, respectively.

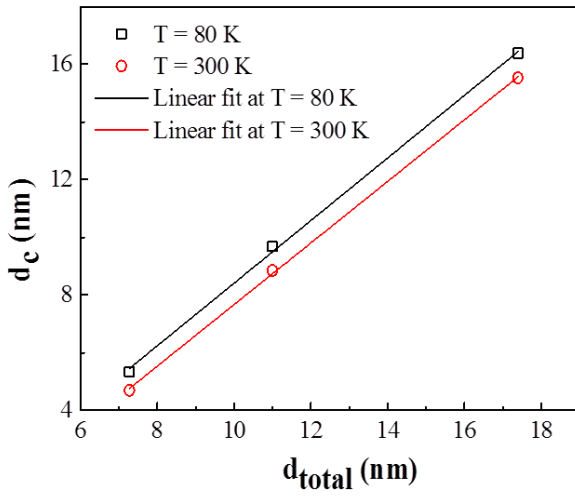


Figure 4.22

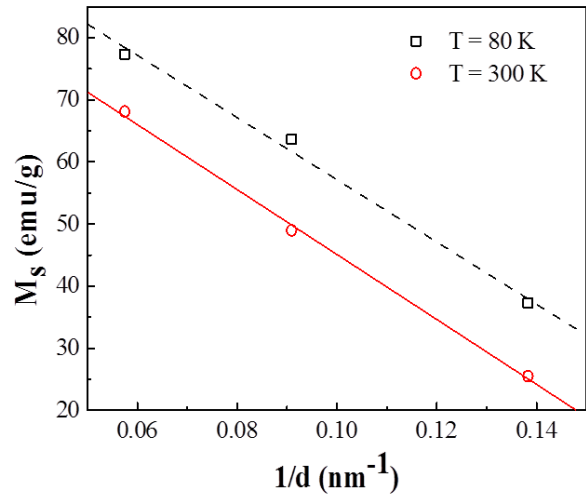


Figure 4.23

Figure 4.22 Core diameters (d_c) calculated using Eq. (4.3.3) vs. total diameter (d_{total}) plot at 80 K and 300 K. **Figure 4.23** Saturation magnetization (M_s) as a function of inverse of diameter ($1/d$) at 80 K and 300 K. Straight lines are the regression fit to the data.

The corresponding values of d_{total} , d_c and nonmagnetic shell thickness (t), as calculated using Eq. (4.12), at different temperatures are summarized in Table 4.3.

Table 4.3 Values of d_c and t calculated from d_{total} using Eq. (4.12) at $T = 80$ and 300 K

T = 80 K			T = 300 K		
d_{total} (nm)	d_c (nm)	t (nm)	d_{total} (nm)	d_c (nm)	t (nm)
7.27	5.34	1.93	7.27	4.69	2.58
11	9.68	1.32	11	8.85	2.14
17.4	16.38	1.02	17.4	15.53	1.87

Here the nonmagnetic shell thickness increases with temperature which is obvious because thermal fluctuation helps in canting of the superficial spins which makes more spins to be in disordered state [44]. But in our case, the thickness of the nonmagnetic shell decreases as the particle size increases from 7 nm to 17 nm at both the temperatures [12]. This trend of variation of shell thickness is against to that reported by other groups which state the increase of nonmagnetic shell thickness with increasing total particle diameter (d_{total}) [44, 45]. In present case, increase of shell thickness (t) with decreasing total particle diameter (d_{total}) may be a consequence of larger fraction of superficial iron ions in smaller particles [42]. These iron ions possess uncompensated coordination spheres due to fewer fractions of oxygen ions at the surface and also due to their bond formation with the phosphate backbone of DNA ligand [40, 12].

The saturation magnetization at $T = 80$ K and 300 K is found to decrease linearly when plotted against the inverse of particle diameter, i.e. with the surface to volume ratio ($1/d$) (as shown in Fig. 4.23). This type of behavior has been observed in several ferrite systems [45]. This linear dependence of magnetization with $1/d$ confirms the proposition that the magnetization is really effected by the surface of the particles [44, 45].

It is interesting to note that for the DNA templated Fe_3O_4 particles the coercivity decreases with increasing volume at room temperature. This type of behavior can be well explained by the Stoner-Wohlfarth theory which predicts that for single-domain nano-sized particles having uniaxial anisotropy axis, the coercivity (H_C) depends on anisotropy constant (K) and also the saturation magnetization (M_S) of the particles. The relation can be written as follows:

$$H_C = \frac{2K}{\mu_0 M_S}, \quad (4.13)$$

where, μ_0 is the permeability of free space [42, 43, 46]. Thus as in our case, as the particles are single domain and have uniaxial anisotropy, the decrease of coercivity

with increasing volume seems to be logical with both the decrease of anisotropy constant and the increase of the saturation magnetization.

The magnetic relaxation dynamics was investigated using AC magnetic susceptometry analysis. Figure 4.24 shows the AC susceptibility measurements of the DNA templated smallest Fe_3O_4 nanoparticles (7 nm diameter) at different frequencies ranging from 10 Hz to 1000 Hz. Both the components χ' (T) and χ'' (T) of AC susceptibility show same trend of variation as expected for superparamagnetic particles. At each frequency both the components exhibit a maximum at temperature that corresponds to the blocking temperature (T_B) of the system which drifts towards higher value with increasing frequency [43].

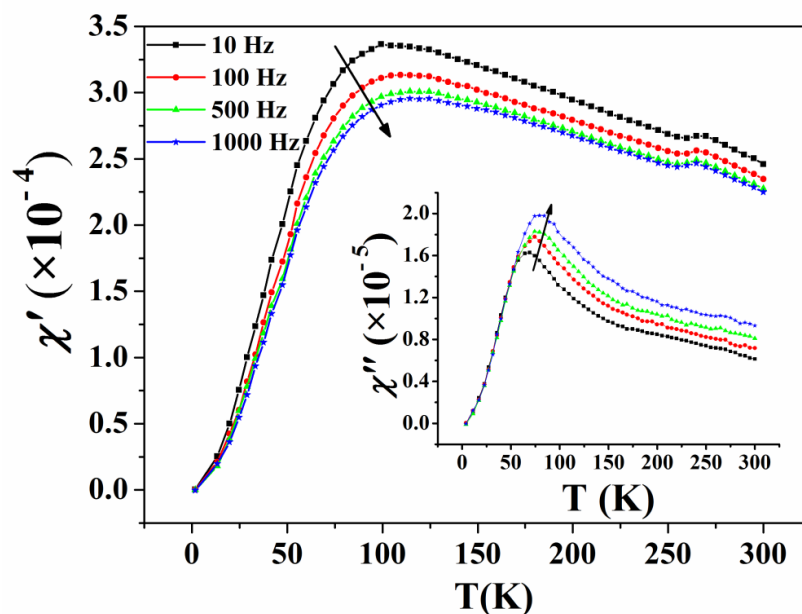


Figure 4.24 Temperature dependence of the in-phase (real) component χ' (T) of the magnetic susceptibility for DNA templated smallest Fe_3O_4 nanocrystals (7 nm diameter) at different excitation frequencies. Arrows indicate increasing frequencies. Inset: Out of phase (imaginary) component χ'' (T).

Now to provide a model independent classification between the freezing/blocking processes of canonical spin glasses, other magnetically disordered systems where freezing happens in steps and the superparamagnetic particles, we can use an empirical parameter ' p ', which is known as the frequency sensitivity of blocking temperature (T_B) and is represented as follows [47, 48]:

$$p = \frac{\Delta T_B}{T_B \Delta \log_{10}(\nu)}, \quad (4.14)$$

where, ΔT_B is the difference between T_B measured in $\Delta \log_{10}(\nu)$ frequency interval. In our case the value of ' p ' for the smallest Fe_3O_4 nanoparticles is found to be 0.086 which is very close to the 0.10 value found for superparamagnetic particles [43]. Slightly lesser value of ' p ' may be due to surface effect or interparticle interaction [43, 49]. But in this case former one is more effective as discussed earlier.

For a system of single domain noninteracting particles with uniaxial anisotropy direction, the thermal relaxation process follows the Neel-Arrhenus law given as [43, 50, 51]:

$$f = f_0 \exp\left(-\frac{E_a}{k_B T}\right), \quad (4.15)$$

where, f_0 is the Larmor frequency which falls in the range of $10^9 - 10^{13}$ Hz for superparamagnetic particles, E_a is the anisotropy energy barrier and k_B is the Boltzmann constant. In absence of an external magnetic field the anisotropy energy barrier is proportional to the volume of the particles and can be expressed as $E_a = K_{eff} V \sin^2 \theta$, where K_{eff} is the effective anisotropy constant and θ is the angle between the magnetic easy axis of the particle and the direction of the magnetic moment [42, 43].

Now to investigate if there is any type of interparticle interaction is present or not among the particles, we have plotted $\ln(f)$ versus blocking temperature (T_B), calculated from the in-phase component of AC susceptibility χ' (T) data, then try to fit the data with the Neel-Arrhenus law (as shown in Fig. 4.25). The values obtained for the Larmor frequency and the activation energy for the DNA templated Fe_3O_4 particles of smallest size are 3.97×10^{11} Hz and 2417.2 K, respectively. As the calculated value of Larmor frequency falls in its accepted range (10^9 - 10^{13} Hz), we can conclude that the Neel-Arrhenus model perfectly describes this type of system [50]. Now using the TEM data of smallest particle diameter and using the expression for E_a (as given above), the value of K_{eff} is found to be 1.84×10^5 J/m³ which is in a good

agreement with the value of anisotropy energy constant as obtained earlier ($K = 1.47 \times 10^5 \text{ J/m}^3$) from the Stoner-Wohlfarth theory. The obtained value of K_{eff} is an order of magnitude higher than its bulk value, the cause of which has been already discussed earlier.

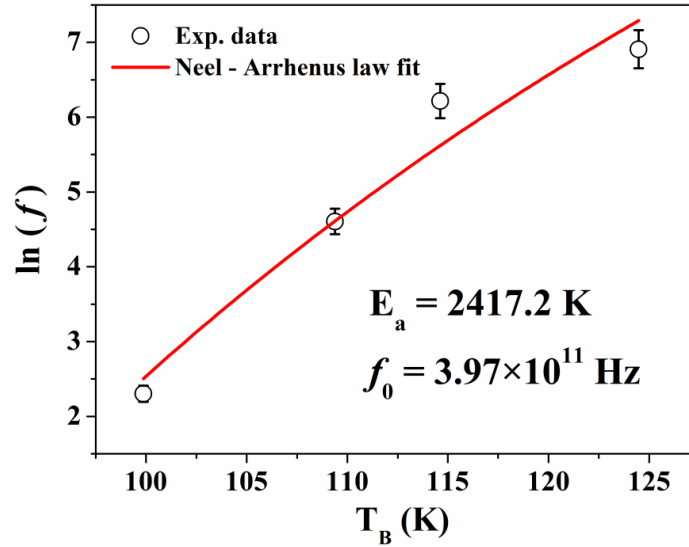


Figure 4.25 Arrhenius plot of the relaxation frequency f vs. blocking temperature T_B measured from the real component $\chi'(T)$ of ac susceptibility. Solid line is the best fit using the logarithmic version of Eq. (4.15) with $E_a = 2417.2 \text{ K}$ and $f_0 = 3.97 \times 10^{11} \text{ Hz}$.

4.4 Conclusion

We have synthesized chainlike nano-bio- $\text{Fe}_{\text{core}} - \text{Au}_{\text{shell}}$, $\alpha\text{-Fe}_2\text{O}_3$ and Fe_3O_4 system by simple chemical process exploiting DNA chain as templating agent. In case of $\text{Fe}_{\text{core}} - \text{Au}_{\text{shell}}$ nanochain, Au is conductive, DNA has optical activity and Fe is ferromagnetic. This sample is ferromagnetic in character with low coercive value and very stable. Bare Fe nanoparticles are not stable at all in ambient atmosphere. They are very prone to be oxidized by air. But gold is noble and very stable. So after a gold coating over iron nanoparticles make it very stable. Though the iron particles are very small, they show soft ferromagnetic behavior instead of being superparamagnetic.

For DNA templated α -Fe₂O₃ nanochain, spectroscopic analysis confirms the formation of α -Fe₂O₃ nanoparticles along the DNA chain due to electrostatic attraction between cationic Fe and anionic phosphate group of DNA. The unique structure of DNA remains unaltered after the formation of nanoparticles onto it as confirmed from CD analysis. For this DNA templated chainlike α -Fe₂O₃ nanoparticles T_M value is found to be slightly higher than the T_M as observed for free α -Fe₂O₃ nanoparticles with same dimensions. This increase of T_M is due to templating action of DNA. Magnetic measurements reveal the moderately high coercive nature of the particles at room temperature that may be useful to fabricate bio-devices like biocomputers, biosensors, hyperthermia treatment materials etc.

In case of DNA templated Fe₃O₄ nanochain, effect of surface anisotropy on the magnetic properties of the nanoparticles can be clearly observed from all the magnetization data. Bonding between metal cations and oxygen anions of the DNA chain also affect the anisotropy energy; thus plays an important role in changing the magnetic behavior of these magnetite nanoparticles from superparamagnetic to ferromagnetic state. Both static and dynamic magnetic characterization supports the noninteracting, single domain, superparamagnetic nature of the smallest magnetite nanoparticles (7 nm diameter).

Such type of biologically functionalized bio-friendly, nontoxic materials with magnetic, conducting and optical properties will have great scope of applicability in bio-medical research, bio instrument and computer device fabrication after a proper engineering of this material.

Bibliography

- [1] J. M. Kinsella, and A. Ivanisevic, *Langmuir*, 23, 3886 (2007).
- [2] J. M. Kinsella, and A. Ivanisevic, *J. Phys. Chem. C*, 112(9), 3191 (2008).
- [3] C. A. Mirkin, R. L. Letsinger, R. C. Mucic, and J. J. Storhoff, *Nature*, 382, 607 (1996).
- [4] S. Kundu, and H. Liang, *Langmuir*, 24, 9668, (2008).
- [5] J. Wang, *Anal. Chim. Acta*, 469, 63, (2002).
- [6] T. G. Drummond, M. G. Hill, and J. K. Barton, *Nature Biotech.* 21, 1192 (2003).
- [7] B. D. Malhotra, R. Singhal, A. Chaubey, S. K. Sharma, and A. Kumar, *Current Appl. Phys.* 5, 92 (2005).
- [8] D. Sarkar, K. Mandal, and M. Mandal, *IEEE Transactions on Magnetics*, 47, 3163 (2011).
- [9] Y. Zhu, J. C. Zhang, J. Zhai, and L. Jiang, *Thin Solid Films* 510, 271 (2006).
- [10] D. Chen, and L. Gao, *Chem. Phys. Lett.* 395, 316 (2004).
- [11] D. Sarkar, K. Mandal, and M. Mandal, *Nanosci. Nanotech. Lett.* 3, 1 (2011).
- [12] D. Sarkar, and M. Mandal, *J. Phys. Chem. C*, 116, 3227 (2012).
- [13] S. J. Parikh, and J. Chorover, *Langmuir*. 22, 8492 (2006).
- [14] M. Cagnasso, V. Boero, M. A. Franchini, and J. Chorover, *Colloids and Surfaces B: Biointerfaces*, 76, 456 (2010).
- [15] S. Mitra, K. Mandal, and P. Anil Kumar, *J. Magn. Magn. Mater.* 306, 254 (2006).
- [16] Y. J. Kima, Z. Lia, D. H. Kima, D. W. Leea, J. H. Ahn, *J. Ceramic Processing Research* 10, 216 (2009)
- [17] E. E. Carpenter, *J. Magn. Magn. Mater.* 225, 17 (2001)
- [18] S. J. Cho, B. R. Jarrett, A. Y. Louie, and S. M. Kauzlarich, *Nanotechnology* 17, 640 (2006).
- [19] K. Mandal, and S. K. Ghatak, *Solid State Communications*, 8, 743 (1992).
- [20] A. K. Majumdar, V. Oestreich, and D. Weschenfelder, *Phys. Rev. B*, 27, 5618 (1983).

- [21] V. Senz, R. R. ohlsberger, J. Bansmann, O. Leupold, and K.H. Meiwes-Broer, *New Journal of Physics*, 5, 47.1 (2003).
- [22] G. Xiao, and C. L. Chien, *J. Appl. Phys.* 61, 3308 (1987).
- [23] P. V. Hendriksen, S. Linderoth, and P. A. Lindgrad, *Phys. Rev. B*, 48, 7259 (1993).
- [24] R.H. Kodama, *J. Magn. Magn. Mater.* 200, 359 (1999).
- [25] S. N. Khanna, and S. Linderoth, *Phys. Rev. Lett.* 67, 742 (1991).
- [26] H. Skaat, G. Belfort, and S. Margel, *Nanotechnology* 20, 225106 (2009).
- [27] H. Jaganathan, and A. Ivanisevic, *Colloids and Surfaces B: Biointerfaces* 67, 279 (2008).
- [28] J. O. Artman, J. C. Murphy, and S. Foner, *Phys. Rev.* 138, 912 (1965).
- [29] S. Mitra, S. Das, S. Basu, P. Sahu, and K. Mandal, *J. Magn. Magn. Mater.* 321, 2925 (2009).
- [30] Y. Zhuang, J. Liu, F. Zhao, and J. G. Stevens, *Phys. Lett. A* 156, 127 (1991).
- [31] L. Suber, D. Fiorani, P. Imperatori, S. Foglia, A. Montone, and R. Zysler, *NanoStructured Materials* 11, 797 (1999).
- [32] C. Díaz-Guerra, L. Pérez, J. Piqueras, and M. F. Chioncel, *J. Appl. Phys.* 106, 104302 (2009).
- [33] R. D. Zysler, D. Fiorani, A. M. Testa, L. Suber, E. Agostinelli, and M. Godinho, *Phys. Rev. B* 68, 212408 (2003).
- [34] N. Amin, and S. Arajs, *Phys. Rev. B*, 35, 4810 (1987).
- [35] H. Qiana, G. Hanb, H. Yanga, G. Lina, and R. Xu, *AJChE* 8, 51 (2008).
- [36] S. Mitra, K. Mandal, and P. A. Kumar, *J. Magn. Magn. Mater.* 306, 6 (2006).
- [37] S. Ahmad, U. Riaz, A. Kaushik, and J. Alam, *J. Inorg. Organomet. Polym.* 19, 355 (2009).
- [38] X. Sun, C. Zheng, F. Zhang, Y. Yang, G. Wu, A. Yu, and N. Guan, *J. Phys. Chem. C*, 113, 16002 (2009).
- [39] J. Sun, S. Zhou, P. Hou, Y. Yang, J. Weng, X. Li, and M. Li, *J. Biomed. Mater. Res.* 80A, 333 (2006).

- [40] R. H. Kodama, A. E. Berkowitz, E. J. McNiff, and S. Foner, *J. Appl. Phys.* 81, 5552 (1997).
- [41] X. Batlle, M. Garcia del Muro, J. Tejada, H. Pfeiffer, P. Gornert, and E. Sinn, *J. Appl. Phys.* 74, 3333 (1993).
- [42] D. Caruntu, G. Caruntu, and C. J. O'Connor, *J. Phys. D: Appl. Phys.* 40, 5801 (2007).
- [43] G. F. Goya, T. S. Berquo, F. C. Fonseca, and M. P. Morales, *J. Appl. Phys.* 94, 8 (2003).
- [44] S. Gangopadhyay, G. C. Hadjipanayis, B. Dale, C. M. Sorensen, K. J. Klabunde, V. Papaefthymiou, and A. Kostikas, *Physical Review B*, 45, 9778 (1992).
- [45] D.H. Manh, P.T. Phong, T.D. Thanh, D.N.H. Nam, L.V. Hong, and N. X. Phuc, *J. Alloys Compd.* 509, 1373 (2011).
- [46] C. R. Vestal, and Z. J. Zhang, *Chem. Mater.* 14, 3817 (2002).
- [47] J. L. Dormanni, L. Bessaist, and D. Fiorani, *J. Phys. C: Solid State Phys.* 21, 2015 (1988).
- [48] J. L. Dormann, D. Fiorani, and E. Tronc, *J. Magn. Magn. Mater.* 202, 251 (1999).
- [49] J. A. De Toro, M. A. Lo'pez de la Torre, M. A. Arranz, J. M. Riveiro, J. L. Mart'inez, P. Palade, and G. Filoti, *Phys. Rev. B*, 64, 094438 (2001).
- [50] N. A. Frey, M. H. Phan, H. Srikanth, S. Srinath, C. Wang, and S. Sun, *J. Appl. Phys.* 105, 07B502 (2009).
- [51] R. H. Kodama, *J. Magn. Magn. Mater.* 200, 359 (1999).

Chapter 5

α -Fe₂O₃ Nanowires and Their Multidimensional Properties

In this chapter we have discussed about the preparation of α -Fe₂O₃ nanowires and its surface modification by metal, semiconductor etc. to improve their magnetic, electronic, optoelectronic and electrochemical performance.

5.1 Au and ZnO Modified α -Fe₂O₃ Nanowires: Enhanced Electronic, Opto-electronic and Magnetic properties

5.1.1 Preamble

One dimensional (1D) oxide semiconductor nanostructures have attracted considerable attention because of their unique tuneable physical and chemical properties suitable for multifunctional applications. Like many other oxide semiconductors the nanostructures of the transition metal oxide Hematite (α -Fe₂O₃) has also been extensively investigated being inspired by both of the interesting properties of iron oxide and the exciting features of the material at the nanometer length scale [1-4]. α -Fe₂O₃ is an n-type oxide semiconductor ($E_g = 2.14$ eV) which is also known as a most stable iron oxide under ambient conditions [5]. 1D α -Fe₂O₃ nanostructures have drawn special attention because of their unique morphology and high aspect ratios, which lead them efficiently for the wide varieties technological applications in electronics [6-8], electronic field emissions [9], electrochemical [8], gas sensors[1] and electrode materials for lithium ion batteries [1, 10]. The luminescence behaviour of the α -Fe₂O₃ nanostructures being very weak, the optical properties of the α -Fe₂O₃ NWs including their luminescence characteristics are still not well studied. Furthermore, although the magnetic properties of the α -Fe₂O₃ nanostructures have been studied extensively [11, 12], reporting the weak room temperature ferromagnetism (RTFM) of the α -Fe₂O₃ NWs, the origin of the RTFM in the α -Fe₂O₃ NWs is still not understood properly. It has been reported that the surface modification of the oxide semiconductor nanostructures through some metal (Au, Pd etc), semiconductor (ZnO, SnO₂ etc) leads to a substantial change both in their electronic, opto-electronic and magnetic properties through surface plasmon resonance (SPR), spin polarization and spin injection, band bending at the interface of the materials and also due to creation of different intrinsic vacancies (such as cation vacancy, oxygen vacancy etc.) during their nanostructure formation[13-17].

In this backdrop, the present study reports the effect of coating of some metallic (Au nanoparticles (NPs))[18] and semiconducting (ZnO)[19] materials on

the photoluminescence (PL), electrical and magnetic properties of α -Fe₂O₃ NWs. Significant enhancement in the luminescence, electrical conductive as well as magnetic properties has been observed after Au and ZnO modification of the pristine α -Fe₂O₃ NWs which have different independent reasons that we are going to discuss in this chapter.

5.1.2 Experimental

Synthesis of α -Fe₂O₃ nanowires

High-density arrays of α -Fe₂O₃ NWs have been fabricated by high temperature oxidation of the metallic Fe NWs synthesized by the template assisted electrochemical route. Anodic alumina oxide (AAO) template (average pore diameter of ~200 nm with thickness of ~50 μ m and average pore density of ~10⁹ /cm²) with a layer of Au sputtered onto one side has been used as the working electrode in the electrodeposition process in a three-electrode electrochemical cell (described in *Chapter 2*). Fe NWs have been electrodeposited in the pores of AAO using the aqueous solution of 120 g/L FeSO₄·7H₂O and 45 g/L H₃BO₃ as electrolyte at room temperature (RT). Here, the boric acid plays the role of the buffer. The pH of the electrolyte is maintained at 3.5 and the electrodeposition has been conducted by using the dc voltage of -1.03 V following linear sweep voltametry results. The electrodeposition is carried out for 18 min in order to prepare the Fe NWs of ~15 μ m length. Afterwards, the template containing the Fe NWs has been dipped in the 2M of NaOH solution at RT for a day to release the Fe NWs by dissolving the template. The arrays of α -Fe₂O₃ NWs are fabricated by the oxidation of the as grown metallic Fe NWs at 400 °C for 2 hr in oxygen atmosphere.

Surface modification of α -Fe₂O₃ nanowires by Gold (Au)

The capping Au nanoparticles have been subsequently sputtered onto the surface of the as prepared arrays of α -Fe₂O₃ NWs at room temperature using a dc sputtering system (described in *Chapter 2*). The coverage and the size of Au nanoparticles on the α -Fe₂O₃ NWs have been controlled by using different sputtering times (30, 60, 90 and 120 s) at a fixed current of 20 mA.

Surface modification of α -Fe₂O₃ nanowires by Zinc Oxide (ZnO)

To fabricate ZnO coated α -Fe₂O₃ NWs, the 0.1 M Zn(CH₃COOH)₂·2H₂O solution prepared in ethanol was added drop wise on the arrays of α -Fe₂O₃ NWs till the surface of the NWs get wet and then it was left for 30 mins for drying at room temperature. This process was repeated for three times. Afterwards, the zinc acetate coated arrays of α -Fe₂O₃ NWs was annealed in a furnace at 450 °C for 40 mins in air. During annealing the ZnO/ α -Fe₂O₃ SNHs was fabricated where the ZnO nanolayer grows on the surface of the α -Fe₂O₃ NWs through the decomposition of zinc acetate salt at high temperature.

5.1.3 Results and Discussions: Au NP decorated α -Fe₂O₃ nanowires

Morphology and crystallography

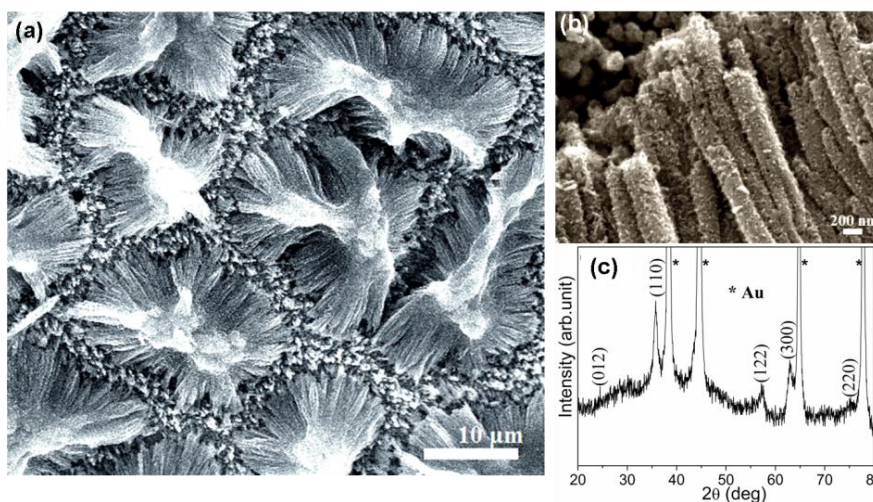


Figure 5.1.1 (a) and (b) SEM micrographs and (c) XRD pattern of the as prepared arrays of α -Fe₂O₃ NWs.

Figure 5.1.1(a) and 1(b) shows the SEM micrographs of the arrays of as prepared α -Fe₂O₃ NWs. It is evident from Fig. 5.1.1(b) that the highly porous surface structure of the α -Fe₂O₃ NWs should increase the effective surface area of the NWs. The average diameter of the α -Fe₂O₃ NWs is about 200 nm, which is found to be comparable to the diameter of the pores of the AAO template. Figure 5.1.1(c) shows the XRD pattern of the as papered NWs, where the diffraction peaks are indexed to a pure rhombohedral phase (space group R3c) of α -Fe₂O₃ (JCPDS No. 89-0597, a =

5.039 Å, $c = 13.77$ Å). The XRD pattern clearly designates the polycrystalline nature of the α -Fe₂O₃ NWs without the presence of any other impurity phases. This result indicates the all the metallic Fe has converted into α -Fe₂O₃ during the oxidation at ambient temperature. The Au peaks in the XRD pattern are originated from the underneath metallic Au layer on which the NWs are grown. The elemental composition of the α -Fe₂O₃ NWs investigated by EDAX microanalysis confirms the presence of only Fe and O. The quantitative ratio of Fe/Au in the Au sputtered α -Fe₂O₃ NWs is calculated from the EDAX study. The Fe: Au ratios are found to be 3.1, 2.82, 2.72, and 2.61 for 30, 60, 90 and 120s Au sputtered α -Fe₂O₃ NWs, respectively. The gradual decrease of the Fe: Au ratio with the increase of Au sputtering time clearly indicates the increase of Au concentration on α -Fe₂O₃ NWs with the increase of sputtering time.

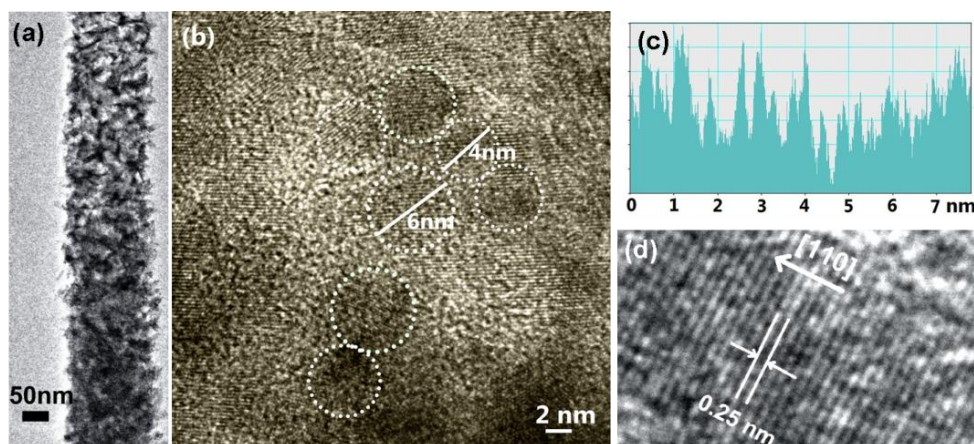


Figure 5.1.2 (a) and (b) TEM images of the α -Fe₂O₃ NWs. (c) The cross sectional profile of the lattice fringe obtained from the marked part of image (b). (d) HRTEM image of the α -Fe₂O₃ NWs.

TEM and high-resolution TEM (HRTEM) images (Fig. 5.1.2 (a),(b) and (d)) of the as prepared α -Fe₂O₃ NWs provide further information about the microstructure and morphology of the NWs. The good polycrystalline nature of the α -Fe₂O₃ NWs is further confirmed by the selective area electron diffraction pattern. Figure 5.1.2(a) and 2(b) clearly shows that the whole NW body contains large numbers of α -Fe₂O₃ nanoclusters. This kind of structure of the as grown α -Fe₂O₃ NWs is quite reasonable as the whole part of the metallic Fe NWs can not be oxidized into α -Fe₂O₃ at a time. Initially the surface of the Fe NWs gets oxidized at high temperature forming porous

α -Fe₂O₃ layer. Afterwards, the next inner parts of the Fe NWs close to the oxide surface start oxidizing while the oxygen reaches to them through the pores and defects of the outer oxide surface. In this way whole Fe NWs are transformed into α -Fe₂O₃ NWs forming tiny oxide nanoclusters containing high proportion of crystalline defects as shown in Fig. 5.1.2 (b) and 2(c). The structural properties of the α -Fe₂O₃ NWs fabricated by oxidation of Fe have been studied extensively and it is found that the oxygen vacancy defects are the major defects present in the core region of α -Fe₂O₃ NWs caused by the oxygen deficiency [2, 4]. However, the HRTEM image (Fig. 5.1.2(d)) shows that the *d*-spacings of 0.25 nm are consistent with the *d*-values of (110) lattice planes of α -Fe₂O₃. The HRTEM images of the Au decorated α -Fe₂O₃ NWs are shown in Fig. 5.1.3(a) and 3(b). The Au NPs on the surface of the α -Fe₂O₃ NWs almost form a continuous nanolayer after the Au sputtering of 120 s (Fig. 5.1.3(b)).

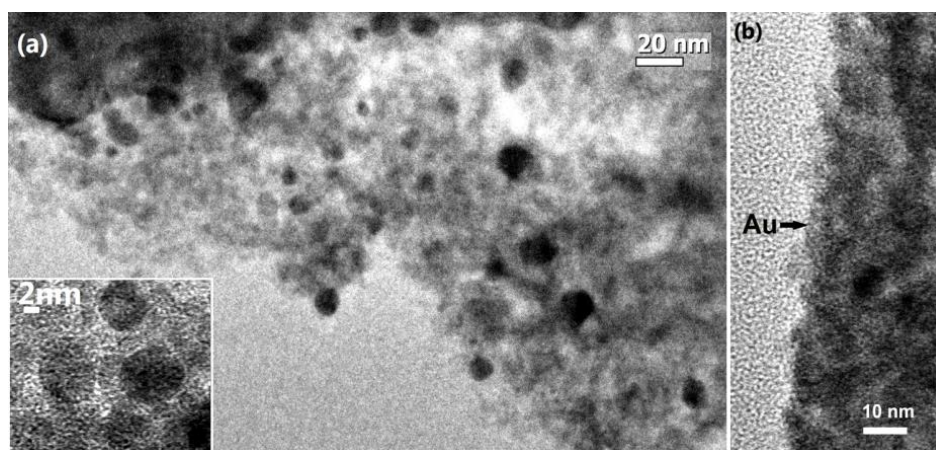


Figure 5.1.3 HRTEM images of the Au sputtered α -Fe₂O₃ NWs with Au sputtering times of (a) 90 and (b) 120s. The black dots represent the Au NPs decorated on α -Fe₂O₃ NWs.

The image of the mapping of compositional elements of α -Fe₂O₃ NWs as obtained from the energy filtered TEM (EFTEM) is shown in Fig. 5.1.4(a). It is evident from figure that the presence of two different elements (as shown by two different colors in Fig. 5.1.4(a)) is uniform through out the diameter and length of the α -Fe₂O₃ NWs. This indicates that all the Fe NWs are uniformly oxidized into α -Fe₂O₃ NWs leaving no metallic iron part unoxidized. However, to provide further insight into the chemical analysis along with the electronic structure of the α -Fe₂O₃ NWs the

EELS study has been conducted. Figure 5.1.4(b) shows the EELS spectrum of the oxygen k-edge energy loss near the edge fine structure (ELNES) of a representative α -Fe₂O₃ NW. In general, peak 'a' is attributed to the oxygen 1s to 2p core level hybridized with the iron 3d orbital whereas, peak 'b' is ascribed to the oxygen 2p states hybridized with the 4s and 4p states of iron [20]. Similarly, the iron L_{2,3} edge spectra of the α -Fe₂O₃ NWs as shown in Fig. 5.1.4(c) can help us in determining the ionization status of metal cations by identifying the

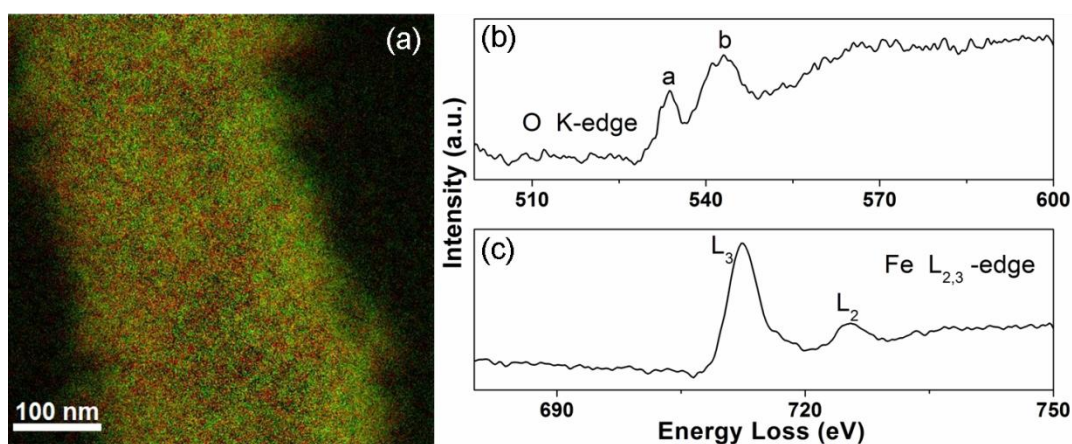


Figure 5.1.4 (a) The energy filtered TEM image of the α -Fe₂O₃ NWs indicating the presence of iron (red dots) and oxygen (green dots). The representative EELS spectra of oxygen (b) and iron (c) for the α -Fe₂O₃ NWs.

relative positions and intensity of individual L₃ and L₂ edges [21]. Here, the L₃ and L₂ peaks of Fe appear at 712 and 725 eV, respectively. The energy difference between L₃ and L₂ of Fe in α -Fe₂O₃ NWs is 13 eV, which is nearly 0.5 eV larger than that of the reported values for pure α -Fe₂O₃ powder most likely results from the oxygen vacancy defects in the NWs causing reduction of the hybridization between iron 3d orbitals with oxygen 2p orbitals [2, 21].

Photoluminescence properties

The photoluminescence properties of the as grown and Au sputtered α -Fe₂O₃ NWs are investigated by the room temperature PL (RTPL) spectroscopy. Figure 5.1.5(a) shows the RTPL spectra of the samples. It is found that all the NWs exhibit strong band edge emission centered around 496 nm (2.5 eV) and no other defect

related peaks are observed. A significant blue shift of the band gap emission of about 82 nm is observed for all the bare and Au sputtered α -Fe₂O₃ NWs compared with that of the bulk α -Fe₂O₃ semiconductor (2.14 eV) [5, 21]. The noticeable quantum confinement effect or the blue shift of the band gap emission shown by the bare and Au coated α -Fe₂O₃ NWs is quite reasonable as the body of the α -Fe₂O₃ NWs contains large numbers of tiny α -Fe₂O₃ nanoclusters of average diameter \sim 4-6 nm (Fig. 5.1.2(b)). Now, considering the nanoclusters roughly as spherical one (like spherical nanoparticles) we can calculate the corresponding band gap energy. The bandgap energy of the small nanoclusture increases because of the additional energy from the degree of confinement and Coulomb correlations. Therefore, the effective bandgap can be calculated as [22],

$$E_g = E_g^{Bulk} + \frac{n^2 \hbar^2 \pi^2}{2\mu r^2} - \frac{1.8e^2}{\epsilon r} \quad (5.1.1)$$

where, E_g^{bulk} is the bandgap of the bulk α -Fe₂O₃ and r is the size of the nanoclusters. In Eq. (5.1.1), e is the electronic charge, ϵ is the effective dielectric constant and μ is the reduced effective mass of electron and hole of α -Fe₂O₃. Here, we used $\epsilon = 5.7$, $\mu = 0.08m_0$ (m_0 is the rest mass of electron). The polarization term included in this model is usually negligible. Based on the above equation the E_g for α -Fe₂O₃ NWs are calculated as 2.42 eV considering the size of the nanoclustures as 4 nm, which is close to that of the experimentally obtained value (2.5 eV) and quite consistent with others results [20]. Therefore, the observed blue shift in α -Fe₂O₃ NWs containing nanoclustures of \sim 4-6 nm diameter is quite resonable in our work.

The integrated PL intensity of the α -Fe₂O₃ NWs is found to be enhanced significantly with the sputtering of Au nanoparticles. The intensity of the band edge emission of the α -Fe₂O₃ NWs increases consistently with the Au sputtering time up to 90 s and then decreases. The intensity of the band edge emission of Au coated α -Fe₂O₃ NWs with 90 s Au sputtering is nearly two-fold stronger than that of the bare α -Fe₂O₃ NWs. The band edge emission peak also becomes sharper with the increase of the Au sputtering time up to a certain limit.

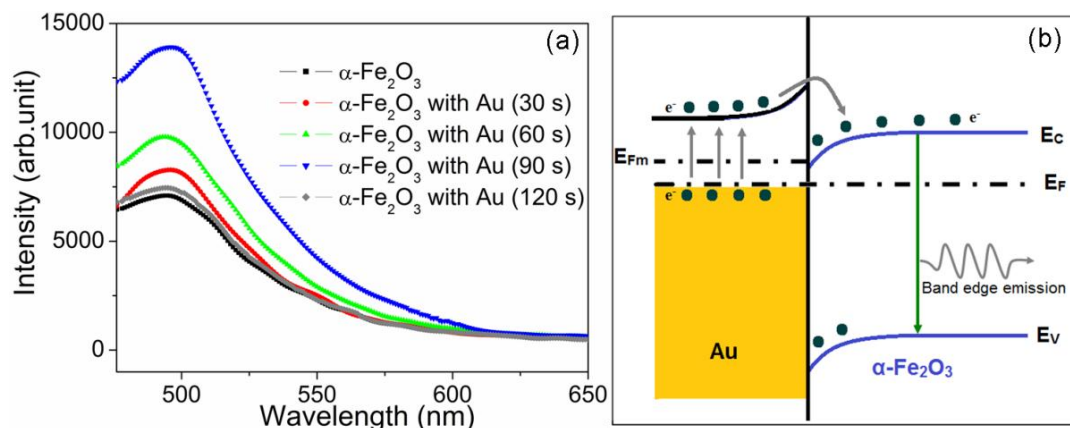


Figure 5.1.5 (a) The room temperature PL spectra of the pure and Au sputtered α -Fe₂O₃ NWs with different Au sputtering times of 30, 60, 90 and 120 s. (b) Schematic diagram of the energy band structure of Au and α -Fe₂O₃ showing the mechanism of electron transfer in Au- α -Fe₂O₃ NWs.

However, the significant enhancement of the band edge emission in α -Fe₂O₃ NWs by Au capping can be attributed to the surface Plasmon (SP) polaritons caused by the direct exciton-plasmon coupling between the excitons of the α -Fe₂O₃ NWs and the localized surface plasmons of Au NPs coating, known as the SPs coupling [13, 14, 23]. When the Au metal NPs are irradiated by the incident light having a wavelength larger than the particle size, the high density electrons of the Au NPs form an oscillating electron cloud confined at the surface. In the Au sputtered α -Fe₂O₃ NWs this high density electron cloud accumulates at the Au/ α -Fe₂O₃ interface leading to the bending of the bands in the semiconductor side towards the low energy region as shown in Fig. 5.1.5(b) [13]. In this condition the electrons from the Fermi level as well as the hot electrons created in high energy states of the Au NPs can easily transfer to the conduction band of the α -Fe₂O₃ NWs, which causes the enhancement of the band gap emission. In the other mechanism for the SP mediated emission, the emission energy because of the excitons generated in the semiconductor due to the incident light can couple with the SPs at the metal/semiconductor interface when the band gap energy of the semiconductor is comparable to the electron oscillation energy of SP [24], leading to enhancement of the band gap emission in the Au sputtered α -Fe₂O₃ NWs. However, most interestingly it is found that the SP coupling is very sensitive to morphology of the metal NPs coated on the semiconductor surface controlled by the sputtering time

[14, 24]. In our experiment, it is expected that the significant enhancement of the band edge emission in the Au coated α -Fe₂O₃ NWs up to 90 s of Au sputtering time is because of the periodic arrays of the tiny Au NPs offering a large amount of scattering medium. Hence, when the sputtered Au particles grew larger and form a continuous thin film during the long time sputtering (beyond 120 s), the adsorption process dominates over the scattering leading to the nonradiative dissipation of the SPs suppressing the free space radiation as photons. This can explain the attenuation of the band edge emission in the Au coated α -Fe₂O₃ NWs beyond the Au sputtering time of 120 s.

Magnetic properties

The room temperature (300 K) magnetic hysteresis loops (M - H plots) of the as prepared pure and Au sputtered α -Fe₂O₃ NWs are shown in Fig. 5.1.6(a) and 6(b). It is evident from figure that all the NW samples exhibit RTFM. The RT ferromagnetic signal is very weak in case of the pure α -Fe₂O₃ NWs although the bulk α -Fe₂O₃ is a well known antiferromagnetic material with the Néel and Morin temperature of 950 and 260 K, respectively [25]. However, in between the temperature range of 260 to 950 K, α -Fe₂O₃ shows weak FM, known as parasitic ferromagnetism [12]. This weak RTFM of α -Fe₂O₃ NWs is supposed to be due to the change of the α -Fe₂O₃ spin axis from c -axis to c -plane with increase in thermal fluctuation (discussed in *Chapter 4*). Another report suggest that the characteristic RTFM of the pristine α -Fe₂O₃ NWs are attributed to the surface spins and the morphological features. In fact, large magnetic moments detected on the surface layers of thin films and nanostructures of different ferromagnetic oxide semiconductors are attributed to the origin of the RTFM in the oxides [26]. However, it has also been demonstrated that the self grown oxygen vacancy defects inside the α -Fe₂O₃ NWs may impose FM by destroying the balance of antiferromagnetic ordering [21]. In our work, we also have found that the α -Fe₂O₃ NWs are enriched with crystalline defects like oxygen vacancies. Furthermore, the surface spins can play a significant role in inducing FM in our case as the highly porous α -Fe₂O₃ NWs have considerably large surface area as found by the SEM study. However, a better understanding about the origin of the RTFM of the NWs

can be further achieved by investigating the magnetic properties of the Au coated α -Fe₂O₃ NWs.

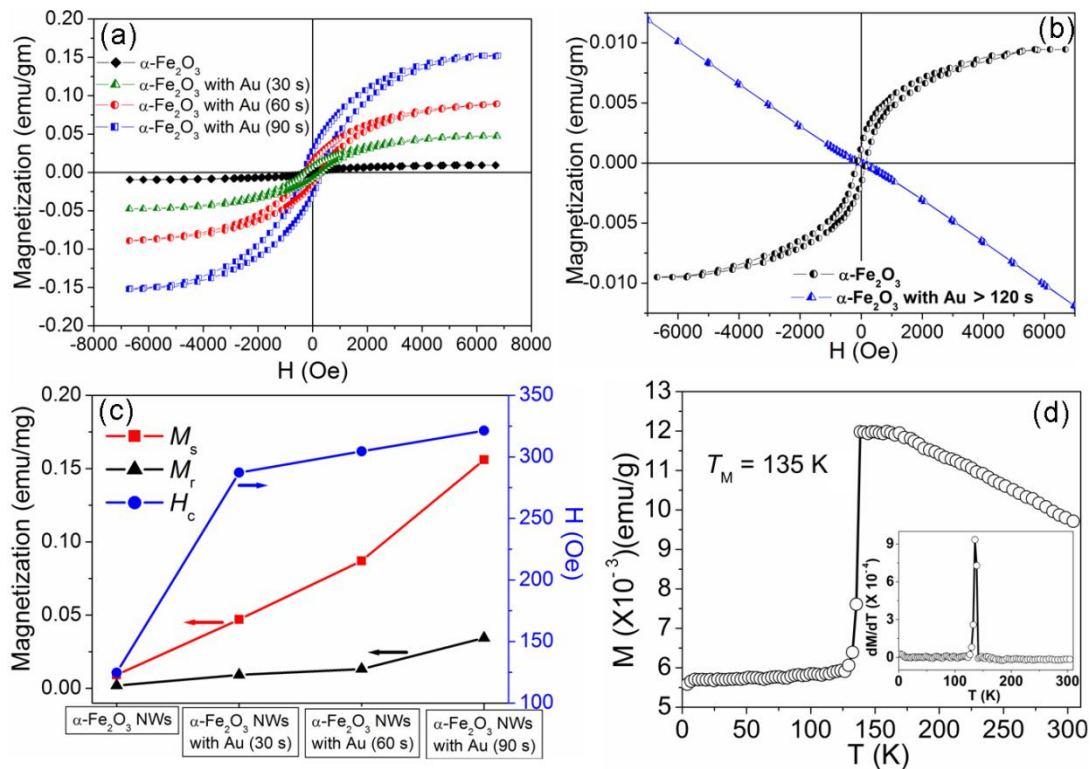


Figure 5.1.6 (a) and (b) The magnetic hysteresis (M-H) loops of the pure and Au sputtered α -Fe₂O₃ NWs measured at 300 K. (c) The variation of the saturation magnetization (M_s), retentivity (M_r) and coercivity (H_c) of the α -Fe₂O₃ NWs with Au sputtering. (d) Temperature dependence of magnetization of the pure α -Fe₂O₃ NWs for an applied field of 100 Oe (inset shows the dM/dT vs. T curve).

Here, most interestingly a distinct increase of the magnetization is observed with the sputtering of Au particles on the surface of α -Fe₂O₃ NWs (Fig. 5.1.6(a)). The magnetization increases with the Au sputtering time, reaches maximum at the Au sputtering time of 90 s (~16 times higher compared with that of the pure α -Fe₂O₃ NWs), remains almost unchanged for the 120s and becomes diamagnetic above 120s of Au sputtering time. The increase of the ferromagnetic signature of α -Fe₂O₃ NWs by the Au coating indicates that the ferromagnetic semiconductor/metal interface should have an important role behind it as the pure Au NPs are diamagnetic in nature. Here, it is expected that the intrinsic oxygen vacancy defects of the NWs have little influence on the magnetic properties as they remain unchanged for all the Au coated α -Fe₂O₃ NWs. One of the possible mechanisms behind the noticeable

enhancement of the magnetization by Au coating on the α -Fe₂O₃ NWs is that the ferromagnetic oxide semiconductor, α -Fe₂O₃ may spin polarizes the sputtered Au NPs in some extend very close to the ferromagnetic oxide/metal interface leading to the net increase of the magnetic moment as well as the effective volume of the ferromagnetic counterpart and hence enhanced magnetization is observed. This spin polarization can even penetrate about 1–2 nm inside the non magnetic metal/alloy in contact with a ferromagnetic material enhancing the net magnetic moment of the composite as observed by others [27]. Here, the penetration distance of the spin polarization is expected to increase with the size of the Au NPs which leads to increase in magnetization.

According to Banerjee et al. [17] the potential gradient at the oxide/metal interface can efficiently traps the conducting electrons of the Au NPs and induce a large interfacial orbital moment to enhance the net magnetization of the core/shell like structures. In this case also the huge surface electron cloud of the Au NPs can accumulate at the Au/ α -Fe₂O₃ interface because of the potential gradient leading to enhanced magnetization due to the orbital moments of the metallic electrons. Here, the interfacial effects are expected to be more significant in our experiment because of the large surface area of the α -Fe₂O₃ NWs. However, the diamagnetic signature of the Au sputtered α -Fe₂O₃ NWs beyond of the Au sputtering time of 120 s is quite reasonable as after 120 s of sputtering the Au metal may form a thick continuous layer on the surface of the NWs and hence diamagnetism of Au dominates over the ferromagnetic characteristics of the α -Fe₂O₃ NWs (Fig. 5.1.6(b)). The temperature dependance of magnetization (M - T) curve for the α -Fe₂O₃ NWs was measured in between the temperature range of 4–300 K at a reference field of 100 Oe and is shown in Fig. 5.1.6(d). Here, the Morin transition temperature (T_M) was observed at $T = 135$ K which is also evident from the dM/dT vs. T plot (inset of Fig. 5.1.6(d)). The T_M of the α -Fe₂O₃ NWs is found to decrease with respect to the bulk value ($T = 260$ K), which is consistent with the previous reports [25, 28].

5.1.4 Results and Discussions: ZnO/ α -Fe₂O₃ semiconductor nano-heterostructures (SNHs)

Morphology and crystallography

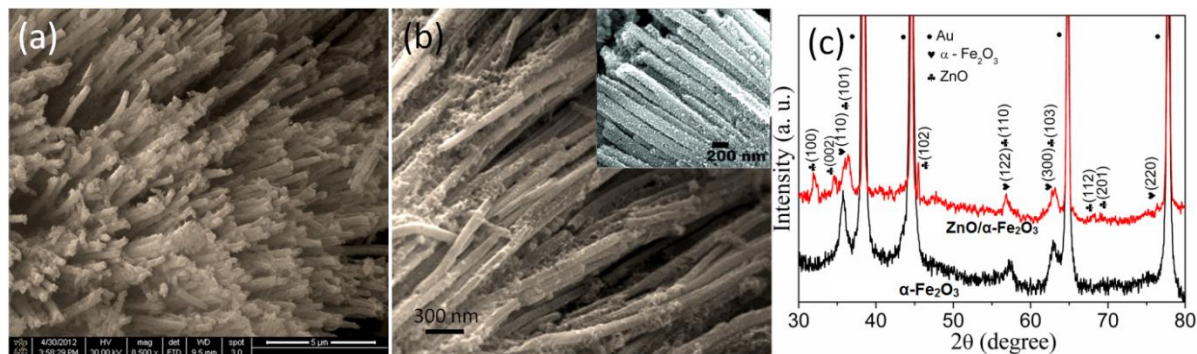


Figure 5.1.7 SEM images of the ZnO/ α -Fe₂O₃ SNHs: (a) top view, (b) side view (Inset: High magnification cross sectional view), and (c) XRD patterns of the ZnO/ α -Fe₂O₃ SNHs and α -Fe₂O₃ NWs.

Figure 5.1.7(a) and 7(b) represents the morphology of the as prepared ZnO/ α -Fe₂O₃ SNHs obtained from the scanning electron microscope (SEM) over the large sample areas. The well aligned 1D arrays of the SNHs, grow vertically on the Au substrate, is evident from Fig. 5.1.7(a). The average diameter of the ZnO/ α -Fe₂O₃ SNHs is found to be nearly 200 nm. Here, the diameter of the as grown α -Fe₂O₃ is found to be \sim 100 nm as they are fabricated using 100 nm diameter porous AAO template. It can be seen that (inset of Fig. 5.1.7(b)) small rough nanocrystals are formed on the surface of α -Fe₂O₃ NWs after ZnO coating, which were confirmed to be the ZnO nanocrystals after spot EDAX experiment, though the core-shell type nature could only be confirmed after TEM analysis.

Figure 5.1.7(c) shows the XRD patterns of the as papered α -Fe₂O₃ NWs and the ZnO/ α -Fe₂O₃ SNHs. The diffraction peaks have indexed to a pure rhombohedral phase (space group R3c) of α -Fe₂O₃ NWs (JCPDS file No. 89-0597, $a = 5.039$ Å, $c = 13.77$ Å) and a pure hexagonal wurtzite phase (space group C6mc) of ZnO (JCPDS file No. 36-1451, $a = 3.296$ Å and $c = 5.2065$ Å) as shown in the Figure 5.1.7(c). The XRD patterns clearly designate the good quality polycrystalline nature of both of the

α -Fe₂O₃ NWs as well as the ZnO/ α -Fe₂O₃ SNHs without the presence of any other impurity phases like metallic Fe and Zn. It also unfolds that the ZnO coating over the α -Fe₂O₃ NWs does not affect the crystalline structure of hematite as the diffraction peaks for the hematite phase in the ZnO/ α -Fe₂O₃ SNHs nearly exist at nearly the same 2θ position as that for the as-synthesized α -Fe₂O₃ NWs.

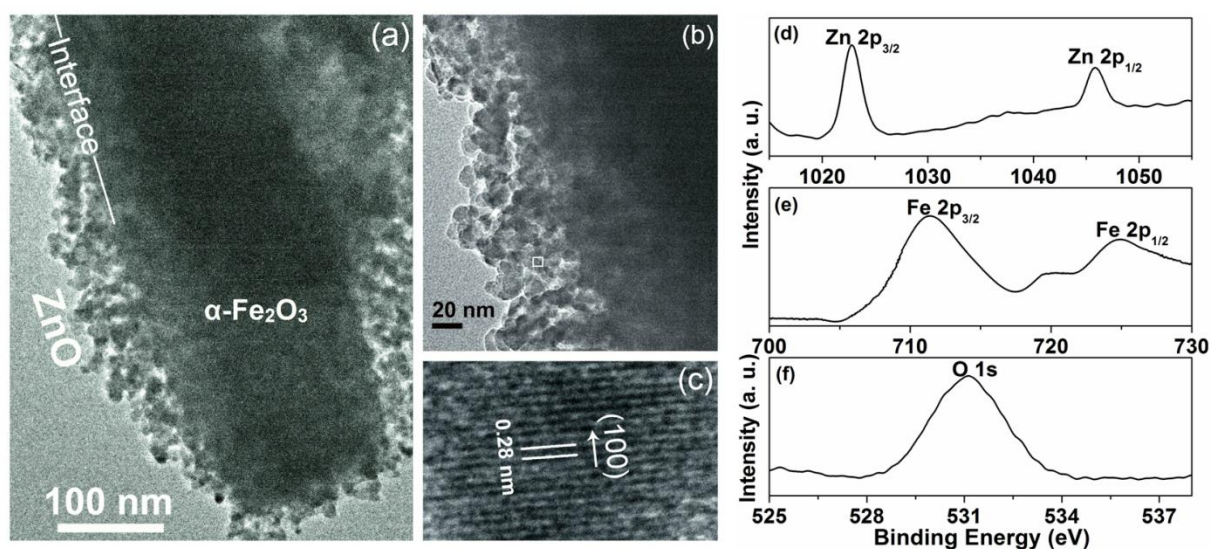


Figure 5.1.8 TEM images of the ZnO/ α -Fe₂O₃ SNHs: (a) and (b); c) HRTEM image of the ZnO nanolayer. XPS spectra for (d) Zn 2p; (e) Fe 2p and (f) Oxygen 1s core level of ZnO/ α -Fe₂O₃ SNHs.

To get a better insight of the crystalline structure of the SNHs as well as to confirm the growth of the core-shell type α -Fe₂O₃/ZnO SNHs, TEM and HRTEM analysis was performed. From the TEM images (Fig. 5.1.8(a) and 8(b)) it is clear that a 1D core-shell type SNHs is formed with α -Fe₂O₃ core and ZnO shell. The diameter of the α -Fe₂O₃ NWs is nearly 200 nm. It is evident from the TEM micrographs that the ZnO coating is quite uniform on the surface of the α -Fe₂O₃ NWs. The thickness of the ZnO nanolayer varies from 30-40 nm. It is also evident that the ZnO nanolayer consists of tiny ZnO nanocrystals/nanocluster. The HRTEM analysis of the selected area of ZnO nanolayer further confirms the good quality crystalline nature of the ZnO (Fig. 5.1.8(c)). However, the formation of the ZnO nanocluster like layer is quite reasonable because the whole zinc acetate layers on the NWs surface might not get decomposed at the same time to form ZnO. The spacing between the crystal planes of ZnO is measured to be \sim 0.28 nm which corresponds to the (100) plane of ZnO.

The account of chemical composition and the valence state of the elements in the pure α -Fe₂O₃ NWs and ZnO/ α -Fe₂O₃ SNHs have been examined by XPS. Figure 5.1.8(d) shows the high-resolution XPS spectrum of the Zn 2p core level displaying doublet located at 1022.6 and 1045.7 eV, respectively, corresponding to the Zn 2p_{3/2} and 2p_{1/2}. The values of the binding energies and the energy difference (23.15 eV) between the two peaks of the Zn 2p spectrum clearly indicate that the Zn is in the +2 oxidation state in ZnO [29]. The XPS spectrum of the Fe core 2p orbital is shown in Fig. 5.1.8(e). The Fe 2p_{3/2} and Fe 2p_{1/2} peaks located at 711.4 and 725 eV, respectively with another tiny peak appears at 719.1 eV corresponds to the Fe³⁺ oxidation state of iron [30]. The O 1s core level spectrum, shown in Fig. 5.1.8(f), shows the peak centred at 530 eV that can be attributed to the O²⁻ in α -Fe₂O₃ [31] and the Zn-O bond formation because of the O²⁻ ions on the wurtzite crystal structure of the ZnO.

Electrical properties

The local electrical measurements of the pure α -Fe₂O₃ NWs and ZnO/ α -Fe₂O₃ SNHs were performed using the conductive AFM probe (c-AFM) with Pt-Ir coating placed on the top of the sample to build an electrical contact. The experimental set-up with the stable DC bias applied to the aligned arrays nano-heterostructures via the Au layer on which the samples are fabricated is shown in the inset of Fig. 5.1.9(a). Figure 5.1.9(a) shows the current-voltage (I-V) characteristics of a bunch of ZnO/ α -Fe₂O₃ SNHs and pure α -Fe₂O₃ NWs measured at room temperature. The I-V curves show the Ohmic behavior, from the slope of which the resistivity of the samples could be calculated by knowing the diameter and length of the NWs measured from the SEM. In our experiment the resistivity of the pure α -Fe₂O₃ is calculated to be $3.2 \times 10^3 \Omega\text{m}$, which is in good agreement with the reported values [32], as the hematite is known as a poor semiconductor, typically exhibiting a high electrical resistivity of about $10^3 \Omega\text{m}$ [33]. It is evident that the ZnO/ α -Fe₂O₃ SNHs are significantly more electrically conductive. This indicates that the coating of the ZnO nanolayer on the surface of the α -Fe₂O₃ NWs effectively improves the conductivity of the nano heterostructures. The resistivity of the ZnO/ α -Fe₂O₃ SNHs

is measured to be $1.05 \times 10^2 \Omega\text{m}$, one order of magnitude enhancement in the electrical conductivity is observed over the pure α -Fe₂O₃ NWs.

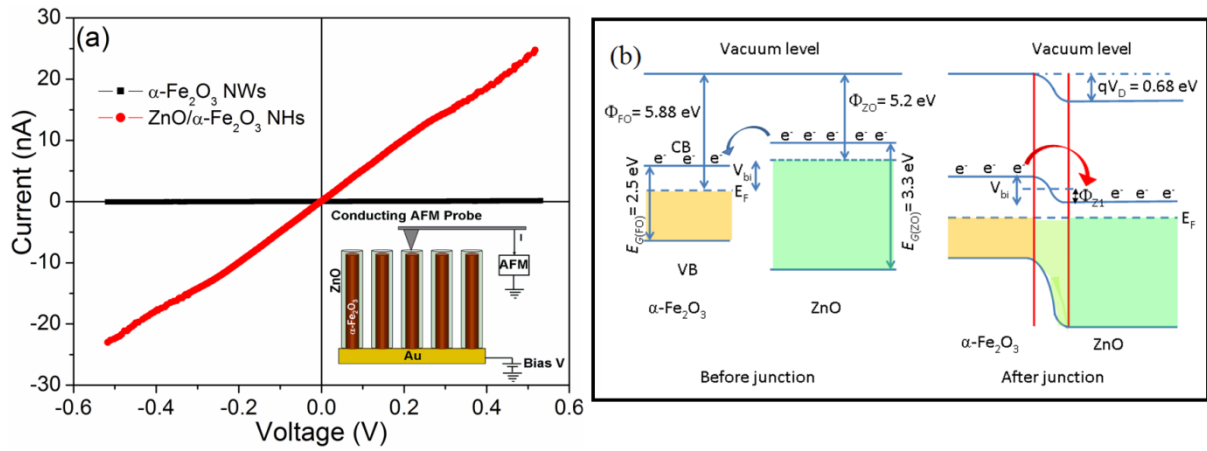


Figure 5.1.9 (a) The room temperature current-voltage curves of the ZnO/ α -Fe₂O₃ SNHs and α -Fe₂O₃ NWs at dark condition. (b) The energy band structures before and after the ZnO/ α -Fe₂O₃ heterojunction is formed.

The enhanced conductivity of the ZnO/ α -Fe₂O₃ SNHs over the pure α -Fe₂O₃ NWs can be explained based on the complex band configuration at the ZnO/ α -Fe₂O₃ semiconductor heterojunction. Both ZnO and α -Fe₂O₃ are n-type semiconductor with different band gap energy and work function. As the work function of ZnO NWs (Φ_{ZnO}) is 5.2 eV which is lower than the work function of α -Fe₂O₃ (Φ_{FO}), i.e. 5.88 eV [34], the electrons are supposed to have easily transferred from ZnO to the α -Fe₂O₃ side if the band bending is not present as shown in Fig. 5.1.9(b) after the heterojunction is formed. Due to the formation of the ZnO/ α -Fe₂O₃ heterojunction a band bending takes place at the interface (see Fig. 5.1.9(b)) and hence a barrier height of Φ_{Z1} is created in the ZnO side, which traps the free electrons in ZnO. Moreover, based on the Anderson model, a 'staggered' type II [19] band configuration is supposed to appear at the ZnO/ α -Fe₂O₃ interface, which will further increase the barrier height to $V_{\text{bi}} = \Phi_{\text{FO}} - \Phi_{\text{ZnO}}$. Therefore, when the heterojunction is formed the free electrons of ZnO nanolayer get trapped in the ZnO side and due to the potential difference at the ZnO/ α -Fe₂O₃ heterojunction interface the free electron from the α -Fe₂O₃ NWs can easily migrate to the ZnO nanolayer as shown in Fig. 5.1.9(b). The formation of the heterojunction brings in more free electrons in the conduction band

of the ZnO/ α -Fe₂O₃ SNHs leading to the enhanced electrical conductivity of the SNHs.

Photoluminescence property

The room temperature (RT) luminescence spectrum of the ZnO/ α -Fe₂O₃ SNHs is shown in Fig. 5.1.10(a). The change of the RTPL characteristics of the ZnO/ α -Fe₂O₃ SNHs with respect to the pure α -Fe₂O₃ NWs is shown in the inset of Fig. 5.1.10(a).

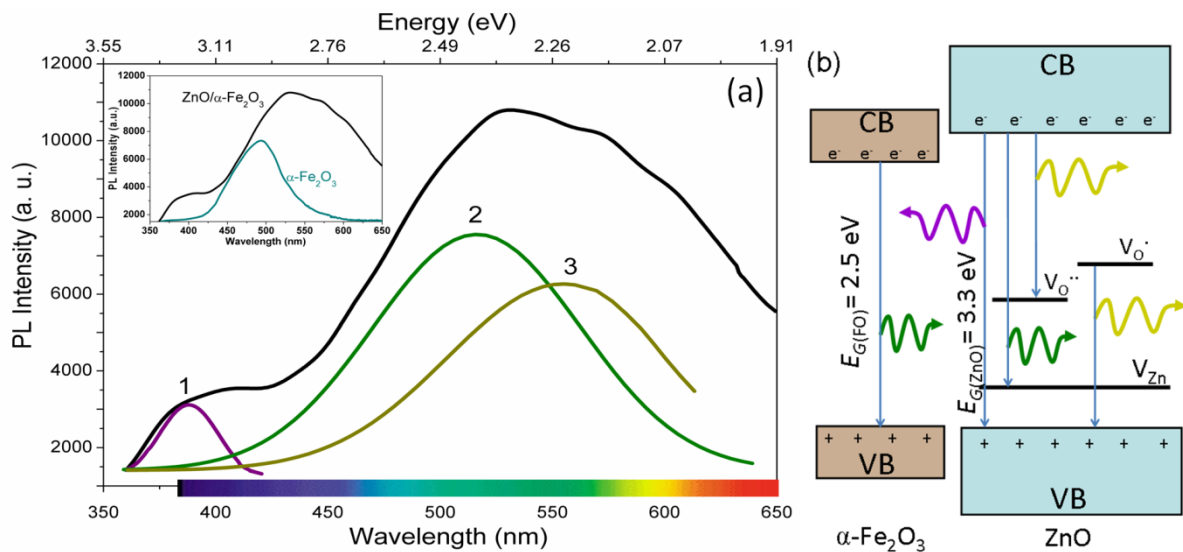


Figure 5.1.10 (a) The deconvolution fitting plots of the room temperature photoluminescence emission spectrum of the ZnO/ α -Fe₂O₃ SNHs. Inset of (a): the change of the photoluminescence emission spectrum of the ZnO/ α -Fe₂O₃ SNHs with respect to pure α -Fe₂O₃ NWs. (b) Schematic model proposed for the different transitions in the α -Fe₂O₃ NWs and ZnO nanolayer to address the PL from the ZnO/ α -Fe₂O₃ SNHs in UV and green wave length region.

Pure α -Fe₂O₃ NWs (inset of Fig. 5.1.10(a)) exhibits a strong band edge green emission peak centred at 496 nm (2.5 eV) as described earlier. Interestingly, after the coating of ZnO nanolayer on α -Fe₂O₃ NWs, the luminescence behaviour of the hybrid nanostructures has improved significantly. The ZnO/ α -Fe₂O₃ SNHs exhibits both the strong near band edge (NBE) UV and the deep level visible green/green-yellow emissions. The complex PL spectrum of the ZnO/ α -Fe₂O₃ NHs can be fitted with three different Gaussian peaks as shown in Fig. 5.1.10(a). The intense UV emission from the ZnO/ α -Fe₂O₃ NHs centred at 387 nm (peak 1) is related to the

NBE emission in ZnO nanolayer corresponds to the free exciton (FX) recombination through an exciton–exciton collision process [35] as shown in Fig. 5.1.10(b). Although, here the UV emission of ZnO nanolayer does not exhibit significant quantum confinement effect, which is quite expected as the Bohr-exciton radius of ZnO is ~ 2 nm. Here, as the intensity of the green emission peak of ZnO/ α -Fe₂O₃ SNHs, situated at 515 nm (peak 2), enhances significantly with respect to that of the pristine α -Fe₂O₃ NWs, it is expected that the most intense green peak (peak 2) of ZnO/ α -Fe₂O₃ NHs is originated due to the band to band electronic transition of α -Fe₂O₃ NWs coupled with the defect related emission from the ZnO nanolayer on α -Fe₂O₃ NWs surface. ZnO nanostructures exhibits visible green/yellow-green emission in the region ranging from 510-560 nm because of the several structural defects such as Zn vacancy (V_{Zn}), oxygen vacancy (V_O), Zn interstitial (Zn_i) and oxygen interstitial (O_i)[36]. Here, the green emission from ZnO nanostructures centred around 510-515 nm is attributed to the V_{Zn} defects [19]. Therefore, the most intense emission ‘peak 2’ of the ZnO/ α -Fe₂O₃ SNHs is ascribed to the combine effect of the band edge emission in α -Fe₂O₃ NWs and the V_{Zn} acceptor-type defect emission [19] from ZnO leading to enhance green emission from the SNHs as shown schematically in Fig. 5.1.10(b). On the other hand, the emission peak 3 situated at 556 nm in the visible yellow-green region is believed to be originated from the oxygen vacancy related defect in ZnO [19]. It is believed that the recombination of the electrons trapped in the singly charged oxygen vacancy (V_O^\bullet) with photoexcited holes at valence band results in the yellow-green emission from ZnO. Another mechanism demonstrates that the surface of the ZnO can trap the photoexcited holes of the valance band and then this hole tunnels back inside the ZnO matrix to recombine with V_O^\bullet to form doubly ionized oxygen vacancy ($V_O^{\bullet\bullet}$) defects. Thereafter, the electronic transition between the conduction band and the $V_O^{\bullet\bullet}$ provide luminescence in the yellow-green wavelength region in ZnO [19].

Magnetic property

Figure 5.1.11(a) shows the room temperature magnetic hysteresis (M - H) loops of the ZnO/ α -Fe₂O₃ SNHs and pristine α -Fe₂O₃ NWs. The α -Fe₂O₃ NWs show weak

room temperature ferromagnetism (RTFM) with saturation magnetization ~ 0.12 emu/g due to canted spin structure and also surface spin disorder (discussed earlier, Chapter 5.1.3).

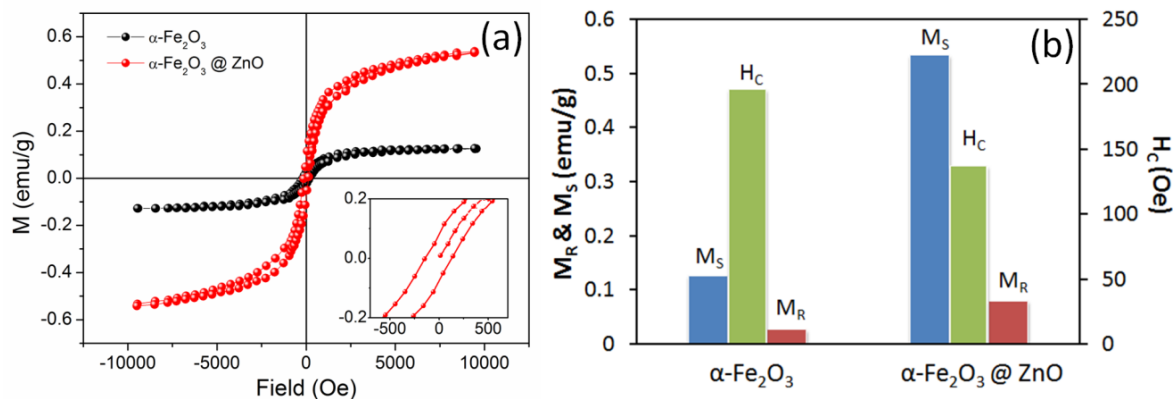


Figure 5.1.11 (a) The M-H plots of the ZnO/ α -Fe₂O₃ SNHs and pure α -Fe₂O₃ NWs measured at $T = 300$ K. Inset of (a) shows the close view of the hysteresis loops of the ZnO/ α -Fe₂O₃ SNHs. (b) The variation of the saturation magnetization (M_s), retentivity (M_r) and coercivity (H_c) of the ZnO/ α -Fe₂O₃ SNHs over the α -Fe₂O₃ NWs.

It is found that after the ZnO coating on α -Fe₂O₃ NWs the magnetic response of the ZnO/ α -Fe₂O₃ SNHs has enhanced significantly. A distinct increase in the saturation magnetization nearly five times of the magnitude in ZnO/ α -Fe₂O₃ SNHs is observed compared with the pure α -Fe₂O₃ NWs. The variation of the saturation magnetization (M_s), retentivity (M_r) and coercivity (H_c) of the ZnO/ α -Fe₂O₃ NHs over the α -Fe₂O₃ NWs is summarized in Fig. 5.1.11(b). However, the enhanced RTFM in the ZnO/ α -Fe₂O₃ SNHs is believed to be not because of a single source but from the contribution of the different origins. In ZnO/ α -Fe₂O₃ SNHs it is expected that the uncompensated spins at the ZnO/ α -Fe₂O₃ interface can strongly influence the order of the core spins through large exchange interaction resulting the ferromagnetic ordering in the matrix. Several reports suggest that injection of spin-polarized carriers can take place at the ferromagnet-semiconductor interface leading to enhance ferromagnetism [19, 38]. Furthermore, the surface spins of the ZnO nanolayer can also induce moments in the ZnO nano shell layer through exchange interaction. Therefore, this exchange coupling between the interfacial/surface spin and the core spin enhances the magnetization of the ZnO/ α -Fe₂O₃ SNHs as a whole.

However, along with this uncompensated interfacial/surface spins the structural defects like V_{Zn} (cation vacancy) and singly ionized oxygen vacancies (Vo^{\bullet}) present in ZnO, as indicated by the PL investigation, can also induce moment in the SNHs. The V_{Zn} defects in ZnO are believed to induce local magnetic moments because of the unpaired $2p$ electrons of the O atoms in the immediate vicinity of the Zn vacancies [19, 39]. Hence, the magnetization of the ZnO/ α -Fe₂O₃ SNHs is found to increase significantly because of the magnetic moments introduced by different sources.

5.1.5 Conclusion

In summary, α -Fe₂O₃ NWs of large surface area have been successfully fabricated by high temperature oxidation of the electrochemically grown metallic iron NWs. These nanowires are composed of large number of nanocrystalline grains making it highly porous. Significant enhancement in band edge emission after Au sputtering is mainly due to the coupling between excited electron-hole pairs in α -Fe₂O₃ NWs and the surface plasmon of Au particles. Magnetization is found to increase almost 16 orders of magnitude which arises due to the trapped metallic electrons at the Au/ α -Fe₂O₃ NWs interface leading to large interfacial moment. In case of ZnO/ α -Fe₂O₃ SNHs, the semiconductor/semiconductor interfacial interaction significantly enhances the electrical conductivity, visible green PL along with the UV emission and the room-temperature ferromagnetism. It is found that the reconstructed band structure at the semiconductor interface of the SNHs helps to enhance their electrical conductivity by increasing the conducting electrons at the surface of the SNHs. The nanoscale coupling of the ZnO/ α -Fe₂O₃ SNHs also influences their PL characteristics, leading to enhancement of the visible green light emission. The uncompensated interfacial spin coupled to the structural defects is found to mediate enhanced magnetization in the SNHs. Therefore, the ZnO/ α -Fe₂O₃ SNHs demonstrate enhanced multifunctionality ideal for electronic, optical, and spintronics device fabrication.

5.2 High Performance Pseudocapacitor Electrodes Based on α -Fe₂O₃/MnO₂ Core - Shell Nanowire Heterostructure Arrays

5.2.1 Preamble

Electrochemical capacitors or supercapacitors are a special class of energy storage materials where energy is stored either by adsorption of ions on electrode surface (Electrical double layer capacitors (EDLCs)) or by fast surface redox reactions (pseudocapacitors) [40-42]. This type of materials can effectively replace conventional batteries in the field of energy harvesting and storage when higher power delivery and uptake is required. Recent advancement in understanding the charge storage mechanism and also huge development in synthesis of different nanostructured materials, significant improvement in the performance of such supercapacitors has been achieved. Generally, the carbon based EDLCs have high power density but they suffer from low specific capacitance and rate capability [4]. In this regard, the pseudocapacitors, based on the transition metal oxides or nitrides can provide higher specific capacitance with good charge/discharge rate capability and long-term cycling stability compared with the EDLCs [41, 44]. The transition metal oxides (TMOs) like MnO₂, nickel oxide, iron oxide, cobalt oxide, TiO₂, MoO₂ and VO_x etc. [45-50] are demonstrated as the ideal electrode materials for pseudocapacitors because of their variant oxidation states for efficient redox charge transfer [40, 51]. Moreover, the low cost, good stability, nontoxic and environment friendly nature of the α -Fe₂O₃ and MnO₂ coupled with their high redox activity makes them suitable for the extensive applications in pseudocapacitors [49, 52]. However, the reported values of the specific capacitance for the nanostructured MnO₂ and α -Fe₂O₃ electrodes are still far below the theoretical values (theoretical specific capacitance for MnO₂ is $\sim 1,370 \text{ F g}^{-1}$ [53] and the theoretical capacity of α -Fe₂O₃ is $\sim 1007 \text{ mAh g}^{-1}$ [54]) as they both suffer from the poor electrical conductivity.

In this section we will discuss about the fabrication of a special kind of 1D core-shell type α -Fe₂O₃/MnO₂ nano-heterostructures (NHs) and explore its electrochemical properties. The α -Fe₂O₃/MnO₂ NHs have the following advantages

as the electrode materials for pseudocapacitors: (1) both of the materials having high redox electroactivity are combined into one ordered nanostructure would potentially help to increase the value of the specific capacitance [49]; (2) the effective surface area of the electrode has been enhanced by many orders of magnitude by using arrays of 1D NWs heterostructure; (3) thin layer of MnO₂ would provide a short ion diffusion path to enable the fast and reversible faradic reaction; (4) the electrical conductivity of α -Fe₂O₃ and MnO₂ are in the range of 10⁻⁴–10⁻⁵ and 10⁻⁵–10⁻⁶ Scm⁻¹, respectively [46, 55, 56] hence, α -Fe₂O₃ NWs being more electrically conducting compare to MnO₂, the α -Fe₂O₃ core would provide a path for the fast electron transport; and (5) α -Fe₂O₃ NWs would also create channels for the effective mass transport of electrolyte too.

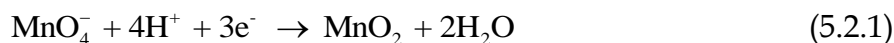
5.2.2 Experimental Methods

Synthesis of the α -Fe₂O₃ NWs

High-density arrays of α -Fe₂O₃ NWs on Au substrate were synthesized by the high-temperature oxidation of the metallic Fe NWs prepared by the template assisted electrochemical deposition route as described earlier in *Chapter 5.1.2*.

Coating of MnO₂ on α -Fe₂O₃ NWs

The nanolayer of MnO₂ was grown on the surface of α -Fe₂O₃ NWs through the reduction of Mn (VII) of the KMnO₄ solution according to the following chemical reaction where the electrons for reduction come from the Au substrate.



For coating process 5 mmol of KMnO₄ and 5 mmol of H₂SO₄ were mixed with 50 mL of deionized water to prepare the precursor solution. To fabricate MnO₂ coated α -Fe₂O₃ NWs, the α -Fe₂O₃ NWs grown on the metallic Au substrate was immersed into the precursor solution maintained at 85°C for 15 min. The thickness of MnO₂ nanolayer on the α -Fe₂O₃ NWs can be easily controlled by adjusting the immersion time. Then the MnO₂ coated α -Fe₂O₃ NWs were rinsed with deionized water and subsequently annealed at 400°C for 30 min in oxygen atmosphere.

5.2.3 Results and Discussions

Morphology, crystallography and chemical composition

The photograph of the as-synthesized α -Fe₂O₃/MnO₂ core-shell NHs is shown in Fig. 5.2.1(a). Figure 5.2.1(b) shows the scanning electron microscopy (SEM) image of the well aligned arrays of as-prepared α -Fe₂O₃/MnO₂ core-shell NHs grown perpendicular to the supporting Au substrate. It is evident from Fig. 5.2.1(b) that the length and the diameter of the 1D NHs are uniform in nature. The transmission electron microscope (TEM) and the scanning transmission electron microscope (STEM) micrographs of the Fe₂O₃/MnO₂ core-shell NHs shown in Fig. 5.2.1(c) and 1(d), respectively, clearly shows the formation of core-shell type NW heterostructure with a nearly uniform coating of the MnO₂ nanolayer on the surface of the 200 nm diameter α -Fe₂O₃ NWs.

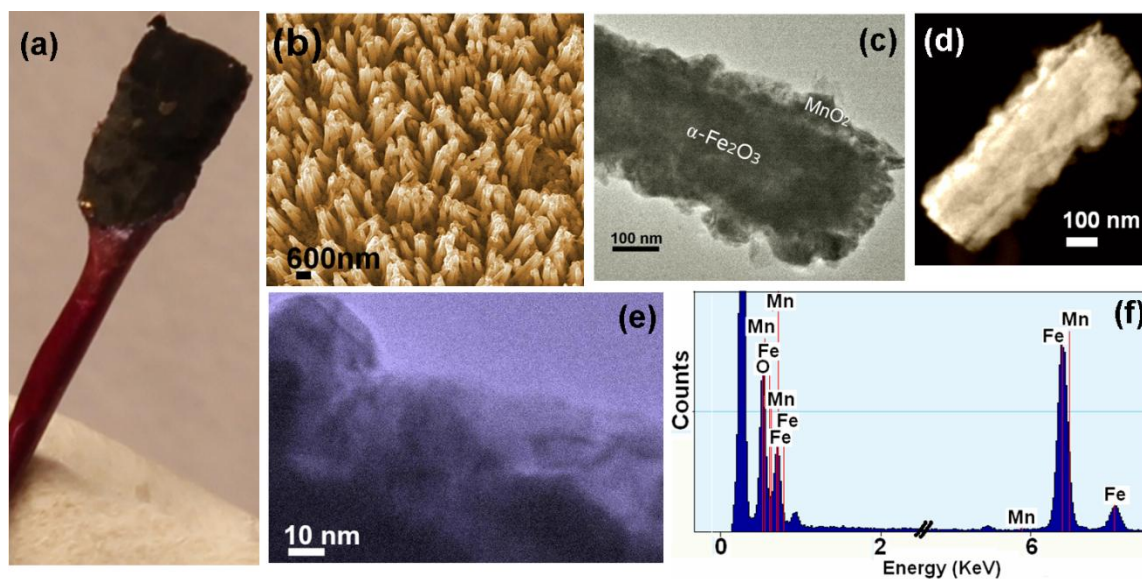


Figure 5.2.1 Photograph of the as-prepared α -Fe₂O₃/MnO₂ core-shell NHs. The (b) SEM, (c) TEM and (d) STEM micrographs of the as-prepared α -Fe₂O₃/MnO₂ core-shell NHs. (e) The HRTEM image of the MnO₂ nanolayer grown on the α -Fe₂O₃ NWs. (f) The EDAX spectrum of the α -Fe₂O₃/MnO₂ core-shell NHs.

It is also evident from figure that the thickness of the MnO₂ nanolayer grown on α -Fe₂O₃ NWs varies in between 40-70 nm. The scanning transmission electron microscopy (STEM) image (Fig. 5.2.1(d)) clearly indicates the formation of good quality α -Fe₂O₃/MnO₂ core-shell NHs. The crystallographic nature of the arrays of

α -Fe₂O₃/MnO₂ core-shell NHs investigated by XRD (Fig. 5.2.2(a)) indicates that the as grown MnO₂ nanolayer on α -Fe₂O₃ NWs is poorly crystallized [43], as there is no peaks corresponding to MnO₂ in the XRD pattern. The diffraction peaks in the XRD pattern appear from the pure rhombohedral phase (space group *R3c*) of the α -Fe₂O₃ NWs (JCPDS file no. 89-0597, *a* = 5.039 Å, *c* = 13.77 Å) and the metallic Au layer underneath the NHs [55]. More information about the crystallographic nature of the MnO₂ nanolayer can be revealed from the HRTEM micrograph (Fig. 5.2.1(e)), which clearly indicates the amorphous/poor crystalline nature of the as-prepared MnO₂ nanolayer. The energy dispersive x-ray (EDAX) spectrum of the α -Fe₂O₃/MnO₂ core-shell NHs, shown in Fig. 5.2.1(f), clearly indicates the presence of Fe, Mn and O in the NHs.

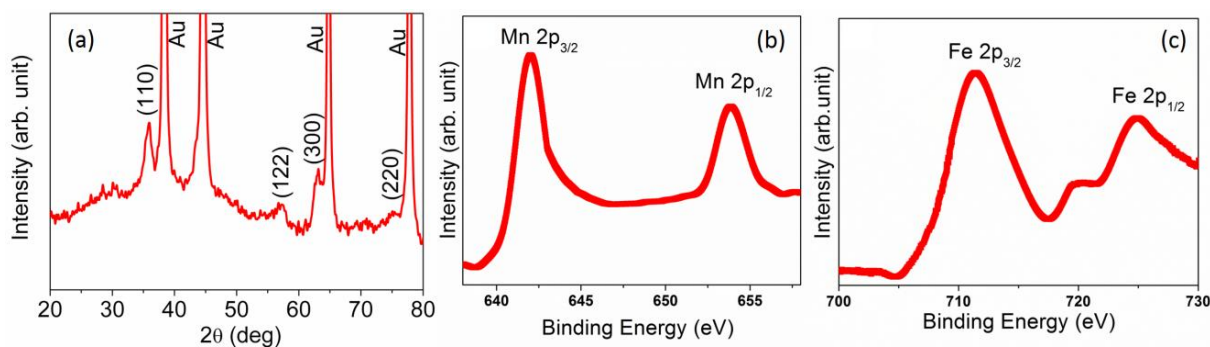


Figure 5.2.2 (a) XRD spectra of α -Fe₂O₃/MnO₂ core-shell NHs; (b) and (c) represent the core level XPS spectra of Mn and Fe elements, respectively, of α -Fe₂O₃/MnO₂ core-shell NHs.

The chemical composition and the valence state of the elements in the as-prepared α -Fe₂O₃/MnO₂ core-shell NHs have been further investigated by the x-ray photoelectron spectroscopy (XPS) (Fig. 5.2.2 (b) and 2(c)). The peaks of Mn 2p_{3/2} and Mn 2p_{1/2} located at 642 and 653.8 eV, respectively, with an energy separation of 11.8 eV, are in good agreement with reported data of Mn 2p_{3/2} and Mn 2p_{1/2} in MnO₂ [57]. The Fe 2p_{3/2} and Fe 2p_{1/2} peaks centered at 711.4 and 725 eV, respectively, with another tiny peak at 719.1 eV correspond to the Fe³⁺ oxidation state of Fe in α -Fe₂O₃ NWs [55]. In this work, the nanolayer of MnO₂ has been grown on the surface of the α -Fe₂O₃ NWs by a facile wet chemical route through the reduction of Mn (VII) of the KMnO₄ solution where the required electron for the reduction was expected to be

supplied by the metallic Au counterpart, on which the α -Fe₂O₃/MnO₂ core-shell NHs have been fabricated.

Electrochemical analysis

The electrochemical properties of the as-prepared α -Fe₂O₃ NWs and the α -Fe₂O₃/MnO₂ NHs were investigated by a three electrode system in 1 M KOH solution (described in *Chapter 2.4.4*). The Faradic redox reactions as represented by the cyclic voltammetry (CV) curves of the as-prepared α -Fe₂O₃ NWs at different scan rates from 2 to 100 mVs⁻¹ are shown in the Fig. 5.2.3(a). All the cyclic voltammograms show distinct pair of redox peaks during the anodic and cathodic sweeps within a voltage window between -0.1 to 0.6 V. These redox peaks arise due to conversion between different oxidation states of iron [Fe (II) \leftrightarrow Fe (III)]. The possible anodic and cathodic reactions can be written as the following reversible reaction:

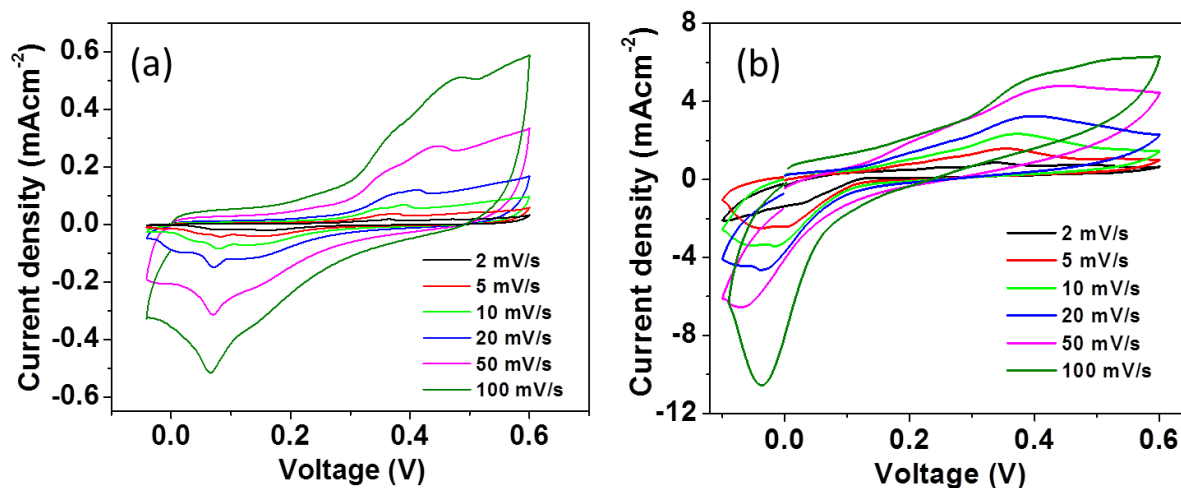
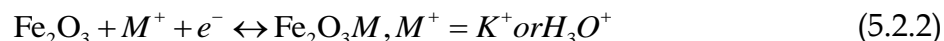


Figure 5.2.3 Cyclic voltammetry curves of the as prepared (a) α -Fe₂O₃ NWs and (b) α -Fe₂O₃/MnO₂ NHs at different scan rates in a 1M KOH solution.

The shape of the CV curves represents the pseudocapacitive behavior of the hematite NWs sample which is significantly different from the typical rectangular CV curves characteristics of the EDLCs [40, 48]. Pseudocapacitance of α -Fe₂O₃ NWs

arises due to the interaction of the Fe³⁺ ions with the K⁺ ions of electrolyte which intercalates/deintercalates at the surface of the α -Fe₂O₃ NWs and also into it through the channels and the pores in the crystal structure of the NWs [40, 48]. The CV curve changes much with increasing scan rate characterized by increasing area under the curve representing the higher capacitive performance and continuous shifting of anodic and cathodic peaks towards higher and lower potentials, respectively leading to a larger potential separation between oxidation and reduction peaks. It is evident from Fig. 5.2.3(a) that all the CV curves exhibit a current leap especially at the upper potential limit which indicates an obvious electrochemical oxidation process.

Figure 5.2.3(b) shows the CV curves of the α -Fe₂O₃/MnO₂ NHs measured at different scan rates and within the same voltage window as that of the hematite NWs. Here, distinct pair of redox peaks can also be observed even at scan rate of 100 mV s⁻¹, indicating that the α -Fe₂O₃/MnO₂ NHs are beneficial for fast redox reactions similar to the α -Fe₂O₃ NW electrodes. The area under the CV curves increases with the increase in scan rate voltage which indicates the higher capacitive charge storage capability of this nanocomposite. Comparison between the CV curves of α -Fe₂O₃/MnO₂ NHs and α -Fe₂O₃ NWs at scan rate of 100 mV s⁻¹ is shown in Fig. 5.2.4(a).

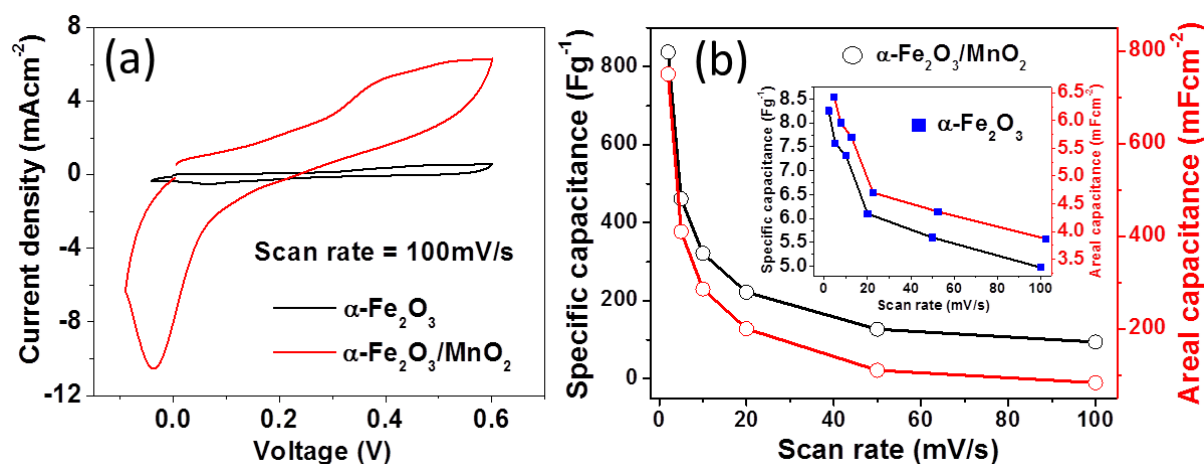


Figure 5.2.4 (a) Comparison between the CV curves of α -Fe₂O₃/MnO₂ NHs and α -Fe₂O₃ NWs at scan rate of 100 mVs⁻¹. (b) Variation of specific capacitance (C_s) and areal capacitance (C_a) as a function of scan rate of α -Fe₂O₃/MnO₂ NHs and α -Fe₂O₃ NWs (Inset).

The larger area of the CV curves in α -Fe₂O₃/MnO₂ NHs as compared to α -Fe₂O₃ NWs at a particular scan rate indicates higher capacitive capability of the former electrode. Nearly 13 times enhancement in current density has been observed in case of α -Fe₂O₃/MnO₂ NHs over the as prepared α -Fe₂O₃ NWs indicating significant enhancement in capacitive performance of α -Fe₂O₃ NWs after MnO₂ coating. However, in this case no obvious current leap at the upper potential limit of the CV curves has been observed, which indicates that the electrochemical oxidation process is completed. Furthermore, it can be seen that the current of the α -Fe₂O₃ electrode and α -Fe₂O₃/MnO₂ nanocomposite electrode responds rapidly to the switching potential, particularly at the potential switching point of 0.6 V, representing smaller equivalent series resistance (ESR) of both the electrodes which is very important to achieve long rate capability and high power density.

To have a quantitative insight of the capacitive performance of the electrode materials, the areal capacitance (C_a , mF cm⁻²) and specific capacitance (C_{sp} , F g⁻¹) of all the nanostructure electrodes were calculated according to the following equations:

$$C_a = \frac{I}{fA} \quad (5.2.3)$$

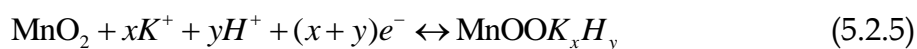
$$\text{and } C_{sp} = \frac{I}{fm} \quad (5.2.4)$$

where, ' $I(A)$ ' is the average cathodic current of the CV loop, ' $f(V/s)$ ' is the scan rate, ' $A(\text{cm}^2)$ ' is the area of the working electrode and ' $m(g)$ ' is the mass of the redox active material of the electrode.

Figure 5.2.4(b) shows the plot of the calculated values of C_{sp} and C_a of the α -Fe₂O₃/MnO₂ NHs electrode as a function of scan rate whereas the corresponding variation for α -Fe₂O₃ NWs electrode is shown in the inset of Fig. 5.2.4(b). Maximum values of the C_{sp} and C_a of the as-prepared α -Fe₂O₃ NWs electrode were found to be nearly 8.3 Fg⁻¹ and 6.4 mFcm⁻², respectively at scan rate of 2 mVs⁻¹. However, after MnO₂ coating over the α -Fe₂O₃ NWs significant enhancement in the values of C_{sp} and

C_a has been observed. For α -Fe₂O₃/MnO₂ nanocomposite electrode, the values of C_{sp} and C_a are found to be nearly 838 Fg⁻¹ and 750 mFcm⁻², respectively at scan rate of 2 mVs⁻¹. Though in case of α -Fe₂O₃/MnO₂ NHs electrode MnO₂ resides on the surface in contact with the electrolyte for charge storage process, effect of α -Fe₂O₃ cannot be neglected because of its finite/considerable capacitance values which will be clarified further when we discuss the galvanostatic charging/discharging process of these electrodes. However, the significant enhancement of the capacitance of the α -Fe₂O₃/MnO₂ NHs electrode is believe to be because of the MnO₂ nanolayer present on the surface of α -Fe₂O₃ NWs. The value of C_{sp} for the α -Fe₂O₃/MnO₂ NHs electrode is found to be much higher than that of the other reported MnO₂ and MnO₂ based nanocomposite electrode such as, thin films of MnO₂ (~ 698 Fg⁻¹), SnO₂@MnO₂ nanowire (~ 637 Fg⁻¹, calculated from CV loops) [43], MnO₂/ZTO/CMF hybrid composite (~ 621.6 Fg⁻¹) [58] and TiN/MnO₂ nanotubes (~ 480 Fg⁻¹) [59]. The specific and areal capacitance of both the nanostructure electrodes decreases with the increase of scan rates. This is because of the fact that higher scan rate limits the accessibility of ions inside every pores of the electrode and only the outermost portion of electrode is utilized for the ion diffusion. However, at higher scan rate of 100 mVs⁻¹ the specific capacitance remains almost 95 Fg⁻¹ for α -Fe₂O₃/MnO₂ nanocomposite electrode whereas the pristine α -Fe₂O₃ NWs retain nearly 60% of its initial charge, as evident from the inset of Fig. 5.2.4(b). This high rate capability of the pristine α -Fe₂O₃ NWs electrode is mainly due to its higher conductivity and porous structure evidenced in our earlier studies (see *Chapter 5.1.3*)[60]. These pores present on the surface of the α -Fe₂O₃ NWs enhance the accessibility of ions inside the NWs which can even possible at higher scan rates rendering high rate capability of specific capacitance.

In case of the α -Fe₂O₃/MnO₂ NHs electrode the charge storage mechanism in MnO₂ is conducted through surface adsorption of electrolyte cations as well as proton incorporation and can be described by following equation:



From Eq. (5.2.2) and Eq. (5.2.5) it can be seen that both the cations and electrons take part in redox reactions of α -Fe₂O₃ and α -Fe₂O₃/MnO₂ nanocomposites. Therefore, it can be concluded that the extent of diffusion of cations on the surface and into the electrode materials followed by the transport of electrons to the current collectors actually decides the pseudocapacitive performance of the electrodes. Increase in specific capacitance after MnO₂ modification of the hematite NWs may be attributed to the fast reversible redox activity of MnO₂ and unique 1D core/shell structure of α -Fe₂O₃/MnO₂ NHs. In this core/shell structure, the high surface area of the thin MnO₂ nanolayer serves as the huge platform for intercalation/deintercalation of the K⁺ ions of electrolyte whereas the core consist of α -Fe₂O₃ NWs having higher conductivity than MnO₂ [55, 57] serves as a fast path for electron transport to the current collector. The thin nanolayer of MnO₂ also serves as the shorter diffusion path for the ions, which can easily diffuse through MnO₂ to intercalate into highly porous and highly redox active α -Fe₂O₃ core providing the high specific capacitance of the NHs at lower scan rates. However, the only 13% capacitance retention of the α -Fe₂O₃/MnO₂ NHs electrode at higher scan rates can be ascribed to the non-uniformity of MnO₂ nanolayer over the α -Fe₂O₃ NWs as evidenced from the TEM image. Relatively thick MnO₂ layer on some places over α -Fe₂O₃ NWs limits the movement of electrons through it to the core due to its lower conductivity ($10^{-5} - 10^{-6}$ Scm⁻¹) together with the lesser ion diffusion into the electrode material at higher scan rates lead to substantial decrease of capacitance at higher scan rates. Furthermore, in the thicker portion, specifically the MnO₂ layer far from the surface layer cannot take part in the ion diffusion effectively because of its low proton diffusion constant ($\sim 10^{-13}$ cm²/ (Vs)) [61]. However, this type of unique 1D core/shell structure of the α -Fe₂O₃/MnO₂ nanocomposite where both of the materials are redox active and porous in nature has its extra advantage for the fabrication of NWs based supercapacitors. It is interesting to observe that the shape of the CV curves for both of the α -Fe₂O₃ NWs and α -Fe₂O₃/MnO₂ NHs electrodes change slightly when the scan rate changes from 2 to 100 mVs⁻¹ indicating that the electrodes possess low polarization because of their higher conductivity.

The electrochemical performance of these 1D asymmetric supercapacitors has been investigated further by galvanostatic (GV) charge/discharge method which is very important for this type of supercapacitor electrodes. As the current density is one of the important parameter that controls the capacitive performance of the electrode, the GV charge/discharge curves of the α -Fe₂O₃ NWs and the α -Fe₂O₃/MnO₂ NHs in 1M KOH solution have been recorded at different current densities and are shown in Fig. 5.2.5(a) and 5(b), respectively.

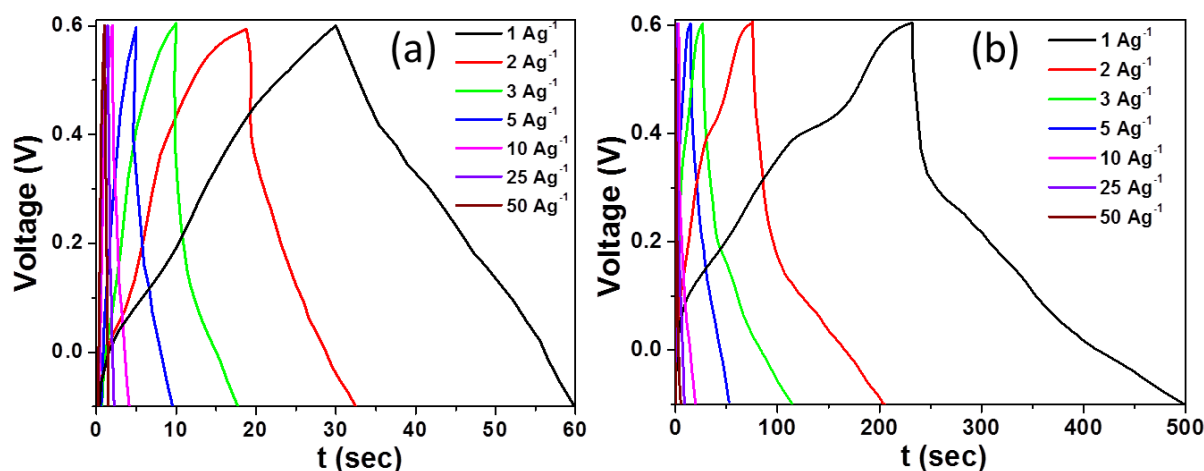


Figure 5.2.5 Constant current charge/discharge curves of the as-prepared (a) α -Fe₂O₃ NWs and (b) α -Fe₂O₃/MnO₂ NHs at different current density.

It is found that the charge/discharge curves of the α -Fe₂O₃ NWs are not ideally linear; the discharging curves are very much symmetric compared with the charging one with a very low voltage drop even at high current density of 2 Ag⁻¹ indicating low internal resistance of the α -Fe₂O₃ NWs electrode. The charging/discharging curves of the α -Fe₂O₃/MnO₂ NHs electrode are not symmetric too but substantially prolonged over the α -Fe₂O₃ NWs electrode indicating the enhanced capacitive behavior of the α -Fe₂O₃ NWs by MnO₂ coating. The discharging process of the α -Fe₂O₃/MnO₂ NHs electrode at different current densities shows two stages; a fast voltage drop which increases with increasing current density followed by a slow discharge. The fast voltage drop is related to the internal resistance of the electrodes however the slow discharge with nonlinear slope represents that the faradic reactions occur on the surface of the α -Fe₂O₃/MnO₂ NHs electrode. Figure 5.2.6(a) shows the comparison of charging/discharging behavior of both types of

electrodes at a constant current density of 1 Ag⁻¹. Higher charging/discharging time for the same voltage window (here 0.7 V) of the α -Fe₂O₃/MnO₂ NHs electrode as compared to α -Fe₂O₃ NWs represents the superior capacitive performance of the former electrode.

The discharge specific capacitance of the asymmetric supercapacitors has been calculated from the discharge curves using following equation:

$$C_{sp} = \frac{I\Delta t}{m\Delta V} \quad (5.2.6)$$

where ' I (A)' is the discharge current, ' Δt (s)' is the discharge time consumed in the potential range of ' ΔV (V)', ' m (g)' is the mass of the active material (or mass of the electrode materials) and ΔV is the potential window.

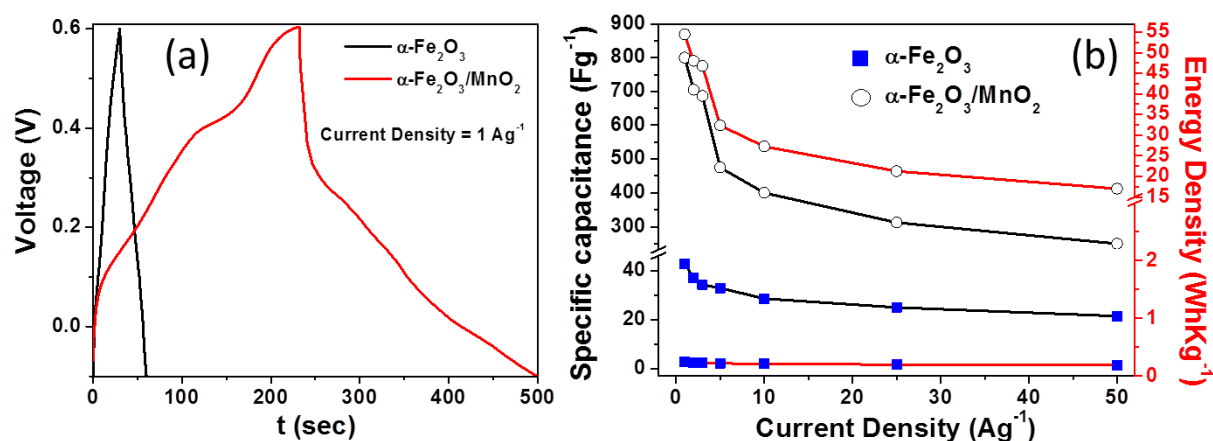


Figure 5.2.6 (a) Comparison between the charge/discharge curves of the α -Fe₂O₃ NWs and α -Fe₂O₃/MnO₂ NHs at the current density of 1 Ag⁻¹. (b) Plotted curve of specific capacitance and energy density of both type of capacitors as a function of current density.

Variation of specific capacitance calculated from the discharge curves as a function of current density for the α -Fe₂O₃ NWs and α -Fe₂O₃/MnO₂ NHs electrodes are shown in Fig. 5.2.6(b). Maximum values of specific capacitance for the α -Fe₂O₃ NWs and α -Fe₂O₃/MnO₂ NHs electrodes have been found to be nearly 42.7 and 801 Fg⁻¹, respectively at a current density of 1 Ag⁻¹. The value of C_{sp} for α -Fe₂O₃/MnO₂ NHs electrode is consistent with the value as calculated from the CV curves, however in case of α -Fe₂O₃ NWs electrode it is much higher than that obtained from

CV loops. This might be because at low current density the cations can intercalate more effectively into the pores of the α -Fe₂O₃ NWs and also in pores of MnO₂. Particularly these pores of the NW based electrodes can serve as “ion-buffering reservoirs” which can supply the OH⁻ ions to sustain sufficient redox reactions at higher current densities for energy storage [62]. From the Fig. 5.2.6(a), it is evident that the Coulombic efficiency (η = discharging time/charging time), which is the measure of competence of ion/charge transfer during an electrochemical reaction is much higher in case of α -Fe₂O₃/MnO₂ NHs electrode as compared with the α -Fe₂O₃ NWs electrode. The specific capacitance decreases with the increase in current density for both the electrodes and tends to stabilize after current density of 3 Ag⁻¹. This behavior is similar to that one as observed in the case of increasing scan rate voltage. This decrease in specific capacitance is mainly due to the limited accessible areas for ions for diffusion with increasing current density. Interestingly, in this charging/discharging process the capacitance retention of the electrodes is much higher than that observed from the CV analysis. Nearly 68% and 52% capacity retention have been observed for α -Fe₂O₃/MnO₂ NHs and α -Fe₂O₃ NWs electrode, respectively at a current density of 50 Ag⁻¹ demonstrating the relatively good high-rate capability of these electrodes.

Energy density and power density are another two important parameters that defines the performance of an electrochemical capacitor. A good electrochemical supercapacitor should possess a high energy density or high specific capacitance at higher current densities. Here, in our studies we also have investigated the performance of the prepared asymmetric supercapacitor electrode materials in terms of these above parameters. The energy density and the power density of both types of electrodes have been calculated according to the following equations:

$$E = \frac{1}{2} C_{sp} (\Delta V)^2 \quad (5.2.7)$$

$$\text{and } P = \frac{E}{t} \quad (5.2.8)$$

where, E (WhKg⁻¹), C_{sp} (F g⁻¹), ΔV (V), t (s) and P (kWkg⁻¹) are the energy density, specific capacitance, potential window of discharge, time of discharge and power density, respectively. The variation of ' E ' with current density for both of the electrode materials is shown in Figure 5.2.6(b). Nearly 18 times enhancement of energy density has been observed for the α -Fe₂O₃/MnO₂ NHs electrode (54 Whkg⁻¹) compare to the α -Fe₂O₃ NWs electrode (2.9 Whkg⁻¹) at a current density of 1 Ag⁻¹. The energy density of α -Fe₂O₃/MnO₂ NHs electrode remains 17 Whkg⁻¹ at the current density as high as 50 Ag⁻¹, indicating good energy storage capability once again.

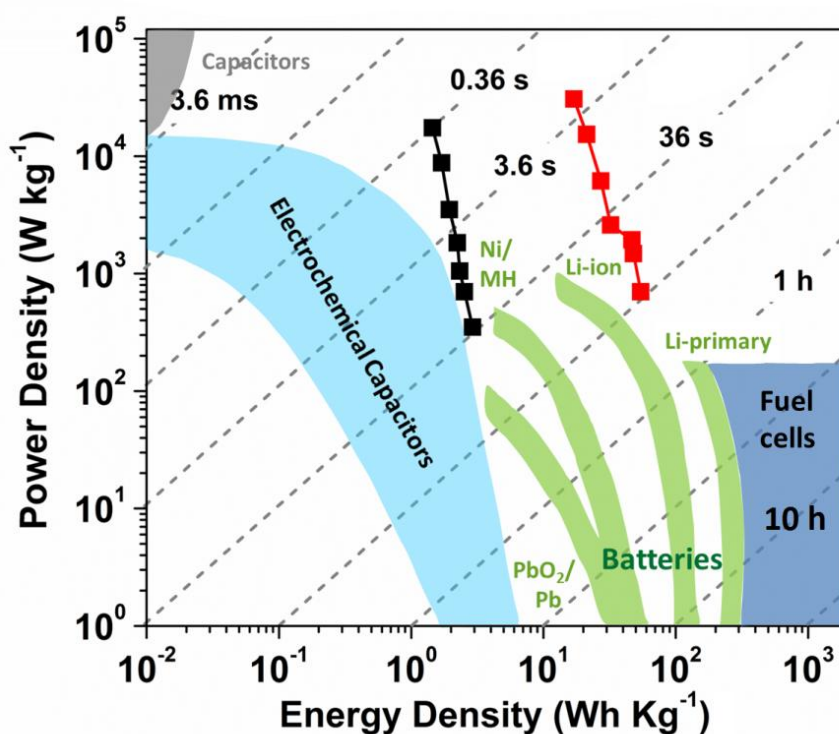


Figure 5.2.7 Ragone plot of the asymmetric supercapacitors consisting of α -Fe₂O₃ NWs (■ black one) and α -Fe₂O₃/MnO₂ NHs (■ red one) as cathode and Pt as anode in comparison with various electrical energy storage devices. Times shown are the time constants of the devices as obtained by dividing energy density by power.

Figure 5.2.7 shows the Ragone plot (power density vs. energy density) of the supercapacitors based on α -Fe₂O₃ NWs and α -Fe₂O₃/MnO₂ NHs electrodes derived from the constant current charging/discharging curves in comparison with some advanced aqueous-based supercapacitors. The power density of α -Fe₂O₃ NWs

electrode is found to be $\sim 17.4 \text{ kWkg}^{-1}$ at an energy density of 1.5 Whkg^{-1} , which is competitive with the Ni-MH batteries and significantly higher as compared with the other currently available electrochemical capacitors. Interestingly, this amount of power density of pristine α -Fe₂O₃ NWs electrode can solely fulfill the power target (15 kWkg^{-1}) of the Partnership for a New Generation of Vehicles (PNGV) [43]. Moreover, the energy density reaches as high as 54.4 Whkg^{-1} at a power density of 700 Wkg^{-1} for the α -Fe₂O₃/MnO₂ NHs supercapacitor. However, the α -Fe₂O₃/MnO₂ nanocomposite electrode can still possess a specific energy of 17 Whkg^{-1} as the power density increases even as high as 30.6 kWkg^{-1} . This type of high power and energy performance of the α -Fe₂O₃/MnO₂ NHs electrode is much more superior to the Ni-MH batteries and other conventional electrochemical supercapacitors and even highly competitive with the Li-ion batteries as is also evident from the Ragone plot.

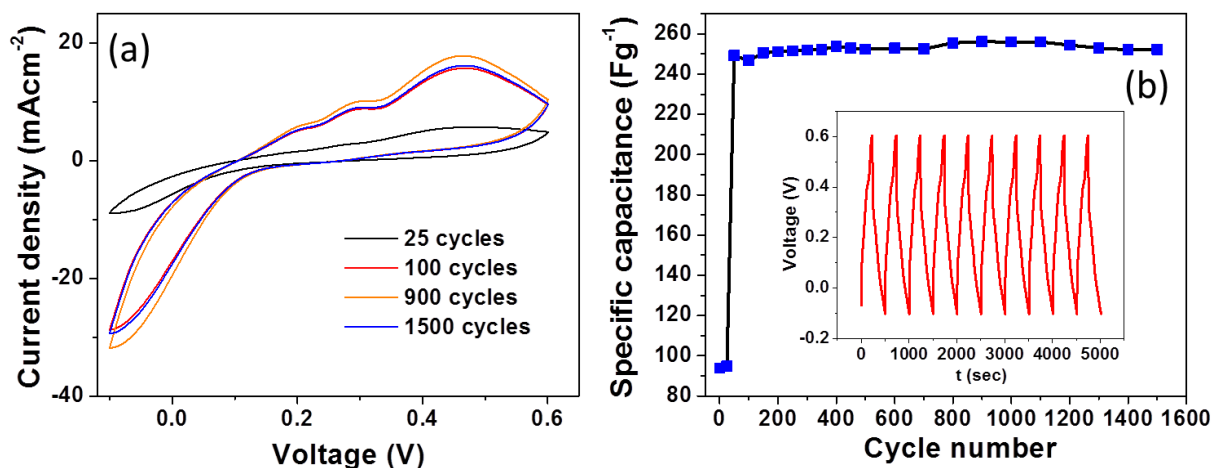


Figure 5.2.8 (a) Cyclic voltammetry curves of different cycles of α -Fe₂O₃/MnO₂ composite capacitor measured in a 1M KOH solution at a scan rate of 100 mVs^{-1} ; (b) variation of specific capacitance of α -Fe₂O₃/MnO₂ composite with cycle number for their long cycle stability test (Inset shows the charging-discharging nature after 10 cycles).

The long cycle life is another important parameter for investigating the performance of a supercapacitor. The long term cycle ability of the α -Fe₂O₃/MnO₂ NHs electrode was evaluated by repeating the CV test at a scan rate of 100 mVs^{-1} for 1500 cycles, as shown in Fig. 5.2.8(a). All the CV curves are nearly symmetric in nature and the curves after 50 cycles are almost overlapping indicating good cyclic

capability of the 1D nanocomposite pseudocapacitor. The specific capacitance, calculated using Eq. (5.2.4), as a function of cycle number is presented in Fig. 5.2.8(b). It is evident from the figure that the specific capacitance remains almost constant at the beginning ($\sim 93 \text{ Fg}^{-1}$ up to 25 cycles), then suddenly jumps to a value of $\sim 249 \text{ Fg}^{-1}$ after 50 cycles. Specific capacitance increases up to a maximum value of 256.1 Fg^{-1} after 800 cycles, then subsequently decreases slightly and becomes almost constant at a value of 253 Fg^{-1} at the end of 1500 cycles. It is interesting that the specific capacitance increases almost 2.6 times after 50 cycles. This phenomenon is indicative of the fact that there is an initial activation process for the faradic pseudocapacitance of the α -Fe₂O₃/MnO₂ NHs electrodes [45, 62]. After 800 cycles specific capacitance decreases only 1.5% of the maximum value of capacitance. This decrease of capacitance can be ascribed to the mechanical expansion of MnO₂ nanolayer due to continuous ion insertion/deinsertion process or dissolution of some amount of MnO₂ into electrolyte. The galvanostatic charge-discharge cyclic curves of the first ten cycles at 1 Ag^{-1} for the α -Fe₂O₃/MnO₂ NHs electrodes (as shown in the inset of Fig. 5.2.8(b)) also confirm the long cycle stability of these nanowire electrodes. However, the electrolyte remains transparent after 1500 cycles, indicates minimal dissolution of MnO₂ into the electrolyte solution after the long-term cycling test which has been considered as the main reason behind the capacitance loss of MnO₂ based supercapacitors. Therefore, this study suggests that the α -Fe₂O₃/MnO₂ NHs electrode is very stable during the long term cycling test.

5.2.4 Conclusions

In this section we have described the facile synthesis of 1D core-shell α -Fe₂O₃/MnO₂ nanoheterostructures and analyzed their electrochemical properties for their use as pseudocapacitors electrodes. The α -Fe₂O₃ NWs electrode exhibits specific capacity of nearly 42 Fg^{-1} at a current density of 1 Ag^{-1} due to its highly porous structure which allows the cations to diffuse more into the electrode material. The specific capacitance is found to increase remarkably when the surface of α -Fe₂O₃

NWs is modified with MnO₂ nanolayer. Nearly 801 Fg⁻¹ of specific capacitance have been observed for the α -Fe₂O₃/MnO₂ NHs electrode at a current density of 1 Ag⁻¹. The superior electrochemical performance of the MnO₂/ α -Fe₂O₃ NHs can be ascribed to the unique 1D core/shell structure of the nanocomposite where the thin highly redox active MnO₂ shell serves as large platform for ion diffusion and the higher conductive core (α -Fe₂O₃) provides highway for fast electron transport. Transparent electrolyte solution after 1500 electrochemical cycles indicates minimal dissolution of MnO₂ i.e. long cycle stability of the α -Fe₂O₃/MnO₂ NHs. The energy density and power density of the α -Fe₂O₃/MnO₂ NHs electrode have been found to be 17 Whkg⁻¹ and 30.6 kWkg⁻¹, respectively at a current density of 50 Ag⁻¹, indicates the good rate capability of the nanocomposite electrode. Here, it is found that the unique 1D core/shell α -Fe₂O₃/MnO₂ nanoheterostructure made of environment friendly, light-weight, extremely low cost, highly redox active and nontoxic materials is highly efficient in energy conversion and storage systems for the effective use of renewable energy.

Bibliography

- [1] J. Chen, L. Xu, W. Li, and X. Gou, *Adv. Mater.* 17, 582 (2005).
- [2] Y. C Lee, Y. L Chueh, C. H Hsieh, M. T Chang, L. J Chou, Z. L Wang, Y. W Lan, C. D Chen, H. Kurata, and S. Isoda, *Small* 3,1356 (2007).
- [3] X. Hu, J. C. Yu, J. Gong, Q. Li, and G. Li, *Adv. Mater.* 19, 2324 (2007).
- [4] Z. Chen, U. Cvelbar, M. Mozetic, J. He, and M. K. Sunkara, *Chem. Mater.* 20, 3224 (2008).
- [5] R. Dieckmann, *Phil. Mag. A* 68, 725 (1993).
- [6] Z. Y. Fan, X. G. Wen, S. H. Yang, and J. G. Lu, *Appl. Phys. Lett.* 87, 013113 (2005).
- [7] L. C Hsu, Y. Y Li, and C. Y. Hsiao, *Nanoscale Res. Lett.* 3, 330 (2008).
- [8] N. Beermann, L. Vayssieres, S. E. Lindquist, and A. Hagfeldt, *J. Electrochem. Soc.* 147, 2456 (2000).
- [9] Y. W. Zhu, T. Yu, C. H. Sow, Y. J. Liu, A. T. S. Wee, X. J. Xu, C. T. Lim, and J. T. L. Thong, *Appl. Phys. Lett.* 87, 023103 (2005).
- [10] W. Zhou , C. Cheng , J. Liu , Y. Y. Tay , J. Jiang , X. Jia, J. Zhang , H. Gong , H. H. Hng , T. Yu, and H. J. Fan, *Adv. Funct. Mater.* 21, 2439 (2011).
- [11] J. Jin, S. Ohkoshi, and K. Hashimoto, *Adv. Mater.* 16, 48 (2004).
- [12] M. F. Hansen, C. B. Koch, and S. Mørup, *Phys. Rev. B* 62, 1124 (2000).
- [13] M. K. Lee, T. G. Kim, W. Kim, and Y. M Sung, *J. Phys. Chem. C* 112, 10079 (2008).
- [14] C. W. Cheng, E. J. Sie, B. Liu, C. H. A. Huan, T. C. Sum, H. D. Sun, and H. J. Fan, *Appl. Phys. Lett.* 96, 071107 (2010).
- [15] A. Bera, and D. Basak, *Nanotechnology* 22, 265501 (2011).
- [16] L. Wang, J. Luo, Q. Fan, M. Suzuki, I. S. Susuki, M. H. Engelhard, Y. Lin, N. Kim, J. Q. Wang, and C. J. Zhong, *J. Phys. Chem. B* 109, 21593 (2005).
- [17] S. Banerjee, S. O. Raja, M. Sardar, N. Gayathri, B. Ghosh, and A. Dasgupta, *J. Appl. Phys.* 109, 123902 (2011).
- [18] G. G. Khan, D. Sarkar, A. K. Singh and K. Mandal, *RSC Advances* 3, 1722 (2013).

- [19] D. Sarkar, G. G. Khan, A. K. Singh and K. Mandal, *J. Phys. Chem. C* 116, 23540 (2012).
- [20] C. Colliex, T. Manoubi and C. Ortiz, *Phys. Rev. B* 44, 11402 (1991).
- [21] Y. L. Chueh, M. W. Lai, J. Q. Liang, L. J. Chou, and Z. L. Wang, *Adv. Funct. Mater.* 16, 2243 (2006).
- [22] M. B. Sahana, C. Sudakar, G. Setzler, A. Dixit, J. S. Thakur, G. Lawes, R. Naik, V. M. Naik, and P. P. Vaishnava, *Appl. Phys. Lett.* 93, 231909 (2008).
- [23] K. Okamoto, I. Niki, A. Shvartser, Y. Narukawa, T. Mukai, and A. Scherer, *Nat. Mater.* 3, 601 (2004).
- [24] W. F. Yang, R. Chen, B. Liu, G. G. Gurzadyan, L. M. Wong, S. J. Wang, and H. D. Sun, *Appl. Phys. Lett.* 97, 061104 (2010).
- [25] N. Amin, and S. Arajs, *Phys. Rev. B* 35, 4810 (1987).
- [26] M. Venkatesan, C. B. Fitzgerald, and J. M. D. Coey, *Nature* 430, 630 (2004).
- [27] A. M. Clogston, *Phys. Rev. Lett.* 19, 583(1967).
- [28] D. Schroerer, and R. C. Nininger, *Phys. Rev. Lett.* 19, 632 (1967).
- [29] D.K. Mishra, P. Kumar, M. K. Sharma, J. Das, S.K. Singh, B.K. Roul, S. Varma, R. Chatterjee, V.V. Srinivasu, and D. Kanjilal, *Physica B* 405, 2659 (2010).
- [30] W. B. Luo, J. Zhu, Y. R. Li, X. P. Wang, D. Zhao, J. Xiong, and Y. Zhang, *Appl. Phys. Lett.* 91, 082501 (2007).
- [31] T. Fujii, F.M.F. de. Groot, G.A. Sawatzky, F.C. Voogt, T. Hibma, and K. Okada, *Phys. Rev. B* 59, 3195 (1999).
- [32] J. A. Glasscock, P. R. F. Barnes, I. C. Plumb, and N. J. Savvides, *J. Phys. Chem. C* 111, 16477 (2007).
- [33] F. J. Morin, *Phys. Rev.* 83, 1005 (1951).
- [34] J. Zhang, X. Liu, L. Wang, T. Yang, X. Guo, S. Wu, S. Wang, and S. Zhang, *Nanotechnology* 22, 185501 (2011).
- [35] Y. C. Kong, D. P. Yu, B. Zhang, W. Fang, and S. Q. Feng, *Appl. Phys. Lett.* 78, 407 (2001).
- [36] C. H. Ahn, Y. Y. Kim, D. C. Kim, S. K. Mohanta, and H. K. Cho, *J. App. Phys.* 105, 013502 (2009).

- [37] A. F. Kohan, G. Ceder, D. Morgan, and C. G. V. d. Walle, *Phys. Rev. B* 61, 15019 (2000).
- [38] P. R. Hammar, B. R. Bennett, M. J. Yang, and M. Johnson, *Phys. Rev. Lett.* 83, 203 (1999).
- [39] Q. Wang, Q. Sun, G. Chen, Y. Kawazoe, and P. Jena, *Phys Rev. B* 77, 205411 (2008).
- [40] P. Simon, and Y. Gogotsi, *Nat. Mater.* 7, 845 (2008).
- [41] G. Yu, L. Hu, N. Liu, H. Wang, M. Vosgueritchian, Y. Yang, Y. Cui, and Z. Bao, *Nano. Lett.* 11, 4438 (2011).
- [42] W. Chen, R. B. Rakhi, L. B. Hu, X. Xie, Y. Cui, and H. N. Alshareef, *Nano Lett.* 11, 5165 (2011).
- [43] J. Yan, E. Khoo, A. Sumboja, and P. S. Lee, *ACS Nano* 4, 4247 (2010).
- [44] C. C. Hu, K. H. Chang, M. C. Lin, and Y. T. Wu, *Nano Lett.* 6, 2690 (2006).
- [45] R. B. Rakhi, W. Chen, D. Cha, and H. N. Alshareef, *Nano Lett.* 12, 2559 (2012).
- [46] X. Lu, G. Wang, T. Zhai, M. Yu, J. Gan, Y. Tong, and Y. Li, *Nano Lett.* 12, 1690 (2012).
- [47] M. Toupin, T. Brousse, and D. Bélanger, *Chem. Mater.* 16, 3184 (2004).
- [48] M. Zhu, Y. Wang, D. Meng, X. Qin, and G. Diao, *J. Phys. Chem. C* 116, 16276 (2012).
- [49] J. Liu, J. Jiang, M. Bosman, and H. J. Fan, *J. Mater. Chem.* 22, 2419 (2012).
- [50] C. C. Huang, W. Xing, and S. P. Zhuo, *Scr. Mater.* 61, 985 (2009).
- [51] M. Jayalakshmi, and K. Balasubramanian, *Int. J. Electrochem. Sci.* 3, 1196 (2008).
- [52] H.-W. Lee, P. Muralidharan, R. Ruffo, C. M. Mari, Y. Cui, and D. K. Kim, *Nano Lett.* 10, 3852 (2010).
- [53] J.-G. Wang, Y. Yang, Z.-H. Huang, and F. Kang, *J. Mater. Chem.* 22, 16943 (2012).
- [54] S.-L. Chou, J.-Z. Wang, D. Wexler, K. Konstantinov, C. Zhong, H.-K. Liuab, and S.-X. Dou, *J. Mater. Chem.* 20, 2092 (2010).
- [55] D. Sarkar, G. G. Khan, A. K. Singh, and K. Mandal, *J. Phys. Chem. C* 116, 23540 (2012).

- [56] L. B. Hu, W. Chen, X. Xie, N. Liu, Y. Yang, H. Wu, Y. Yao, P. Mauro, H. N. Alshareef, and Y. Cui., ACS Nano 8904 (2011).
- [57] A. L. M. Reddy, M. M. Shaijumon, S. R. Gowda, and P. M. Ajayan, Nano Lett. 9, 1002 (2009).
- [58] L. Bao , J. Zang , and X. Li, Nano Lett. 11, 1215 (2011).
- [59] S. Dong, X. Chen, L. Gu , X. Zhou , L. Li , Z. Liu , P. Han , H. Xu , J. Yao , H. Wang , X. Zhang , C. Shang , G. Cui, and L. Chen, Energy Environ. Sci. 4, 3502 (2011).
- [60] G. G. Khan, D. Sarkar, A. K. Singh, and K. Mandal, RSC Advances 3, 1722 (2013).
- [61] Y. He, W. Chen, X. Li, Z. Zhang, J. Fu, C. Zhao, and E. Xie, ACS Nano DOI: 10.1021/nm304833s.
- [62] X. Zhang, W. Shi, J. Zhu, W. Zhao, J. Ma, S. Mhaisalkar, T. L. Maria, Y. Yang, H. Zhang, H. H. Hng, and Q. Yan, Nano Res. 3, 643 (2010).

Chapter 6

Conclusion and Scope for Future Work

This chapter gives an overall conclusion of the work described so far and also the scopes for further work in this specific field.

6.1 Epilogue

This thesis contains the details about the synthesis of different interesting nanostructures of Iron and its oxides (α -Fe₂O₃ and Fe₃O₄) and study of their structure dependent electronic, opto-electronic and magnetic properties.

We have prepared nano-hollow spheres of Fe₃O₄, nanochains of core-shell Fe-Au, α -Fe₂O₃ and Fe₃O₄ and nanowires of α -Fe₂O₃ by template free and templated assisted chemical routes. The uniform shape of the hollow spheres is confirmed by the SEM images which also suggest that the spheres are made of nanocrystalline Fe₃O₄ grains. We have changed the size of the hollow spheres by changing the PVP concentration in the solution. The size of the spheres has significantly influenced the magnetic and electronic properties of these spheres. Actually, the size changes the domain structures, as evident from the MFM images, which controls the magnetic properties. However, with increase of size the domains changes from PSD to MD configuration estimated from the Day's plot. On the other hand, reducing the sphere size incorporates larger number of grain boundaries which reduces the electronic conductivity of the material. All the spheres show ferromagnetic behavior with maximum magnetization (87 emu/g) for largest sphere (725 nm diameter). The AC magnetic behavior of these spheres has measured in a lab made setup. The coercivity increases with increasing frequency due to larger fraction of ferromagnetic particles at higher frequencies. The power loss, measured from the AC hysteresis loops, is higher for smaller spheres and increases with increasing frequency. These hollow spheres have large effective surface area because of their accessible inner and outer surfaces which is very efficient for dye adsorption. The dye adsorption capacity of these spheres is measured by applying Langmuir isotherm model. The maximum adsorption capacity (q_m) is found to be 96.7 mg/g and 141.6 mg/g for Eosin and MB dye, respectively for 185 nm hollow spheres.

DNA is effectively used for fabrication of chainlike structure of the nanoparticles. Electrostatic attraction between oxygen anion of the phosphate backbone of DNA with the metallic cations makes this technique possible. This interaction is evidenced from the FTIR spectrum of the DNA-metal/metal oxide

nanochains. Gold coating over the iron nanoparticles prevents it from oxidation and also suppresses its high surface activity. This interaction also enhances the anisotropy energy of the functional nanoparticles which results ferromagnetic behavior of $\text{Fe}_{\text{core}}\text{-Au}_{\text{shell}}$ nanochains of 16 nm width and higher Morin temperature for $\alpha\text{-Fe}_2\text{O}_3$ nanochains. For Fe_3O_4 nanochains, size changes the anisotropy energy resulting change in blocking temperature (T_B) as evident from the FC-ZFC measurements. Formation of nonmagnetic shell over the ferromagnetic core reduces the M_S value of Fe_3O_4 nanoparticles compare to the bulk. It is found that the thickness of the nonmagnetic shell increases with decreasing size of the nanoparticles. AC susceptibility measurement shows non-interacting single domain behavior of the smallest Fe_3O_4 particles (7 nm diameter).

At last, we have prepared arrays of $\alpha\text{-Fe}_2\text{O}_3$ NWs through electrodeposition technique followed by annealing in ambient atmosphere. The NWs are composed of smaller nanocrystals formed during oxidation process which shows significant quantum confinement effect as evidenced from the PL spectrum. The surface modification of these NWs with Au and ZnO enhances their magnetic and PL properties though have different reasons. However, the ZnO coating is more efficient because of the presence of intrinsic vacancies (cation vacancy, oxygen vacancy etc.) of ZnO that have significant contribution in enhancing the PL and magnetic properties of the $\alpha\text{-Fe}_2\text{O}_3/\text{ZnO}$ hybrid nanostructure. ZnO coating also enhances the electrical conductive property of the $\alpha\text{-Fe}_2\text{O}_3/\text{ZnO}$ semiconductor nanoheterostructure (SNHs). Pseudocapacitive performance of these $\alpha\text{-Fe}_2\text{O}_3$ NWs is found to be much profound because of its high redox activity and porous surface morphology. Moreover, this capacitive performance is enhanced significantly (16 times enhancement of specific capacity) after the MnO_2 coating over the pristine $\alpha\text{-Fe}_2\text{O}_3$ NWs. Not only that, the energy and the power density has also increased for core/shell $\alpha\text{-Fe}_2\text{O}_3/\text{MnO}_2$ NWs which is due to unique core-shell nature of this nanostructure where the thin layer of highly redox active MnO_2 provides short diffusion path for electrons to the core whereas the core consists of higher conductive $\alpha\text{-Fe}_2\text{O}_3$, acts as highway for fast electron transport to the current collector.

6.2 Scope for future work

Ferrites have been widely used for high frequency applications during last few decades. Hollow sphere of magnetite will be very efficient in this field because of its hollow nature which also changes the refractive index of the material. The significant power loss of these spheres at high frequencies can be utilized to destroy diseased cells through magnetic hyperthermia. Moreover, the hollow interior can be an efficient platform for drug delivery and their controlled release. Additionally, as these spheres are efficient in dye adsorption, they can be used to isolate heavy metals like arsenic (As), antimony (Sb) etc. from ground water through the same adsorption procedure.

Functionalization of magnetic materials with DNA makes it more biocompatible. This template route synthesis of nanoparticles can also be used for the formation of various unagglomerated nanostructures. These DNA templated materials can be attached to the cancer cells selectively and also to kill those cells.

Multifunction pristine α -Fe₂O₃ and hybrid nanowires can be used for fabrication of magnetic, electronic and also opto-electronic devices. The intrinsic properties of α -Fe₂O₃ NWs can also be improved via surface modification by TiO₂, SnO₂ etc. Pristine α -Fe₂O₃ NWs and its composites can be very effective as electrode material for supercapacitors. As it is mainly a surface related process, fabrication of intricate nanostructures of α -Fe₂O₃ with very large effective surface area is very promising for fabrication of supercapacitors with high power as well as high energy density.